Diplexers and Multiplexers Design by Using Coupling Matrix Optimisation

Wenlin Xia

A thesis submitted to the University of Birmingham for the degree of Doctor of Philosophy

School of Electronic, Electrical and Systems Engineering

The University of Birmingham

April, 2015

Abstract

Microwave filters and multiplexers are used in many application areas and have been studied for decades. However, with increasing demands on communications and radar systems more complex filters are required which not only have superior performance but also are required to be small and lightweight. This thesis looks at new techniques in microwave filter design to achieve these aims.

Coupled resonator circuits are of importance for design of RF/microwave narrow-band filters with any type of resonator regardless its physical structure. The coupling matrix is used to represent the coupled resonator circuit. Each matrix entry value refers to a physical dimension of the circuit. The response of the circuit can also be calculated by using the coupling matrix.

Different methods are developed to generate the coupling matrix. This thesis presents designs of the coupled resonator based diplexers and multiplexers by using the coupling matrix local optimisation technique. By altering the values of the matrix, the optimisation program search for a particular matrix with the desired circuit response. The initial values of the matrix, which is used as the input of the optimiser, have a great effect on the convergence of the final result of the optimisation. The principles of generating the good initial values of the matrix are included in this thesis. The design procedures and measurement performance of 3 X-band (8.2-12.4 GHz) rectangular waveguide circuits, including a 10th order diplexer, a 4th order diplexer with cross-couplings and a 4-channel multiplexer, are presented.

A novel computer-aided physical structure tuning technique, called Step Tune method, is also presented in this thesis. Instead of conventionally tuning the whole structure, we simulate and tune just part of the circuit by using the new method. As only limited number of physical dimensions is tuned each time, the final result is more reliable.

Acknowledgement

I would like to express my deepest gratitude to my supervisor Professor Michael Lancaster for his support and guidance throughout my research. I would also like to express my appreciation to my progress report assessor Dr. Fred Huang for his useful advices.

I would like to extend my sincerest thanks to my colleagues in the Emerging Device Technology Research Group at the University of Birmingham for their support over these years. In particular, I would like to thank Dr. Xiaobang Shang for many inspiring discussions over the project, Mofei Guo for both academic and personal help, Ekasit Nugoolcharoenlap for the discussion on the n+2 coupling matrix theory, Rashad Hassan Mahmud for the discussion on my thesis writing, Tianhao He for his talented photography technique. I'm also thankful Mr. Warren Hay for fabricating the waveguide devices presented in the thesis.

Thanks to all of my friends at the University of Birmingham, especially, Mao Li, Yang Yue, Hao Li and Bing Hua, for their support after hours; and my Big Chefs, Leyang Xu and Yang Yang, for their guidance on my cooking.

My appreciation goes to all of my friends in China, especially, Lei Wang and Hongbing Wang, for their encouragement over my life aboard.

Special thanks to Mr Dongqing Cao and Mr Xigen Zhu, my high school teachers, for their words and experiences which raised me up.

Finally, my sincere gratitude goes to my family: my father Bangren Xia, my mother Suying Lin and my uncle Zhigang Dai. Their love and support made my success possible. My life is meaningful because of my family.

Table of Contents

Chapter 1 Introduction

1.1 Overview of Diplexers and Multiplexers, and Their Applications

Signals are transmitted (TX) and received (RX) through antennas in a wireless communication system. In order to save the space and cost, a single antenna is generally shared by both TX and RX channels working at different frequencies [1]. Diplexers and Multiplexers are applied here to channelize signals of different frequencies. Diplexers are for 2 channels while multiplexers are for multiple channels. As the key components in the communication system, diplexers and multiplexers are used in cellular base stations, satellite payload systems, Wi-Fi and WiMAX systems, and many other microwave systems.

Conventionally, a multiplexer is formed of a set of filters, usually known as the channel filters, and a common junction for the signal division [2]. The structure of a traditional multiplexer with *n*-channel is given in Figure 1.1.

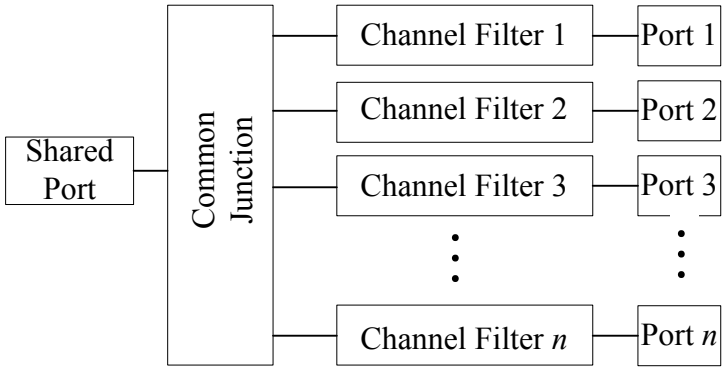

Figure 1.1 Block diagram of the multiplexer.

The multiplexer is critical part of the conventional satellite payload system [2]. The block diagram of a satellite payload system is shown in Figure 1.2. It is formed of an antenna for signal reception and transmission, a low-noise receiver, input and output multiplexers, and high-power amplifiers.

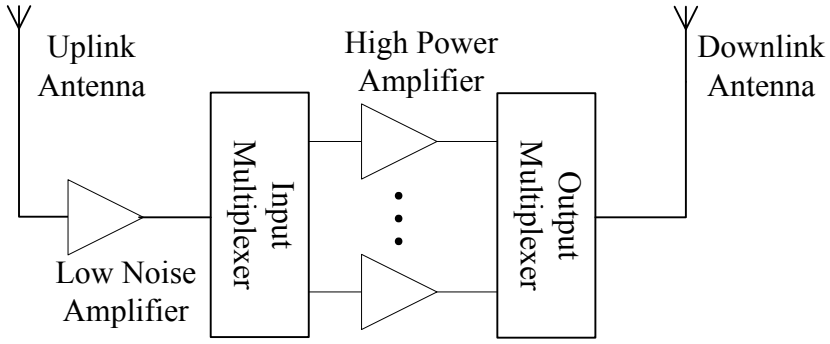

Figure 1.2 Simplified block diagram of the satellite pay load system [3].

One of the main applications of the diplexer is used as the front-end transmit/receive (Tx/Rx) diplexer [3]. It has one channel for the signal transmission and the other channel for the signal reception.

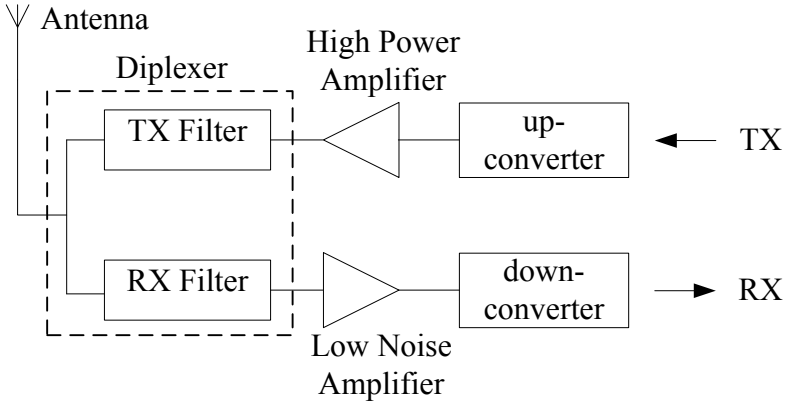

Figure 1.3 Block diagram of the RF front end of a cellular radio base station [3].

The structure of the front-end transmit/receive is given in Figure 1.3. It is widely used in the cellular base stations [2].

1.2 Thesis Motivation

In a communication system, there is a demand for miniature devices with smaller size and less weight. A diplexer configuration by Skaik and Lancaster [4] removes the need of the common junction. This allows a significant reduction in size of the diplexer. In this thesis, this configuration is studied further as well as being extended to multiplexers with more channels

and complex topologies.

Coupled resonator circuits are very important in RF/microwave filters design [5]. The topology and filter characteristics of a circuit based on coupled resonators can be described by a matrix M, called the coupling matrix M, and its external quality factors Q_e whatever the physical structure of the device [6]. A typical matrix is given below in (1.1).

$$M = \begin{bmatrix} M_{1,1} & M_{1,2} & 0 & 0 \\ M_{2,1} & M_{2,2} & M_{2,3} & 0 \\ 0 & M_{3,2} & M_{3,3} & M_{3,4} \\ 0 & 0 & M_{4,3} & M_{4,4} \end{bmatrix} = \begin{bmatrix} 0 & 0.091 & 0 & 0 \\ 0.091 & 0 & 0.070 & 0 \\ 0 & 0.070 & 0 & 0.091 \\ 0 & 0 & 0.091 & 0 \end{bmatrix} \tag{1.1}$$

$$Q_{e1} = 9.314 \quad Q_{e2} = 9.314$$

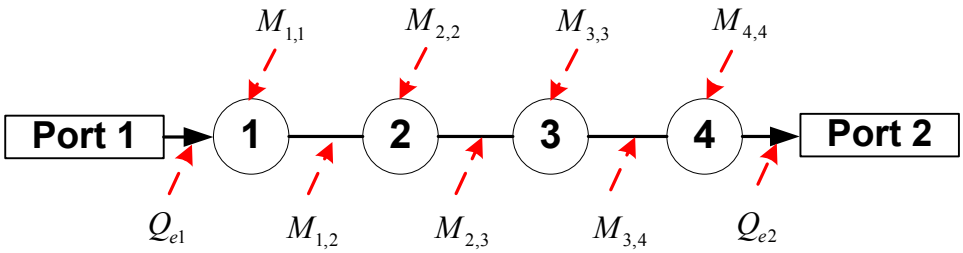

(a)

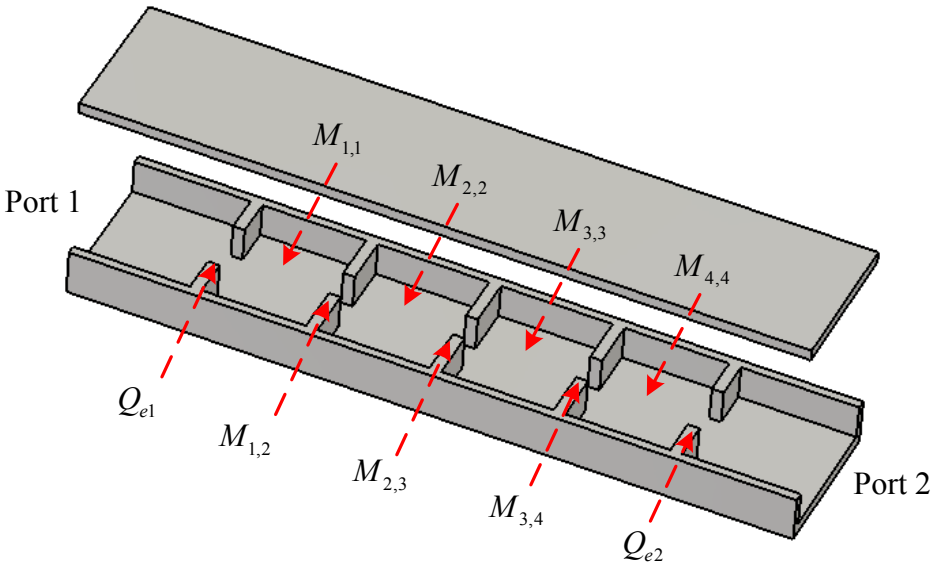

(b)

Figure 1.4 (a) Schematic of the 4th order filter. Each circle represents a resonator and the short lines between resonators are for the couplings between resonators. The line between the port and resonator represents the external coupling. (b) Its equivalent rectangular waveguide circuit.

The schematic of the matrix in (1.1) and one of its practical circuits in the form of rectangular waveguides are shown in Figure 1.4 (More details will be given in the later chapters). Each matrix entry $M_{i,j}$ and Q_e in (1.1) is related to a physical dimension of the circuit shown in Figure 1.4(b).

After the matrix is calculated, a physical structure of the circuit is determined. It is followed by the extraction of each physical dimensions based on the matrix entry values. After putting all the physical dimensions together, a computer-aided overall structure tuning or optimisation work is undertaken to make the device satisfy the specifications. For the circuit with a large number of resonators and complex topology, the traditional design technique becomes unreliable. This is because too many physical dimensions are altered each time in the optimiser, the convergence of the tuning of the overall structure is not guaranteed.

To solve the problem, a novel design technique, called the Step Tune method [7], is reported in the thesis. Instead of tuning the whole circuit all the time, we simulate and tune just part of the circuit by using the new method.

For example, as shown in Figure 1.5, the process of tuning the 4^{th} order filter can be divided into 4 steps. In Step One, only one resonator is simulated and tuned. The schematic of the circuit in Step One is shown in Figure 1.5(a). After finishing tuning the first resonator, one more resonator is added and then the circuit, in Figure 1.5(b), is tuned again. Resonators are added successively in the remaining steps, in Figure 1.5(c) and (d). At each step, the old resonators, which have been tuned in the previous steps, are kept the same values. For each step, a new coupling matrix is required for the tuning. By using the Step Tune method, only limited number of physical dimensions (just one resonator) is tuned each time. The response of the device is very close to the desired one.

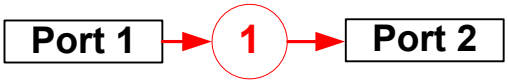

(a)

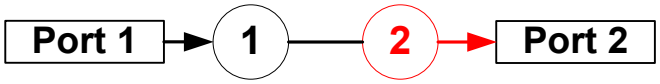

(b)

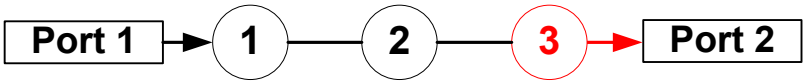

(c)

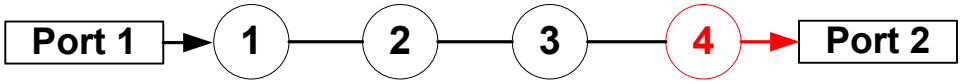

(d)

Figure 1.5 Process of tuning the 4th order filter by using Step Tune method. (a) Step One. (b) Step Two. (c) Step Three and (d) Step Four. The part of the circuit being tuned in each step is marked in red.

1.3 Thesis Overview

The thesis is formed of 8 chapters, intended to present the work of coupled resonator based multiplexers with a novel topology.

Chapter 1 contains the objectives and motivation of the work which is presented in the thesis. An overview of the thesis structures is also included in this chapter.

Chapter 2 provides the fundamental theories required by the work presented in the later chapters. It starts with the general filter theory and microwave filter theory. A brief introduction of the coupling matrix theory is given, including the different methods to obtain the coupling matrix. The cross-coupled structures are introduced at the end of the chapter.

In Chapter 3, the derivation of the *n*+X coupling matrix of the *n*-coupled resonators with multiple ports is given in detail. The relationship between the scattering parameters and the

n+X coupling matrix is also derived.

A coupling matrix synthesis method based on a local optimisation technique is discussed in Chapter 4. The topology of the multiplexer is called the Tree Topology. The principles of generating the high quality initial values of the coupling matrix with the Tree Topology are included in the chapter. Numerical coupling matrix examples are illustrated.

For the coupled resonator circuit based on the rectangular waveguides, a traditional design procedure is given in Chapter 5. It is followed by the design of an X-band 10-resonator rectangular waveguide diplexer. By using the Step Tune method, the redesign of the 10-resonator diplexer is given at the end of Chapter 5.

In Chapter 6, the design of an X-band 4-resonator rectangular waveguide diplexer with cross couplings is given. With the help of the cross-couplings, the response of the diplexer has been improved.

The Tree Topology is extended to the multiplexers with 4 channels. The design of an X-band 4-channel multiplexer is presented in Chapter 7.

The whole thesis is concluded in Chapter 8. Suggestions for future work are included at the end of the chapter.

[1] K. Dong-Ho, K. Dongsu, R. Jong-In, K. Jun-Chul, P. Jong-Chul, and P. Chong-Dae, "A novel integrated Tx-Rx diplexer for dual-band WiMAX system," in *Microwave Symposium Digest (MTT), 2010 IEEE MTT-S International*, 2010, pp. 1736-1739.

[2] R. J. Cameron, R. Mansour, and C. M. Kudsia, *Microwave Filters for Communication Systems: Fundamentals, Design and Applications*: Wiley, 2007.

[3] I. Hunter, *Theory and Design of Microwave Filters*: IEE, 2001.

[4] T. F. Skaik and M. J. Lancaster, "Coupled Resonator Diplexer without External Junctions," *Journal of Electromagnetic Analysis & Applications,* vol. 3, pp. 238-241, 2011.

[5] W. Xia, X. Shang, and M. J. Lancaster., "Responses comparisons for coupled-resonator based diplexers," in *Passive RF and Microwave Components, 3rd Annual Seminar on*, 2012, pp. 67-75.

[6] J.-S. Hong and M. J. Lancaster, *Microstrip filters for RF/microwave applications*. New York ; Chichester: Wiley, 2001.
[7] X. Shang, W. Xia, and M. J. Lancaster, "The design of waveguide filters based on cross-coupled resonators," *Microwave and Optical Technology Letters,* vol. 56, pp. 3-8, 2014.

Chapter 2 Literature Review

2.1 General Filter Theory

A filter is a two-port frequency selective device to attenuate signals of undesired frequency range (called stop-band) while allowing desired ones (pass band) to pass through.

Filters are classified in several ways. In terms of the attenuation characteristics, filters can be classified into four categories, including low-pass, high-pass, band-pass and band-stop. According to the location of the poles and zeros of the transmission function, filters can also be defined into different response functions. For example, as given in Figure 2.1, a filter has a Chebyshev response if the transmission response (S_{21}) has equal-ripple within the passband.

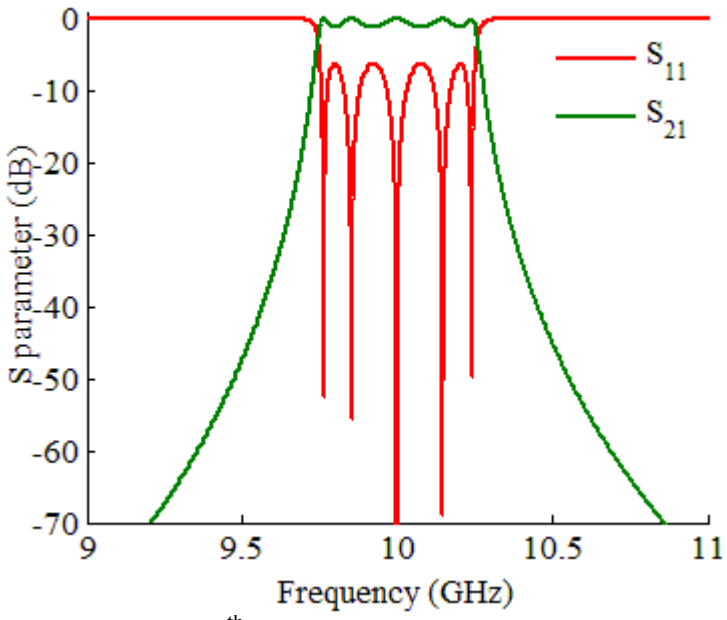

Figure 2.1 S-parameters of a 5th-order Chebyshev band-pass filter. Where S_{21} is the transmission response of the filter and S_{11} is its reflection response.

General filter theory is based on lumped elements. A lumped element based filter circuit is formed of independent capacitors, inductors and resistors. In order to attenuate signals more quickly (i.e. sharp slope at the cut-off), the simplest method is to increase the number of

lumped elements in a periodic topology or the circuit leading to a higher order *n*. The ladder topology is the most commonly used periodic topology in filter design. The low-pass all-pole lumped filter with ladder topologies are given in Figure 2.2 [1].

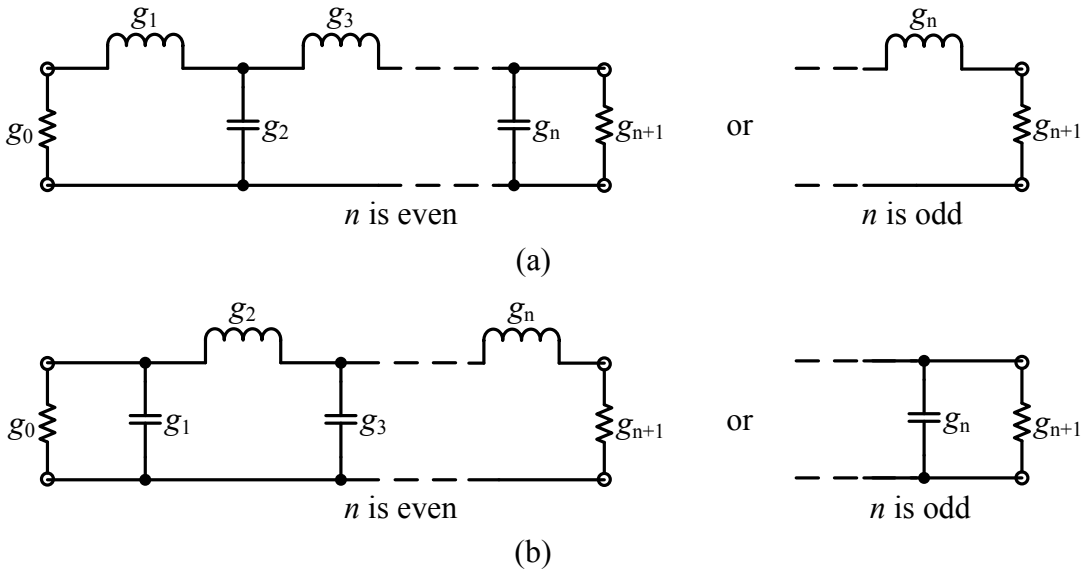

Figure 2.2 Lumped element based low-pass filters with all pole responses in (a) a ladder topology and (b) its dual.

Where *n* is the order of the filter or the total number of reactive elements (inductors and capacitors) in the circuit. g_0 and g_{n+1} are the resistance or conductance of the source and the load. g_i (i=1 to n) represents the inductance of the series inductor or the capacitance of the parallel capacitor. The circuit either in (a) or (b) may be used to generate the same response as they are dual to each other. Similar ladder topologies for the high-pass, band-pass and band-stop lumped filters are illustrated in [1].

2.2 Microwave Filter Theory

2.2.1 Lumped and Distributed Elements for Microwave Filters

Microwave filters commonly refer to filters working at frequencies ranging from 300MHz to 300GHz [1]. Although there is usually a limited range of values available for the lumped

element components, many microwave circuits today are formed of lumped elements for their more compact size [2]. But during the early years of the last century, lumped circuits were not feasible at very high frequency due to the high energy loss of the lumped elements and the serious radiation of the transmission lines [3].

The distributed elements, such as waveguides, are explored as the substitute for the lumped elements[4]. For example, a waveguide cavity is introduced as a replacement for the resonant circuit formed of lumped elements while hollow-pipe waveguides are used as the transmission lines.

In contrast to lumped elements, in a distributed circuit, it is not possible to separate out individual resistances, capacitances and inductances [3]. So the general filter theory based on the lumped elements is not suitable for the distributed circuits.

2.2.2 Microwave Filter Theory for Narrowband and Wideband Filters

In 1957, a theory derived from the lumped low-pass prototype with immittance inverters by Cohn[5] gave simple formulas restricted to designing the narrow and some moderate bandwidth microwave filters. A low-pass prototype circuit with lumped elements is generated first. A frequency transformation is applied to convert the low-pass circuit into a band-pass lumped circuit. Based on the values of the lumped elements of the band-pass circuit, the dimensions of the distributed elements are extracted. The implementation of the ideal immittance inverters, which are frequency invariant elements, is the key to the theory.

For wider bandwidth filters, however, a more complicated method given by Young [6] is available. The theory is based on low-pass distributed prototype circuit using quarter-wave transformer. The transformer is a frequency variant element. A great deal of design data and graphs are needed to get the coupling reactance of the transformers.

Later work by Levy [7] combining and extending [5] and [6] gave a general method in microwave filter design. A simple insertion loss formula was used to derive the distributed prototype based on the filter parameters including the order n, the ripple level L_{Ar} and the band edges. The extraction of distributed element values is similar to previous works [5-6].

For extremely broad-band filters, no theory exists to predict the equivalent circuit. But some work based on approximations have been developed [8].

The project is to design devices with the narrow bandwidth. So the ideal immittance inverters and the frequency transformation will be introduced in the following sections.

2.2.3 Immittance Inverters

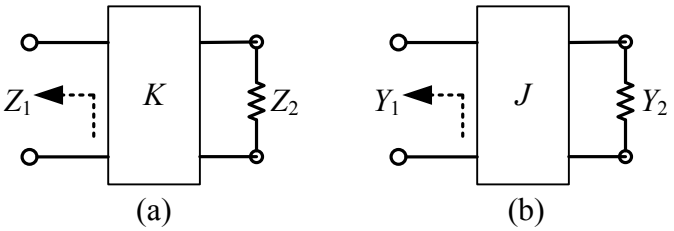

Figure 2.3 Network representation of the single terminated (a) *K*-inverter and (b) *J*-inverter

Immittance inverters turn an impedance into an admittance (*K*-inverter) or turn an admittance into an impedance (*J*-inverter). The property of an idealized immittance inverter is frequency invariant. Referring to Figure 2.3, when the inverter is terminated with an immittance (Z_2 or Y_2) at one end, the immittance seen at the other end will be [1]:

$$Z_1 = \frac{K^2}{Z_2} \quad , \quad Y_1 = \frac{J^2}{Y_2} \tag{2.1}$$

Where K is real and defined as the characteristic impedance of the *K*-inverter, J is real and defined as the characteristic admittance of the *J*-inverter. The equivalent lumped circuits of the immittance inverters, as well as the evaluation of the characteristic impedance K and characteristic admittance J, are given in Figure 2.4 [1].

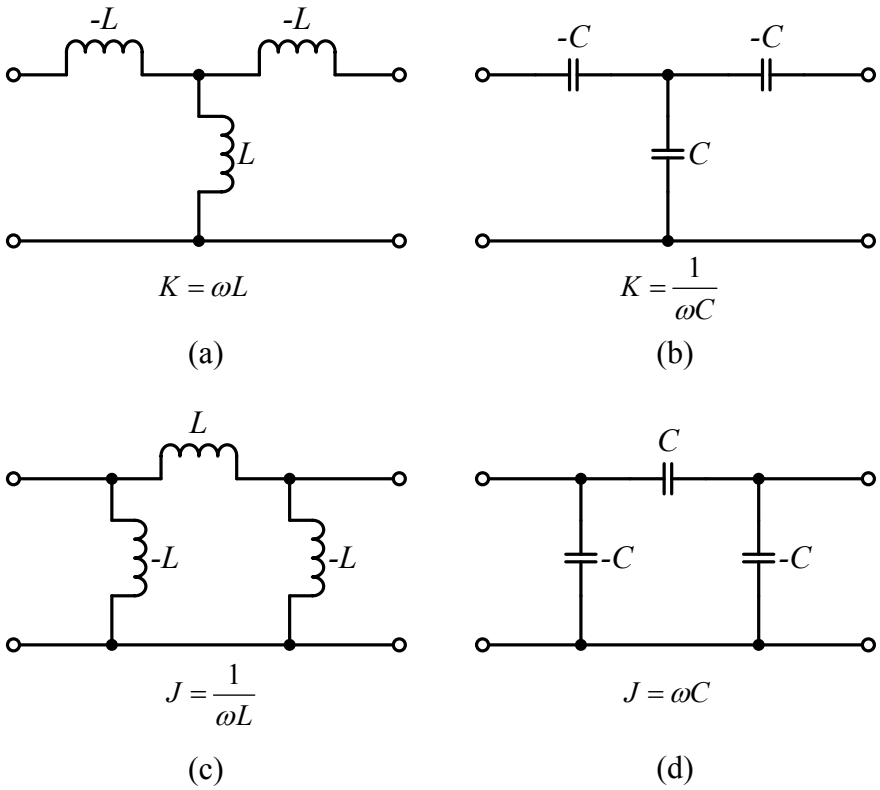

Figure 2.4 Lumped-element immittance inverters

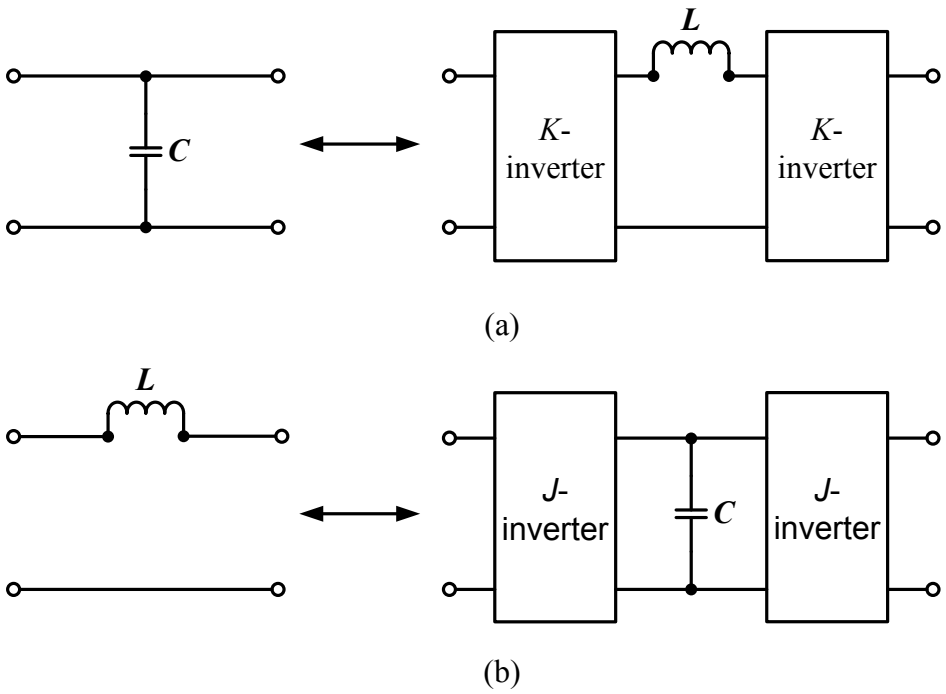

Figure 2.5 (a) Immittance inverters are used to convert a shunt capacitor into the equivalent circuit with a series inductor. (b) Immittance inverters are used to convert a series inductor into the equivalent circuit with a shunt capacitor.

As illustrated in Figure 2.5(a), by introducing immittance inverters, a series inductor with *K*-inverters at two ends is equivalent to a parallel capacitor. Meanwhile, a parallel capacitor with *J*-inverters at two ends, shown in Figure 2.5(b), is the same as a series inductor. With immittance inverters, it is feasible to convert the ladder lumped circuit into new circuit with only one type of component. For example, the low-pass circuits in Figure 2.2 have two equivalent circuits shown in Figure 2.6 using immittance inverters. The equivalent circuit is formed of either series inductors (a) or shunt capacitors (b).

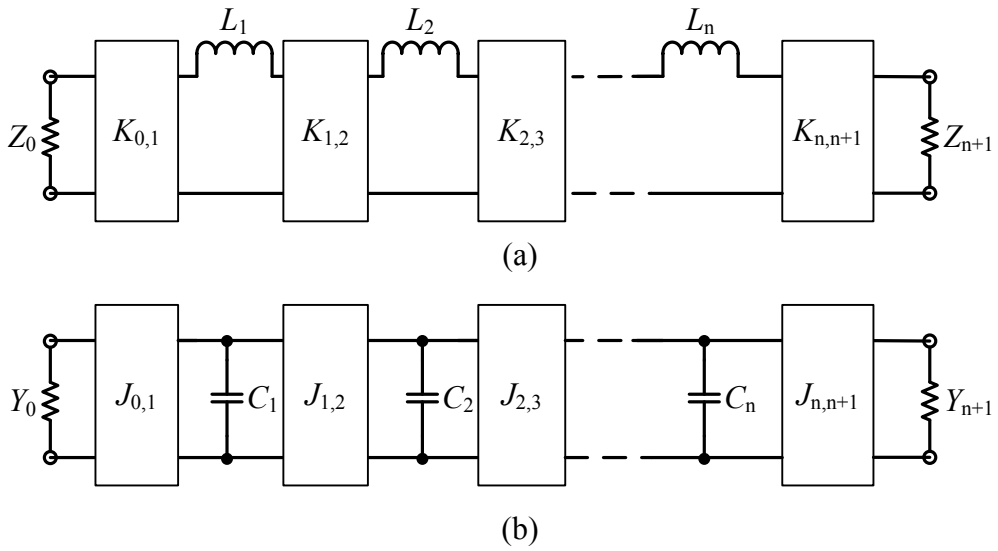

Figure 2.6 Lowpass filters with immittance inverters

2.2.4 Low-Pass to Band-Pass Transformation

The low-pass lumped filter circuits with immittance inverters are introduced in the previous sections. With the well known frequency and element transformation[1], a low-pass circuit can be transformed into the high-pass, band-pass or band-stop one. The low-pass to band-pass transformation is presented in this section.

A prototype low-pass filter is to be transformed to a band-pass one with a passband $\omega_2 - \omega_1$, where ω_1 and ω_2 are the angular frequencies of the passband edges. The frequency

transformation is [1]

$$\omega \rightarrow \frac{\omega_c}{FBW}\left(\frac{\omega}{\omega_0}-\frac{\omega_0}{\omega}\right) \tag{2.2}$$

with

$$\begin{aligned} FBW &= \frac{\omega_2-\omega_1}{\omega_0} \\ \omega_0 &= \sqrt{\omega_1 \cdot \omega_2} \end{aligned} \tag{2.3}$$

where ω is the frequency variable, ω_c is the low-pass prototype cut-off frequency, ω_0 denotes the centre angular frequency and *FBW* is defined as the fractional bandwidth. Applying this frequency transformation to a parallel capacitor *C* and a series inductor *L* of the low-pass prototype filter in Figure 2.6, we have

$$\begin{aligned} j\omega C &\rightarrow j\omega\frac{\omega_c C}{FBW\,\omega_0}+\frac{1}{j\omega\dfrac{FBW}{\omega_c\omega_0 C}} \\ j\omega L &\rightarrow j\omega\frac{\omega_c L}{FBW\,\omega_0}+\frac{1}{j\omega\dfrac{FBW}{\omega_c\omega_0 L}} \end{aligned} \tag{2.4}$$

which implies that a parallel capacitor *C* or a series inductor *L* in the low-pass prototype will transform to a parallel or series *LC* resonant circuit. Figure 2.7 shows the basic element transformation. Figure 2.8 gives the bandpass filters transformed from the low-pass ones in Figure 2.6.

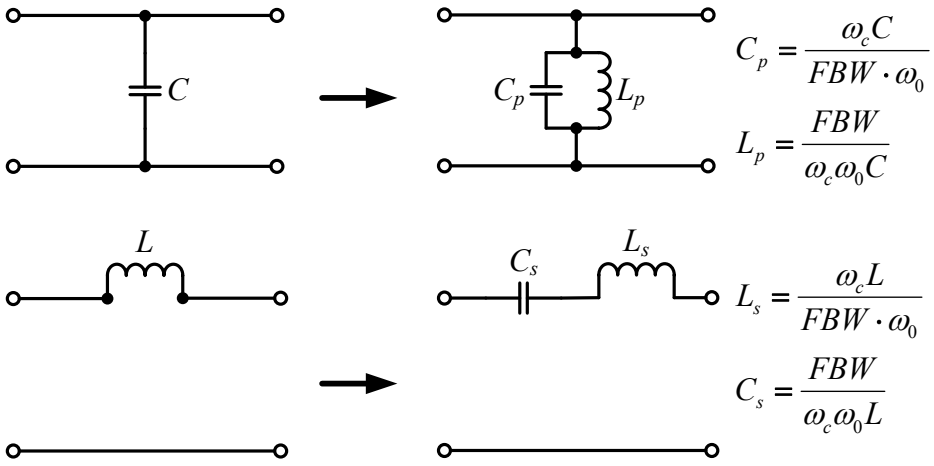

Figure 2.7 Low-pass to band-pass element transformation

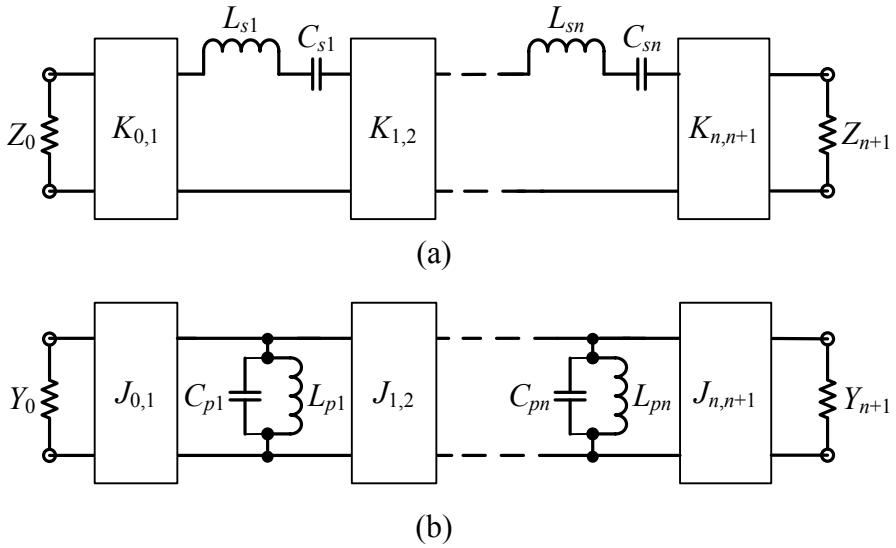

Figure 2.8 Band-pass filters with immittance inverters

The band-pass filters shown in Figure 2.8 are the coupled-resonator filter circuits, as the circuits are formed of immittance inverters and *LC* resonators. With different techniques, such lumped circuits can be converted into different forms of distributed circuits including waveguides or microstrips [4].

2.2.5 Coupling Matrix Theory

The coupled resonator circuit can be converted into matrix form called coupling matrix. The coupling matrix theory has advantages of applying matrix operations such as matrix rotations

(similarity transformation) and matrix inversions during circuit design. Reconfiguring the circuit topology and synthesis of the circuit are simplified by such matrix operations [9]. The coupling matrix theory is still only suitable for the narrow-band filtering circuits, as the theory is based on the narrow bandwidth assumption.

Coupling matrix can be classified into two categories. The first one is the general $n \times n$ coupling matrix. n is the order of the circuit. The other category, including n+2 coupling matrix, has additional columns and rows for the ports. Section 2.2.5.1 gives a brief introduction of the general $n \times n$ coupling matrix for two-port circuits. Section 2.2.5.2 gives the extension of the $n \times n$ coupling matrix to multi-port circuits. Section 2.2.5.3 gives an introduction of the n+2 coupling matrix. The extension of the n+2 coupling matrix to multi-port circuits or the n+X coupling matrix will be discussed in Chapter 3. X is the number of ports of the circuit.

2.2.5.1 General $n \times n$ Coupling Matrix of n-Coupled Resonator Circuit with 2-Port

In the early 1970s, Atia and Williams [10-13] first presented a design method for band-pass waveguide cavity filter based on coupling matrix. The matrix they used is the $n \times n$ coupling matrix. The matrix is derived from a prototype bandpass circuit in Figure 2.9.

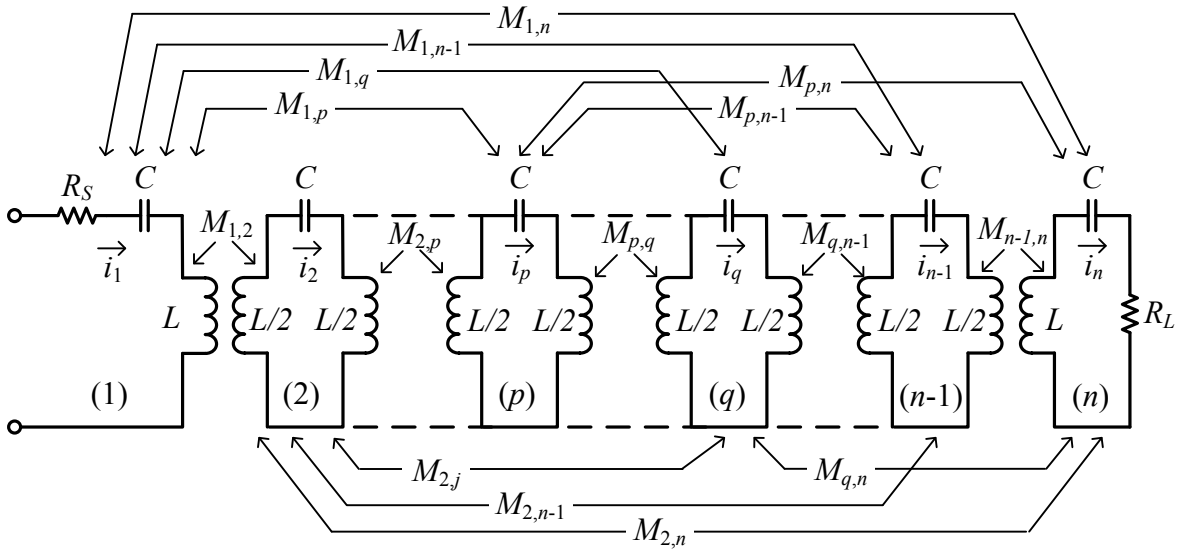

Figure 2.9 A 2-port lumped circuit composed of synchronously tuned magnetically coupled resonators [13].

The filter is an nth order cascaded filter coupled by transformers or magnetic couplings. Each resonator has a capacitor C=1F and an inductor L=1H. So all the resonators are resonating at 1Hz. R_S and R_L are the resistance of the source and the load. (Notice the equivalent lumped circuit is assumed to be lossless, resistance or conductance exists only in the source and load.). i_p is the loop current of each resonator. The coupling between resonator p and q is denoted as $M_{p,q}$, which is a real number and frequency invariant.

The coupling matrix theory can be extended to the circuits with asynchronously tuned resonators or the general $n \times n$ coupling matrix. The formulation of the general $n \times n$ coupling matrix is discussed in [1]. Filters with magnetically and electrically coupled resonators are drawn separately.

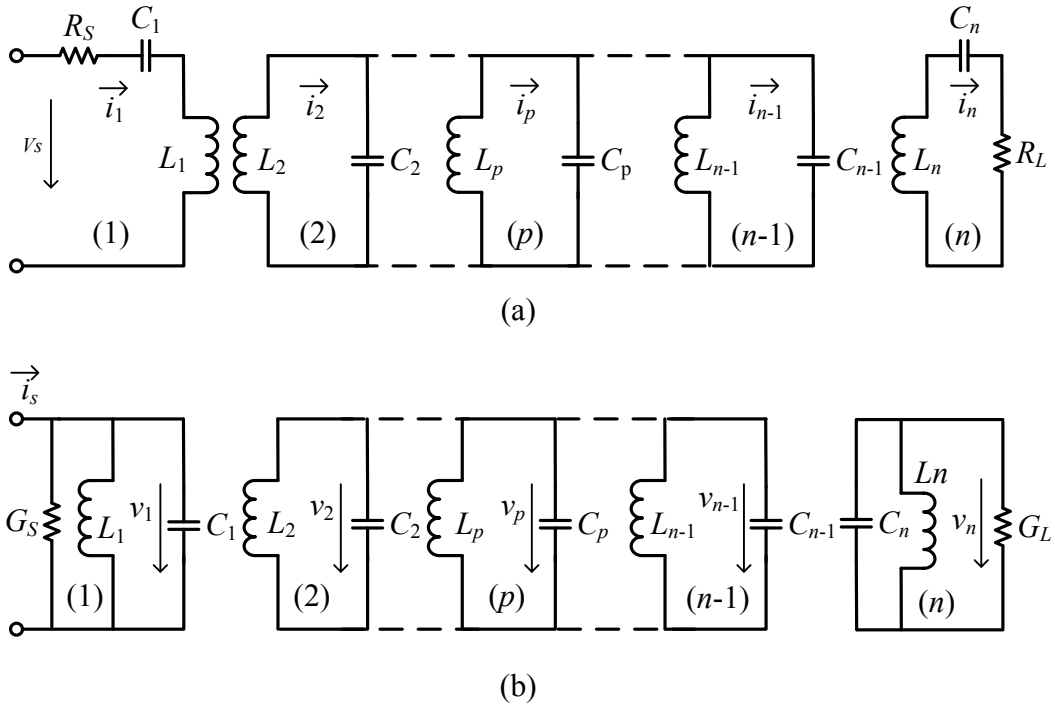

Figure 2.10 Equivalent filter circuit of n-coupled resonators for (a) loop-equation formulation and (b) node-equation formulation[1].

The equivalent circuit with magnetically coupled resonators is given in Figure 2.10(a). Using Kirchoff's voltage law, the coupling matrix is derived via an impedance matrix from a set of loop equations. The other circuit with electrical coupling is given in Figure 2.10(b). The coupling matrix is derived via an admittance matrix formulated by a set of node equations based on Kirchoff's current law. Regardless of the type of coupling, a general matrix [A] formed of coupling coefficients $m_{p,q}$ and external quality factors q_{ei} is presented in [1] as:

$$[A]=[q]+p[U]-j[m]=\begin{bmatrix}\frac{1}{q_{e1}} & 0 & \cdots & 0\\ 0 & 0 & \cdots & 0\\ \vdots & \vdots & \ddots & \vdots\\ 0 & 0 & \cdots & \frac{1}{q_{en}}\end{bmatrix}+p\begin{bmatrix}1 & 0 & \cdots & 0\\ 0 & 1 & \cdots & 0\\ \vdots & \vdots & \ddots & \vdots\\ 0 & 0 & \cdots & 1\end{bmatrix}-j\begin{bmatrix}m_{1,1} & m_{1,2} & \cdots & m_{1,n}\\ m_{2,1} & m_{2,2} & \cdots & m_{2,n}\\ \vdots & \vdots & \ddots & \vdots\\ m_{n,1} & m_{n,2} & \cdots & m_{n,n}\end{bmatrix} \quad (2.5)$$

$$p=j\frac{1}{FBW}\left(\frac{\omega}{\omega_0}-\frac{\omega_0}{\omega}\right) \quad (2.6)$$

Where, matrix [U] is an identity matrix, p is the complex lowpass frequency variable, ω_0 is the centre frequency of the filter, FBW is the fractional bandwidth of the filter. q_{ei} (i=1 and n) is the scaled external quality factors of the resonator i. $m_{p,q}$ $(p \neq q)$ is the normalised coupling coefficients between the resonator p and q. They are:

$$\begin{aligned} q_{ei} &= Q_{ei} \times FBW \\ m_{p,q} &= \frac{M_{p,q}}{FBW} \end{aligned} \tag{2.7}$$

Q_{ei} is defined as the external quality factor of resonator i. $M_{p,q}$ is defined as the coupling coefficient between resonator p and q. $m_{i,i}$ is the self coupling of resonator i. The filter is an asynchronously tuned one if some of $m_{i,i}$ are non-zero entries.

As given in [1], the S-parameters can be calculated using the scaled external quality factors q_{ei} and matrix [A] as:

$$\begin{aligned} S_{11} &= \pm\left(1 - \frac{2}{q_{e1}}[A]^{-1}_{1,1}\right) \\ S_{21} &= 2\frac{1}{\sqrt{q_{e1} \cdot q_{en}}}[A]^{-1}_{n,1} \end{aligned} \tag{2.8}$$

2.2.5.2 $n \times n$ Coupling Matrix of n-Coupled Resonator Circuit with Multi-Port

In order to design the coupled-resonator based multi-port circuits including diplexers and multiplexers, the general 2-port equivalent circuit needs to be extended to multi-port one [14]. As given in Figure 2.11, the equivalent n-port filtering circuits with n-coupled resonators are with either magnetically coupled resonators, in Figure 2.11(a), or electrically coupled resonators, in Figure 2.11(b).

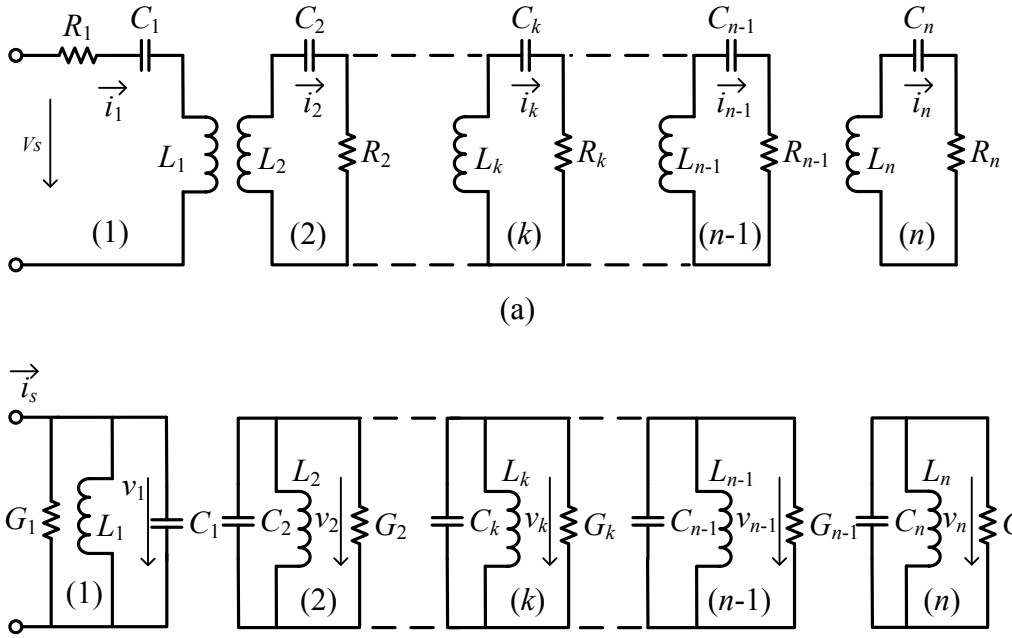

Figure 2.11 *n*-port network with *n* coupled resonators [14]

Where R_1 and G_1 are the source resistance and the source conductance. R_i and G_i are the load resistance and the load conductance at the port i.

The derivation of the coupling matrix is similar to the 2-port one in Section 2.2.5.1. The general matrix $[A]$ of n-port is presented in [14] as:

$$[A]=[q]+p[U]-j[m]=\begin{bmatrix} \frac{1}{q_{e1}} & 0 & \cdots & 0 \\ 0 & \frac{1}{q_{e2}} & \cdots & 0 \\ \vdots & \vdots & \ddots & \vdots \\ 0 & 0 & \cdots & \frac{1}{q_{en}} \end{bmatrix}+p\begin{bmatrix} 1 & 0 & \cdots & 0 \\ 0 & 1 & \cdots & 0 \\ \vdots & \vdots & \ddots & \vdots \\ 0 & 0 & \cdots & 1 \end{bmatrix}-j\begin{bmatrix} m_{1,1} & m_{1,2} & \cdots & m_{1,n} \\ m_{2,1} & m_{2,2} & \cdots & m_{2,n} \\ \vdots & \vdots & \ddots & \vdots \\ m_{n,1} & m_{n,2} & \cdots & m_{n,n} \end{bmatrix} \quad (2.9)$$

Where, matrix $[U]$ is an identity matrix, p is the complex lowpass frequency variable defined by (2.6). q_{ei} and $m_{p,q}$, defined by (2.7), denote the scaled external quality factors and scaled coupling coefficients.

The *S*-parameters can be calculated using the scaled external quality factors q_{ei} and matrix [*A*] as [14]:

$$S_{11} = \pm\left(1 - \frac{2}{q_{e1}}[A]^{-1}_{1,1}\right)$$
$$S_{i1} = 2\frac{1}{\sqrt{q_{e1} \cdot q_{ei}}}[A]^{-1}_{i,1} \qquad (i = 2 \ to \ n) \tag{2.10}$$

2.2.5.3 *n*+2 and *n*+*X* Coupling Matrix

Extended from the general $n \times n$ coupling matrix, the *n*+2 coupling matrix is used to express a two-port circuit. A general *n*+2 coupling matrix is presented in Figure 2.12.

$$[m]_{(n+2)\times(n+2)} = \begin{bmatrix} m_{s,s} & m_{s,1} & \cdots & m_{s,n-1} & m_{s,n} & m_{s,l} \\ m_{1,s} & m_{1,1} & \cdots & m_{1,n-1} & m_{1,n} & m_{1,l} \\ \vdots & \vdots & \ddots & \vdots & \vdots & \vdots \\ m_{n-1,s} & m_{n-1,1} & \cdots & m_{n-1,n-1} & m_{n-1,n} & m_{n-1,l} \\ m_{n,s} & m_{n,1} & \cdots & m_{n,n-1} & m_{n,n} & m_{n,l} \\ m_{l,s} & m_{l,1} & \cdots & m_{l,n-1} & m_{l,n} & m_{l,l} \end{bmatrix}_{(n+2)\times(n+2)}$$

General $n \times n$ coupling matrix

Figure 2.12 the *n*+2 coupling matrix

Where the subscript *s* and *l* refer to the source and load.

Comparing to the general $n \times n$ coupling matrix, the *n*+2 coupling matrix has additional columns and rows for the source and the load surrounding the general $n \times n$ coupling matrix. $m_{s,i}$ and $m_{i,s}$ are the coupling between the source and resonator *i*, $m_{l,i}$ and $m_{i,l}$ are the coupling between the load and resonator *i*. $m_{s,s}$ and $m_{l,l}$ are the self coupling of the source and the load. With the additional port columns and rows, the *n*+2 coupling matrix has the following advantages[15]:

1) One port can be coupled to multi resonators while a single resonator can be coupled to multi ports.

2) Coupling between the source and the load is possible so as to make fully canonical filtering function (i.e. the number of finite-position transmission zeros is equal to the number of resonators n).

So the n+2 coupling matrix is more general than the $n \times n$ coupling matrix. Furthermore, the n+2 coupling matrix can be extended to multi-port one as n+X coupling matrix. X is the total number of ports of the circuit. The derivation of n+X coupling matrix, as well as its transfer and reflection functions, is given in Chapter 3.

2.2.6 Synthesis of the Coupling Matrix

For filters with standard responses such as Chebyshev, Butterworth and Elliptic, all lumped element values or g values can be calculated by formulas or found from tables directly[1].

For Chebyshev lowpass prototype filters with a passband ripple L_{Ar} dB and the cut-off frequency $\Omega_c = 1$, the g values for the two-port networks shown in Figure 2.2 can be calculated using the following formulas [1]:

$$
\begin{aligned}
g_0 &= 1 \\
g_1 &= \frac{2}{\gamma}\sin\left(\frac{\pi}{2n}\right) \\
g_i &= \frac{1}{g_{i-1}} \frac{4\sin\left(\frac{(2i-1)\pi}{2n}\right)\cdot\sin\left(\frac{(2i-3)\pi}{2n}\right)}{\gamma^2 + \sin^2\left(\frac{(i-1)\pi}{n}\right)} \quad (i = 2 \text{ to } n) \\
g_{n+1} &= \begin{cases} 1 & \text{for } n \text{ odd} \\ \coth^2\left(\frac{\beta}{4}\right) & \text{for } n \text{ even} \end{cases}
\end{aligned}
\tag{2.11}
$$

Where

$$\beta = \ln\left[\coth\left(\frac{L_{Ar}}{17.37}\right)\right]$$
$$\gamma = \sinh\left(\frac{\beta}{2n}\right)$$

With given g values, the coupling coefficient $M_{i,i+1}$ and the external quality factor Q_{ei} are formulated directly [1] as

$$\begin{aligned} Q_{e1} &= \frac{g_0 g_1}{FBW} \qquad & Q_{en} &= \frac{g_n g_{n+1}}{FBW} \\ M_{i,i+1} &= \frac{FBW}{\sqrt{g_i g_{i+1}}} \qquad & &\text{for } i = 1 \text{ to } n-1 \end{aligned} \tag{2.12}$$

According to (2.7), the normalised coupling coefficient $m_{i,i+1}$ and the external quality factor q_{ei} can be found as

$$\begin{aligned} q_{e1} &= Q_{e1} \times FBW = g_0 g_1, \;\; q_{en} = Q_{en} \times FBW = g_n g_{n+1} \\ m_{i,i+1} &= \frac{M_{i,i+1}}{FBW} = \frac{1}{\sqrt{g_i g_{i+1}}} \qquad \text{for } i = 1 \text{ to } n-1 \end{aligned} \tag{2.13}$$

For filters with arbitrary responses, however, there is no simple solution. Two ways are generally applied to solve the problem. One is based on recursive methods and matrix rotation, the other way is optimisation.

2.2.6.1 Synthesis Method Using Matrix Rotation

Complex filters with transmission zeros are summarised by Cameron [15-16] and divided into 3 steps:

(1) A recursive method for deriving polynomials, which represent the transmission and reflection responses.

(2) The synthesis of a coupling matrix based on the derived polynomials and,

(3) A similarity transformation or matrix rotation technique to reconfigure the coupling matrix into a new one relating to the practical topology.

Realisation of the original coupling matrix in (2) would be difficult, since all possible couplings are present or the matrix is full of non-zero entries. The key point of such synthesis method is to reconfigure the derived original coupling matrix in (2) into one with less non-zero entries relating to the filter topology by a set of matrix rotations. The rotated matrix has exactly the same filter characteristics as the original matrix.

2.2.6.2 Synthesis Method Using Optimisation

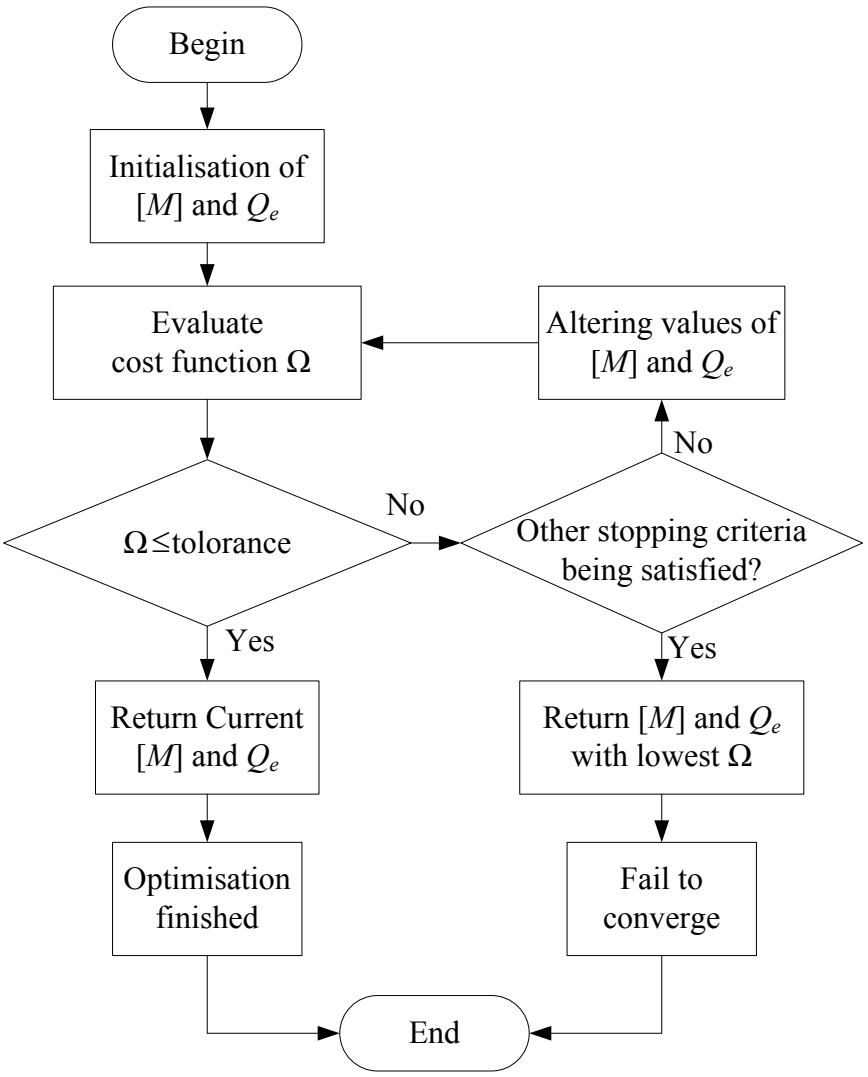

Figure 2.13 Flowchart of the optimisation

The second way for coupling matrix synthesis is based on optimisation techniques. The principle of the optimisation is to minimise a cost function Ω by altering the values of each non-zero entries in the coupling matrix. The cost function Ω is used to quantify the difference between the *S*-parameters of the current matrix and the expected circuit specifications. Before optimisation, a particular circuit topology is given. In other words, locations of non-zero entries in the coupling matrix are determined at the very beginning. The flow chart of optimisation process is given in Figure 2.13.

2.2.6.3 Comparison of Two Synthesis Methods

The first synthesis method, including matrix rotation techniques, is quite useful. With the help of computers, the original coupling matrix may be easily found in a recursive way. But matrix rotation techniques, which are used to reconfigure the original coupling matrix, cannot handle all the problems. Many practical topologies may fail to be generated by the matrix rotation. The sequence of the rotation angles is difficult to determine in order to guarantee the convergence of the rotated result. In practice, for a given topology, restricted by the manufacturing or the requirement of the application, coupling matrix synthesised by optimisation is still of importance for design of microwave filters.

For coupling matrix synthesis by optimisation, there are two categories of optimisation techniques that can be applied. The first one is called global optimisation. For optimising operation based on global optimisation, values of the starting point have little effect on the final result and total computation times. Such optimisation method searches a global best with lowest cost function values at the cost of poor efficiency to converge the result.

The other way of optimising is based on local optimisation technique. It takes less computation time than the global method. However, a good guess of the starting point is

essential otherwise the optimiser may converge to a non-optimum local minimum.

This project is based on local optimisation techniques. Chapter 4 introduces how to generate the starting point of some multi-port circuits. The cost function Ω applied in this project is presented in the same chapter as well.

2.2.7 Microwave Filter Design

The coupling matrix [*M*] is synthesised by one of the above synthesis techniques. The next step is to configure a distributed circuit based on the coupling matrix. By the application of the full-wave electromagnetic (EM) simulators, the physical dimensions of each distributed element are separately extracted according to the entry values of [*M*] and Q_e.

The design of a 4th order Chebyshev band-pass filter is given here as an example. The specifications of the filter are given as: centre frequency f_c=10GHz, fractional bandwidth *FBW*=0.01, passband ripple L_{Ar}=0.043dB. According to (2.11) and (2.12), the coupling matrix *M* and the external quality factors Q_e of the filter are:

$$M = \begin{bmatrix} M_{1,1} & M_{1,2} & 0 & 0 \\ M_{2,1} & M_{2,2} & M_{2,3} & 0 \\ 0 & M_{3,2} & M_{3,3} & M_{3,4} \\ 0 & 0 & M_{4,3} & M_{4,4} \end{bmatrix} = \begin{bmatrix} 0 & 0.0091 & 0 & 0 \\ 0.0091 & 0 & 0.0070 & 0 \\ 0 & 0.0070 & 0 & 0.0091 \\ 0 & 0 & 0.0091 & 0 \end{bmatrix} \tag{2.14}$$

$$Q_{e1} = 93.14 \quad Q_{e2} = 93.14$$

One possible structure of the filter using rectangular waveguide is given in Figure 2.14.

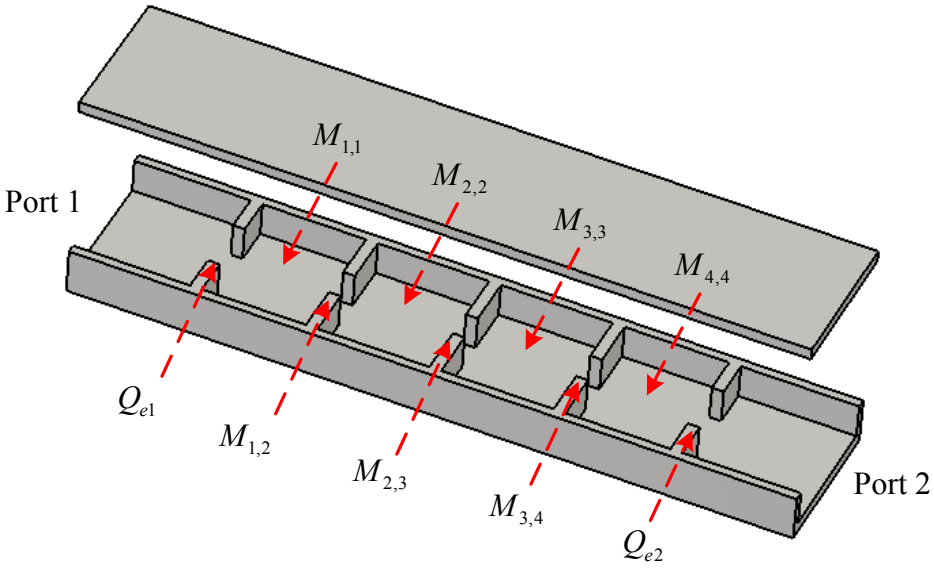

Figure 2.14 The structure of a 4th order Chebyshev filter formed by rectangular waveguides. The dimensions of each waveguide elements are relating to the values of each matrix entries given in (2.14).

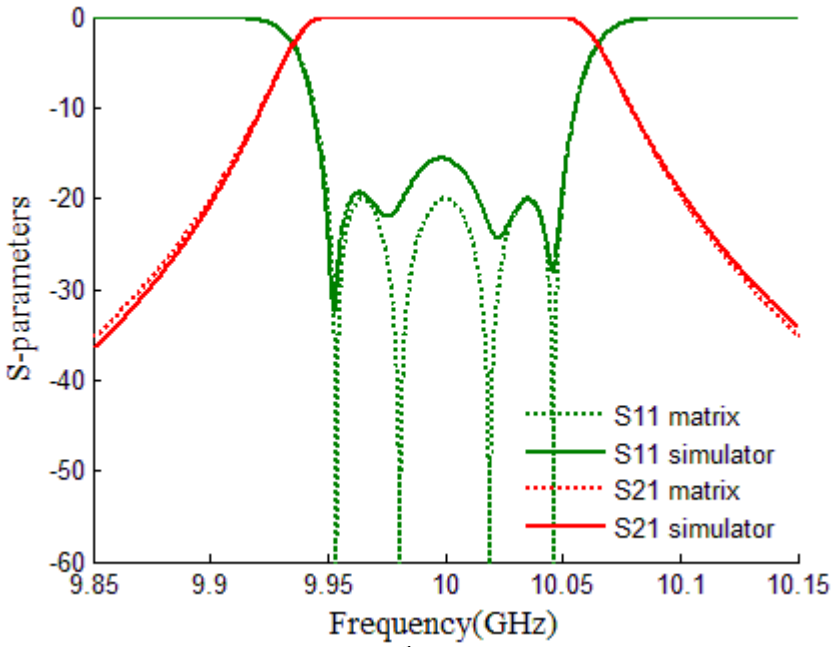

Figure 2.15 S-parameters of a 4th-order Chebyshev band-pass filter.

The filter responses are obtained by putting all distributed elements together using the EM simulator. Figure 2.15 gives the response comparison between the ideal one from the coupling matrix and the simulated one from the EM simulator. In order to eliminate the response difference, further adjustment or optimisation on the all physical dimensions is needed. More

details of the exact process to get the initial dimensions is given later in the thesis.

Today, with the EM simulators, microwave filter design is highly dependent on the dimensional optimisation [17]. The simulation results give responses very close to measured ones. However, a set of good initial dimensions of the distributed elements is essential as input to the optimisation on all physical dimensions. Otherwise, the simulators will fail to generate an acceptable solution or even no solution at all.

More design examples for the multi-port circuits are presented in Chapter 5 to 7.

2.3 Diplexers and Multiplexers

One common application of filters is to channelize signals by using diplexers and multiplexers [4]. Multiplexers are of two types: non-contiguous multiplexers (with intervening guard bands between pass bands of each branch) and contiguous multiplexers (of which the pass bands are adjacent). The structure of a conventional multiplexer is illustrated in Figure 1.1.

As shown in Figure 1.1, channel filters connect to the shared port through a common junction. The function of the common junction in such a frequency distribution network is to eliminate the interaction between channels. The common junction may be formed of circulators, hybrid couplers, directional filters or a manifold [9].

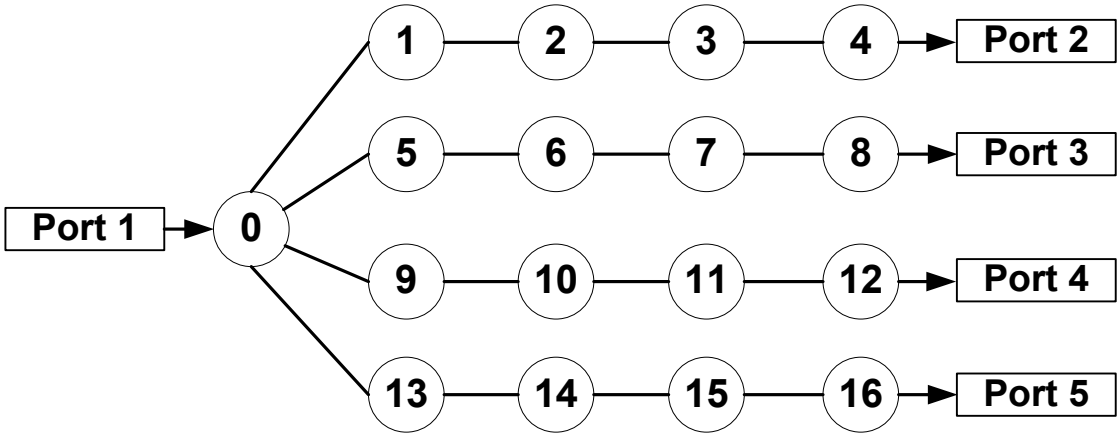

Figure 2.16 A 4-channel multiplexer with the Star-junction.

Figure 2.16 shows a new type of multiplexer. It is based on an all resonant structure with the Star-junction[18]. Each circle represents a resonator and the lines are the internal couplings between resonators. The arrowed lines between resonators and ports represent external couplings. All channel filters are connected through the "extra" resonator 0. Since the multiplexer is only formed of coupled resonators, the response of a multiplexer with a Star-junction can be fully described by the coupling matrix. However, the Star-Junction multiplexer is usually implemented when the number of channels is no more than four [9]. Each channel filter is coupled to the Star-junction resonator via coupling elements. More channels lead to more coupling elements connecting to the Star-junction resonator, making it difficult to allocate too many coupling elements to a single resonator within a limited space.

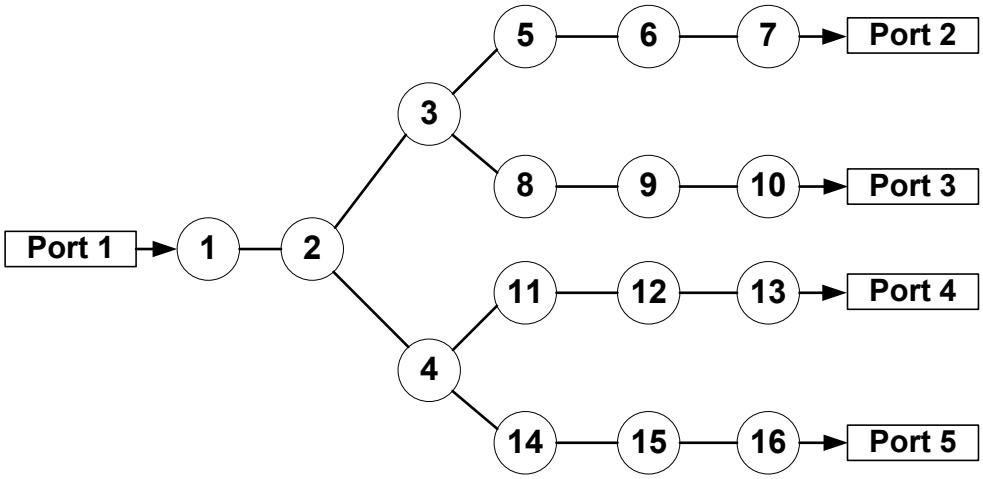

Figure 2.17 A 4-channel multiplexer with Tree topology.

The other all resonant structure, Tree Topology, is presented in [19-23] and offers a different method to solve the problem. As shown in Figure 2.17, each of resonators has maximally 3 main couplings no matter how much the total number of channels is. Comparing to the multiplexers with common junctions, this multiplexer structure eliminates the need for separate transmission-line based frequency distribution networks leading to a reduction in the overall component size and volume.

2.4 Cross Couplings and Transmission Zeros

The main application of the cross coupling is to generate transmission zeros in order to increase the attenuation over a required frequency range. However, a compromise exists that the attenuation over some other frequency range may be less efficient than that without the cross coupling.

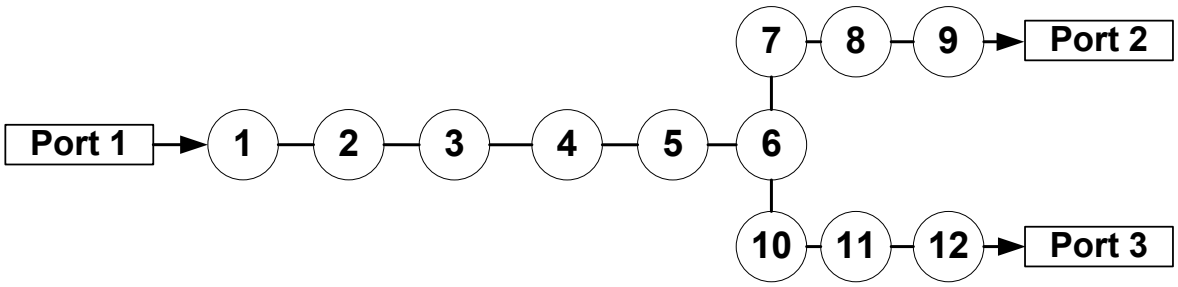

(a)

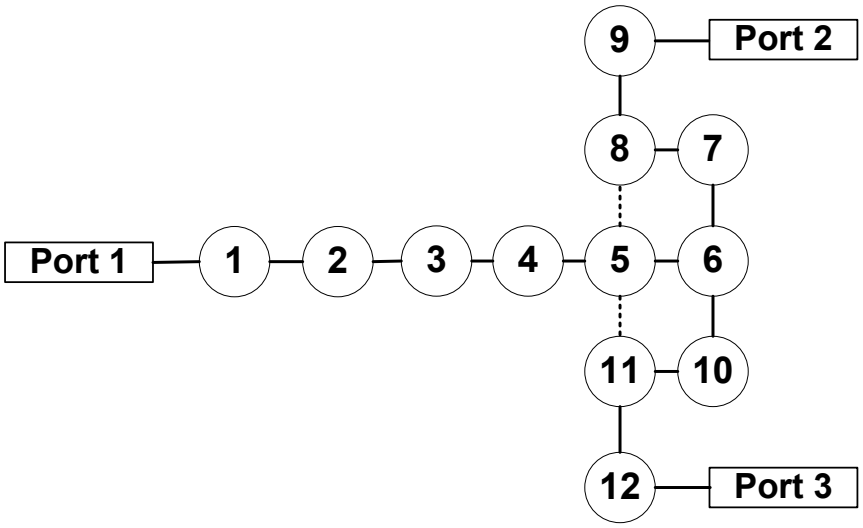

(b)

Figure 2.18 Diplexers (a) without and (b) with cross couplings.

In Figure 2.18(b), a folded structure is used. One cross coupling is added between Resonator 5 and 8, the other one is between Resonator 5 and 11. Figure 2.19 shows the transmission responses comparison between the diplexers in Figure 2.18. It can be seen that a compromise exists, with the improvement of attenuation or rejection close to the passband giving more energy reflection far from the passband.

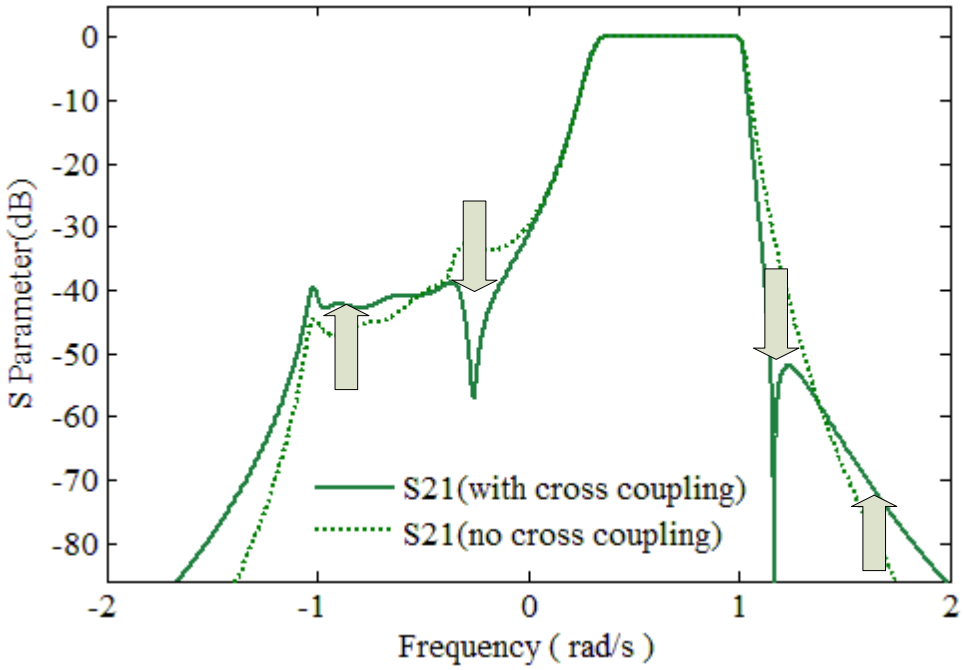

Figure 2.19 Two possible diplexer prototype transmission responses, with (solid line) and without (dashed line) finite transmission zeros generated by cross coupling. Note the increase of attenuation close to the pass band and decrease of attenuation far from the pass band.

The coupling matrices of the diplexers shown in Figure 2.18(a) and (b) are listed here. How to get the coupling values are discussed in Chapter 4 and 6.

(a): $m_{i,i+1}=m_{i+1,i}$= [0.794, 0.481, 0.636, 0.410, 0.647, 0.275, 0.203, 0.274, 0, 0.203, 0.274], $m_{6,10}=m_{10,6}$=0.275, $m_{i,i}$=[0, 0, 0, 0, 0, 0, 0.632, 0.668, 0.67, -0.632, -0.668, -0.67], q_{e1}=1.536, $q_{e2}=q_{e3}$=3.073.

(b): $m_{i,i+1}=m_{i+1,i}$= [0.793, 0.481, 0.633, 0.408, 0.631, 0.286, 0.187, 0.275, 0, 0.187, 0.275], $m_{6,10}=m_{10,6}$=0.286, $m_{5,8}=m_{8,5}=m_{5,11}=m_{11,5}$= -0.08, $m_{i,i}$=[0, 0, 0, 0, 0, 0, 0.727, 0.665, 0.665, -0.727, -0.665, -0.665,], q_{e1}=1.506, $q_{e2}=q_{e3}$=3.012.

In many cases, the attenuation over some frequency ranges is more important than that over other frequency ranges. Take the transmit/receive (Tx/Rx) diplexers in cellular base stations for example, high attenuation (sometimes as high as -120dB [16]) is required over the

neighbouring channel frequency range to avoid interactions between two channels [16]. In the meantime, the attenuation outside two channels is not so important. By introducing cross couplings or transmission zeros, the requirement may be satisfied with a limited number of resonators so as to guarantee a compact size, a minimal insertion loss and a moderate group delay.

[1] J.-S. Hong and M. J. Lancaster, *Microstrip filters for RF/microwave applications*. New York ; Chichester: Wiley, 2001.

[2] R. Levy, R. V. Snyder, and G. Matthaei, "Design of microwave filters," *Microwave Theory and Techniques, IEEE Transactions on,* vol. 50, pp. 783-793, 2002.

[3] G. L. Ragan and M. I. o. T. R. Laboratory, *Microwave transmission circuits*: published and distributed by Boston Technical Publishers, 1964.

[4] G. L. Matthaei, *Microwave filters, impedance-matching networks, and coupling structures*: McGraw-Hill, 1964.

[5] S. B. Cohn, "Direct-Coupled-Resonator Filters," *Proceedings of the IRE,* vol. 45, pp. 187-196, 1957.

[6] L. Young, "Direct-Coupled Cavity Filters for Wide and Narrow Bandwidths," *Microwave Theory and Techniques, IEEE Transactions on,* vol. 11, pp. 162-178, 1963.

[7] R. Levy, "Theory of Direct-Coupled-Cavity Filters," *Microwave Theory and Techniques, IEEE Transactions on,* vol. 15, pp. 340-348, 1967.

[8] R. Levy and S. B. Cohn, "A History of Microwave Filter Research, Design, and Development," *Microwave Theory and Techniques, IEEE Transactions on,* vol. 32, pp. 1055-1067, 1984.

[9] R. J. Cameron, C. M. Kudsia, and R. R. Mansour, *Microwave filters for communication systems : fundamentals, design, and applications*. Hoboken, N.J.: Wiley ; Chichester : John Wiley [distributor], 2007.

[10] A. E. Atia; and A. E. Williams, "New types of bandpass filters for satellite transponders," *COMSAT Tech. Rev.,* vol. 1, pp. 21-43, Fall 1971.

[11] A. E. Atia and A. E. Williams, "Narrow-Bandpass Waveguide Filters," *Microwave Theory and Techniques, IEEE Transactions on,* vol. 20, pp. 258-265, 1972.

[12] A. E. Atia, A. E. Williams, and R. W. Newcomb, "Narrow-band multiple-coupled cavity synthesis," *Circuits and Systems, IEEE Transactions on,* vol. 21, pp. 649-655, 1974.

[13] A. E. Atia and A. E. Williams, "New types of bandpass filters for satellite transponders," *COMSAT Tech. Rev.,* vol. 1, pp. 21-43, Fall 1971.

[14] T. Skaik, "Synthesis of Coupled Resonator Circuits with Multiple Outputs using Coupling Matrix Optimization," Ph.D thesis, School of Electronic, Electrical and Computer Engineering, The University of Birmingham, Birmingham, 2011 http://etheses.bham.ac.uk/1534/.

[15] R. J. Cameron, "Advanced coupling matrix synthesis techniques for microwave filters," *Microwave Theory and Techniques, IEEE Transactions on,* vol. 51, pp. 1-10, 2003.

[16] R. J. Cameron, "General coupling matrix synthesis methods for Chebyshev filtering functions," *Microwave Theory and Techniques, IEEE Transactions on,* vol. 47, pp. 433-442, 1999.

[17] D. Swanson and G. Macchiarella, "Microwave filter design by synthesis and optimization," *Microwave Magazine, IEEE,* vol. 8, pp. 55-69, 2007.

[18] G. Macchiarella and S. Tamiazzo, "Synthesis of Star-Junction Multiplexers," *Microwave Theory and Techniques, IEEE Transactions on,* vol. 58, pp. 3732-3741, 2010.

[19] T. Skaik, M. Lancaster, K. Maolong, and W. Yi, "A micromachined WR-3 band waveguide diplexer based on coupled resonator structures," in *Microwave Conference (EuMC), 2011 41st European*, 2011, pp. 770-773.

[20] T. F. Skaik and M. J. Lancaster, "Coupled Resonator Diplexer without External Junctions," *Journal of Electromagnetic Analysis & Applications,* vol. 3, pp. 238-241, 2011.

[21] T. F. Skaik, M. J. Lancaster, and F. Huang, "Synthesis of multiple output coupled resonator circuits using coupling matrix optimisation," *Microwaves, Antennas & Propagation, IET,* vol. 5, pp. 1081-1088, 2011.

[22] W. Xia, X. Shang, and M. J. Lancaster., "Responses comparisons for coupled-resonator based diplexers," in *Passive RF and Microwave Components, 3rd Annual Seminar on*, 2012, pp. 67-75.

[23] X. Shang, Y. Wang, W. Xia, and M. J. Lancaster, "Novel Multiplexer Topologies Based on All-Resonator Structures," *Microwave Theory and Techniques, IEEE Transactions on,* vol. 61, pp. 3838-3845, 2013.

Chapter 3 Representation of *n*+*X* Coupling Matrix

The *n*+2 coupling matrix is not capable of describing an *n*-coupled-resonator circuit with *X* ports $(X \geq 3)$. It's necessary to extend the *n*+2 coupling matrix for the multi-port circuit, this will be detailed in this chapter.

Section 3.1 gives the derivation of the *n*+*X* coupling matrix from the electrically coupled resonator circuit. Section 3.2 shows how to derive the *n*+*X* coupling matrix from the magnetically coupled resonator circuit. A general formula regardless the type of couplings is given in Section 3.3.

3.1 Node Equation Formulation for Electrically Coupled Circuit

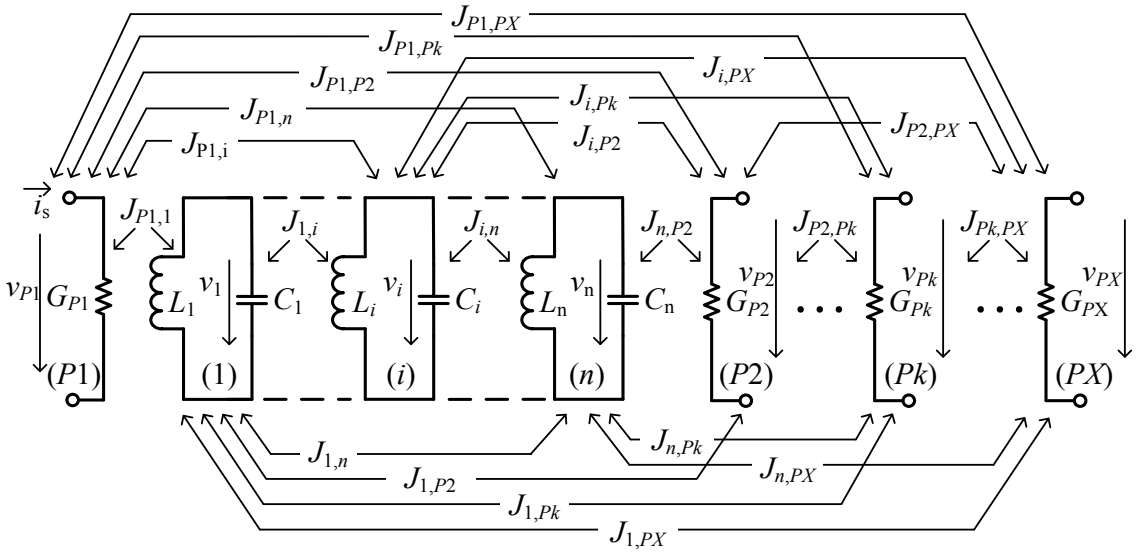

Figure 3.1 Equivalent lumped circuit for node-equation formulation in X-port network.

Figure 3.1 gives a multi-port lumped circuit coupled by *J*-inverters. The characteristic admittance of *J*-inverters is denoted as *J*. v_i (*i*=1 to *n*) and v_{Pk} (*k*=1 to *X*) are the node voltages. i_s is the source current. G_{Pk} (*k*=1 to *X*) is the conductance at port *k*. L_i and C_i are the inductors and capacitors of resonator *i*.

Based on Kirchoff's current law, a set of node equations is generated as:

$$\begin{aligned}
G_{P1}v_{P1} - jJ_{P1,1}v_1 - jJ_{P1,2}v_2 \ldots - jJ_{P1,n}v_n - jJ_{P1,P2}v_{P2} \ldots - jJ_{P1,PX}v_{PX} &= i_s \\
-jJ_{1,P1}v_{P1} + \left(\frac{1}{j\omega L_1} + j\omega C_1\right)v_1 - jJ_{1,2}v_2 \ldots - jJ_{1,n}v_n - jJ_{1,P2}v_{P2} \ldots jJ_{1,PX}v_{PX} &= 0 \\
-jJ_{2,P1}v_{P1} - jJ_{2,1}v_1 + \left(\frac{1}{j\omega L_2} + j\omega C_2\right)v_2 \ldots - jJ_{2,n}v_n - jJ_{2,P2}v_{P2} \ldots jJ_{2,PX}v_{PX} &= 0 \\
&\vdots \\
-jJ_{n,P1}v_{P1} - jJ_{n,1}v_1 - jJ_{n,2}v_2 \ldots + \left(\frac{1}{j\omega L_n} + j\omega C_n\right)v_n - jJ_{n,P2}v_{P2} \ldots jJ_{n,PX}v_{PX} &= 0 \\
-jJ_{P2,P1}v_{P1} - jJ_{P2,1}v_1 - jJ_{P2,2}v_2 \ldots - jJ_{P2,n}v_n + G_{P2}v_{P2} \ldots - jJ_{P2,PX}v_{PX} &= 0 \\
&\vdots \\
-jJ_{PX,P1}v_{P1} - jJ_{PX,1}v_1 - jJ_{PX,2}v_2 \ldots - jJ_{PX,n}v_n - jJ_{PX,P2}v_{P2} \ldots + G_{PX}v_{PX} &= 0
\end{aligned} \tag{3.1}$$

In matrix form:

$$\begin{bmatrix}
G_{P1} & -jJ_{P1,1} & -jJ_{P1,2} & \cdots & -jJ_{P1,n} & -jJ_{P1,P2} & \cdots & -jJ_{P1,PX} \\
-jJ_{1,P1} & \left(\frac{1}{j\omega L_1} + j\omega C_1\right) & -jJ_{1,2} & \cdots & -jJ_{1,n} & -jJ_{1,P2} & \cdots & -jJ_{1,PX} \\
-jJ_{2,P1} & -jJ_{2,1} & \left(\frac{1}{j\omega L_2} + j\omega C_2\right) & \cdots & -jJ_{2,n} & -jJ_{2,P2} & \cdots & -jJ_{2,PX} \\
\vdots & \vdots & \vdots & \ddots & \vdots & \vdots & \vdots & \vdots \\
-jJ_{n,P1} & -jJ_{n,1} & -jJ_{n,2} & \cdots & \left(\frac{1}{j\omega L_n} + j\omega C_n\right) & -jJ_{n,P2} & \cdots & -jJ_{n,PX} \\
-jJ_{P2,P1} & -jJ_{P2,1} & -jJ_{P2,2} & \cdots & -jJ_{P2,n} & G_{P2} & \cdots & -jJ_{P2,PX} \\
\vdots & \vdots & \vdots & \vdots & \vdots & \vdots & \ddots & \vdots \\
-jJ_{PX,P1} & -jJ_{PX,1} & -jJ_{PX,2} & \cdots & -jJ_{PX,n} & -jJ_{PX,P2} & \cdots & G_{PX}
\end{bmatrix}
\begin{bmatrix} v_{P1} \\ v_1 \\ v_2 \\ \vdots \\ v_n \\ v_{P2} \\ \vdots \\ v_{PX} \end{bmatrix}
=
\begin{bmatrix} i_s \\ 0 \\ 0 \\ \vdots \\ 0 \\ 0 \\ \vdots \\ 0 \end{bmatrix} \tag{3.2}$$

or

$$[Y]\cdot[v] = [i] \tag{3.3}$$

Where $[Y]$ is the $n+X$ admittance matrix.

Next step is to find the relationship between the admittance matrix $[Y]$ and the scattering parameters. According to [1], a lumped multi-port n-coupled-resonator circuit can be

simplified into its network representation with impedance matrix as in Figure 3.2(a).

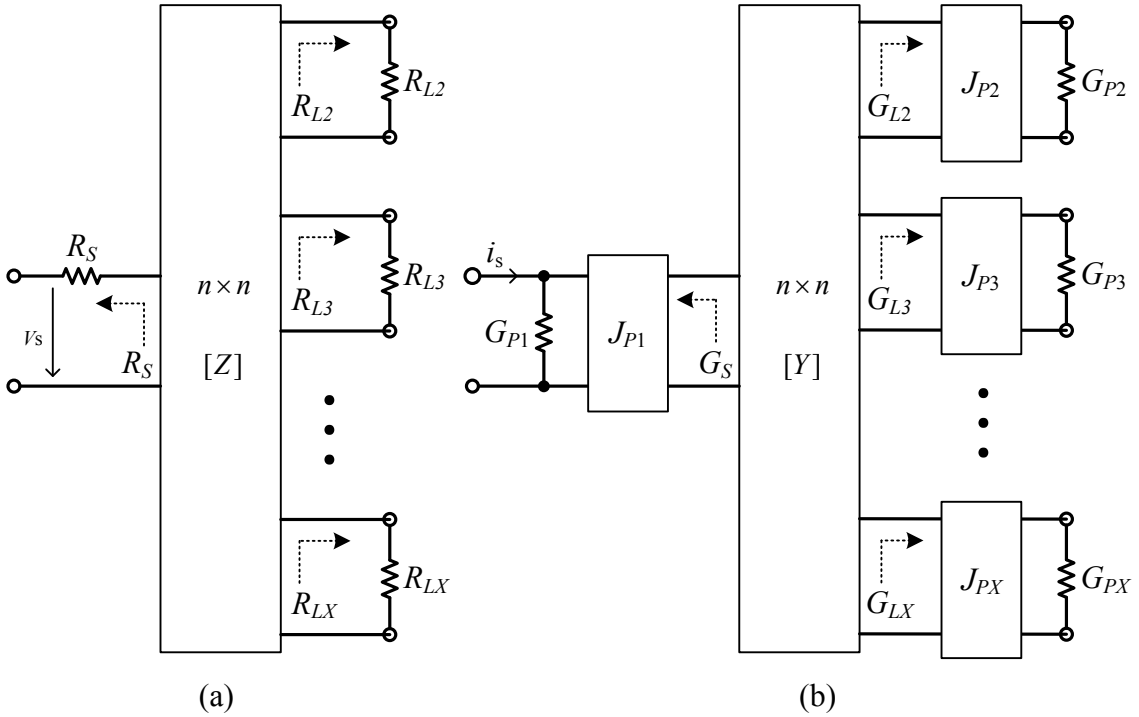

Figure 3.2 Network representation of X-port n-coupled-resonator circuit in (a) the general $n \times n$ impedance matrix form [Z] and (b) its dual $n \times n$ admittance matrix form [Y] with port J-inverters.

Here the network is in the form of general $n \times n$ impedance matrix $[Z]_{n \times n}$ and the resistance in the source R_S and loads R_{Li}. Due to the limitation of the general $n \times n$ matrix, each resonator/port can connect to no more than one port/resonator.

To turn the general $n \times n$ matrix into the $n+X$ matrix form, each port resistance is replaced by a port conductance G_{Pk} with a J-inverter [1]. In order to match the additional J-inverters, the impedance matrix $[Z]_{n \times n}$ is replaced by its dual admittance matrix [Y]. Figure 3.2(b) gives the equivalent $[Y]_{n \times n}$ matrix network surrounded by additional J-inverters between the port conductances and the resonators.

In order to simplify the circuit, each conductance G_{Pk} at the port k is normalised to 1 or

$$G_{Pk} = 1/1\Omega \quad (k = 1 \text{ to } X) \tag{3.4}$$

According to (2.1), the characteristic admittance of the *J*-inverter at the source port is:

$$J_{P1} = \sqrt{Y_1 Y_2} = \sqrt{G_s G_{P1}} = \sqrt{G_s} \tag{3.5}$$

where $Y_1 = G_s = \dfrac{1}{R_s}, Y_2 = G_{P1} = 1/1\Omega$.

Similarly, the characteristic admittance of *J*-inverters at the load port *i* is:

$$J_{Pi} = \sqrt{Y_1' Y_2'} = = \sqrt{G_{Li} G_{P1}} = \sqrt{G_{Li}} \quad (i = 2 \text{ to } X) \tag{3.6}$$

where $Y_1' = G_{Li} = \dfrac{1}{R_{Li}}, Y_2' = G_{Pi} = 1/1\Omega$.

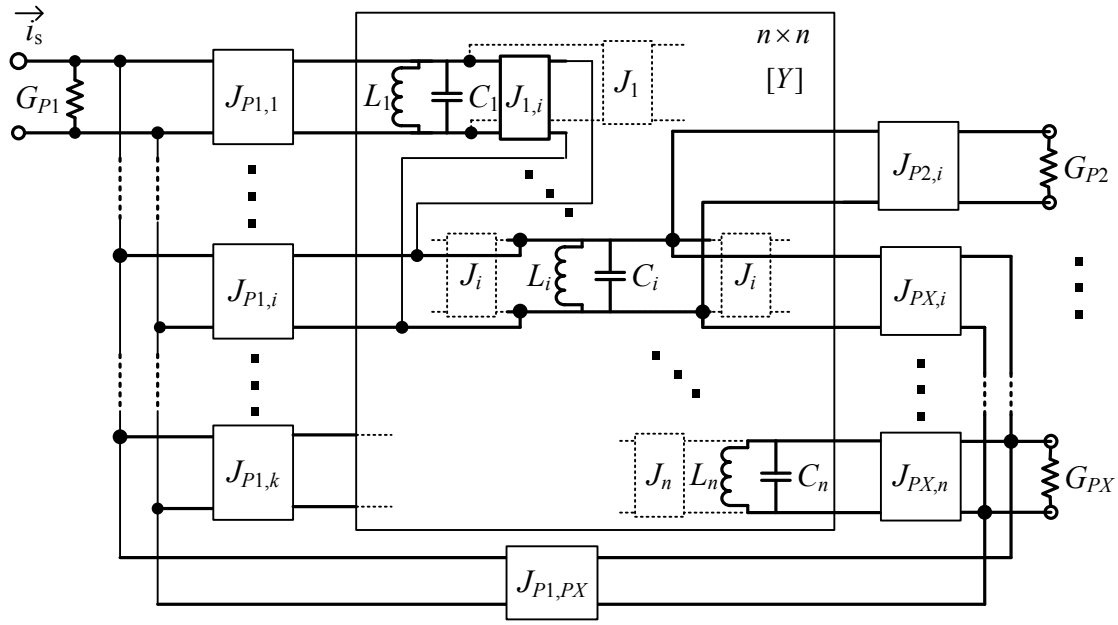

Figure 3.3 The network representation of an *X*-port *n*-coupled-resonator circuit. The network is formed of the general $n \times n$ admittance matrix [Y], the conductance G_{Pk} of port *k* and the *J*-inverters. $J_{1,i}$ is the inverter between Resonator 1 and *i*. $J_{Pk,h}$ is the inverter between the port *k* and resonator *h*. $J_{P1,PX}$ is the port inverter between port 1 and *X*. Some resonators of the circuit are illustrated. The other resonators, as well as the other *J*-inverters between the resonators, are omitted.

As given in Figure 3.3, with the application of the port inverters, a port can be coupled to multiple resonators while the resonator i can be coupled to multiple ports. A direct coupling between two ports is also possible. Comparing to the $n \times n$ coupling matrix discussed in Chapter 2, the $n+X$ matrix is more general.

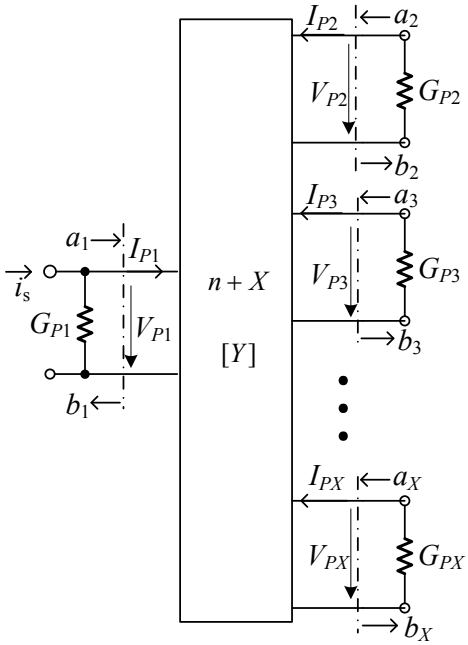

Figure 3.4 The network representation of an X-port n-coupled-resonator circuit in the $n+X$ admittance matrix form for node-equation formulation. Where G_{Pk}, V_{Pk} and I_{Pk} are the conductance, voltage and current at port k, and the wave variables a_k and b_k at port k are defined as (3.7).

By absorbing the port inverters into the admittance matrix $[Y]_{n\times n}$, a new network representation in the $n+X$ admittance matrix form is shown in Figure 3.4, where G_{Pk}, V_{Pk} and I_{Pk} are the conductance, voltage and current at port k, and the wave variables a_k and b_k are defined as [2]:

$$a_k = \frac{1}{2}\left(V_{Pk}\sqrt{Y_{Pk}} + \frac{I_{Pk}}{\sqrt{Y_{Pk}}} \right) \qquad (k = 1 \text{ to } X)$$
$$b_k = \frac{1}{2}\left(V_{Pk}\sqrt{Y_{Pk}} - \frac{I_{Pk}}{\sqrt{Y_{Pk}}} \right) \qquad (k = 1 \text{ to } X) \tag{3.7}$$

According to [2], the relationships between the scattering parameters and the wave variables a_k and b_k are:

$$S_{k1} = \left.\frac{b_k}{a_1}\right|_{a2=a3...=aX=0} \qquad (k=1)$$
$$S_{k1} = \left.\frac{b_k}{a_1}\right|_{a2=a3...=aX=0} \qquad (k = 2 \text{ to } X) \tag{3.8}$$

The admittance network in Figure 3.4 has the equivalent lumped circuit in Figure 3.1. By inspecting the network representation in Figure 3.4 and the circuit in Figure 3.1, it can be recognized that V_{Pk}=v_{Pk} , I_{Pk}=-i_{Pk} (k=1 to X), $I_{P1} = i_s - V_{P1}\cdot G_{P1}$. Considering (3.4), we have

$$a_1 = \frac{i_s}{2\sqrt{G_1}} = \frac{i_s}{2} \qquad b_1 = \frac{2v_{P1}G_1 - i_s}{2\sqrt{G_1}} = \frac{2v_{P1} - i_s}{2}$$
$$a_k = 0 \qquad b_k = v_{Pk}\sqrt{G_k} = v_{Pk} \tag{3.9}$$

According to [2], the relationships between scattering parameters and wave variables are:

$$S_{k1} = \left.\frac{b_k}{a_1}\right|_{a2=a3...=aX=0} = \frac{2v_{Pk}}{i_s} - 1 \qquad (k=1)$$
$$S_{k1} = \left.\frac{b_k}{a_1}\right|_{a2=a3...=aX=0} = \frac{2v_{Pk}}{i_s} \qquad (k = 2 \text{ to } X) \tag{3.10}$$

v_{Pk} are found from (3.2) as

$$v_{Pk} = i_s \cdot [Y]^{-1}_{Pk,P1} \tag{3.11}$$

where $[Y]^{-1}_{Pk,P1}$ is denoted as the entry element on row Pk and column $P1$ of $[Y]^{-1}$. Replacing

the node voltages in (3.10) with those given by (3.11) results in

$$\begin{aligned} S_{11} &= 2[Y]^{-1}_{P1,P1} - 1 \\ S_{k1} &= 2[Y]^{-1}_{Pk,P1} \qquad (k = 2 \text{ to } X) \end{aligned} \tag{3.12}$$

The next step is to normalise the admittance matrix [Y] in order to get the coupling matrix. For simplicity, the circuit in Figure 3.1 is considered as a synchronously tuned network first. The centre frequency $\omega_0 = \frac{1}{\sqrt{LC}}$. L_1=L_2...=L_n=L. C_1=C_2=…=C_n=C. Each row i and column i of [Y] in (3.2) is multiplied by $\left(\sqrt{\omega_0 C \cdot FBW}\right)^{-1}$. $FBW = \Delta\omega / \omega_0$ is the fractional bandwidth of the network. In addition, as (3.4) assumed, the conductance at each port is unity. The row P_k and column P_k (k=1 to X) need not be scaled. The normalised matrix $[\overline{Y}]$ is

$$\begin{bmatrix} 1 & -j\frac{J_{P1,1}}{\sqrt{\omega_0 C \cdot FBW}} & -j\frac{J_{P1,2}}{\sqrt{\omega_0 C \cdot FBW}} & \cdots & -j\frac{J_{P1,n}}{\sqrt{\omega_0 C \cdot FBW}} & -jJ_{P1,P2} & \cdots & -jJ_{P1,PX} \\ -j\frac{J_{1,P1}}{\sqrt{\omega_0 C \cdot FBW}} & p & -j\frac{J_{1,2}}{\omega_0 C \cdot FBW} & \cdots & -j\frac{J_{1,n}}{\omega_0 C \cdot FBW} & -j\frac{J_{1,P2}}{\sqrt{\omega_0 C \cdot FBW}} & \cdots & -j\frac{J_{1,PX}}{\sqrt{\omega_0 C \cdot FBW}} \\ -j\frac{J_{2,P1}}{\sqrt{\omega_0 C \cdot FBW}} & -j\frac{J_{2,1}}{\omega_0 C \cdot FBW} & p & \cdots & -j\frac{J_{2,n}}{\omega_0 C \cdot FBW} & -j\frac{J_{2,P2}}{\sqrt{\omega_0 C \cdot FBW}} & \cdots & -j\frac{J_{2,PX}}{\sqrt{\omega_0 C \cdot FBW}} \\ \vdots & \vdots & \vdots & \ddots & \vdots & \vdots & \vdots & \vdots \\ -j\frac{J_{n,P1}}{\sqrt{\omega_0 C \cdot FBW}} & -j\frac{J_{n,1}}{\omega_0 C \cdot FBW} & -j\frac{J_{n,2}}{\omega_0 C \cdot FBW} & \cdots & p & -j\frac{J_{n,P2}}{\sqrt{\omega_0 C \cdot FBW}} & \cdots & -j\frac{J_{n,PX}}{\sqrt{\omega_0 C \cdot FBW}} \\ -jJ_{P2,P1} & -j\frac{J_{P2,1}}{\sqrt{\omega_0 C \cdot FBW}} & -j\frac{J_{P2,2}}{\sqrt{\omega_0 C \cdot FBW}} & \cdots & -j\frac{J_{P2,n}}{\sqrt{\omega_0 C \cdot FBW}} & 1 & \cdots & -jJ_{P2,PX} \\ \vdots & \vdots & \vdots & \vdots & \vdots & \vdots & \ddots & \vdots \\ -jJ_{PX,P1} & -j\frac{J_{PX,1}}{\sqrt{\omega_0 C \cdot FBW}} & -j\frac{J_{PX,2}}{\sqrt{\omega_0 C \cdot FBW}} & \cdots & -j\frac{J_{PX,n}}{\sqrt{\omega_0 C \cdot FBW}} & -jJ_{PX,P2} & \cdots & 1 \end{bmatrix} \tag{3.13}$$

Where p is the complex lowpass frequency variable, i.e.

$$p = \frac{j\omega C_i + \frac{1}{j\omega L_i}}{\omega_0 C \cdot FBW} = j\frac{1}{FBW}\left(\frac{\omega C_i}{\omega_0 C} - \frac{1}{\omega_0 C \cdot \omega L_i}\right) = j\frac{1}{FBW}\left(\frac{\omega}{\omega_0} - \frac{\omega_0}{\omega}\right) \tag{3.14}$$

$J_{i,j}$=$J_{j,i}$ ($i, j = 1$ to n, $i \neq j$) is the characteristic admittance between resonator i and j.

For simplicity, all the resonators are assumed to be coupled by electrical couplings or mutual capacitors. According to Figure 2.4(d), the characteristic admittance J is formulated as:

$$J_{i,j} = J_{j,i} = \omega C_{i,j} = \omega C_{j,i} \tag{3.15}$$

Where $C_{i,j} = C_{j,i}$ represents the mutual capacitance between resonator i and j.

According to (3.5) and (3.6), the characteristic admittance $J_{Pk,i} = J_{i,Pk}$ ($k = 1$ to X, $i = 1$ to n) is presented in terms of the source and load conductances as:

$$\begin{aligned} J_{P1,i} &= J_{i,P1} = \sqrt{G_{S,i}} = \sqrt{G_{i,S}} \\ J_{Pk,i} &= J_{i,Pk} = \sqrt{G_{Lk,i}} = \sqrt{G_{i,Lk}} \end{aligned} \quad (k = 2 \text{ to } X, i = 1 \text{ to } n) \tag{3.16}$$

Where $G_{S,i}$ and $G_{i,S}$ are the equivalent source conductance at Resonator i, $G_{Lk,i}$ and $G_{i,Lk}$ are the equivalent conductance of load k at Resonator i. So the normalised admittance matrix $[\overline{Y}]$ is replaced as:

$$\begin{bmatrix} 1 & -j\sqrt{\frac{G_{S,1}}{\omega_0 C \cdot FBW}} & -j\sqrt{\frac{G_{S,2}}{\omega_0 C \cdot FBW}} & \cdots & -j\sqrt{\frac{G_{S,n}}{\omega_0 C \cdot FBW}} & -jJ_{P1,P2} & \cdots & -jJ_{P1,PX} \\ -j\sqrt{\frac{G_{1,S}}{\omega_0 C \cdot FBW}} & p & -j\frac{\omega C_{1,2}}{\omega_0 C \cdot FBW} & \cdots & -j\frac{\omega C_{1,n}}{\omega_0 C \cdot FBW} & -j\sqrt{\frac{G_{1,L2}}{\omega_0 C \cdot FBW}} & \cdots & -j\sqrt{\frac{G_{1,LX}}{\omega_0 C \cdot FBW}} \\ -j\sqrt{\frac{G_{2,S}}{\omega_0 C \cdot FBW}} & -j\frac{\omega C_{2,1}}{\omega_0 C \cdot FBW} & p & \cdots & -j\frac{\omega C_{2,n}}{\omega_0 C \cdot FBW} & -j\sqrt{\frac{G_{2,L2}}{\omega_0 C \cdot FBW}} & \cdots & -j\sqrt{\frac{G_{2,LX}}{\omega_0 C \cdot FBW}} \\ \vdots & \vdots & \vdots & \ddots & \vdots & \vdots & \vdots & \vdots \\ -j\sqrt{\frac{G_{n,S}}{\omega_0 C \cdot FBW}} & -j\frac{\omega C_{n,1}}{\omega_0 C \cdot FBW} & -j\frac{\omega C_{n,2}}{\omega_0 C \cdot FBW} & \cdots & p & -j\sqrt{\frac{G_{n,L2}}{\omega_0 C \cdot FBW}} & \cdots & -j\sqrt{\frac{G_{n,LX}}{\omega_0 C \cdot FBW}} \\ -jJ_{P2,P1} & -j\sqrt{\frac{G_{L2,1}}{\omega_0 C \cdot FBW}} & -j\sqrt{\frac{G_{L2,2}}{\omega_0 C \cdot FBW}} & \cdots & -j\sqrt{\frac{G_{L2,X}}{\omega_0 C \cdot FBW}} & 1 & \cdots & -jJ_{P2,PX} \\ \vdots & \vdots & \vdots & \vdots & \vdots & \vdots & \ddots & \vdots \\ -jJ_{PX,P1} & -j\sqrt{\frac{G_{LX,1}}{\omega_0 C \cdot FBW}} & -j\sqrt{\frac{G_{LX,2}}{\omega_0 C \cdot FBW}} & \cdots & -j\sqrt{\frac{G_{LX,X}}{\omega_0 C \cdot FBW}} & -jJ_{PX,P2} & \cdots & 1 \end{bmatrix} \tag{3.17}$$

It should be noticed that [2]:

$$\frac{G}{\omega_0 C} = \frac{1}{Q_e}, \quad \frac{C_{i,j}}{C} = M_{i,j} \tag{3.18}$$

$$q_e = Q_e \cdot FBW, \;\; m_{i,j} = \frac{M_{i,j}}{FBW} \quad \left(i, j = 1 \text{ to } n, \; i \neq j\right) \tag{3.19}$$

Q_e is defined as the external quality factor of the resonator at the port. $M_{i,j}$ is defined as the coupling coefficient between Resonator i and j. q_e and $m_{i,j}$ are the scaled external quality factor and scaled coupling coefficient, respectively.

Defining the coupling coefficient $M_{pi,pj}$ between port i and j as:

$$M_{pi,pj} = J_{pi,pj} \;\; (i, j = 1 \text{ to } X, \; i \neq j) \tag{3.20}$$

During the scaling of the $[Y]$ matrix, the characteristic admittance between ports is kept constant. So the normalised port coupling coefficient is

$$m_{pi,pj} = M_{pi,pj} \tag{3.21}$$

Substituting (3.18) and (3.20) into (3.17), we have $[\overline{Y}]$ as

$$\begin{bmatrix}
1 & -j\sqrt{\frac{1}{Q_{eS,1} \cdot FBW}} & -j\sqrt{\frac{1}{Q_{eS,2} \cdot FBW}} & \cdots & -j\sqrt{\frac{1}{Q_{eS,n} \cdot FBW}} & -jM_{P1,P2} & \cdots & -jM_{P1,PX} \\
-j\sqrt{\frac{1}{Q_{e1,S} \cdot FBW}} & p & -j\frac{\omega \cdot M_{1,2}}{\omega_0 \cdot FBW} & \cdots & -j\frac{\omega \cdot M_{1,n}}{\omega_0 \cdot FBW} & -j\sqrt{\frac{1}{Q_{e1,L2} \cdot FBW}} & \cdots & -j\sqrt{\frac{1}{Q_{e1,LX} \cdot FBW}} \\
-j\sqrt{\frac{1}{Q_{e2,S} \cdot FBW}} & -j\frac{\omega \cdot M_{2,1}}{\omega_0 \cdot FBW} & p & \cdots & -j\frac{\omega \cdot M_{2,n}}{\omega_0 \cdot FBW} & -j\sqrt{\frac{1}{Q_{e2,L2} \cdot FBW}} & \cdots & -j\sqrt{\frac{1}{Q_{e2,LX} \cdot FBW}} \\
\vdots & \vdots & \vdots & \ddots & \vdots & \vdots & \vdots & \vdots \\
-j\sqrt{\frac{1}{Q_{en,S} \cdot FBW}} & -j\frac{\omega \cdot M_{n,1}}{\omega_0 \cdot FBW} & -j\frac{\omega \cdot M_{n,2}}{\omega_0 \cdot FBW} & \cdots & p & -j\sqrt{\frac{1}{Q_{en,L2} \cdot FBW}} & \cdots & -j\sqrt{\frac{1}{Q_{en,LX} \cdot FBW}} \\
-jM_{P2,P1} & -j\sqrt{\frac{1}{Q_{eL2,1} \cdot FBW}} & -j\sqrt{\frac{1}{Q_{eL2,2} \cdot FBW}} & \cdots & -j\sqrt{\frac{1}{Q_{eL2,X} \cdot FBW}} & 1 & \cdots & -jM_{P2,PX} \\
\vdots & \vdots & \vdots & \vdots & \vdots & \vdots & \ddots & \vdots \\
-jM_{PX,P1} & -j\sqrt{\frac{1}{Q_{eLX,1} \cdot FBW}} & -j\sqrt{\frac{1}{Q_{eLX,2} \cdot FBW}} & \cdots & -j\sqrt{\frac{1}{Q_{eLX,X} \cdot FBW}} & -jM_{PX,P2} & \cdots & 1
\end{bmatrix} \tag{3.22}$$

Assuming $\omega/\omega_0 \approx 1$ for a narrow band approximation (for a wide band circuit, $\omega/\omega_0 \neq 1$ and m is frequency-variant), $[\overline{Y}]$ in (3.22) is simplified as

$$\begin{bmatrix}
1 & -j\sqrt{\frac{1}{Q_{eS,1}\cdot FBW}} & -j\sqrt{\frac{1}{Q_{eS,2}\cdot FBW}} & \cdots & -j\sqrt{\frac{1}{Q_{eS,n}\cdot FBW}} & -jM_{P1,P2} & \cdots & -jM_{P1,PX} \\
-j\sqrt{\frac{1}{Q_{e1,S}\cdot FBW}} & p & -j\frac{M_{1,2}}{FBW} & \cdots & -j\frac{M_{1,n}}{FBW} & -j\sqrt{\frac{1}{Q_{e1,L2}\cdot FBW}} & \cdots & -j\sqrt{\frac{1}{Q_{e1,LX}\cdot FBW}} \\
-j\sqrt{\frac{1}{Q_{e2,S}\cdot FBW}} & -j\frac{M_{2,1}}{FBW} & p & \cdots & -j\frac{M_{2,n}}{FBW} & -j\sqrt{\frac{1}{Q_{e2,L2}\cdot FBW}} & \cdots & -j\sqrt{\frac{1}{Q_{e2,LX}\cdot FBW}} \\
\vdots & \vdots & \vdots & \ddots & \vdots & \vdots & \vdots & \vdots \\
-j\sqrt{\frac{1}{Q_{en,S}\cdot FBW}} & -j\frac{M_{n,1}}{FBW} & -j\frac{M_{n,2}}{FBW} & \cdots & p & -j\sqrt{\frac{1}{Q_{en,L2}\cdot FBW}} & \cdots & -j\sqrt{\frac{1}{Q_{en,LX}\cdot FBW}} \\
-jM_{P2,P1} & -j\sqrt{\frac{1}{Q_{eL2,1}\cdot FBW}} & -j\sqrt{\frac{1}{Q_{eL2,2}\cdot FBW}} & \cdots & -j\sqrt{\frac{1}{Q_{eL2,X}\cdot FBW}} & 1 & \cdots & -jM_{P2,PX} \\
\vdots & \vdots & \vdots & \vdots & \vdots & \vdots & \ddots & \vdots \\
-jM_{PX,P1} & -j\sqrt{\frac{1}{Q_{eLX,1}\cdot FBW}} & -j\sqrt{\frac{1}{Q_{eLX,2}\cdot FBW}} & \cdots & -j\sqrt{\frac{1}{Q_{eLX,X}\cdot FBW}} & -jM_{PX,P2} & \cdots & 1
\end{bmatrix} \tag{3.23}$$

Substituting (3.19) and (3.21) into (3.23), $[\overline{Y}]$ is simplified as

$$\begin{bmatrix}
1 & -j\sqrt{\frac{1}{q_{eS,1}}} & -j\sqrt{\frac{1}{q_{eS,2}}} & \cdots & -j\sqrt{\frac{1}{q_{eS,n}}} & -jm_{P1,P2} & \cdots & -jm_{P1,PX} \\
-j\sqrt{\frac{1}{q_{1,eS}}} & p & -jm_{1,2} & \cdots & -jm_{1,n} & -j\sqrt{\frac{1}{q_{1,L2}}} & \cdots & -j\sqrt{\frac{1}{q_{1,LX}}} \\
-j\sqrt{\frac{1}{q_{2,eS}}} & -jm_{2,1} & p & \cdots & -jm_{2,n} & -j\sqrt{\frac{1}{q_{2,L2}}} & \cdots & -j\sqrt{\frac{1}{q_{2,LX}}} \\
\vdots & \vdots & \vdots & \ddots & \vdots & \vdots & \vdots & \vdots \\
-j\sqrt{\frac{1}{q_{n,eS}}} & -jm_{n,1} & -jm_{n,2} & \cdots & p & -j\sqrt{\frac{1}{q_{n,L2}}} & \cdots & -j\sqrt{\frac{1}{q_{n,LX}}} \\
-jm_{P2,P1} & -j\sqrt{\frac{1}{q_{L2,1}}} & -j\sqrt{\frac{1}{q_{L2,1}}} & \cdots & -j\sqrt{\frac{1}{q_{L2,1}}} & 1 & \cdots & -jm_{P2,PX} \\
\vdots & \vdots & \vdots & \vdots & \vdots & \vdots & \ddots & \vdots \\
-jm_{PX,P1} & -j\sqrt{\frac{1}{q_{LX,1}}} & -j\sqrt{\frac{1}{q_{LX,2}}} & \cdots & -j\sqrt{\frac{1}{q_{LX,n}}} & -jm_{PX,P2} & \cdots & 1
\end{bmatrix} \tag{3.24}$$

Defining the normalised coupling coefficient between ports and resonators as:

$$
\begin{aligned}
m_{P1,i} &= m_{i,P1} = \sqrt{\frac{1}{q_{eS,i}}} = \sqrt{\frac{1}{q_{ei,S}}}; \\
m_{Pk,i} &= m_{i,Pk} = \sqrt{\frac{1}{q_{eLk,i}}} = \sqrt{\frac{1}{q_{ei,Lk}}};
\end{aligned}
\quad \left(i = 1 \text{ to } n,\ k = 2 \text{ to } X\right) \tag{3.25}
$$

$[\overline{Y}]$ in (3.24) is further simplified as

$$
\begin{bmatrix}
1 & -jm_{P1,1} & -jm_{P1,2} & \cdots & -jm_{P1,n} & -jm_{P1,P2} & \cdots & -jm_{P1,PX} \\
-jm_{1,P1} & p & -jm_{1,2} & \cdots & -jm_{1,n} & -jm_{1,P2} & \cdots & -jm_{1,PX} \\
-jm_{2,P1} & -jm_{2,1} & p & \cdots & -jm_{2,n} & -jm_{2,P2} & \cdots & -jm_{2,PX} \\
\vdots & \vdots & \vdots & \ddots & \vdots & \vdots & \vdots & \vdots \\
-jm_{n,P1} & -jm_{n,1} & -jm_{n,2} & \cdots & p & -jm_{n,P2} & \cdots & -jm_{n,PX} \\
-jm_{P2,P1} & -jm_{P2,1} & -jm_{P2,2} & \cdots & -jm_{P2,n} & 1 & \cdots & -jm_{P2,PX} \\
\vdots & \vdots & \vdots & \vdots & \vdots & \vdots & \ddots & \vdots \\
-jm_{PX,P1} & -jm_{PX,1} & -jm_{PX,2} & \cdots & -jm_{PX,n} & -jm_{PX,P2} & \cdots & 1
\end{bmatrix} \tag{3.26}
$$

As shown in [3], the inverse of a matrix can be expressed as:

$$
\begin{aligned}
[Y]^{-1}_{Pi,Pj} &= \frac{cof\left(Y_{Pi,Pj}\right)}{|Y|}, \left(|Y| \neq 0\right) \\
[\overline{Y}]^{-1}_{Pi,Pj} &= \frac{cof\left(\overline{Y}_{Pi,Pj}\right)}{|\overline{Y}|}, \left(|\overline{Y}| \neq 0\right)
\end{aligned} \tag{3.27}
$$

where $|Y|$ and $|\overline{Y}|$ are the determinant of matrix $[Y]$ and $[\overline{Y}]$. $cof\left(Y_{Pi,Pj}\right)$ and $cof\left(\overline{Y}_{Pi,Pj}\right)$ are the entries in column P_i and row P_j of the cofactor matrices of $[Y]$ and $[\overline{Y}]$. By inspecting matrix $[Y]$ in (3.2) and $[\overline{Y}]$ in (3.13), we obtain the relationships of their determinants and cofactors as:

$$
\begin{aligned}
|Y| &= \left(\sqrt{\omega_0 C \cdot FBW}\right)^{2n} \cdot |\overline{Y}| \\
cof\left(Y_{Pi,Pj}\right) &= \left(\sqrt{\omega_0 C \cdot FBW}\right)^{2n} \cdot cof\left(\overline{Y}_{Pi,Pj}\right) \quad \left(i, j = 1 \text{ to } X,\ i \neq j\right)
\end{aligned} \tag{3.28}
$$

Substituting (3.28) into (3.27) yields:

$$[Y]^{-1}_{Pi,Pj} = [\overline{Y}]^{-1}_{Pi,Pj} \tag{3.29}$$

Notice that this equation is valid only for entries in row P_i and row P_j. Substituting (3.29) into (3.12) yields:

$$\begin{aligned} S_{11} &= 2[\overline{Y}]^{-1}_{P1,P1} - 1 \\ S_{k1} &= 2[\overline{Y}]^{-1}_{Pk,P1} \qquad (k = 2 \text{ to } X) \end{aligned} \tag{3.30}$$

In the case of asynchronously tuned coupled-resonator circuit in Figure 3.1, the resonant frequency of Resonator i is given by $\omega_i = \frac{1}{\sqrt{L_i C_i}}$, the coupling coefficient between asynchronously tuned Resonator i and j is defined as

$$\frac{C_{i,j}}{\sqrt{C_i C_j}} = M_{i,j} \quad (i, j = 1 \text{ to } n,\ i \neq j) \tag{3.31}$$

And the normalised matrix $[\overline{Y}]$ in (3.26) becomes

$$\begin{bmatrix} 1 & -jm_{P1,1} & -jm_{P1,2} & \cdots & -jm_{P1,n} & -jm_{P1,P2} & \cdots & -jm_{P1,PX} \\ -jm_{1,P1} & p - jm_{1,1} & -jm_{1,2} & \cdots & -jm_{1,n} & -jm_{1,P2} & \cdots & -jm_{1,PX} \\ -jm_{2,P1} & -jm_{2,1} & p - jm_{2,2} & \cdots & -jm_{2,n} & -jm_{2,P2} & \cdots & -jm_{2,PX} \\ \vdots & \vdots & \vdots & \ddots & \vdots & \vdots & \vdots & \vdots \\ -jm_{n,P1} & -jm_{n,1} & -jm_{n,2} & \cdots & p - jm_{n,n} & -jm_{n,P2} & \cdots & -jm_{n,PX} \\ -jm_{P2,P1} & -jm_{P2,1} & -jm_{P2,2} & \cdots & -jm_{P2,n} & 1 & \cdots & -jm_{P2,PX} \\ \vdots & \vdots & \vdots & \vdots & \vdots & \vdots & \ddots & \vdots \\ -jm_{PX,P1} & -jm_{PX,1} & -jm_{PX,2} & \cdots & -jm_{PX,n} & -jm_{PX,P2} & \cdots & 1 \end{bmatrix} \tag{3.32}$$

The normalised admittance matrix of (3.32) is nearly the same as (3.26) except for extra entries $m_{i,i}$ along the diagonal to account for asynchronous tuning.

3.2 Loop Equation Formulation for Magnetically Coupled Circuit

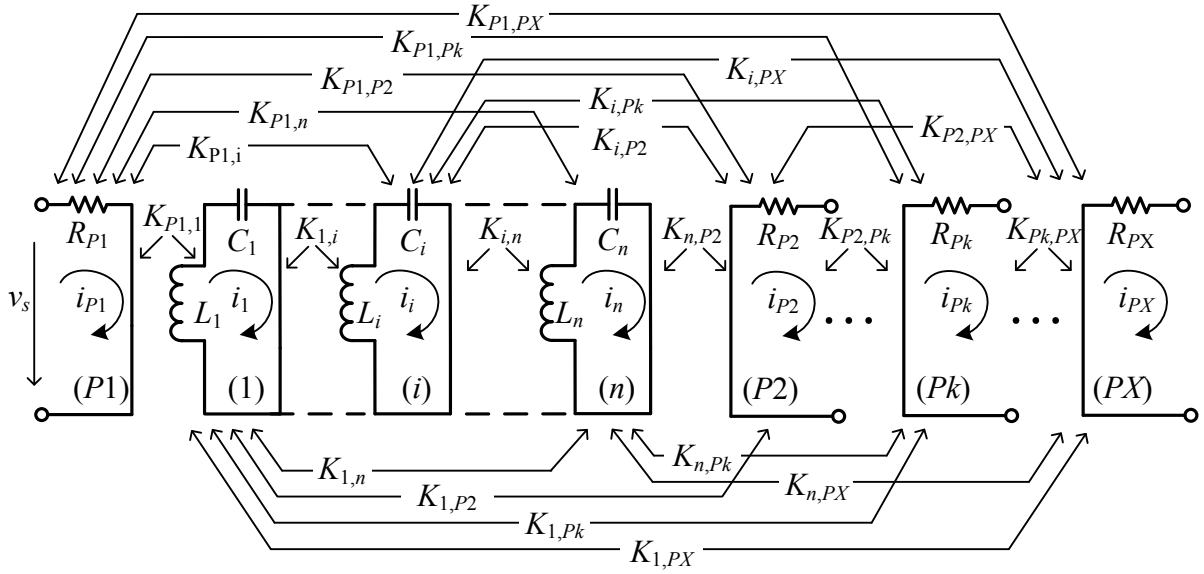

Figure 3.5 Equivalent lumped circuit for *X*-port coupled-resonator circuit with *K*-inverters.

A multiport coupled-resonator circuit with *K*-inverters is shown in Figure 3.5. The characteristic impedance of *K*-inverters is denoted as *K*. i_i and i_{Pk} are the loop currents. v_s is the source voltage. L_i and C_i are the inductor and capacitor of resonator *i*. R_{Pk} is the resistance at port *k*.

Based on Kirchoff's voltage law, a set of loop equations is generated as:

$$
\begin{aligned}
R_{P1}i_{P1} - jK_{P1,1}i_1 - jK_{P1,2}i_2 \ldots - jK_{P1,n}i_n - jK_{P1,P2}i_{P2} \ldots - jK_{P1,PX}i_{PX} &= v_s \\
-jK_{1,P1}i_{P1} + \left(\frac{1}{j\omega C_1} + j\omega L_1\right)i_1 - jK_{1,2}i_2 \ldots - jK_{1,n}i_n - jK_{1,P2}i_{P2} \ldots jK_{1,PX}i_{PX} &= 0 \\
-jK_{2,P1}i_{P1} - jJ_{2,1}i_1 + \left(\frac{1}{j\omega C_2} + j\omega L_2\right)i_2 \ldots - jK_{2,n}i_n - jK_{2,P2}i_{P2} \ldots jK_{2,PX}i_{PX} &= 0 \\
&\vdots \\
-jK_{n,P1}i_{P1} - jK_{n,1}i_1 - jK_{n,2}i_2 \ldots + \left(\frac{1}{j\omega C_n} + j\omega L_n\right)i_n - jK_{n,P2}i_{P2} \ldots jK_{n,PX}i_{PX} &= 0 \\
-jK_{P2,P1}i_{P1} - jK_{P2,1}i_1 - jK_{P2,2}i_2 \ldots - jK_{P2,n}i_n + R_{P2}i_{P2} \ldots - jK_{P2,PX}i_{PX} &= 0 \\
&\vdots \\
-jK_{PX,P1}i_{P1} - jK_{PX,1}i_1 - jK_{PX,2}i_2 \ldots - jK_{PX,n}i_n - jK_{PX,P2}i_{P2} \ldots + R_{PX}i_{PX} &= 0
\end{aligned}
\tag{3.33}
$$

In matrix form:

$$\begin{bmatrix} R_{P1} & -jK_{P1,1} & -jK_{P1,2} & \cdots & -jK_{P1,n} & -jK_{P1,P2} & \cdots & -jK_{P1,PX} \\ -jK_{1,P1} & \left(\frac{1}{j\omega C_1}+j\omega L_1\right) & -jK_{1,2} & \cdots & -jK_{1,n} & -jK_{1,P2} & \cdots & -jK_{1,PX} \\ -jK_{2,P1} & -jK_{2,1} & \left(\frac{1}{j\omega C_2}+j\omega L_2\right) & \cdots & -jK_{2,n} & -jK_{2,P2} & \cdots & -jK_{2,PX} \\ \vdots & \vdots & \vdots & \ddots & \vdots & \vdots & \vdots & \vdots \\ -jK_{n,P1} & -jK_{n,1} & -jK_{n,2} & \cdots & \left(\frac{1}{j\omega C_n}+j\omega L_n\right) & -jK_{n,P2} & \cdots & -jK_{n,PX} \\ -jK_{P2,P1} & -jK_{P2,1} & -jK_{P2,2} & \cdots & -jK_{P2,n} & R_{P2} & \cdots & -jK_{P2,PX} \\ \vdots & \vdots & \vdots & \vdots & \vdots & \vdots & \ddots & \vdots \\ -jK_{PX,P1} & -jK_{PX,1} & -jK_{PX,2} & \cdots & -jK_{PX,n} & -jK_{PX,P2} & \cdots & R_{PX} \end{bmatrix} \begin{bmatrix} i_{P1} \\ i_1 \\ i_2 \\ \vdots \\ i_n \\ i_{P2} \\ \vdots \\ i_{PX} \end{bmatrix} = \begin{bmatrix} v_s \\ 0 \\ 0 \\ \vdots \\ 0 \\ 0 \\ \vdots \\ 0 \end{bmatrix} \tag{3.34}$$

or

$$[Z]\cdot[i]=[v] \tag{3.35}$$

Where $[Z]$ is the n+X impedance matrix.

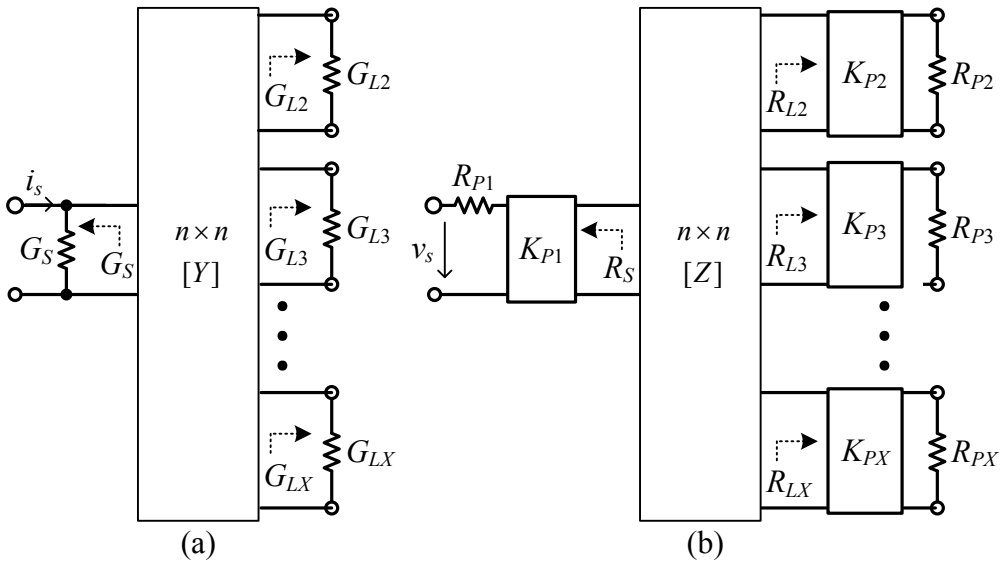

Figure 3.6 Network representation of an X-port n-coupled-resonator circuit in (a) the general $n\times n$ admittance matrix form $[Y]$ and (b) its dual $n\times n$ impedance matrix form $[Z]$ with port K-inverters.

To derive the S-parameters of the circuit, the lumped circuit needs to be turned into its

network representation. According to [1], a multi-port *n*-coupled-resonator circuit can be simplified into its network representation with its general $n \times n$ admittance matrix [*Y*] in Figure 3.6(a). G_S and G_{Lk} are the conductance in the source and loads. Due to the limitation of the general $n \times n$ matrix, each resonator/port can connect to no more than one port/resonator.

To turn the general $n \times n$ matrix into the $n+X$ matrix form, each conductance *G* in the source and loads is replaced by a port resistance R_{Pk} with a port *K*-inverter. For simplicity, the port resistance R_{Pk} is assumed to be unity or

$$R_{Pk} = 1\Omega \ (k = 1 \text{ to } X) \tag{3.36}$$

In order to match the additional *K*-inverters, the admittance matrix $[Y]_{n\times n}$ is replaced by its dual impedance matrix $[Z]_{n\times n}$. Figure 3.6(b) gives the equivalent $[Z]_{n\times n}$ matrix network surrounded by the additional *K*-inverters between the port resistances and the resonators.

According to (2.1), the characteristic impedance of the *K*-inverter at the source port 1 is:

$$K_{P1} = \sqrt{Z_1 Z_2} = \sqrt{R_s R_{P1}} = \sqrt{R_s} \tag{3.37}$$

where $Z_1 = R_s = \dfrac{1}{G_s}, Z_2 = R_{P1} = 1\Omega$.

Similarly, the characteristic impedance of the *K*-inverter at the load port *i* is:

$$K_{Pi} = \sqrt{Z_1' Z_2'} == \sqrt{R_{Li} R_{P1}} = \sqrt{R_{Li}} \ \ (i = 2 \text{ to } X) \tag{3.38}$$

where $Z_1' = R_{Li} = \dfrac{1}{G_{Li}}, Z_2' = R_{Pi} = 1\Omega$.

As given in Figure 3.7, with the help of the port *K*-inverters, a single resonator can be coupled to multiple ports while one port can be connected to multiple resonators. A direct coupling

between ports is also possible.

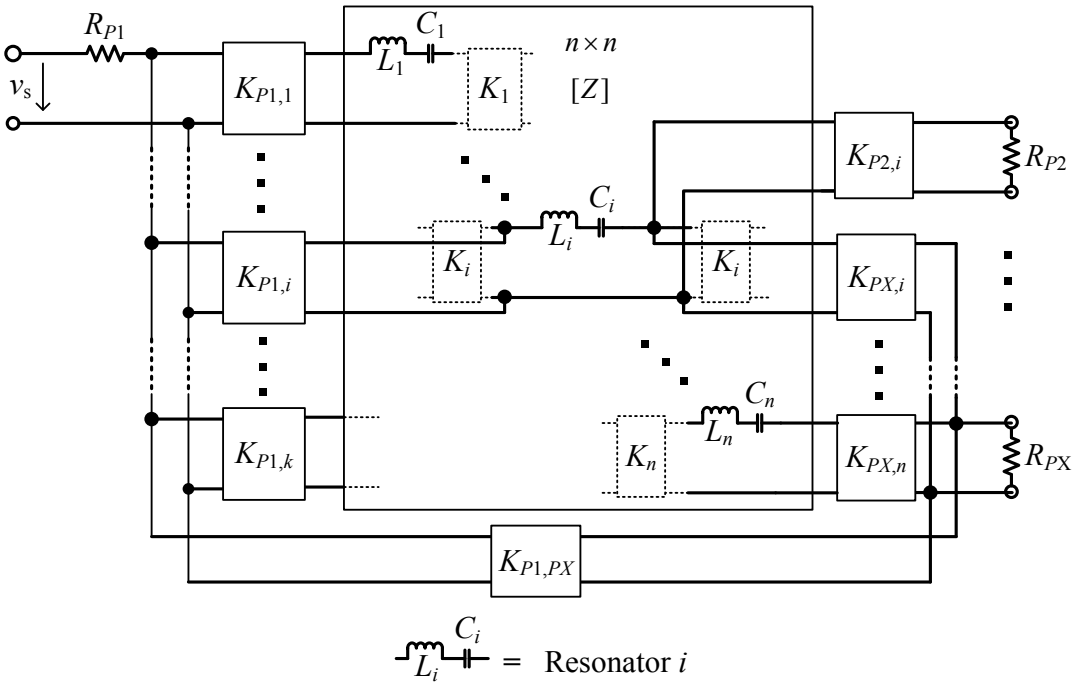

Figure 3.7 Network representation of an X-port n-coupled-resonator circuit with K-inverters. The network is formed of a general $n \times n$ impedance matrix $[Z]$, the resistance R_{Pk} of Port k and the port K-inverters. $K_{Pk,h}$ is the inverter between Port k and Resonator h. $K_{P1,PX}$ is the port inverter between Port 1 and X.

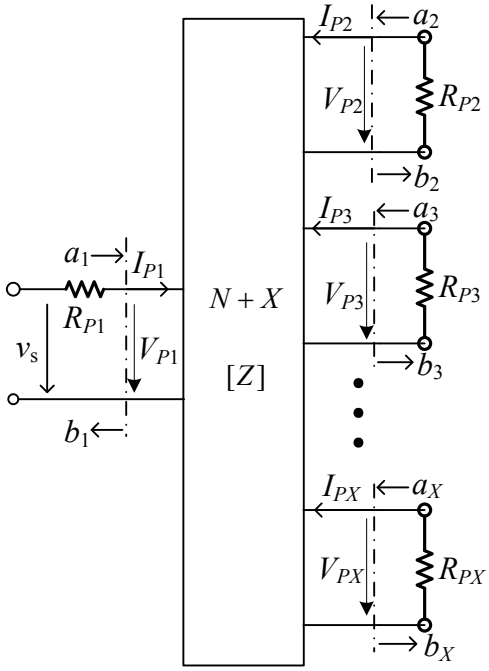

Figure 3.8 The network representation for X-port coupled-resonator circuit with the n+X impedance matrix for the loop equation formulation. Where v_s is the source vaotage, R_{Pk}, V_{Pk} and I_{Pk} are the resistance, voltage and current at port k, and the wave variables a_k and b_k at port k are defined as (3.7).

By absorbing the port K-inverters into the impedance matrix, a new $n+X$ impedance matrix $[Z]$ is obtained and a new network representation is given in Figure 3.8.

By inspecting the lumped circuit in Figure 3.5 and the network representation in Figure 3.8, it can be recognized that $I_{P1}=i_{P1}$, $I_{Pk}=-i_{Pk}$ (k=2 to X), $V_{Pk}=v_{Pk}$ (k=1 to X), $V_{P1}=v_s-I_{P1}\cdot R_{P1}$. Considering (3.36) into (3.7), we have

$$\begin{aligned} a_1 &= \frac{v_s}{2\sqrt{R_1}}=\frac{v_s}{2} \qquad & b_1 &= \frac{v_s-2i_{P1}R_1}{2\sqrt{R_1}}=\frac{v_s-2i_{P1}}{2} \\ a_k &= 0 & b_k &= i_{Pk}\sqrt{R_k}=i_{Pk} \end{aligned} \tag{3.39}$$

The relationships between scattering parameters and wave variables are:

$$\begin{aligned} S_{k1} &= \left.\frac{b_k}{a_1}\right|_{a2=a3...=aX=0} = 1-\frac{2i_{P1}}{v_s} \qquad (k=1) \\ S_{k1} &= \left.\frac{b_k}{a_1}\right|_{a2=a3...=aX=0} = \frac{2i_{Pk}}{v_s} \qquad (k=2 \text{ to } X) \end{aligned} \tag{3.40}$$

i_{Pk} are found from (3.34) as

$$i_{Pk} = v_s\cdot[Z]^{-1}_{Pk,P1} \tag{3.41}$$

where $[Z]^{-1}_{Pk,P1}$ is denoted as the entry element in row P_k and column P_1 of $[Z]^{-1}$. Replacing the loop currents in (3.40) with those given by (3.41) results in

$$\begin{aligned} S_{11} &= 1-2[Z]^{-1}_{P1,P1} \\ S_{k1} &= 2[Z]^{-1}_{Pk,P1} \qquad (k=2 \text{ to } X) \end{aligned} \tag{3.42}$$

To normalise the $[Z]$ matrix of a synchronously tuned circuit, the capacitance and inductance of each resonator are assumed to be the same. The centre frequency $\omega_0=\frac{1}{\sqrt{LC}}$.

$L_1=L_2...=L_n=L$. $C_1=C_2=\ldots=C_n=C$. Each row i and column i (i=1 to n) is multiplied by $\left(\sqrt{\omega_0 L\cdot FBW}\right)^{-1}$. $FBW=\Delta\omega/\omega_0$ is the fractional bandwidth of the network. In addition, as (3.36) assumed, the resistance at each port is unity. The row P_k and column P_k need not be scaled. The normalised matrix $[\overline{Z}]$ is given in (3.43) as

$$\begin{bmatrix}
1 & -j\frac{K_{P1,1}}{\sqrt{\omega_0 L\cdot FBW}} & -j\frac{K_{P1,2}}{\sqrt{\omega_0 L\cdot FBW}} & \cdots & -j\frac{K_{P1,n}}{\sqrt{\omega_0 L\cdot FBW}} & -jK_{P1,P2} & \cdots & -jK_{P1,PX} \\
-j\frac{K_{1,P1}}{\sqrt{\omega_0 L\cdot FBW}} & p & -j\frac{K_{1,2}}{\omega_0 L\cdot FBW} & \cdots & -j\frac{K_{1,n}}{\omega_0 L\cdot FBW} & -j\frac{K_{1,P2}}{\sqrt{\omega_0 L\cdot FBW}} & \cdots & -j\frac{K_{1,PX}}{\sqrt{\omega_0 L\cdot FBW}} \\
-j\frac{K_{2,P1}}{\sqrt{\omega_0 L\cdot FBW}} & -j\frac{K_{2,1}}{\omega_0 L\cdot FBW} & p & \cdots & -j\frac{K_{2,n}}{\omega_0 L\cdot FBW} & -j\frac{K_{2,P2}}{\sqrt{\omega_0 L\cdot FBW}} & \cdots & -j\frac{K_{2,PX}}{\sqrt{\omega_0 L\cdot FBW}} \\
\vdots & \vdots & \vdots & \ddots & \vdots & \vdots & \vdots & \vdots \\
-j\frac{K_{n,P1}}{\sqrt{\omega_0 L\cdot FBW}} & -j\frac{K_{n,1}}{\omega_0 L\cdot FBW} & -j\frac{K_{n,2}}{\omega_0 L\cdot FBW} & \cdots & p & -j\frac{K_{n,P2}}{\sqrt{\omega_0 L\cdot FBW}} & \cdots & -j\frac{K_{n,PX}}{\sqrt{\omega_0 L\cdot FBW}} \\
-jK_{P2,P1} & -j\frac{K_{P2,1}}{\sqrt{\omega_0 L\cdot FBW}} & -j\frac{K_{P2,2}}{\sqrt{\omega_0 L\cdot FBW}} & \cdots & -j\frac{K_{P2,n}}{\sqrt{\omega_0 L\cdot FBW}} & 1 & \cdots & -jK_{P2,PX} \\
\vdots & \vdots & \vdots & \vdots & \vdots & \vdots & \ddots & \vdots \\
-jK_{PX,P1} & -j\frac{K_{PX,1}}{\sqrt{\omega_0 L\cdot FBW}} & -j\frac{K_{PX,2}}{\sqrt{\omega_0 L\cdot FBW}} & \cdots & -j\frac{K_{PX,n}}{\sqrt{\omega_0 L\cdot FBW}} & -jK_{PX,P2} & \cdots & 1
\end{bmatrix} \tag{3.43}$$

Where p is the complex lowpass frequency variable. $K_{i,j}=K_{j,i}$ ($i,j=1$ *to* n, $i\neq j$) is the characteristic impedance between Resonator i and j. When the resonators are magnetically coupled, as given in Figure 2.4(a), the characteristic admittance $K_{i,j}$ and $K_{j,i}$ are formulated as:

$$K_{i,j}=K_{j,i}=\omega L_{i,j}=\omega L_{j,i} \tag{3.44}$$

Where $L_{i,j}$= $L_{j,i}$ represents the mutual inductance between Resonator i and j.

According to the (2.2), the characteristic impedance $K_{Pk,i}$ and $K_{i,Pk}$ of the port inverters are:

$$\begin{aligned}
K_{Pk,i}=K_{i,Pk}&=\sqrt{Z_1\cdot Z_2}=\sqrt{R_{Pk}\cdot R_{S,i}}=\sqrt{R_{S,i}}=\sqrt{R_{i,S}} \qquad (k=1, i=1 \text{ to } n)\\
K_{Pk,i}=K_{i,Pk}&=\sqrt{Z_1\cdot Z_2}=\sqrt{R_{Pk}\cdot R_{Lk,i}}=\sqrt{R_{Lk,i}}=\sqrt{R_{i,Lk}} \quad (k=2 \text{ to } X, i=1 \text{ to } n)
\end{aligned} \tag{3.45}$$

Where $R_{S,i}$ and $R_{i,S}$ are the equivalent source resistance at resonator i, $R_{Lk,i}$ and $R_{i,Lk}$ are the

equivalent resistance of load k at resonator i. So the normalised impedance matrix $[\overline{Z}]$ is replaced as:

$$\begin{bmatrix}
1 & -j\sqrt{\frac{R_{S,1}}{\omega_0 L\cdot FBW}} & -j\sqrt{\frac{R_{S,2}}{\omega_0 L\cdot FBW}} & \cdots & -j\sqrt{\frac{R_{S,n}}{\omega_0 L\cdot FBW}} & -jK_{P1,P2} & \cdots & -jK_{P1,PX} \\
-j\sqrt{\frac{R_{1,S}}{\omega_0 L\cdot FBW}} & p & -j\frac{\omega L_{1,2}}{\omega_0 L\cdot FBW} & \cdots & -j\frac{\omega L_{1,n}}{\omega_0 L\cdot FBW} & -j\sqrt{\frac{R_{1,L2}}{\omega_0 L\cdot FBW}} & \cdots & -j\sqrt{\frac{R_{1,LX}}{\omega_0 L\cdot FBW}} \\
-j\sqrt{\frac{R_{2,S}}{\omega_0 L\cdot FBW}} & -j\frac{\omega L_{2,1}}{\omega_0 L\cdot FBW} & p & \cdots & -j\frac{\omega L_{2,n}}{\omega_0 L\cdot FBW} & -j\sqrt{\frac{R_{2,L2}}{\omega_0 L\cdot FBW}} & \cdots & -j\sqrt{\frac{R_{2,LX}}{\omega_0 L\cdot FBW}} \\
\vdots & \vdots & \vdots & \ddots & \vdots & \vdots & \vdots & \vdots \\
-j\sqrt{\frac{R_{n,S}}{\omega_0 L\cdot FBW}} & -j\frac{\omega L_{n,1}}{\omega_0 L\cdot FBW} & -j\frac{\omega L_{n,2}}{\omega_0 L\cdot FBW} & \cdots & p & -j\sqrt{\frac{R_{n,L2}}{\omega_0 L\cdot FBW}} & \cdots & -j\sqrt{\frac{R_{n,LX}}{\omega_0 L\cdot FBW}} \\
-jK_{P2,P1} & -j\sqrt{\frac{R_{L2,1}}{\omega_0 L\cdot FBW}} & -j\sqrt{\frac{R_{L2,2}}{\omega_0 L\cdot FBW}} & \cdots & -j\sqrt{\frac{R_{L2,X}}{\omega_0 L\cdot FBW}} & 1 & \cdots & -jK_{P2,PX} \\
\vdots & \vdots & \vdots & \vdots & \vdots & \vdots & \ddots & \vdots \\
-jK_{PX,P1} & -j\sqrt{\frac{R_{LX,1}}{\omega_0 L\cdot FBW}} & -j\sqrt{\frac{R_{LX,2}}{\omega_0 L\cdot FBW}} & \cdots & -j\sqrt{\frac{R_{LX,X}}{\omega_0 L\cdot FBW}} & -jK_{PX,P2} & \cdots & 1
\end{bmatrix} \tag{3.46}$$

As noticed in [2]:

$$\begin{aligned}
&\frac{R}{\omega_0 L}=\frac{1}{Q_e}, \qquad q_e = Q_e\cdot FBW \\
&\frac{L_{i,j}}{L}=M_{i,j}, \quad m_{i,j}=M_{i,j}\cdot FBW \qquad \left(i,j=1 \text{ to } n,\ i\neq j\right)
\end{aligned} \tag{3.47}$$

where Q_e is the external quality factor. $M_{i,j}$ is the coupling coefficient between Resonator i and j. q_e and $m_{i,j}$ are the scaled external quality factor and scaled coupling coefficient, respectively.

Defining the normalised coupling coefficient $m_{pk,i}$ and $m_{i,pk}$ between Port k and Resonator i as:

$$
\begin{aligned}
m_{P1,i} &= m_{i,P1} = \sqrt{\frac{1}{q_{eS,i}}} = \sqrt{\frac{1}{q_{ei,S}}}; \\
m_{Pk,i} &= m_{i,Pk} = \sqrt{\frac{1}{q_{eLk,i}}} = \sqrt{\frac{1}{q_{ei,Lk}}};
\end{aligned}
\quad \left(i = 1 \text{ to } n,\ k = 2 \text{ to } X\right) \tag{3.48}
$$

Defining the coupling coefficient $M_{Pi,Pj}$ between port i and j as:

$$
M_{pi,pj} = K_{pi,pj} \ (i, j = 1 \text{ to } X,\ i \neq j) \tag{3.49}
$$

And the normalised ports coupling coefficient $m_{pi,pj} = M_{pi,pj}$.

Assuming $\omega / \omega_0 \approx 1$ for a narrow band approximation (for a wide band circuit, $\omega / \omega_0 \neq 1$ and m is frequency-variant), the matrix $[\overline{Z}]$ in (3.46) is simplified as

$$
\begin{bmatrix}
1 & -jm_{P1,1} & -jm_{P1,2} & \cdots & -jm_{P1,n} & -jm_{P1,P2} & \cdots & -jm_{P1,PX} \\
-jm_{1,P1} & p & -jm_{1,2} & \cdots & -jm_{1,n} & -jm_{1,P2} & \cdots & -jm_{1,PX} \\
-jm_{2,P1} & -jm_{2,1} & p & \cdots & -jm_{2,n} & -jm_{2,P2} & \cdots & -jm_{2,PX} \\
\vdots & \vdots & \vdots & \ddots & \vdots & \vdots & \vdots & \vdots \\
-jm_{n,P1} & -jm_{n,1} & -jm_{n,2} & \cdots & p & -jm_{n,P2} & \cdots & -jm_{n,PX} \\
-jm_{P2,P1} & -jm_{1,} & -jm_{1,} & \cdots & -jm_{1,} & 1 & \cdots & -jm_{P2,PX} \\
\vdots & \vdots & \vdots & \vdots & \vdots & \vdots & \ddots & \vdots \\
-jm_{PX,P1} & -jm_{1,} & -jm_{1,} & \cdots & -jm_{1,} & -jm_{PX,P2} & \cdots & 1
\end{bmatrix} \tag{3.50}
$$

By inspecting matrix $[Z]$ in (3.34) and $[\overline{Z}]$ in (3.43), we obtain the relationships of their determinants and cofactors as:

$$
\begin{aligned}
|Z| &= \left(\sqrt{\omega_0 L \cdot FBW}\right)^{2n} \cdot |\overline{Z}| \\
cof\left(Z_{Pi,Pj}\right) &= \left(\sqrt{\omega_0 L \cdot FBW}\right)^{2n} \cdot cof\left(\overline{Z}_{Pi,Pj}\right) \quad \left(i, j = 1 \text{ to } X,\ i \neq j\right)
\end{aligned} \tag{3.51}
$$

Where $|Z|$ and $|\overline{Z}|$ are the determinants of matrix $[Z]$ and $[\overline{Z}]$. $cof\left(Z_{Pi,Pj}\right)$ and $cof\left(\overline{Z}_{Pi,Pj}\right)$ are the entries in column P_i and row P_j of the cofactor matrices of $[Z]$ and $[\overline{Z}]$.

As shown in [3], the entries of the inverse matrix can be expressed as:

$$[Z]^{-1}_{Pi,Pj} = \frac{cof\left(Z_{Pi,Pj}\right)}{|Z|}, \quad \left(|Z| \neq 0\right)$$
$$[\overline{Z}]^{-1}_{Pi,Pj} = \frac{cof\left(\overline{Z}_{Pi,Pj}\right)}{|\overline{Z}|}, \quad \left(|\overline{Z}| \neq 0\right) \tag{3.52}$$

Substituting (3.52) into (3.51) yields:

$$[Z]^{-1}_{Pi,Pj} = [\overline{Z}]^{-1}_{Pi,Pj} \tag{3.53}$$

So the *S*-parameters in (3.42) can be expressed in terms of the normalised matrix $[\overline{Z}]$ as:

$$S_{11} = 1 - 2[\overline{Z}]^{-1}_{P1,P1}$$
$$S_{k1} = 2[\overline{Z}]^{-1}_{Pk,P1} \quad \left(k = 2 \text{ to } X\right) \tag{3.54}$$

In the case of asynchronously tuned coupled-resonator circuit, the resonant frequency of Resonator *i* is given by $\omega_i = \frac{1}{\sqrt{L_i C_i}}$, the coupling coefficient between Resonator *i* and *j* of the asynchronously tuned filter is defined as

$$\frac{L_{i,j}}{\sqrt{L_i L_j}} = M_{i,j} \quad \left(i, j = 1 \text{ to } n,\ i \neq j\right) \tag{3.55}$$

And the normalised matrix $[\overline{Z}]$ becomes

$$\left[\overline{Z}\right] = \begin{bmatrix} 1 & -jm_{P1,1} & -jm_{P1,2} & \cdots & -jm_{P1,n} & -jm_{P1,P2} & \cdots & -jm_{P1,PX} \\ -jm_{1,P1} & p - jm_{1,1} & -jm_{1,2} & \cdots & -jm_{1,n} & -jm_{1,P2} & \cdots & -jm_{1,PX} \\ -jm_{2,P1} & -jm_{2,1} & p - jm_{2,2} & \cdots & -jm_{2,n} & -jm_{2,P2} & \cdots & -jm_{2,PX} \\ \vdots & \vdots & \vdots & \ddots & \vdots & \vdots & \vdots & \vdots \\ -jm_{n,P1} & -jm_{n,1} & -jm_{n,2} & \cdots & p - jm_{n,n} & -jm_{n,P2} & \cdots & -jm_{n,PX} \\ -jm_{P2,P1} & -jm_{P2,1} & -jm_{P2,1} & \cdots & -jm_{P2,1} & 1 & \cdots & -jm_{P2,PX} \\ \vdots & \vdots & \vdots & \vdots & \vdots & \vdots & \ddots & \vdots \\ -jm_{PX,P1} & -jm_{PX,1} & -jm_{PX,2} & \cdots & -jm_{PX,n} & -jm_{PX,P2} & \cdots & 1 \end{bmatrix} \tag{3.56}$$

The normalised impedance matrix $[\overline{Z}]$ in (3.56) is nearly the same as (3.50) except for the extra entries $m_{i,i}$ along the diagonal to account for asynchronous tuning.

3.3 General *n*+*X* Coupling Matrix

As given in the previous sections, the formulation of the normalised admittance matrix $[\overline{Y}]$, in (3.32), is identical to that of the normalised impedance matrix $[\overline{Z}]$, in (3.56). Thereby, regardless of the types of couplings (magnetic, electrical or mixed), a unified formulation for an *X*-port network with *n*-coupled-resonator exists. (3.30) and (3.54) are combined into a general equation as:

$$\begin{aligned} S_{11} &= \pm\left(1-2[A]^{-1}_{P1,P1}\right) \\ S_{k1} &= 2[A]^{-1}_{Pk,P1} \qquad \left(k=2 \text{ to } X\right) \end{aligned} \tag{3.57}$$

with

$$[A] = [X] + p[U] - j[m] \tag{3.58}$$

Where $[A]$ is the *n*+*X* normalised immittance matrix, $[X]$ and $[U]$ are the $(n+X)\times(n+X)$ matrices with all entries zero, except for $X_{Pk,Pk}$=1(*k*=1 to *X*) and $U_{i,i}$=1 (*i*=1 to *n*). $[m]$ is the $n+X$ normalised coupling matrix and is allowed to have nonzero diagonal entries $m_{i,i}$ for asynchronously tuned filters.

The self coupling $m_{i,i}$ is used to quantify the difference between the resonant frequency f_i of Resonator *i* and the centre frequency f_c of the circuit. When Resonator *i* is asynchronously tuned, the self coupling $m_{i,i}$ is an non-zero entry. The relationship between the resonant frequency f_i of Resonator *i* and its self coupling $m_{i,i}$ is derived from the immittance matrix $[A]$ of the circuit. f_i is the resonant frequency of Resonator *i* when

$$[A]_{i,i}(\omega_i) = p(\omega_i) - jm_{i,i} = 0 \tag{3.59}$$

where $\omega_i = 2\pi f_i$ is the angular speed of f_i.

Substitute (3.14) into (3.59), we have

$$\frac{1}{FBW}\left(\frac{\omega_i}{\omega_0} - \frac{\omega_0}{\omega_i}\right) - m_{i,i} = \frac{1}{FBW}\left(\frac{f_i}{f_0} - \frac{f_0}{f_i}\right) - m_{i,i} = 0 \tag{3.60}$$

where f_0 is the centre frequency of the circuit, $\omega_0 = 2\pi f_0$ is the angular speed of f_0, FBW is the fractional bandwidth of the device. According to (3.60), we have

$$f_i^2 - FBW \cdot m_{i,i} f_0 \cdot f_i - f_0^2 = 0 \tag{3.61}$$

So the solutions of (3.61) are

$$f_i = f_0\left[\frac{FBW \cdot m_{i,i}}{2} \pm \sqrt{\left(\frac{FBW \cdot m_{i,i}}{2}\right)^2 + 1}\right] \tag{3.62}$$

As the resonant frequency f_i is positive, so the valid solution of (3.61) is

$$f_i = f_0\left[\frac{FBW \cdot m_{i,i}}{2} + \sqrt{\left(\frac{FBW \cdot m_{i,i}}{2}\right)^2 + 1}\right] \tag{3.63}$$

So $f_i < f_0$ when $m_{i,i} < 0$, $f_i > f_0$ when $m_{i,i} > 0$ and $f_i = f_0$ when $m_{i,i} = 0$.

3.4 Scale the *n*+*X* Coupling Matrix during the Frequency Transformation

During the frequency transformation, the normalised $n+X$ coupling matrix $[m]$ of the prototype lowpass circuit is scaled by the fractional bandwidth FBW into the un-normalised

coupling matrix [M] of the desired bandpass circuit. By inspecting (3.56), the n+X coupling matrix [m] having normalised response is given as

$$[m]=\begin{bmatrix} 0 & m_{P1,1} & m_{P1,2} & \cdots & m_{P1,n} & m_{P1,P2} & \cdots & m_{P1,PX} \\ m_{1,P1} & m_{1,1} & m_{1,2} & \cdots & m_{1,n} & m_{1,P2} & \cdots & m_{1,PX} \\ m_{2,P1} & m_{2,1} & m_{2,2} & \cdots & m_{2,n} & m_{2,P2} & \cdots & m_{2,PX} \\ \vdots & \vdots & \vdots & \ddots & \vdots & \vdots & \vdots & \vdots \\ m_{n,P1} & m_{n,1} & m_{n,2} & \cdots & m_{n,n} & m_{n,P2} & \cdots & m_{n,PX} \\ m_{P2,P1} & m_{P2,1,} & m_{P2,2} & \cdots & m_{P2,n} & 0 & \cdots & m_{P2,PX} \\ \vdots & \vdots & \vdots & \vdots & \vdots & \vdots & \ddots & \vdots \\ m_{PX,P1} & m_{PX,1} & m_{PX,2} & \cdots & m_{PX,n} & m_{PX,P2} & \cdots & 0 \end{bmatrix} \tag{3.64}$$

Substituting (3.25) into (3.64), [m] turns into the form as

$$[m]=\begin{bmatrix} 0 & \sqrt{1/q_{eS,1}} & \sqrt{1/q_{eS,2}} & \cdots & \sqrt{1/q_{eS,n}} & m_{P1,P2} & \cdots & m_{P1,PX} \\ \sqrt{1/q_{1,eS}} & m_{1,1} & m_{1,2} & \cdots & m_{1,n} & \sqrt{1/q_{1,L2}} & \cdots & \sqrt{1/q_{1,LX}} \\ \sqrt{1/q_{2,eS}} & m_{2,1} & m_{1,2} & \cdots & m_{2,n} & \sqrt{1/q_{2,L2}} & \cdots & \sqrt{1/q_{2,LX}} \\ \vdots & \vdots & \vdots & \ddots & \vdots & \vdots & \vdots & \vdots \\ \sqrt{1/q_{n,eS}} & m_{n,1} & m_{n,2} & \cdots & m_{n,n} & \sqrt{1/q_{n,L2}} & \cdots & \sqrt{1/q_{n,LX}} \\ m_{P2,P1} & \sqrt{1/q_{L2,1}} & \sqrt{1/q_{L2,1}} & \cdots & \sqrt{1/q_{L2,1}} & 0 & \cdots & m_{P2,PX} \\ \vdots & \vdots & \vdots & \vdots & \vdots & \vdots & \ddots & \vdots \\ m_{PX,P1} & \sqrt{1/q_{LX,1}} & \sqrt{1/q_{LX,2}} & \cdots & \sqrt{1/q_{LX,n}} & m_{PX,P2} & \cdots & 0 \end{bmatrix} \tag{3.65}$$

Similarly, the un-normalised n+X coupling matrix [M] is given as

$$[M]=\begin{bmatrix} 0 & M_{P1,1} & M_{P1,2} & \cdots & M_{P1,n} & M_{P1,P2} & \cdots & M_{P1,PX} \\ M_{1,P1} & M_{1,1} & M_{1,2} & \cdots & M_{1,n} & M_{1,P2} & \cdots & M_{1,PX} \\ M_{2,P1} & M_{2,1} & M_{2,2} & \cdots & M_{2,n} & M_{2,P2} & \cdots & M_{2,PX} \\ \vdots & \vdots & \vdots & \ddots & \vdots & \vdots & \vdots & \vdots \\ M_{n,P1} & M_{n,1} & M_{n,2} & \cdots & M_{n,n} & M_{n,P2} & \cdots & M_{n,PX} \\ M_{P2,P1} & M_{P2,1} & M_{P2,2} & \cdots & M_{P2,N} & 0 & \cdots & M_{P2,PX} \\ \vdots & \vdots & \vdots & \vdots & \vdots & \vdots & \ddots & \vdots \\ M_{PX,P1} & M_{PX,1} & M_{PX,2} & \cdots & M_{PX,n} & M_{PX,P2} & \cdots & 0 \end{bmatrix}$$

$$=\begin{bmatrix} 0 & \sqrt{1/Q_{eS,1}} & \sqrt{1/Q_{eS,2}} & \cdots & \sqrt{1/Q_{eS,n}} & M_{P1,P2} & \cdots & M_{P1,PX} \\ \sqrt{1/Q_{1,eS}} & M_{1,1} & M_{1,2} & \cdots & M_{1,n} & \sqrt{1/Q_{1,L2}} & \cdots & \sqrt{1/Q_{1,LX}} \\ \sqrt{1/Q_{2,eS}} & M_{2,1} & M_{2,2} & \cdots & M_{2,n} & \sqrt{1/Q_{2,L2}} & \cdots & \sqrt{1/Q_{2,LX}} \\ \vdots & \vdots & \vdots & \ddots & \vdots & \vdots & \vdots & \vdots \\ \sqrt{1/Q_{n,eS}} & M_{n,1} & M_{n,2} & \cdots & M_{n,n} & \sqrt{1/Q_{n,L2}} & \cdots & \sqrt{1/Q_{n,LX}} \\ M_{P2,P1} & \sqrt{1/Q_{L2,1}} & \sqrt{1/Q_{L2,1}} & \cdots & \sqrt{1/Q_{L2,1}} & 0 & \cdots & M_{P2,PX} \\ \vdots & \vdots & \vdots & \vdots & \vdots & \vdots & \ddots & \vdots \\ M_{PX,P1} & \sqrt{1/Q_{LX,1}} & \sqrt{1/Q_{LX,2}} & \cdots & \sqrt{1/Q_{LX,n}} & M_{PX,P2} & \cdots & 0 \end{bmatrix} \quad (3.66)$$

where

$$M_{i,P1}=\sqrt{1/Q_{1,S}}, M_{i,Pk}=\sqrt{1/Q_{i,Lk}} (i=1 \text{ to } n, k=2 \text{ to } X) \quad (3.67)$$

Substituting (3.19) and (3.21) into (3.66), we have

$$[M]=\begin{bmatrix} 0 & \sqrt{FBW/q_{eS,1}} & \sqrt{FBW/q_{eS,2}} & \cdots & \sqrt{FBW/q_{eS,n}} & m_{P1,P2} & \cdots & m_{P1,PX} \\ \sqrt{FBW/q_{1,eS}} & m_{1,1}\cdot FBW & m_{1,2}\cdot FBW & \cdots & m_{1,n}\cdot FBW & \sqrt{FBW/q_{1,L2}} & \cdots & \sqrt{FBW/q_{1,LX}} \\ \sqrt{FBW/q_{2,eS}} & m_{2,1}\cdot FBW & m_{2,2}\cdot FBW & \cdots & m_{2,n}\cdot FBW & \sqrt{FBW/q_{2,L2}} & \cdots & \sqrt{FBW/q_{2,LX}} \\ \vdots & \vdots & \vdots & \ddots & \vdots & \vdots & \vdots & \vdots \\ \sqrt{FBW/q_{n,eS}} & m_{n,1}\cdot FBW & m_{n,2}\cdot FBW & \cdots & m_{n,n}\cdot FBW & \sqrt{FBW/q_{n,L2}} & \cdots & \sqrt{FBW/q_{n,LX}} \\ m_{P2,P1} & \sqrt{FBW/q_{L2,1}} & \sqrt{FBW/q_{L2,1}} & \cdots & \sqrt{FBW/q_{L2,1}} & 0 & \cdots & m_{P2,PX} \\ \vdots & \vdots & \vdots & \vdots & \vdots & \vdots & \ddots & \vdots \\ m_{PX,P1} & \sqrt{FBW/q_{LX,1}} & \sqrt{FBW/q_{LX,2}} & \cdots & \sqrt{FBW/q_{LX,n}} & m_{PX,P2} & \cdots & 0 \end{bmatrix} \tag{3.68}$$

Substituting (3.25) into (3.68), we have

$$[M]=\begin{bmatrix} 0 & m_{P1,1}\cdot\sqrt{FBW} & m_{P1,2}\cdot\sqrt{FBW} & \cdots & m_{P1,n}\cdot\sqrt{FBW} & m_{P1,P2} & \cdots & m_{P1,PX} \\ m_{1,P1}\cdot\sqrt{FBW} & m_{1,1}\cdot FBW & m_{1,2}\cdot FBW & \cdots & m_{1,n}\cdot FBW & m_{1,P2}\cdot\sqrt{FBW} & \cdots & m_{1,PX}\cdot\sqrt{FBW} \\ m_{2,P1}\cdot\sqrt{FBW} & m_{2,1}\cdot FBW & m_{2,2}\cdot FBW & \cdots & m_{2,n}\cdot FBW & m_{2,P2}\cdot\sqrt{FBW} & \cdots & m_{2,PX}\cdot\sqrt{FBW} \\ \vdots & \vdots & \vdots & \ddots & \vdots & \vdots & \vdots & \vdots \\ m_{n,P1}\cdot\sqrt{FBW} & m_{n,1}\cdot FBW & m_{n,2}\cdot FBW & \cdots & m_{n,n}\cdot FBW & m_{n,P2}\cdot\sqrt{FBW} & \cdots & m_{n,PX}\cdot\sqrt{FBW} \\ m_{P2,P1} & m_{P2,1}\cdot\sqrt{FBW} & m_{P2,2}\cdot\sqrt{FBW} & \cdots & m_{P2,n}\cdot\sqrt{FBW} & 0 & \cdots & m_{P2,PX} \\ \vdots & \vdots & \vdots & \vdots & \vdots & \vdots & \ddots & \vdots \\ m_{PX,P1} & m_{PX,1}\cdot\sqrt{FBW} & m_{PX,2}\cdot\sqrt{FBW} & \cdots & m_{PX,n}\cdot\sqrt{FBW} & m_{PX,P2} & \cdots & 0 \end{bmatrix} \tag{3.69}$$

So (3.69) shows how to scale the normalised coupling matrix [m] into the un-normalised matrix [M].

[1] R. J. Cameron, C. M. Kudsia, and R. R. Mansour, *Microwave filters for communication systems : fundamentals, design, and applications*. Hoboken, N.J.: Wiley ; Chichester : John Wiley [distributor], 2007.

[2] J.-S. Hong and M. J. Lancaster, *Microstrip filters for RF/microwave applications*. New York ; Chichester: Wiley, 2001.

[3] A. B. Jayyousi and M. J. Lancaster, "A gradient-based optimization technique employing determinants for the synthesis of microwave coupled filters," in *Microwave Symposium Digest, 2004 IEEE MTT-S International*, 2004, pp. 1369-1372 Vol.3.

Chapter 4 Coupling Matrix Synthesis by Optimisation

The matrix synthesis technique applied in this work is based on a local optimisation algorithm. As stated in Chapter 2, such technique is suited to a specific topology and relies on a set of high quality initial values as the starting point. During the optimisation, a cost function is applied to quantify the difference between the specifications and the optimised results.

The coupling matrix discussed in this chapter corresponds to the low-pass prototypes, i.e. the *S*-parameters of the matrix is centred at 0 Hz. A frequency transformation of the prototype circuit is given in Section 4.1. Section 4.2 describes the concept of the Tree Topology. Section 4.3 gives a brief introduction on how to get the initial values of the coupling matrix for diplexers with a Tree Topology and a Chebyshev response. A cost function is formulated in Section 4.4. The coupling matrix of a 10^{th} order diplexer is synthesised and presented as an example in Section 4.5. More examples are presented in Section 4.6 to 4.10.

4.1 Frequency Transformation of the Diplexer

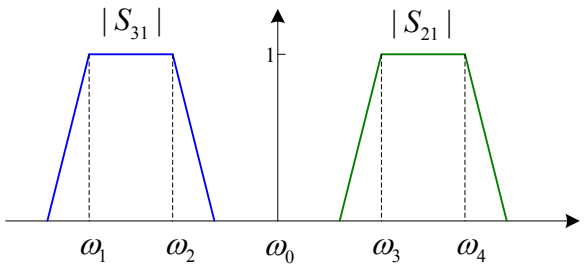

Figure 4.1 The ideal transfer response of the diplexer

The expected transfer response of a diplexer is given in Figure 4.1. ω_0 is the centre frequency of the diplexer, ω_1 to ω_4 are the band edges or cut-offs of the two passbands.

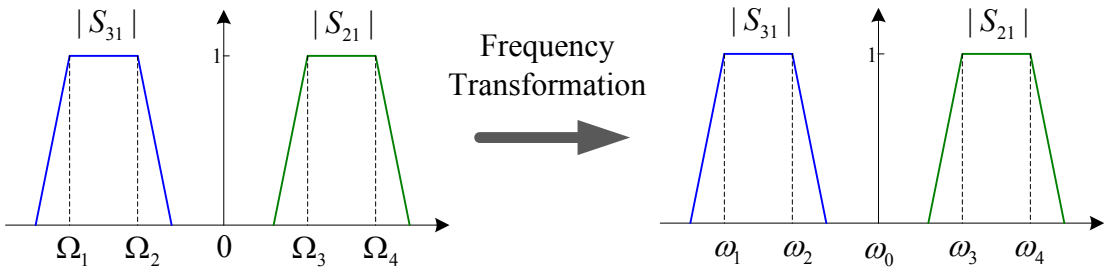

Figure 4.2 Frequency transformation of the diplexer

As shown in Figure 4.2, the diplexer can be transformed from a low-pass. Here Ω_i is the cut-off of the two passbands of the low-pass response. The frequency transformation is given as

$$\Omega \rightarrow \frac{\Omega_4 - \Omega_1}{2} \left(\frac{\omega}{\omega_0} - \frac{\omega_0}{\omega} \right) \tag{4.1}$$

where Ω is the frequency element of the lowpass mode, ω is the frequency element of the transformed circuit. FBW is the fractional bandwidth of the transformed diplexer, which can be expressed as

$$FBW = \frac{\omega_4 - \omega_1}{\omega_0}$$

For a normalised prototype model, $\Omega_1 = -1$ and $\Omega_4 = 1$, and the frequency transformation in (4.1) can be simplified as

$$\Omega \rightarrow \frac{1}{FBW} \left(\frac{\omega}{\omega_0} - \frac{\omega_0}{\omega} \right) \tag{4.2}$$

4.2 Topologies of the Resonator Based Diplexers

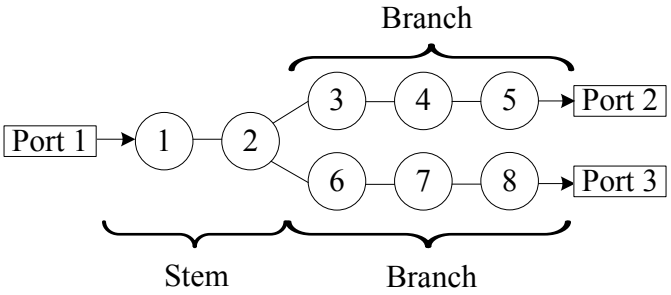

Figure 4.3 An 8-resonator based diplexer with Tree Topology [1]. Each circle represents a resonator, and the short lines between the resonators are the internal couplings. The arrowed lines between the resonators and ports represent the external couplings.

Figure 4.3 illustrates the schematic of a diplexer with 8 coupled resonators. Its prototype matrix in the n+3 coupling matrix form is:

$$[m]=\begin{bmatrix} 0 & m_{P1,1} & 0 & 0 & 0 & 0 & 0 & 0 & 0 & 0 & 0 \\ m_{1,P1} & m_{1,1} & m_{1,2} & 0 & 0 & 0 & 0 & 0 & 0 & 0 & 0 \\ 0 & m_{2,1} & m_{2,2} & m_{2,3} & 0 & 0 & m_{2,6} & 0 & 0 & 0 & 0 \\ 0 & 0 & m_{3,2} & m_{3,3} & m_{3,4} & 0 & 0 & 0 & 0 & 0 & 0 \\ 0 & 0 & 0 & m_{4,3} & m_{4,4} & m_{4,5} & 0 & 0 & 0 & 0 & 0 \\ 0 & 0 & 0 & 0 & m_{5,4} & m_{5,5} & 0 & 0 & 0 & m_{5,P2} & 0 \\ 0 & 0 & m_{2,6} & 0 & 0 & 0 & m_{6,6} & m_{6,7} & 0 & 0 & 0 \\ 0 & 0 & 0 & 0 & 0 & 0 & m_{7,6} & m_{7,7} & m_{7,8} & 0 & 0 \\ 0 & 0 & 0 & 0 & 0 & 0 & 0 & m_{8,7} & m_{8,8} & 0 & m_{8,P3} \\ 0 & 0 & 0 & 0 & 0 & m_{P2,5} & 0 & 0 & 0 & 0 & 0 \\ 0 & 0 & 0 & 0 & 0 & 0 & 0 & 0 & m_{P3,8} & 0 & 0 \end{bmatrix} \quad (4.3)$$

Each entry $m_{i,i}$ along the diagonal stands for the self-coupling coefficient which determines the resonant frequency of Resonator i. The other non-zero entries $m_{i,j}$ are the internal couplings between Resonator i and j. The external coupling coefficients between Port k and Resonator i are denoted as $m_{Pk,i}$ and $m_{i,Pk}$:

$$m_{Pk,i} = m_{i,Pk} = \frac{1}{\sqrt{q_{ei}}} \tag{4.4}$$

Where q_{ei} is the external quality factor of Resonator i.

The diplexer in Figure 4.3 can be divided into two parts. The very leading part, containing Resonator 1 and 2, is called the stem. Two branches, one including Resonator 3 to 5 and the other having Resonator 6 to 8, are coupled to resonator 2 of the stem.

Note that such Tree Topology is not limited to 8 resonators. The number of resonators on the stem and branches can be altered according to specifications. A general Tree Topology of the diplexer is given in Figure 4.4.

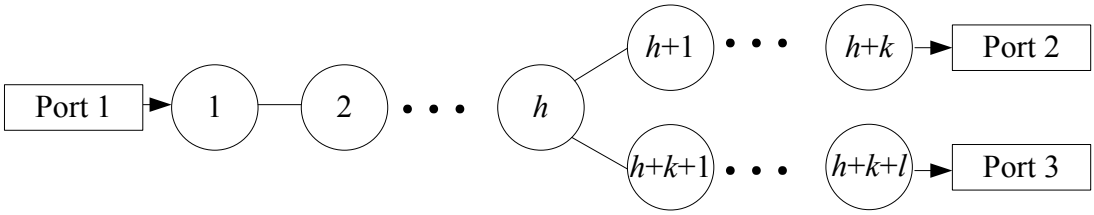

Figure 4.4 General structure of a diplexer with Tree Topology. The number of the resonators on the stem is an even number h. The numbers of resonators on each branch are k and l.

The stem of the diplexer works like a dual-band bandpass filter [2]. It attenuates signals outside of two passbands but plays no role in splitting signals on these two bands [1]. The topology of the dual-band bandpass filter and its response are given in Figure 4.5(a) and (b).

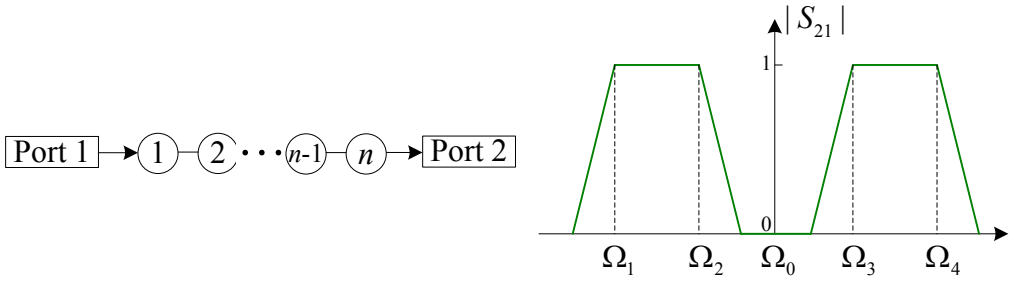

(a) (b)

Figure 4.5 (a) The topology and (b) the ideal response of the dual-band bandpass filter. Where Ω_0 is the centre frequency of the filter, Ω_1 and Ω_2 are the cut-offs of the left passband, Ω_3 and Ω_4 are the cut-offs of the right one. *n* is the order of the filter.

For dual band bandpass filter having symmetric responses, the cut-offs of the filter, in Figure 4.5(b), have a relationship as:

$$\Omega_1 = -\Omega_4, \quad \Omega_2 = -\Omega_3. \tag{4.5}$$

Every two resonators of the dual band filter work as a resonant pair. For example, there is a strong coupling between Resonator 1 and 2, as well as the one between Resonator 3 and 4, but the coupling between Resonator 2 and 3 is weak. As a result, the order of the dual band filter *n* is a multiple of 2 or an even number. The order of each passband is half the order of the filter *n*.

The branch is like a general single band bandpass filter. Each branch of the diplexer occupies one of two pass-bands of the stem and attenuates signals outside of the passband of the branch [1]. Signals passing through the stem will be guided to one of these two branches and reflected by the other [1] so as to split signals to different ports.

4.3 Principles of the Starting Point

The starting point of the coupling matrix of the diplexer can be divided into two parts. One part of the branches and the other part of the stem are initialised in different ways.

4.3.1 Starting Values of the Branch Part

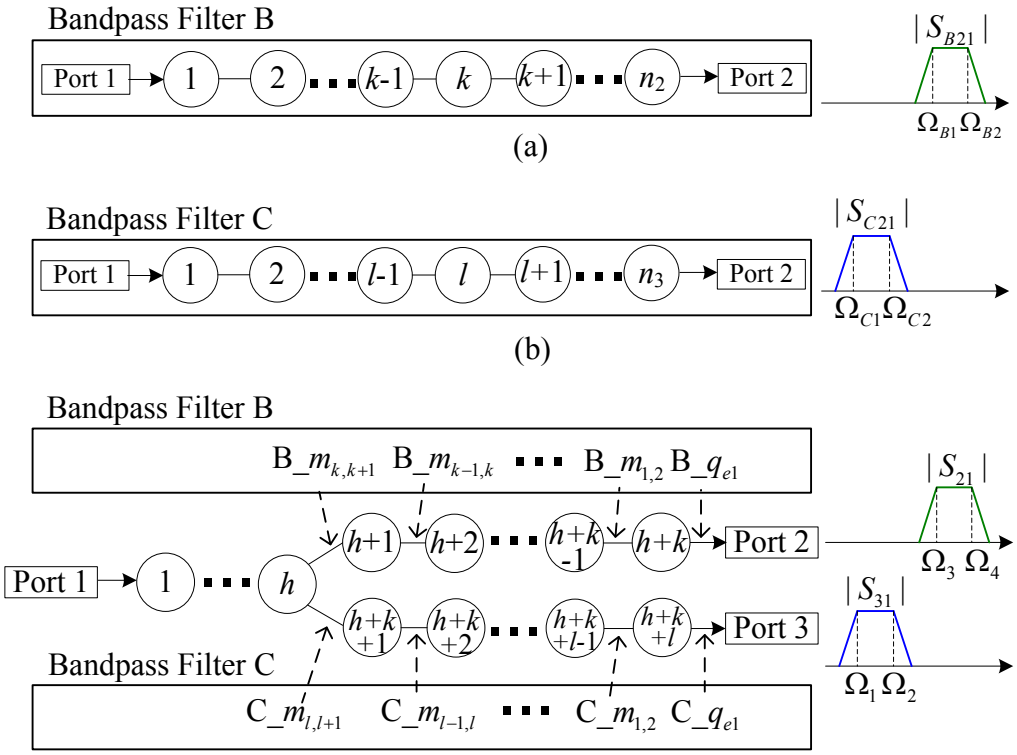

Figure 4.6 (a) Bandpass filter B with n_2 coupled resonators. Its coupling coefficients and external quality factors are denoted as B_$m_{i,j}$ and B_q_{ei}, (b) Bandpass filter C with n_3 coupled resonators. Its coupling coefficients and external quality factors are denoted as C_$m_{i,j}$ and C_q_{ei}. (c) The coupling coefficients and external quality factors of the diplexer branches are originated from those of the band pass filters B and C.

Figure 4.6 demonstrates how to obtain the starting point of the coupling coefficient $m_{i,j}$ and external quality factor q_{ei} for each branch from the single band bandpass filters. For example, the coupling coefficient between resonator h+1 and h+2 of the diplexer in (c) is originated from the coupling between resonator k-1 and k of the band pass filter B in (a). The cut-offs of the single band bandpass filter and those of the diplexer have the relationship as:

$$\Omega_1 = \Omega_{C1},\ \ \Omega_2 = \Omega_{C2},\ \ \Omega_3 = \Omega_{B1},\ \ \Omega_4 = \Omega_{B2}. \tag{4.6}$$

where Ω_1 to Ω_4 are the cut-offs of two passbands of the diplexer, Ω_{B1} and Ω_{B2} are the cut-

offs of the bandpass filter B, Ω_{C1} and Ω_{C2} are the cut-offs of the bandpass filter C. The orders of two band pass filters are n_2 and n_3:

$$n_2 = \frac{h}{2} + k, \quad n_3 = \frac{h}{2} + l \quad (h \text{ is even}) \tag{4.7}$$

where h is the number of resonators on the stem of the diplexer, k and l are the number of resonators on each branch. Similar to the dual band filter, every two resonators on the stem work as a resonant pair and the order of the stem is evenly distributed by the two passbands. So the number of resonators on the stem is a multiple of 2, i.e. an even number.

The band pass filters B and C are scaled and shifted from the prototype low-pass filter. For a single bandpass filter having two cut-offs at Ω_a and Ω_b, the scaled and shifted processes are illustrated in Figure 4.7.

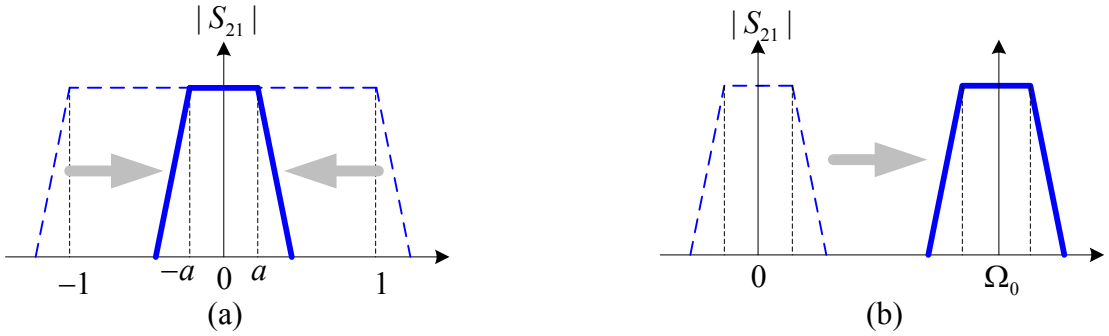

Figure 4.7 (a) An un-normalised low-pass filter scaled from a normalised one. (b) A band pass filter shifted from a lowpass one.

As shown in Figure 4.7(a), a low-pass response, with cut-offs at $\pm a$ shown in a solid line, is scaled from a low-pass prototype, with cut-offs at ± 1 in dashed line. a is defined as

$$a = \frac{|\Omega_a - \Omega_b|}{2} \tag{4.8}$$

This implies that the coupling coefficient m_{scale} of the band pass filter with the scaled response

is proportional to the $m_{\text{prototype}}$ of the prototype lowpass filter as

$$m_{\text{scale}} = a \times m_{\text{prototype}} \tag{4.9}$$

The external quality factor q_{e_scale} is proportional to the $q_{e\_\text{prototype}}$ one as

$$q_{e\_\text{scale}} = \frac{q_{e\_\text{prototype}}}{a} \tag{4.10}$$

Figure 4.7(b) illustrates how to shift a low-pass response, centre at 0Hz, to a new one, centred at Ω_0 . The new centre frequency of the passband Ω_0 is defined as

$$\Omega_0 = \frac{\Omega_a + \Omega_b}{2} \tag{4.11}$$

So the self-coupling $m_{i,i}$ of the single band bandpass filter with shifted response is obtained as

$$m_{i,i} = \Omega_0 = \frac{\Omega_a + \Omega_b}{2} \tag{4.12}$$

4.3.2 Starting Values of the Branches Having Chebyshev Responses

For the diplexer having Chebyshev responses, two branches can be originated from the Chebyshev lowpass prototype filter. The coupling coefficient $m_{i,j}$ and external quality factor q_e on each branch can be obtained by the Chebyshev formulas in Chapter 2 directly. For example, as shown in Figure 4.6, the coupling coefficient $m_{i,j}$ of the diplexer branch, which connects to port 2, and its external quality factor q_{eh+k} can be originated from those of the single band bandpass filter B. According to (4.8) and (4.10), the B_$m_{1,2}$ and B_q_{e1} of the lowpass filter B with cut-offs at Ω_3 and Ω_4 can be found by

$$\begin{aligned} \mathrm{B\_}m_{1,2} &= \frac{|\Omega_3 - \Omega_4|}{2} m_{1,2\ \text{Chebyshev prototype}} \\ \mathrm{B\_}q_{e1} &= \frac{2}{|\Omega_3 - \Omega_4|} q_{e1\ \text{Chebyshev prototype}} \end{aligned} \tag{4.13}$$

So

$$\begin{aligned} m_{h+k-i,h+k-i+1} = \mathrm{B\_}m_{i,i+1} &= \frac{|\Omega_3 - \Omega_4|}{2} m_{i,i+1\ \text{Chebyshev prototype}} \\ (i = 1 \text{ to } k-1) & \\ q_{eh+k} = \mathrm{B\_}q_{e1} &= \frac{2}{|\Omega_3 - \Omega_4|} q_{e1\ \text{Chebyshev prototype}} \end{aligned} \tag{4.14}$$

Substituting (2.13) into (4.14), we have

$$\begin{aligned} m_{h+k-1,h+k} &= \frac{|\Omega_3 - \Omega_4|}{2} \frac{1}{\sqrt{g_1 g_2}} \\ q_{eh+k} &= \frac{2}{|\Omega_4 - \Omega_3|} g_0 g_1 \end{aligned} \tag{4.15}$$

Similarly, the rest of the coupling coefficients along the branch can be formulated as

$$m_{h+k-i,h+k-i+1} = \frac{|\Omega_3 - \Omega_4|}{2} \frac{1}{\sqrt{g_i g_{i+1}}} \quad (i = 1 \text{ to } k-1) \tag{4.16}$$

Where g_i is obtained from (2.11) and the order of the prototype Chebyshev filter n_2 is given in (4.7). The self coupling $m_{i,i}$ of the branch resonator i equals to that of the band pass filter B as

$$m_{i,i} = \Omega_0 = \frac{\Omega_4 + \Omega_3}{2} \quad (i = h+1 \text{ to } h+k) \tag{4.17}$$

As shown in Figure 4.6, the coupling coefficient of the diplexer $m_{h,h+k+1}$ is originated from C_$m_{l,l+1}$ of the single band bandpass filter C. According to (4.8) and (4.10), the C_$m_{l,l+1}$ and C_q_{e1} of the lowpass prototype filter C with cut-offs at Ω_1 and Ω_2 can be found by

$$\begin{aligned} \mathrm{C\_}m_{l,l+1} &= \frac{|\Omega_1 - \Omega_2|}{2} m_{l,l+1\ \text{Chebyshev prototype}} \\ \mathrm{C\_}q_{e1} &= \frac{2}{|\Omega_1 - \Omega_2|} q_{e1\ \text{Chebyshev prototype}} \end{aligned} \tag{4.18}$$

so

$$\begin{aligned} m_{k,k+h+1} &= \frac{|\Omega_1 - \Omega_2|}{2} m_{l,l+1\ \text{Chebyshev prototype}} \\ \mathrm{C\_}q_{e1} &= \frac{2}{|\Omega_1 - \Omega_2|} q_{e1\ \text{Chebyshev prototype}} \end{aligned} \tag{4.19}$$

Substituting (2.13) into (4.18), we have

$$\begin{aligned} m_{h,h+k+1} &= \frac{|\Omega_1 - \Omega_2|}{2} \frac{1}{\sqrt{g_l g_{l+1}}} \\ q_{e1} &= \frac{2}{|\Omega_1 - \Omega_2|} g_0 g_1 \end{aligned} \tag{4.20}$$

Similarly, the rest of the coupling coefficient along the branch can be formulated as

$$m_{h+k+l-i,h+k+l-i+1} = \frac{|\Omega_3 - \Omega_4|}{2} \frac{1}{\sqrt{g_i g_{i+1}}} \quad (i = 1 \text{ to } l-1) \tag{4.21}$$

Where g_i is obtained from (2.11) and the order of the Chebyshev filter is n_3 in (4.7).

The self-coupling $m_{i,i}$ of each branch resonator i should be initialised as the centre frequency of the passband occupied by the branch or

$$m_{i,i} = \Omega_0 = \frac{\Omega_4 + \Omega_3}{2} \quad (i = h+k+1 \text{ to } h+k+l) \tag{4.22}$$

4.3.3 Adjustment of the Branch Starting Point

Actually, only the resonator connecting to the branch port has the self-coupling very close to the branch passband centre frequency Ω_0. The self-coupling $m_{i,i}$ of the other branch resonator

i can be formulated in a recursive way as

$$\begin{aligned} m_{h+k,h+k} &= \Omega_0 = \frac{\Omega_3 + \Omega_4}{2} > 0 \\ m_{i,i} &= m_{i+1,i+1} - \Delta m_i \quad (h < i < h + k - 1,\ \Delta m_i > 0) \end{aligned} \tag{4.23}$$

and

$$\begin{aligned} m_{h+k+l,h+k+l} &= \Omega_0 = \frac{\Omega_1 + \Omega_2}{2} < 0 \\ m_{i,i} &= m_{i+1,i+1} + \Delta m_i \quad (h + k < i < h + k + l - 1, \Delta m_i > 0) \end{aligned} \tag{4.24}$$

Furthermore, in order to make the starting value close to the final result, the coupling coefficient between the stem part and branch part needs to be scaled by a factor. For example, in Figure 4.6, $m_{h,h+1}$ is the coupling between the branch resonator h+1 and the stem resonator k. It is scaled by the factor b as

$$m_{h,h+1} = b \times B\_m_{k,k+1} = b \times \frac{|\Omega_3 - \Omega_4|}{2} m_{k,k+1\ \text{Chebyshev prototype}} \tag{4.25}$$

where b is greater than 1 and varied by the desired topology. To simplify the initialisation of the starting point, the value of b is determined as 1.4 based on the matrix synthesis.

Substituting the Chebyshev formulas (2.13) into (4.25), we have

$$m_{h,h+1} = b \times \frac{|\Omega_3 - \Omega_4|}{2} \frac{1}{\sqrt{g_k g_{k+1}}} \tag{4.26}$$

4.3.4 Starting Values of the Stem Part

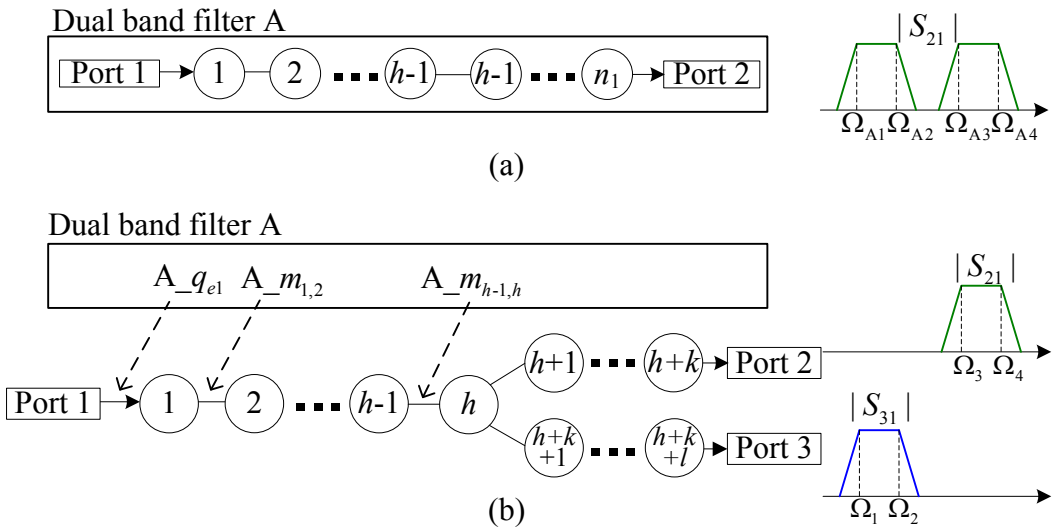

Figure 4.8 (a) A dual band bandpass filter A. Its coupling coefficient and external quality factor are denoted as A_$m_{i,j}$ and A_q_{ei}. (b) The coupling coefficient and external quality factor of the diplexer stem part are originated from those of the dual band filter A.

For the stem part, as illustrated in Figure 4.8, the starting values of the coupling coefficient $m_{i,j}$ and the external quality factor $q_{e1,}$ in Figure 4.8 (b), are originated from those of the dual band bandpass filter, in Figure 4.8 (a). The diplexer and the dual band bandpass filter A have the same cut-offs of two passbands as:

$$\Omega_i = \Omega_{Ai} \ (i=1 \text{ to } 4) \tag{4.27}$$

Where Ω_i is the cut-off of the diplexer, Ω_{Ai} is the cut-off of the dual band bandpass filter A. n_1 is the order of the dual band filter A and

$$n_1 > h \tag{4.28}$$

Where h is the number of the resonators on the stem of the diplexer, both n_1 and h are even numbers.

4.3.5 External Quality Factor q_{e1} of the Stem

The external quality factor q_{e1} on the stem can be directly calculated by the formula as

$$q_{e1} = \frac{q_{e2} \times q_{e3}}{q_{e2} + q_{e3}} \tag{4.29}$$

Where q_{e2} and q_{e3} are the external quality factors on each branch.

4.3.6 Coupling Coefficient $m_{i,j}$ and Self Coupling $m_{i,i}$ of the Stem

Conventionally, the coupling coefficient $m_{i,j}$ of the dual band bandpass filter is obtained by optimisation using a gradient method [2]. For simplicity, the coupling coefficient A_$m_{i,j}$ of the n_1-th order dual band bandpass filter A, in Figure 4.8(a), with symmetric responses has a close approximation to:

$$\begin{aligned}
&\mathrm{A}_m_{1,2} = \mathrm{A}_m_{n_1-1,n_1} \approx 0.4\times|\Omega_4 - \Omega_1| \\
&\mathrm{A}_m_{2,3} = \mathrm{A}_m_{n_1-2,n_1-1} \approx 0.4\times(|\Omega_4 - \Omega_3| + |\Omega_2 - \Omega_1|) \\
&\mathrm{A}_m_{i,i+1} = \mathrm{A}_m_{n_1-i-1,n_1-i} \approx 0.35\times|\Omega_4 - \Omega_1| \ \ (i \text{ is odd and } 1 < i < n_1 - 1) \\
&\mathrm{A}_m_{i,i+1} = \mathrm{A}_m_{n_1-i-1,n_1-i} \approx 0.35\times(|\Omega_4 - \Omega_3| + |\Omega_2 - \Omega_1|) \ (i \text{ is even and } 2 < i < n_1 - 2)
\end{aligned} \tag{4.30}$$

Note that (4.30) is summarised from the matrix synthesis of the work.

As the stem part of the diplexer, in Figure 4.8(b), is originated from the dual band filter A, in Figure 4.8(a), the starting point of the coupling coefficient of the stem part $m_{i,j}$ is:

$$m_{i,j} = \mathrm{A}\_m_{i,j} \quad (i \neq j) \tag{4.31}$$

Substituting (4.30) into (4.42), we have

$$\begin{aligned}
&m_{1,2} \approx 0.4\times|\Omega_4 - \Omega_1| \\
&m_{2,3} \approx 0.4\times(|\Omega_4 - \Omega_3| + |\Omega_2 - \Omega_1|) \\
&m_{i,i+1} \approx 0.35\times|\Omega_4 - \Omega_1| \ \ (i \text{ is odd and } 1 < i < h) \\
&m_{i,i+1} \approx 0.35\times(|\Omega_4 - \Omega_3| + |\Omega_2 - \Omega_1|) \ (i \text{ is even and } 2 < i < h)
\end{aligned} \tag{4.32}$$

The self-coupling A_$m_{i,i}$ of the dual band bandpass filter A is 0 when the filter has a symmetric response. So the self coupling of the stem part $m_{i,i}$ is

$$m_{i,i} = 0 \ (1 \le i \le h) \tag{4.33}$$

Where h is the total number of resonators on the stem.

4.3.7 Initialise the Reflection Zeros

The transfer response $H_n(j\Omega)$ of the n-th order Chebyshev filter can be expressed as [3]

$$H_n(j\Omega) = \frac{1}{\sqrt{1+\varepsilon^2 T_n^2\left(\Omega/\Omega_c\right)}} \tag{4.34}$$

Where $T_n^2\left(\Omega/\Omega_c\right)$ is the Chebyshev polynomials of the first kind (having equal-ripple in passband), Ω_c is the cut-off of the passband, ε represents the maximum value of return loss $S_{11\max}$ in the passband and

$$\varepsilon = 10^{-S_{11\max}/10} \tag{4.35}$$

T_n is defined as [3]:

$$\begin{aligned} T_0(x) &= 1 \\ T_1(x) &= x \\ T_n(x) &= 2x \cdot T_{n-1}(x) - T_{n-2}(x) \quad (n \ge 2) \end{aligned} \tag{4.36}$$

The set of reflection zeros Ω_{RZ} can be found when all the energy is transferred as

$$H_n(j\Omega_{RZ}) = 1 \tag{4.37}$$

By inspecting (4.34), (4.37) is satisfied when $\varepsilon^2 T_n^2\left(\Omega_{RZ}/\Omega_c\right) = 0$. As ε is non-zero, we have

$$T_n^2\left(\Omega_{RZ}/\Omega_c\right) = 0 \tag{4.38}$$

For simplicity, Ω_c is assumed to be unity and (4.38) is simplified as

$$T_n^2\left(\Omega_{RZ}\right)=0 \tag{4.39}$$

So the set of solutions Ω_{RZ} of (4.39) is the set of reflection zeros of the Chebyshev filter. For Chebyshev response having cut-offs at Ω_1 and Ω_2, its set of reflection zeros Ω_{RZ_new} can be shifted and scaled from the normalised one Ω_{RZ} as

$$\Omega_{RZ} \rightarrow \frac{\Omega_{RZ\_new}-\frac{\Omega_1+\Omega_2}{2}}{\frac{\left|\Omega_1-\Omega_2\right|}{2}} \tag{4.40}$$

According to (4.40), we find the relationship as

$$\Omega_{RZ\_new}=\Omega_{RZ}\cdot\frac{\left|\Omega_1-\Omega_2\right|}{2}+\frac{\Omega_1+\Omega_2}{2} \tag{4.41}$$

The set of Ω_{new} is applied as the starting point of the reflection zeros of the diplexer circuit. It is used to calculate the cost function value during the optimisation.

4.4 Cost Function for the Optimisation

The cost function is used to quantify the difference between the optimised results and the desired response.

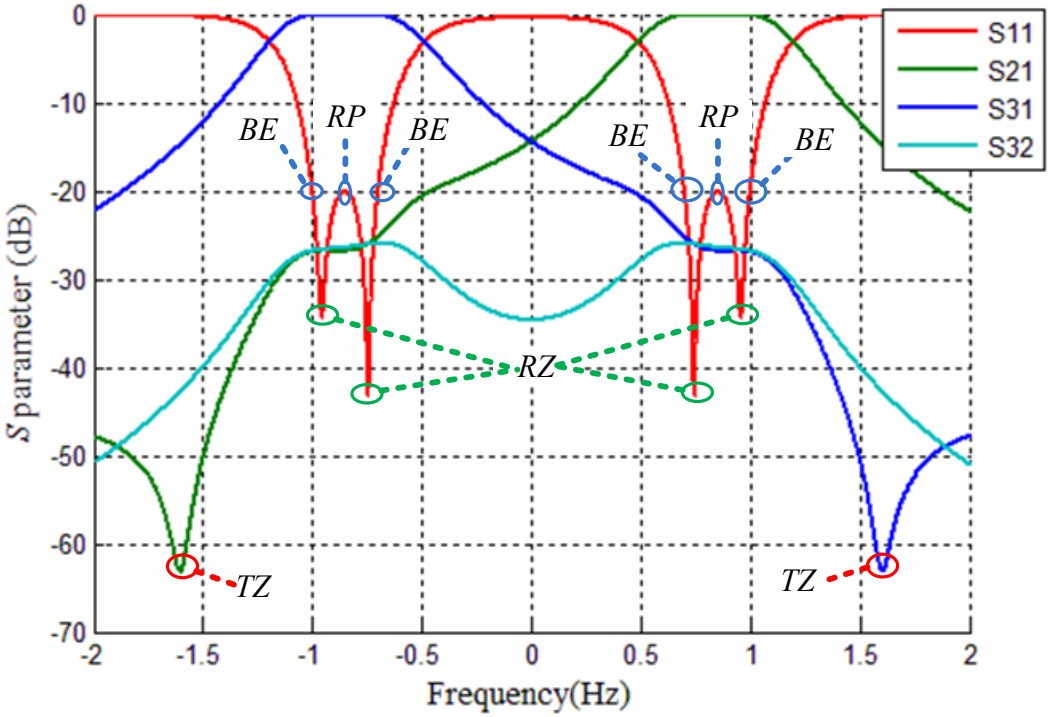

Figure 4.9 The critical points of a diplexer having equal-ripple response on the passband.

In order to make a diplexer with a similar Chebyshev response in Figure 4.9, some critical characteristic points are chosen to form the cost function, including the reflection zeros *RZ*, the transmission zeros *TZ*, the equal-ripple pass-band edges *BE* and the reflection poles within the pass-band *RP*. The cost function *CF* of the project is given as

$$\begin{aligned} CF = & \sum_{i=1}^{n} a_i \left| S_{11}(\Omega_{RZi}) \right| + \sum_{i=1}^{4} b_i \left| \left| S_{11}(\Omega_{BEi}) \right| - \varepsilon \right| + \sum_{i=1}^{n-2} c_i \left| \left| S_{11}(\Omega_{RPi}) \right| - \varepsilon \right| \\ & + \sum_{i=1}^{T_2} d_i \left| S_{21}(\Omega_{T_2Zi}) \right| + \sum_{i=1}^{T_3} e_i \left| S_{31}(\Omega_{T_3Zi}) \right| + \cdots \end{aligned} \tag{4.42}$$

Where a_i, b_i, c_i, d_i and e_i are the weights of each term, n is the number of resonators of the circuit, ε represents the maximum value of return loss in the passband. Replacing the *S*-parameters in (4.42) with (3.54), we have:

$$
\begin{aligned}
CF = & \sum_{i=1}^{n} a_i \left| 1 - 2[A(\Omega_{RZi})]_{P1,P1}^{-1} \right| + \sum_{i=1}^{4} b_i \left\| 1 - 2[A(\Omega_i)]_{P1,P1}^{-1} \right| - \varepsilon \Big| \\
& + \sum_{i=1}^{n-2} c_i \left\| 1 - 2[A(\Omega_i)]_{P1,P1}^{-1} \right| - \varepsilon \Big| + \sum_{i=1}^{T_2} d_i \left| 2[A(\Omega_{T_2Zi})]_{P2,P1}^{-1} \right| \\
& + \sum_{i=1}^{T_3} d_i \left| 2[A(\Omega_{T_3Zi})]_{P3,P1}^{-1} \right| + \cdots
\end{aligned}
\tag{4.43}
$$

Where $[A]^{-1}$ is the inverse matrix of the n+3 diplexer immittance matrix $[A]$. As given in (3.55), $[A]$ contains the n+3 coupling matrix $[m]$. By altering the values of the non-zero entries in $[m]$ (like the internal coupling $m_{i,j}$, external coupling $m_{pk,h}$ and $m_{h,pk}$ and self coupling $m_{i,i}$), the entry values in the inverse matrix $[A]^{-1}$ may change leading to the change of the cost function value CF on the left hand side of (4.43). In a gradient method, the optimisation program is to find a matrix $[m]$ with the lowest cost function value.

4.5 Example A: a Diplexer Matrix Synthesised by Optimisation

In this section, a diplexer example with Chebyshev response is synthesised. The first step is to determine the specifications and the desired topology of the diplexer. After reducing the number of variables based on the specifications and topology, the initial values of the matrix $[m]$ and reflection zeros $[\Omega_{RZ}]$ are generated. The optimised results including the final matrix $[m]$ and the set of reflection zeroes are given at the end of this section.

4.5.1 The Specifications and Topology of the Diplexer

A 10-coupled-resonator based diplexer has been designed. The cut-offs of 2 passbands are determined as $[\Omega_1, \Omega_2, \Omega_3, \Omega_4] = [-1, -0.5, 0.5, 1]$, return loss within the passband is at 20 dB. The chosen diplexer topology is depicted in Figure 4.10.

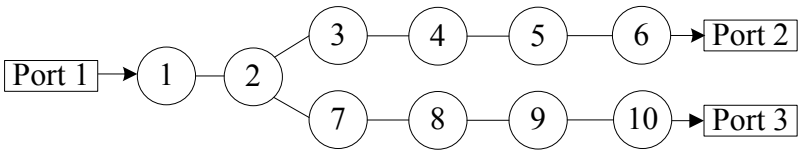

Figure 4.10 Schematic of a 10-coupled-resonator based diplexer.

The n+3 coupling matrix of the diplexer is

$$[m]=\begin{bmatrix}
0 & m_{P1,1} & 0 & 0 & 0 & 0 & 0 & 0 & 0 & 0 & 0 & 0 & 0 \\
m_{1,P1} & m_{1,1} & m_{1,2} & 0 & 0 & 0 & 0 & 0 & 0 & 0 & 0 & 0 & 0 \\
0 & m_{2,1} & m_{2,2} & m_{2,3} & 0 & 0 & 0 & m_{2,7} & 0 & 0 & 0 & 0 & 0 \\
0 & 0 & m_{3,2} & m_{3,3} & m_{3,4} & 0 & 0 & 0 & 0 & 0 & 0 & 0 & 0 \\
0 & 0 & 0 & m_{4,3} & m_{4,4} & m_{4,5} & 0 & 0 & 0 & 0 & 0 & 0 & 0 \\
0 & 0 & 0 & 0 & m_{5,4} & m_{5,5} & m_{5,6} & 0 & 0 & 0 & 0 & 0 & 0 \\
0 & 0 & 0 & 0 & 0 & m_{6,5} & m_{6,6} & 0 & 0 & 0 & 0 & m_{6,P2} & 0 \\
0 & 0 & m_{7,2} & 0 & 0 & 0 & 0 & m_{7,7} & m_{7,8} & 0 & 0 & 0 & 0 \\
0 & 0 & 0 & 0 & 0 & 0 & 0 & m_{8,7} & m_{8,8} & m_{8,9} & 0 & 0 & 0 \\
0 & 0 & 0 & 0 & 0 & 0 & 0 & 0 & m_{9,8} & m_{9,9} & m_{9,10} & 0 & 0 \\
0 & 0 & 0 & 0 & 0 & 0 & 0 & 0 & 0 & m_{10,9} & m_{10,10} & 0 & m_{10,P3} \\
0 & 0 & 0 & 0 & 0 & 0 & m_{P2,6} & 0 & 0 & 0 & 0 & 0 & 0 \\
0 & 0 & 0 & 0 & 0 & 0 & 0 & 0 & 0 & 0 & m_{P3,10} & 0 & 0
\end{bmatrix} \tag{4.44}$$

The set of reflection zeros within two passbands are denoted as $[\Omega_{RZ_1},\Omega_{RZ_2},\Omega_{RZ_3},\Omega_{RZ_4},\Omega_{RZ_5}]$ (for the left passband) and $[\Omega_{RZ_6},\Omega_{RZ_7},\Omega_{RZ_8},\Omega_{RZ_9},\Omega_{RZ_{10}}]$ (for the right passband). The zeros do not correspond to the physical resonators.

4.5.2 Reducing the Total Number of Variables

According to the topology and specifications of the diplexer, the total number of the variables in both the matrix $[m]$ and the set of reflection zeros $[\Omega_{RZ}]$ can be reduced due to symmetry.

(1) As two passbands of the diplexer are symmetric at 0 Hz, the self couplings ($m_{1,1}$ and $m_{2,2)}$ of the resonators on the stem have a relationship as

$$m_{1,1} = m_{2,2} = 0 \tag{4.45}$$

(2) As both branches have 4 resonators and two passbands are symmetric at 0 Hz, the coupling coefficient $m_{i,j}$ along each branch have relationships as

$$\begin{aligned} m_{2,3} &= m_{2,7} \\ m_{i,i+1} &= m_{i+4,i+5} \ \ (i = 3 \ to \ 5) \end{aligned} \tag{4.46}$$

while the self-coupling $m_{k,k}$ of each branch resonator k has the relationship as

$$\begin{aligned} m_{6,6} &= -m_{10,10} \\ m_{k,k} &= -m_{k+5,k+5} = m_{k+1,k+1} - \Delta m_k \ \ (k = 3 \ to \ 5) \end{aligned} \tag{4.47}$$

where Δm is the difference of the self-coupling between the adjacent channel resonators. The external quality factors q_{ei} or the external coupling $m_{Pk,i}$ of the diplexer are

$$2q_{e1} = q_{e6} = q_{e10} \ \ \text{or} \ \ \frac{m_{P1,1}}{\sqrt{2}} = m_{P2,6} = m_{P3,10} \tag{4.48}$$

Also, the reflection zeros Ω_{RZ} of the diplexer have relationships as

$$\Omega_{RZ_i} = -\Omega_{RZ_{10-i}} \ (i = 1 \text{ to } 5) \tag{4.49}$$

According to (4.45) to (4.47), the set of non-zero variables of the matrix $[m]$ in (4.44) is degenerate to the vector X_m as

$$X_m = [m_{1,2}, m_{2,3}, m_{3,4}, m_{4,5}, m_{5,6}, \Delta m_3, \Delta m_4, \Delta m_5, m_{6,6}] \tag{4.50}$$

According to (4.49), the set of variables of the reflection zeros forms the vector X_{RZ} as

$$X_{RZ} = [\Omega_{RZ_6}, \Omega_{RZ_7}, \Omega_{RZ_8}, \Omega_{RZ_9}, \Omega_{RZ_{10}}] \tag{4.51}$$

4.5.3 Initialisation of the Starting Point

After reducing the number of variables, we need to find the initial values of X based on the equations given in Section 4.3. The starting values of X are given in (4.52) as

$$\begin{aligned} X &= [X_m, X_{RZ}] = [m_{1,2}, m_{2,3}, m_{3,4}, m_{4,5}, m_{5,6}, \Delta m_3, \Delta m_4, \Delta m_5, m_{6,6}, \Omega_{RZ_6}, \Omega_{RZ_7}, \Omega_{RZ_8}, \Omega_{RZ_9}, \Omega_{RZ_{10}}] \\ &= [0.8,\ 0.304,\ 0.159,\ 0.159,\ 0.217,\ 0.1,\ 0.1,\ 0.1,\ 0.75,\ 0.512,\ 0.603,\ 0.750,\ 0.897,\ 0.988] \end{aligned} \tag{4.52}$$

How to get the initial values of X is detailed in the following parts.

4.5.3.1 Branch Couplings

According to (4.52), the variables relating to the branch part are

$$[m_{2,3}, m_{3,4}, m_{4,5}, m_{5,6}, \Delta m_3, \Delta m_4, \Delta m_5, m_{6,6}] \tag{4.53}$$

As the number of reflection zeros on each channel is 5, the branch part is originated from a 5th order Chebyshev lowpass filter. For the filter having return loss at -20dB, its g values are

$$[g_0, g_1, g_2, g_3, g_4, g_5, g_6] = [1, 0.9714, 1.3721, 1.8014, 1.3721, 0.9714, 1] \tag{4.54}$$

According to (4.20) and (4.54), the external quality factor q_{e2} of the branch will be

$$q_{e2} = \frac{2}{|\Omega_1 - \Omega_2|} g_0 g_1 = 3.886 \tag{4.55}$$

Similarly, the coupling coefficients $m_{i,j\_\text{chebyshev}}$ of the 5th order Chebyshev filter are

$$m_{i,i+1\_\text{Chebyshev}} = [0.217, 0.159, 0.159, 0.217] \tag{4.56}$$

Considering (4.26), the starting values of the branch coupling are extracted as

$$\begin{aligned} [m_{2,3}, m_{3,4}, m_{4,5}, m_{5,6}] &= [0.217 \times b, 0.159, 0.159, 0.217] \\ &= [0.304, 0.159, 0.159, 0.217] \end{aligned} \tag{4.57}$$

where b=1.4 is produced from running experiments in the MATLAB program . According to (4.23), the self coupling $m_{6,6}$ of Resonator 6 will be

$$m_{6,6} = \frac{\Omega_4 + \Omega_3}{2} = 0.75 \tag{4.58}$$

And Δm_i is assumed as

$$\Delta m_i = 0.1 \ (i = 3 \text{ to } 5) \tag{4.59}$$

4.5.3.2 Stem Couplings

According to (4.30), the initial value of the stem coupling $m_{1,2}$ is

$$m_{1,2} = 0.4 \times | \Omega_4 - \Omega_1 | = 0.8 \tag{4.60}$$

According (4.48) and (4.55), the external quality factor q_{e1} will be

$$q_{e1} = \frac{1}{2} q_{e2} = 1.943 \tag{4.61}$$

4.5.3.3 Reflection Zeros

As the diplexer has a symmetric response, hence the number of reflection zeros of each channel is 5. According to (4.36), we have

$$T_5(\Omega_{RZ}) = 16\Omega_{RZ}^5 - 20\Omega_{RZ}^3 + 5\Omega_{RZ} = 0 \tag{4.62}$$

The set of solutions of (4.62) is

$$\Omega_{RZ} = \left[-\sqrt{\frac{5+\sqrt{5}}{8}}, -\sqrt{\frac{5-\sqrt{5}}{8}}, 0, \sqrt{\frac{5-\sqrt{5}}{8}}, \sqrt{\frac{5+\sqrt{5}}{8}} \right] \tag{4.63}$$

According to (4.41) and (4.63), the set of reflection zeros X_{RZ} within the passband [0.5,1] will

be

$$X_{RZ} = [\Omega_{RZ_6}, \Omega_{RZ_7}, \Omega_{RZ_8}, \Omega_{RZ_9}, \Omega_{RZ_{10}}] = [0.512, 0.603, 0.750, 0.897, 0.988] \quad (4.64)$$

4.5.4 Starting Point of the Diplexer

The set of variables X to be optimised is defined as

$$X = [X_m, X_{rf}] \quad (4.65)$$

Considering (4.57) to (4.60) and (4.64), the starting point of X is given in (4.52) as

$$X = [0.8, 0.304, 0.159, 0.159, 0.217, 0.1, 0.1, 0.1, 0.75, 0.512, 0.603, 0.750, 0.897, 0.988]$$

Setting the boundary condition of X as

upper boundary=[0.88, 0.60, 0.22, 0.22, 0.303, 0.2, 0.2, 0.2, 0.83, 0.532, 0.633, 0.810, 0.937, 0.988]

lower boundary=[0.64, 0.17, 0.14, 0.14, 0.19, 0, 0, 0, 0.68, 0.502, 0.573, 0.69, 0.857, 0.958]

The *S*-parameters produced from the starting point is shown in Figure 4.11.

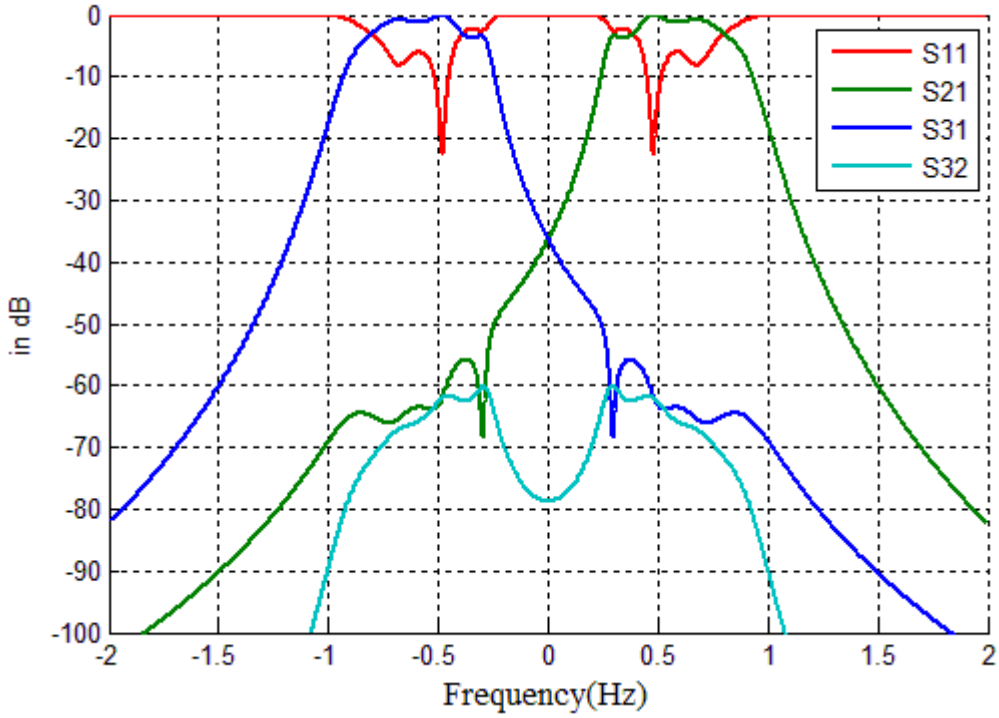

Figure 4.11 The diplexer responses of the starting point

4.5.5 Optimised Result

The optimisation is done in Matlab. The applied optimisation function is called *fmincon*. The algorithm evaluates different sets of X and tries to find the desired one which gives the lowest cost function value. This algorithm is based on a gradient method and it will terminate when some of the stopping criteria are satisfied[4]. The information of the computer used in this work is given below:

CPU: Intel(R) Core(TM) i5 (3.20 GHz)

Memory (RAM): 4.00GB (3.18 GB usable)

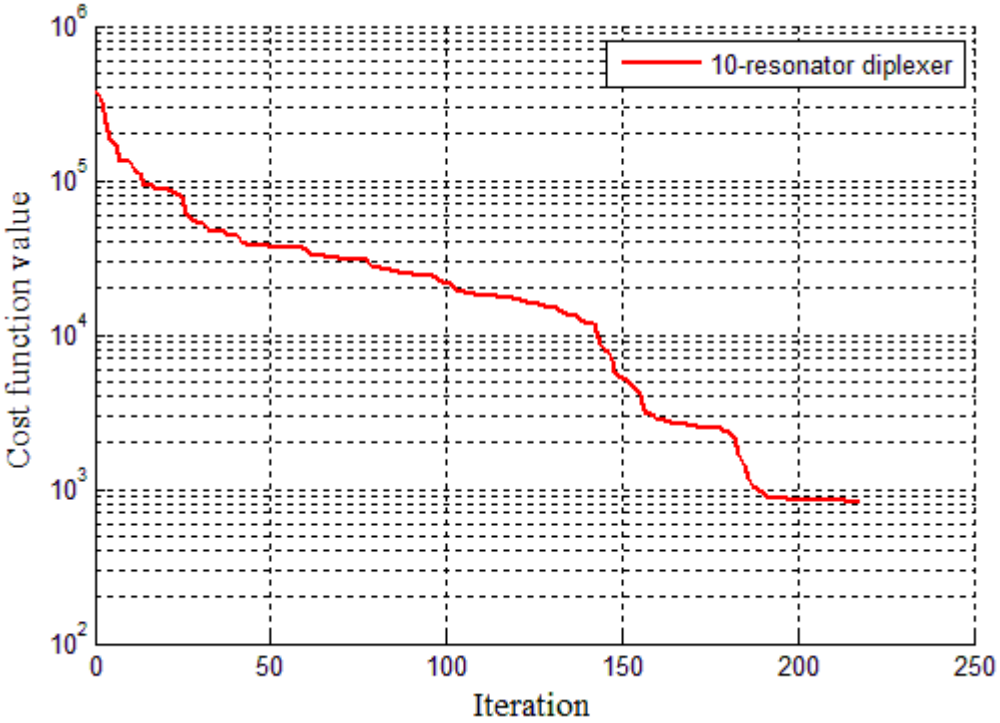

Figure 4.12 The cost function value in each iteration

Figure 4.12 shows how the cost function value changes in each optimisation iteration. It takes 11.7 seconds to converge to a result at the 218th iteration. The program stopped as the maximum relative change among all the elements of X is 5.55e-011 (less than the default value 1.0e-010). The maximum relative change of X is defined as [4]

$$\max\left(\left|\frac{\Delta X}{X}\right|\right) \tag{4.66}$$

where ΔX is the change of X. A very small maximum relative change means the program can not reduce the cost function value by altering any variables of X within the requested boundaries. The S-parameter response of the optimised result is given in Figure 4.13.

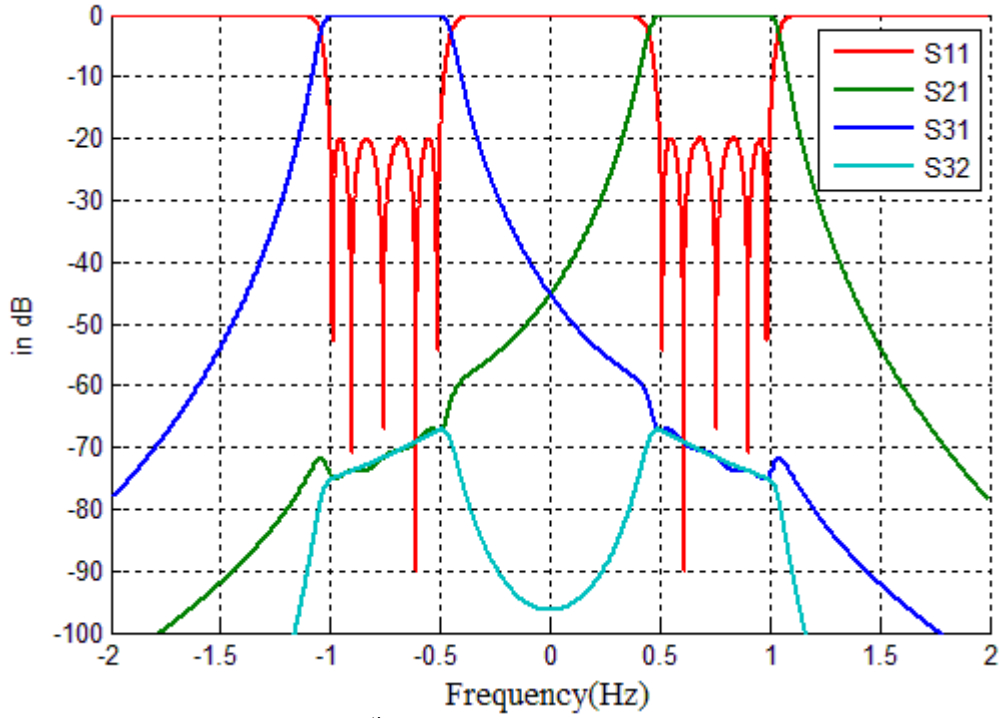

Figure 4.13 Responses of the 10th order diplexer calculated from the optimised coupling matrix.

The final cost function value *CF*=834.9. The errors of some critical points are given in Table 4.1.

Table 4.1 Errors of some critical points of the 10th order diplexer

RZ	Ω_{RZ_6}	Ω_{RZ_7}	Ω_{RZ_8}	Ω_{RZ_9}	$\Omega_{RZ_{10}}$
error	9.7×10^{-6}	4.6×10^{-6}	6.8×10^{-6}	1.4×10^{-6}	1.3×10^{-5}

RP	Ω_{RP_5}	Ω_{RP_6}	Ω_{RP_7}	Ω_{RP_8}
error (in dB)	0.0068	0.0035	0.0399	0.0757

BE	Ω_{BE_3}	Ω_{BE_4}
error (in dB)	4.3×10^{-4}	4.4×10^{-4}

As given in (4.42), the cost function value *CF* is not the sum of the errors but the errors multiplied by the weights. For example, the weights of the reflection zero *RZ* are about 1.5×10^5. The weights of the reflection poles *RP* and equal-ripple band edges *BE* are about

2.2×10^3. According to Table 4.1, all the errors contribute about 300 to the cost function value *CF*. However, the majority part of the cost function value *CF* (about 500) is originated from the errors on the stop band, which is not included in the specifications. Ideally, the energy on the stop band is fully reflected, i.e. $S_{1,1}$ is 0 dB. The weights of the stop band are about 2.2×10^3. The errors on the stop band are listed in Table 4.2

Table 4.2 Errors on the stop band of the 10th order diplexer

Ω (Hz)	0	0.3	1.1	1.2
error (in dB)	2.6×10^{-4}	0.02	0.219	0.0075

A comparison between the initial values and optimised ones of *X* is given in Table 4.3.

Table 4.3 Comparison between the initial values and the optimised values of *X*. (Δm is defined in (4.47))

	$m_{1,2}$	$m_{2,3}$	$m_{3,4}$	$m_{4,5}$	$m_{5,6}$	Δm_3	Δm_4
initial	0.8	0.304	0.159	0.159	0.217	0.1	0.1
optimised	0.821	0.285	0.162	0.159	0.217	0.035	0.003
	Δm_5	$m_{6,6}$	Ω_{RZ_6}	Ω_{RZ_7}	Ω_{RZ_8}	Ω_{RZ_9}	$\Omega_{RZ_{10}}$
initial	0.1	0.75	0.512	0.603	0.750	0.897	0.988
optimised	0.001	0.749	0.513	0.609	0.758	0.902	0.988

The optimised coupling matrix [*m*] is given as

$$\begin{bmatrix}
0 & 0.717 & 0 & 0 & 0 & 0 & 0 & 0 & 0 & 0 & 0 & 0 & 0 \\
0.717 & 0 & 0.821 & 0 & 0 & 0 & 0 & 0 & 0 & 0 & 0 & 0 & 0 \\
0 & 0.821 & 0 & 0.285 & 0 & 0 & 0 & 0.285 & 0 & 0 & 0 & 0 & 0 \\
0 & 0 & 0.285 & 0.71 & 0.162 & 0 & 0 & 0 & 0 & 0 & 0 & 0 & 0 \\
0 & 0 & 0 & 0.162 & 0.745 & 0.159 & 0 & 0 & 0 & 0 & 0 & 0 & 0 \\
0 & 0 & 0 & 0 & 0.159 & 0.748 & 0.217 & 0 & 0 & 0 & 0 & 0 & 0 \\
0 & 0 & 0 & 0 & 0 & 0.217 & 0.749 & 0 & 0 & 0 & 0 & 0.507 & 0 \\
0 & 0 & 0.285 & 0 & 0 & 0 & 0 & -0.71 & 0.162 & 0 & 0 & 0 & 0 \\
0 & 0 & 0 & 0 & 0 & 0 & 0 & 0.162 & -0.745 & 0.159 & 0 & 0 & 0 \\
0 & 0 & 0 & 0 & 0 & 0 & 0 & 0 & 0.159 & -0.748 & 0.217 & 0 & 0 \\
0 & 0 & 0 & 0 & 0 & 0 & 0 & 0 & 0 & 0.217 & -0.749 & 0 & 0.507 \\
0 & 0 & 0 & 0 & 0 & 0 & 0.507 & 0 & 0 & 0 & 0 & 0 & 0 \\
0 & 0 & 0 & 0 & 0 & 0 & 0 & 0 & 0 & 0 & 0.507 & 0 & 0
\end{bmatrix} \tag{4.67}$$

The optimised reflection zeros of the diplexer at port 1 are:

$$\Omega_{RZ} = [\pm 0.513,\ \pm 0.609,\ \pm 0.758,\ \pm 0.902,\ \pm 0.988] \tag{4.68}$$

4.6 Example B to D: 10th Order Diplexer with a Different Topology

The coupling matrix of a 10^{th} order diplexer has been synthesised. The cut-off frequencies of the lowpass prototype are [-1,-0.5] and [0.5,1], the return loss of S_{11} is 20 dB. The desired topology of the diplexer is given in Figure 4.14. The diplexer is denoted as Diplexer D.

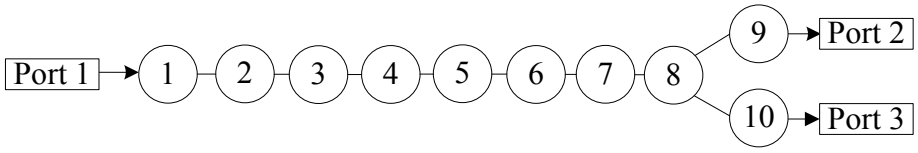

Figure 4.14 Schematic of Diplexer D

The n+3 coupling matrix of Diplexer D is given in Table 4.4.

Table 4.4 The coupling matrix topology of Diplexer D

	P1	1	2	3	4	5	6	7	8	9	10	P2	P3
P1		x											
1	x	x	x										
2		x	x	x									
3			x	x	x								
4				x	x	x							
5					x	x	x						
6						x	x	x					
7							x	x	x				
8								x	x	x	x		
9									x	x		x	
10									x		x		x
P2										x			
P3											x		

Where x is denoted as the non-zero variables in the matrix.

The initial values of the non-zero entries of the coupling matrix are obtained based on the methodology introduced in Section 4.3. It takes 13.62 seconds to converge to a result at the 117th iteration. The initial values and optimised values of each non-zero variable of the coupling matrix are given in Table 4.5.

Table 4.5 The initial values and the optimised ones of the non-zero entries of the coupling matrix of Diplexer D

	$m_{1,2}$	$m_{2,3}$	$m_{3,4}$	$m_{4,5}$	$m_{5,6}$	$m_{6,7}$	$m_{7,8}$
initial	0.8	0.4	0.7	0.35	0.7	0.35	0.7
optimised	0.8156	0.4054	0.7102	0.3316	0.7235	0.3289	0.7275
	$m_{8,9}$	$m_{8,10}$	$m_{9,9}$	$m_{10,10}$	$m_{P1,1}$	$m_{P2,9}$	$m_{P3,10}$
initial	0.3032	0.3032	0.75	-0.75	0.7174	0.5073	0.5073
optimised	0.3025	0.3025	0.7124	-0.7124	0.7174	0.5073	0.5073

The initial values and optimised values of the reflection zeros Ω_{RZ} is given in Table 4.6.

Table 4.6 The initial locations and the optimised ones of the reflection zeros

	Ω_{RZ_1}	Ω_{RZ_2}	Ω_{RZ_3}	Ω_{RZ_4}	Ω_{RZ_5}
initial	-0.9877	-0.8970	-0.75	-0.6030	-0.5123
optimised	-0.9903	-0.9159	-0.7853	-0.6274	-0.5166
	Ω_{RZ_6}	Ω_{RZ_7}	Ω_{RZ_8}	Ω_{RZ_9}	$\Omega_{RZ_{10}}$
initial	0.5123	0.6030	0.750	0.8970	0.9877
optimised	0.5166	0.6274	0.7853	0.9159	0.9903

The S-parameters of the optimised result are given in Figure 4.15.

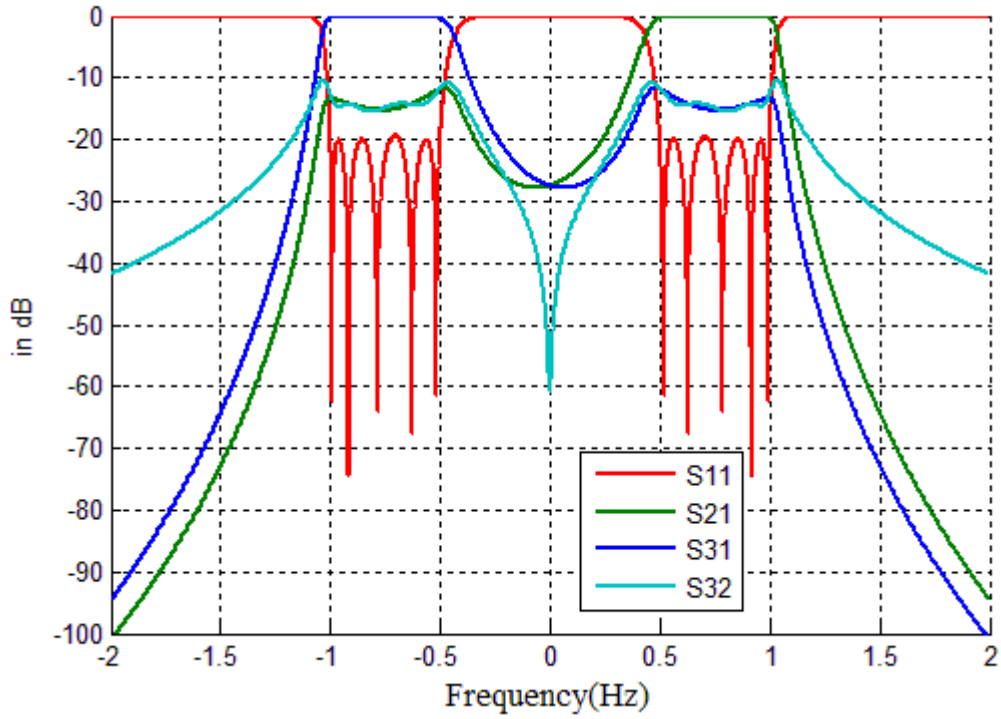

Figure 4.15 Response of Diplexer D

Diplexer A, in Figure 4.10, and Diplexer D, in Figure 4.14, have a different number of resonators on the stem and branches. By altering the number of resonators on the stem and branch, we can get a set of 10^{th} order diplexers. Their topologies are shown in Figure 4.16.

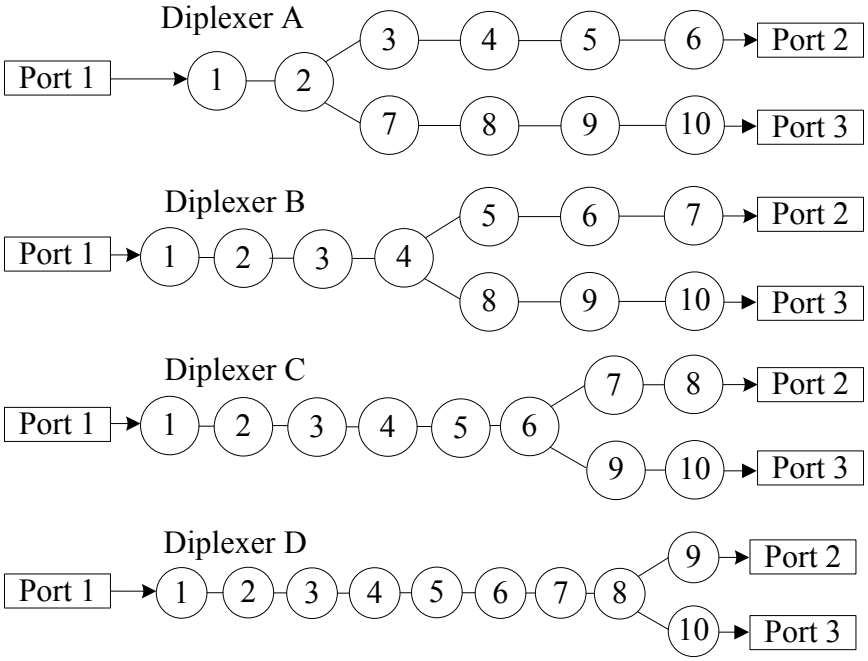

Figure 4.16 Topologies of the 10-th order diplexers with Tree Topology

Similarly, the initial values of the non-zero entries of the coupling matrix of Diplexer B and Diplexer C are obtained based on the methodology introduced in Chapter 4. It takes 20.55 seconds to converge to a result at the 187th iteration. The initial values and optimised values of each non-zero variable of the coupling matrix of Diplexer B are given in Table 4.7.

Table 4.7 The initial values and the optimised ones of the non-zero entries of the coupling matrix of Diplexer B

	$m_{1,2}$	$m_{2,3}$	$m_{3,4}$	$m_{4,5}$	$m_{5,6}$	$m_{6,7}$	$m_{4,8}$
initial	0.8	0.4	0.7	0.2226	0.1590	0.2165	0.2226
optimised	0.8190	0.4033	0.7168	0.2317	0.1613	0.2170	0.2317
	$m_{8,9}$	$m_{9,10}$	$m_{5,5}$	$m_{6,6}$	$m_{7,7}$	$m_{8,8}$	$m_{9,9}$
initial	0.1590	0.2165	0.65	0.70	0.75	-0.65	-0.7
optimised	0.1613	0.2170	0.7168	0.7448	0.7466	-0.7168	-0.7448
	$m_{10,10}$	$m_{P1,1}$	$m_{P2,9}$	$m_{P3,10}$			
initial	-0.75	0.7174	0.5073	0.5073			
optimised	-0.7466	0.7174	0.5073	0.5073			

It takes 10.00 seconds to converge to a result of Diplexer C at the 83th iteration. The initial values and optimised values of each non-zero variable of the coupling matrix of Diplexer are

given in Table 4.8.

Table 4.8 The initial values and the optimised ones of the non-zero entries of the coupling matrix of Diplexer C

	$m_{1,2}$	$m_{2,3}$	$m_{3,4}$	$m_{4,5}$	$m_{5,6}$	$m_{6,7}$	$m_{7,8}$
initial	0.8	0.4	0.7	0.35	0.7	0.2226	0.2165
optimised	0.8181	0.4033	0.7148	0.3284	0.7310	0.2284	0.2187
	$m_{6,9}$	$m_{9,10}$	$m_{7,7}$	$m_{8,8}$	$m_{9,9}$	$m_{10,10}$	$m_{P1,1}$
initial	0.2226	0.2165	0.65	0.75	-0.65	-0.75	0.7174
optimised	0.2284	0.2187	0.7240	0.7440	-0.7240	-0.7440	0.7174
	$m_{P2,9}$	$m_{P3,10}$					
initial	0.5073	0.5073					
optimised	0.5073	0.5073					

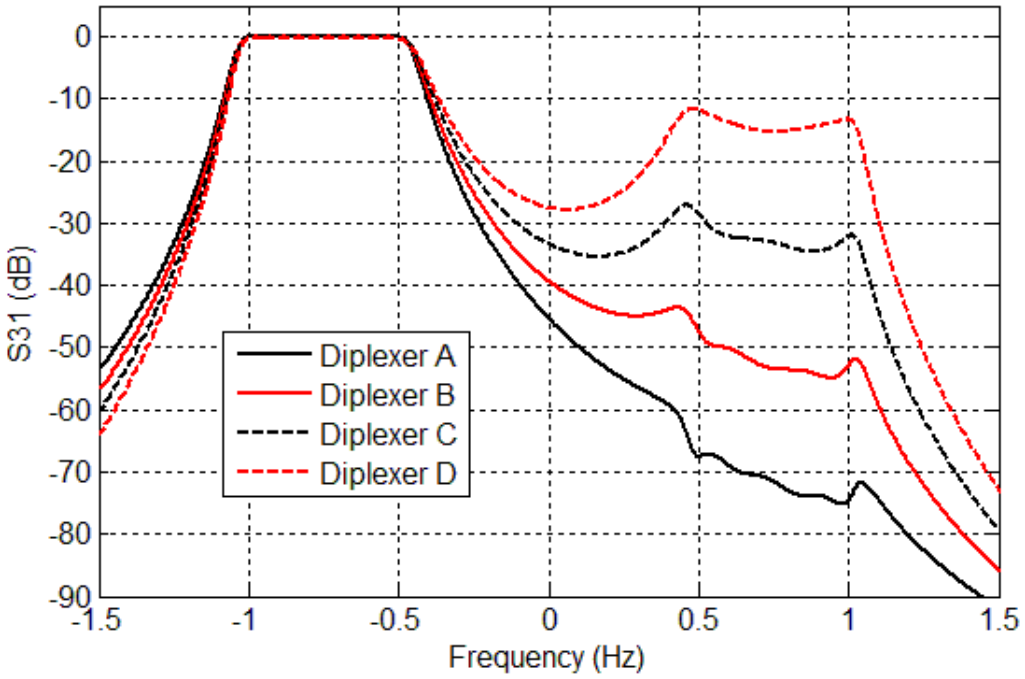

Figure 4.17 Transmission responses of the prototype diplexers [1].

The transmission responses of Diplexer A to D are shown in Figure 4.17. Better adjacent channel rejection is achieved with a higher number of resonators on the branches.

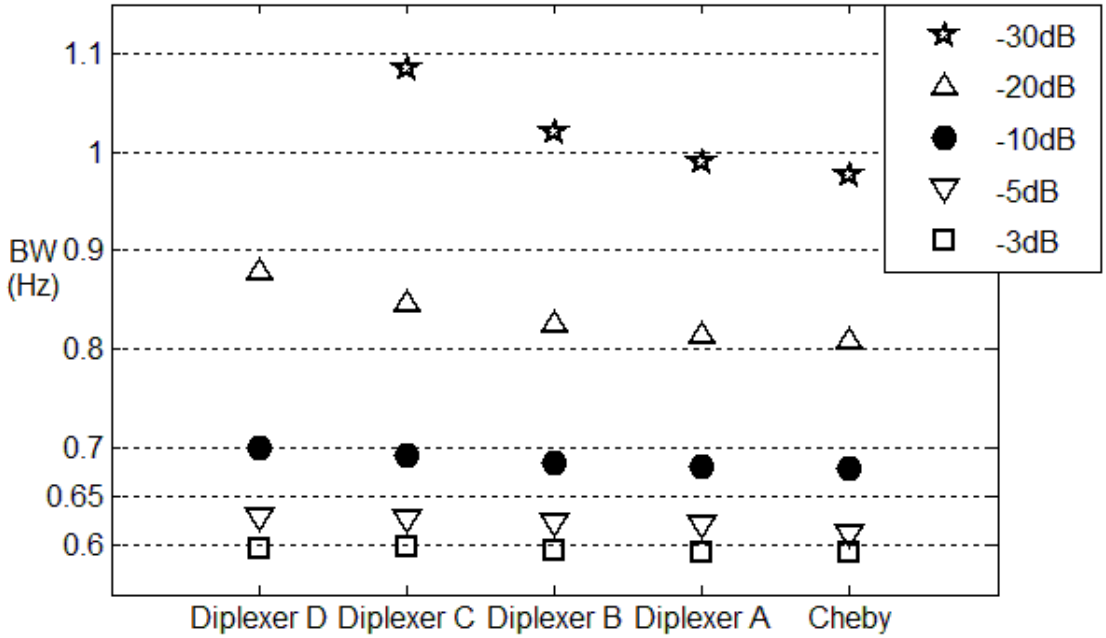

Figure 4.18 Comparison of bandwidth from the diplexers and the equivalent 5th order Chebyshev bandpass filter [1].

A bandwidth comparison between the diplexers and the equivalent 5-th order Chebyshev bandpass filter is given in Figure 4.18. The more resonators on the branches, the closer the response is to the Chebyshev one.

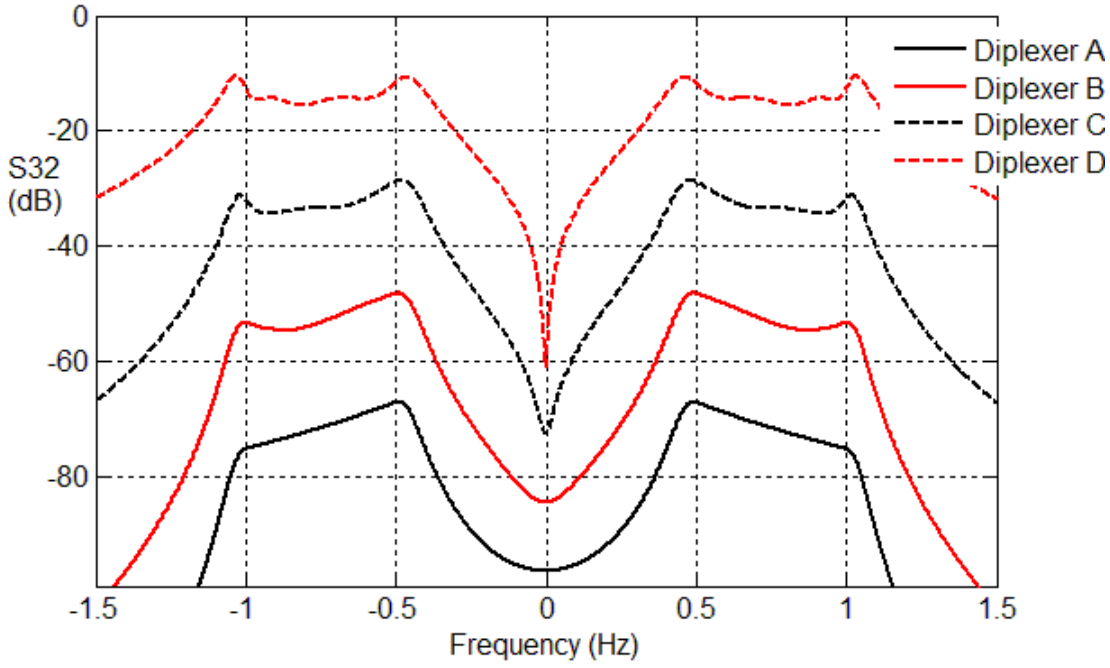

Figure 4.19 Isolations of the prototype diplexers [1].

An isolation comparison of the diplexers is shown in Figure 4.19. The more resonators on the branches, the higher the isolation is.

4.7 Example E: Diplexer with a Different Return Loss of Each Channel

The coupling matrix of a 14-resonator based diplexer has been synthesised. The cut-off frequencies of the low pass prototype are [-1,-0.5] and [0,1], the return loss of S_{11} is 20dB for the left band and 30dB for the right band. The topology of the diplexer is given in Figure 4.20.

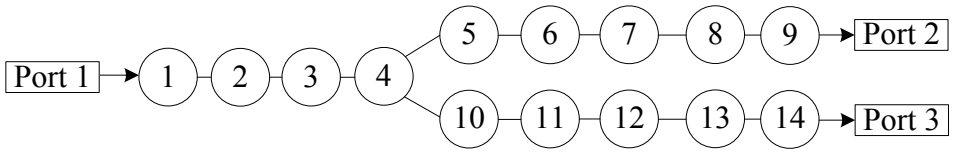

Figure 4.20 Schematic of Diplexer E

The *n*+3 coupling matrix of Diplexer E is given in Table 4.9

Table 4.9 Coupling matrix of Diplexer E

	P1	1	2	3	4	5	6	7	8	9	10	11	12	13	14	P2	P3
P1		x															
1	x		x														
2		x		x													
3			x		x												
4				x		x					x						
5					x	x	x										
6						x	x	x									
7							x	x	x								
8								x	x	x							
9									x	x						x	
10					x						x	x					
11											x	x	x				
12												x	x	x			
13													x	x	x		
14														x	x		x
P2										x							
P3															x		

where x is denoted as the non-zero variables in the matrix.

The initial values of the non-zero entries of the coupling matrix are obtained based on the methodology introduced in Section 4.3. It takes 127.32 seconds to converge to a result at the 300th iteration. The initial values and the optimised ones of the non-zero variables of the coupling matrix are given in Table 4.10.

Table 4.10 The initial values and the optimised ones of the non-zero entries of the coupling matrix of Diplexer E

	$m_{1,2}$	$m_{2,3}$	$m_{3,4}$	$m_{4,5}$	$m_{5,6}$	$m_{6,7}$
initial	0.800	0.600	0.700	0.485	0.305	0.305
optimised	0.822	0.607	0.512	0.542	0.409	0.330
	$m_{7,8}$	$m_{8,9}$	$m_{4,10}$	$m_{10,11}$	$m_{11,12}$	$m_{12,13}$
initial	0.334	0.512	0.210	0.141	0.141	0.150
optimised	0.342	0.515	0.223	0.142	0.141	0.150
	$m_{13,14}$	$m_{1,1}$	$m_{2,2}$	$m_{3,3}$	$m_{4,4}$	$m_{5,5}$
initial	0.208	-0.250	-0.250	-0.250	-0.250	0.100
optimised	0.208	0.164	-0.013	0.089	0.004	0.111
	$m_{6,6}$	$m_{7,7}$	$m_{8,8}$	$m_{9,9}$	$m_{10,10}$	$m_{11,11}$
initial	0.200	0.300	0.400	0.500	-0.550	-0.600
optimised	0.377	0.464	0.481	0.485	-0.725	-0.749
	$m_{12,12}$	$m_{13,13}$	$m_{14,14}$	$m_{P1,1}$	$m_{P2,9}$	$m_{P3,14}$
initial	-0.650	-0.700	-0.750	0.976	0.840	0.498
optimised	-0.750	-0.750	-0.750	0.976	0.840	0.498

where the self-coupling $m_{i,i}<0$ means the resonant frequency f_i of Resonator i is lower than the centre frequency f_c of the circuit ($f_i < f_c$).

The S-parameters of the optimised result are given in Figure 4.21.

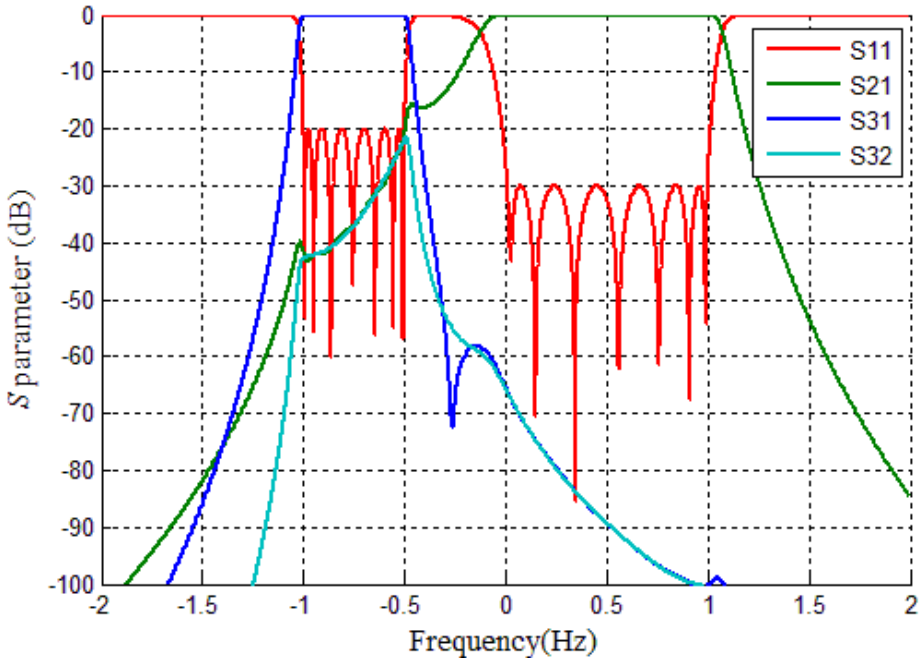

Figure 4.21 Response of Diplexer E

The initial locations and the optimised ones of the reflection zeros Ω_{RZ} of S_{11} is given in Table 4.11

Table 4.11 The initial locations and the optimised ones of Ω_{RZ} of Diplexer E

	Ω_{RZ_1}	Ω_{RZ_2}	Ω_{RZ_3}	Ω_{RZ_4}	Ω_{RZ_5}
initial	-0.9934	-0.9454	-0.8584	-0.75	-0.6416
optimised	-0.9930	-0.9467	-0.8621	-0.7544	-0.6443
	Ω_{RZ_6}	Ω_{RZ_7}	Ω_{RZ_8}	Ω_{RZ_9}	$\Omega_{RZ_{10}}$
initial	-0.5546	-0.5063	0.0126	0.1091	0.2831
optimised	-0.5553	-0.5063	0.0268	0.1486	0.3439
	$\Omega_{RZ_{11}}$	$\Omega_{RZ_{12}}$	$\Omega_{RZ_{13}}$	$\Omega_{RZ_{14}}$	
initial	0.5	0.7169	0.8909	0.9874	
optimised	0.5606	0.7591	0.9092	0.9896	

4.8 Example F: Diplexer with a Different Order of Each Channel

The coupling matrix of a 9-resonator diplexer has been synthesised. The cut-off frequencies

of the lowpass prototype diplexer are [-1, -0.5] and [0.1, 1]. The return loss of S_{11} is 20dB. The topology of the diplexer is shown in Figure 4.22..

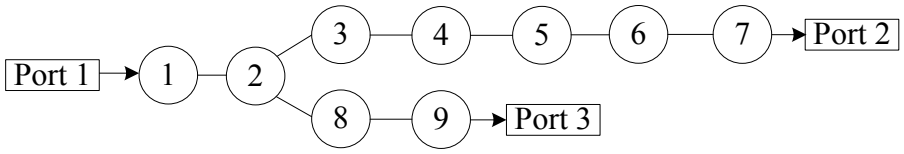

Figure 4.22 Schematic of Diplexer F

The n+3 coupling matrix is shown in Table 4.12.

Table 4.12 Coupling matrix of Diplexer F

	P1	1	2	3	4	5	6	7	8	9	P2	P3
P1		x										
1	x	x	x									
2		x	x	x					x			
3			x	x	x							
4				x	x	x						
5					x	x	x					
6						x	x	x				
7							x	x			x	
8			x						x	x		
9									x	x		x
P2								x				
P3										x		

The initial values of the coupling matrix are obtained based on the methodology in Section 4.3. It takes 43.17 seconds to converge to a result at the 119th iteration. The initial values and the optimised ones of the non-zero entries of the coupling matrix of the diplexer are given in Table 4.13.

Table 4.13 The initial values and the optimised ones of the non-zero entries of the coupling matrix of Diplexer F.

	$m_{1,2}$	$m_{2,3}$	$m_{3,4}$	$m_{4,5}$	$m_{5,6}$	$m_{6,7}$	$m_{2,8}$
initial	0.8	0.4936	0.2751	0.2626	0.2751	0.3797	0.3353
optimised	0.8015	0.4546	0.2900	0.2655	0.2762	0.3804	0.3085
	$m_{8,9}$	$m_{1,1}$	$m_{2,2}$	$m_{3,3}$	$m_{4,4}$	$m_{5,5}$	$m_{6,6}$
initial	0.2579	-0.2	-0.2	0.15	0.25	0.35	0.45
optimised	0.2610	0.0412	-0.0730	0.4213	0.5264	0.5419	0.5457
	$m_{7,7}$	$m_{8,8}$	$m_{9,9}$	$m_{P1,1}$	$m_{P2,7}$	$m_{P3,9}$	
initial	0.54	-0.7	-0.75	0.8639	0.6728	0.5418	
optimised	0.5472	-7007	-0.7391	0.8639	0.6728	0.5418	

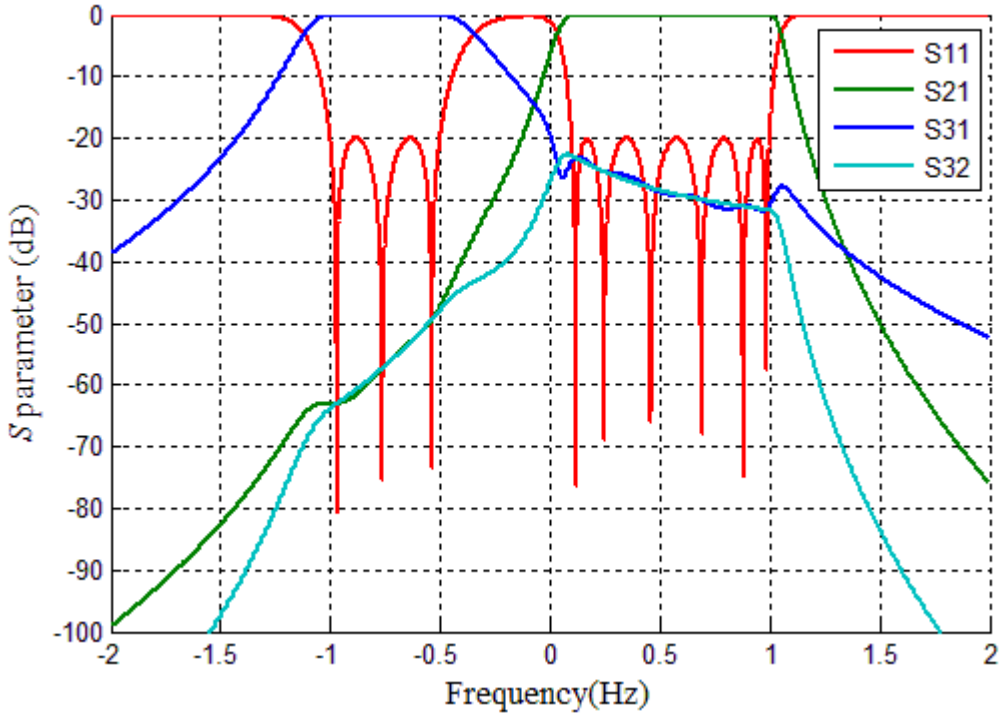

Figure 4.23 Response of Diplexer F

The response of Diplexer F is shown in Figure 4.23. The initial locations and the optimised ones of the reflection zeros of S_{11} are given in Table 4.14.

Table 4.14 The initial locations and the optimised ones of the relection zeros of Diplexer F.

	Ω_{RZ_1}	Ω_{RZ_2}	Ω_{RZ_3}	Ω_{RZ_4}	Ω_{RZ_5}
initial	-0.9666	-0.75	-0.5334	0.1153	0.2319
optimised	-0.9696	-0.7625	-0.5369	0.1176	0.2474
	Ω_{RZ_6}	Ω_{RZ_7}	Ω_{RZ_8}	Ω_{RZ_9}	
initial	0.4334	0.6666	0.8682	0.9847	
optimised	0.4596	0.6893	0.8801	0.9857	

4.9 Example G: Contiguous Channel Diplexer

A 16–resonator diplexer has been synthesised. The cut-off frequencies of the low-pass prototype diplexer are [-1, -0.5] and [-0.5, 1]. The return loss of S_{11} is 20 dB. The topology of the diplexer is given in Figure 4.24.

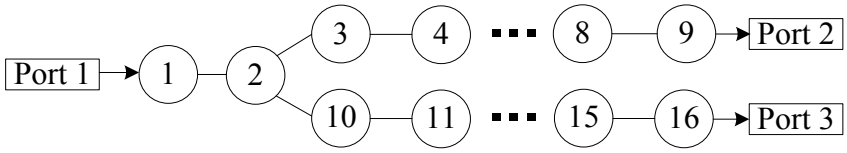

Figure 4.24 Schematic of Diplexer G

The initial values of the coupling matrix are obtained by the methodology introduced in Section 4.3. It takes 354.37 seconds to converge to a result at the 1209th iteration. Both the initial values and the optimised ones of the non-zero entries of the coupling matrix are given in Table 4.15.

Table 4.15 The initial values and the optimised ones of the non-zero entries of the coupling matrix of Diplexer G.

	$m_{1,2}$	$m_{2,3}$	$m_{3,4}$	$m_{4,5}$	$m_{5,6}$	$m_{6,7}$	$m_{7,8}$
initial	0.8000	0.8641	0.4439	0.4154	0.4095	0.4154	0.4439
optimised	0.8187	0.5209	0.4269	0.4054	0.4032	0.4123	0.4430
	$m_{8,9}$	$m_{2,10}$	$m_{10,11}$	$m_{11,12}$	$m_{12,13}$	$m_{13,14}$	$m_{14,15}$
initial	0.6172	0.2880	0.1480	0.1385	0.1365	0.1385	0.1480
optimised	0.6226	0.2620	0.1379	0.1297	0.1297	0.1325	0.1418
	$m_{15,16}$	$m_{1,1}$	$m_{2,2}$	$m_{3,3}$	$m_{4,4}$	$m_{5,5}$	$m_{6,6}$
initial	0.2057	-0.5	-0.5	-0.05	0.000	0.05	0.1
optimised	0.1968	0.0158	0.0070	0.2004	0.2475	0.2523	0.2531
0	$m_{7,7}$	$m_{8,8}$	$m_{9,9}$	$m_{10,10}$	$m_{11,11}$	$m_{12,12}$	$m_{13,13}$
initial	0.15	0.2	0.25	-0.45	-0.5	-0.55	-0.6
optimised	0.2535	0.2526	0.2539	-0.7451	-0.7685	-0.7643	-0.7615
	$m_{14,14}$	$m_{15,15}$	$m_{16,16}$	$m_{P1,1}$	$m_{P2,9}$	$m_{P3,16}$	
initial	-0.65	-0.7	-0.75	1.0085	0.8587	0.4958	
optimised	-0.7604	-0.7604	-0.7607	1.0000	0.8748	0.4845	

The response of Diplexer G is shown in Figure 4.25.

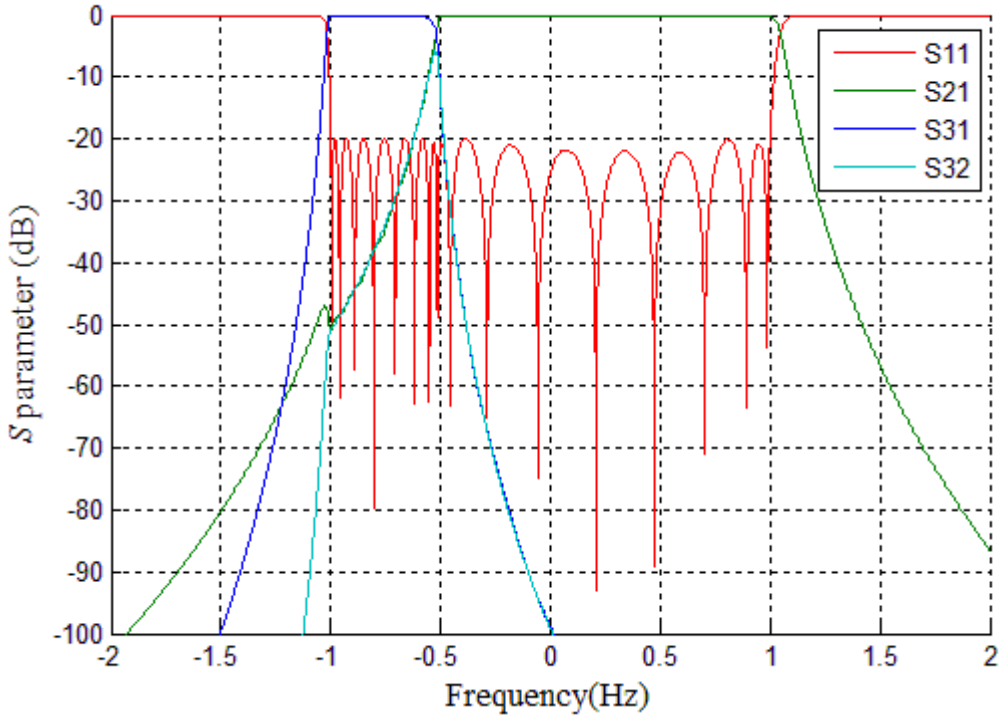

Figure 4.25 Response of Example G

The initial locations and the optimised ones of the reflection zeros of S_{11} are given in Table 4.16.

Table 4.16 The initial locations and the optimised ones of the reflection zeros.

	Ω_{RZ_1}	Ω_{RZ_2}	Ω_{RZ_3}	Ω_{RZ_4}	Ω_{RZ_5}	Ω_{RZ_6}
initial	-0.9952	-0.9579	-0.8889	-0.7988	-0.7012	-0.6111
optimised	-0.9954	-0.9593	-0.8923	-0.8040	-0.7076	-0.6186
	Ω_{RZ_7}	Ω_{RZ_8}	Ω_{RZ_9}	$\Omega_{RZ_{10}}$	$\Omega_{RZ_{11}}$	$\Omega_{RZ_{12}}$
initial	-0.5421	-0.5048	-0.4858	-0.3736	-0.1666	0.1038
optimised	-0.5521	-0.5147	-0.4558	-0.2892	-0.0566	0.2072
	$\Omega_{RZ_{13}}$	$\Omega_{RZ_{14}}$	$\Omega_{RZ_{15}}$	$\Omega_{RZ_{16}}$		
initial	0.3962	0.6666	0.8736	0.9858		
optimised	0.4728	0.7018	0.8925	0.9867		

4.10 Example H: Triplexer

The coupling matrix of an 18-resonator triplexer has been synthesised. The cut-off frequencies of the lowpass prototype triplexer are [-1, -0.5], [-0.25, 0.25] and [-0.5, 1]. The return loss of S_{11} is 20dB. The topology of the triplexer is shown in Figure 4.26.

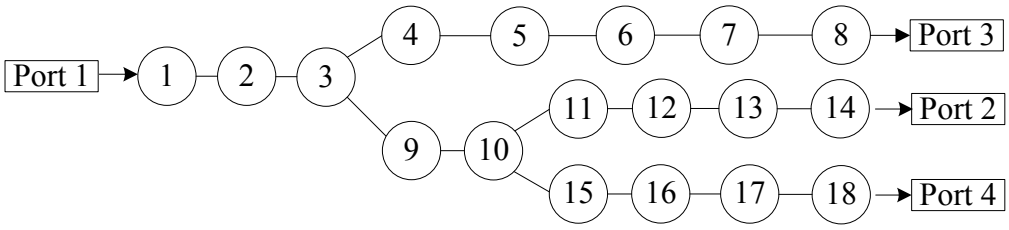

Figure 4.26 Schematic of the triplexer.

Port 2 is for the higher band, Port 3 is for the middle band and Port 4 is for the lower band. It takes 119.65 seconds to converge to a result at the 407th iteration. The initial values and the optimised ones of the coupling matrix of the triplexer are given in Table 4.17.

Table 4.17 The initial values and the optimised ones of the coupling matrix of the triplexer.

	$m_{1,2}$	$m_{2,3}$	$m_{3,4}$	$m_{4,5}$	$m_{5,6}$	$m_{6,7}$	$m_{7,8}$
initial	0.8000	0.6000	0.2531	0.1528	0.1459	0.1528	0.2109
optimised	0.7647	0.5647	0.2750	0.1554	0.1456	0.1527	0.2108
	$m_{3,9}$	$m_{9,10}$	$m_{10,11}$	$m_{11,12}$	$m_{12,13}$	$m_{13,14}$	$m_{10,15}$
initial	1.1200	0.3500	0.2140	0.1459	0.1528	0.2109	0.2140
optimised	0.4313	0.6632	0.2435	0.1522	0.1546	0.2118	0.2435
	$m_{15,16}$	$m_{16,17}$	$m_{17,18}$	$m_{1,1}$	$m_{2,2}$	$m_{3,3}$	$m_{4,4}$
initial	0.1459	0.1528	0.2109	0	0	0	0
optimised	0.1522	0.1546	0.2118	0	0	0	0
	$m_{5,5}$	$m_{6,6}$	$m_{7,7}$	$m_{8,8}$	$m_{9,9}$	$m_{10,10}$	$m_{11,11}$
initial	0	0	0	0	0	0	0.6000
optimised	0	0	0	0	0	0	0.6963
	$m_{12,12}$	$m_{13,13}$	$m_{14,14}$	$m_{15,15}$	$m_{16,16}$	$m_{17,17}$	$m_{18,18}$
initial	0.6500	0.7000	0.7500	-0.6000	-0.6500	-0.7000	-0.7500
optimised	0.7391	0.7444	0.7454	-0.6963	-0.7391	-0.7444	-0.7454

	$m_{P1,1}$	$m_{P2,14}$	$m_{P3,8}$	$m_{P4,18}$
initial	0.8686	0.5015	0.5015	0.5015
optimised	0.8686	0.5015	0.5015	0.5015

The responses of the triplexer is shown in Figure 4.27.

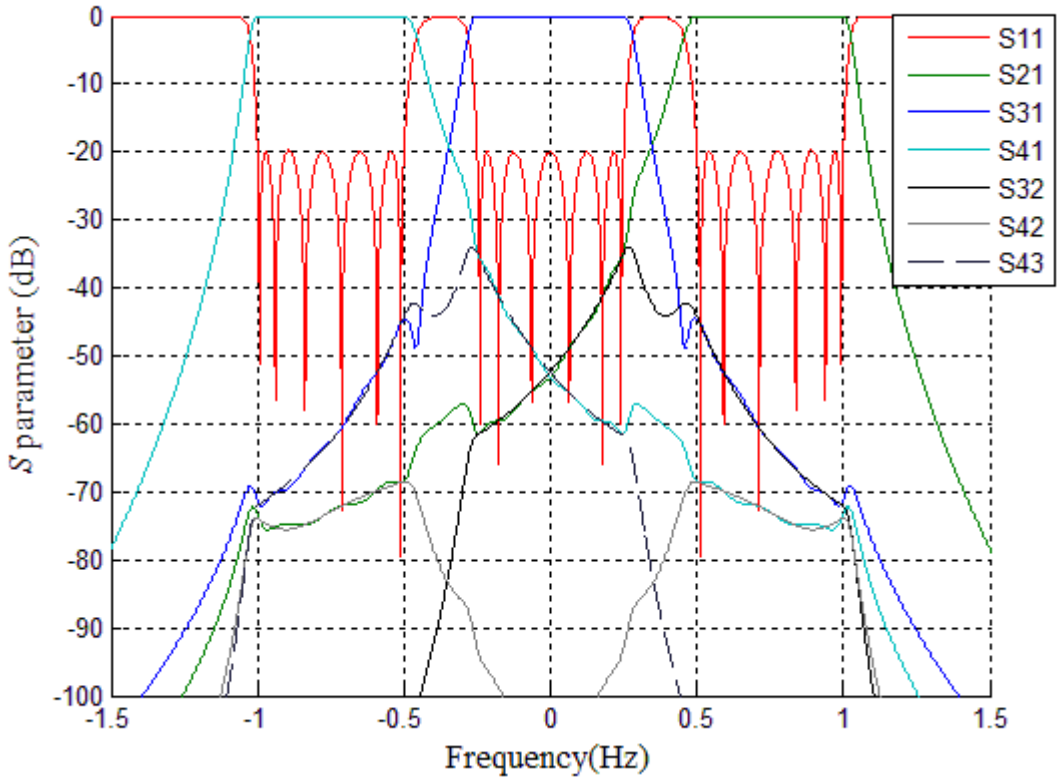

Figure 4.27 Response of the triplexer

The initial locations and the optimised ones of the reflection zeros of S_{11} are given in Table 4.18.

Table 4.18 The initial locations and the optimised ones of the reflection zeros of S_{11}.

	Ω_{RZ_1}	Ω_{RZ_2}	Ω_{RZ_3}	Ω_{RZ_4}	Ω_{RZ_5}	Ω_{RZ_6}
initial	-0.9915	-0.9267	-0.8148	-0.6852	-0.5733	-0.5085
optimised	-0.9925	-0.9388	-0.8380	-0.7129	-0.5909	-0.5112
	Ω_{RZ_7}	Ω_{RZ_8}	Ω_{RZ_9}	$\Omega_{RZ_{10}}$	$\Omega_{RZ_{11}}$	$\Omega_{RZ_{12}}$
initial	-0.2415	-0.1767	-0.0648	0.0648	0.1767	0.2415
optimised	-0.2415	-0.1767	-0.0645	0.0645	0.1767	0.2415
	$\Omega_{RZ_{13}}$	$\Omega_{RZ_{14}}$	$\Omega_{RZ_{15}}$	$\Omega_{RZ_{16}}$	$\Omega_{RZ_{17}}$	$\Omega_{RZ_{18}}$
initial	0.5085	0.5733	0.6852	0.8148	0.9267	0.9915
optimised	0.5112	0.5909	0.7129	0.8380	0.9388	0.9925

[1] W. Xia, X. Shang, and M. J. Lancaster., "Responses comparisons for coupled-resonator based diplexers," in *Passive RF and Microwave Components, 3rd Annual Seminar on*, 2012, pp. 67-75.

[2] X. Shang, Y. Wang, G. L. Nicholson, and M. J. Lancaster, "Design of multiple-passband filters using coupling matrix optimisation," *Microwaves, Antennas & Propagation, IET,* vol. 6, pp. 24-30, 2012.

[3] G. B. Arfken and H. J. Weber, *Mathematical Methods for Physicists: A Comprehensive Guide*: Elsevier Science, 2011.

[4] *MATLAB 10 user's guide (online)*. Available: http://www.mathworks.com

Chapter 5 Diplexer Implementation

The coupling matrix can be applied to any types of coupled resonator circuit regardless of its physical structure [1]. The work presented here is to realise the coupling matrix in the form of the rectangular waveguide circuit. Some of the waveguide components are introduced in Section 5.1. For the coupled-resonator circuit based on the rectangular waveguides, the design procedure is in four steps. The first step is to synthesis the coupling matrix [m] of the device meeting the desired specifications. A local optimisation algorithm, which is one of the synthesis methods, has been discussed in the previous chapters. The second step is to extract the initial dimensions of each waveguide component of the device using the EM simulator. The initial dimensions of the components are based on the values of the synthesised matrix [m]. How to extract the initial dimensions is discussed in Section 5.2. After putting all the initial components together, the third step is to optimise the whole physical structure in the EM simulator so as to meet the desired specifications. After the completion of the overall structure optimisation on the EM simulator, the last step is to fabricate the device and measure its responses by the Vector Network Analyser (VNA). If the measured response is far from its simulated counterpart, additional tuning work may be required to improve the measured results.

In Section 5.3, a coupled-resonator rectangular waveguide based X-band diplexer is manufactured, measured and tuned. A further improvement on the simulation of the device has been made by using a new structure optimising technique, the Step Tune method. The procedures of the Step Tune method is given in Section 5.4.

5.1 Introduction of the Rectangular Cavity Resonator and Coupling Iris

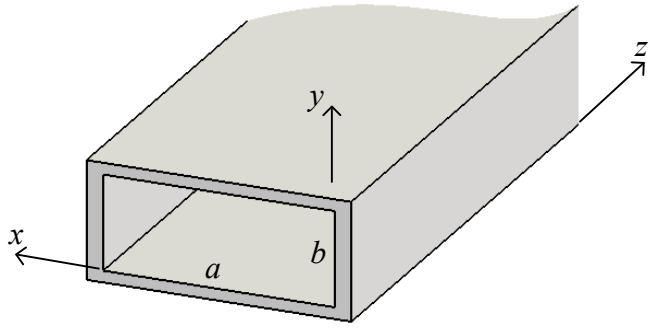

Figure 5.1 Rectangular waveguide illustration

The rectangular waveguide, as shown in Figure 5.1, is a hollow metallic pipe guiding electromagnetic waves. It is one of the distributed elements widely used. By varying the shape of the rectangular waveguide, it can work as a cavity resonator or as a coupling iris to construct the filtering circuit.

5.1.1 Cut-Off Frequency f_{cutoff} of the TE Mode and TM Mode

The cut-off frequency is the lowest frequency which a mode can propagate through the rectangular waveguide. TE waves can propagate through the waveguide[2]. The cut-off frequency f_{cutoff} of each TE mode is given by

$$f_{cutoff} = \frac{c}{2}\sqrt{(\frac{m}{a})^2 + (\frac{n}{b})^2} \tag{5.1}$$

Where m and n is the number of half standing waves along x axis and y axis of the rectangular waveguide, c is the speed of light in vacuum.

The mode with the lowest cut-off frequency is called the dominant mode. Conventionally, for the standard rectangular waveguide, the width a is twice as big as the height b. According to (5.1), the lowest frequency is achieved when m=1 and n=0 (i.e. TE_{10} is the dominant mode of

the rectangular waveguide).

5.1.2 Cavity Resonator and Resonant Frequency

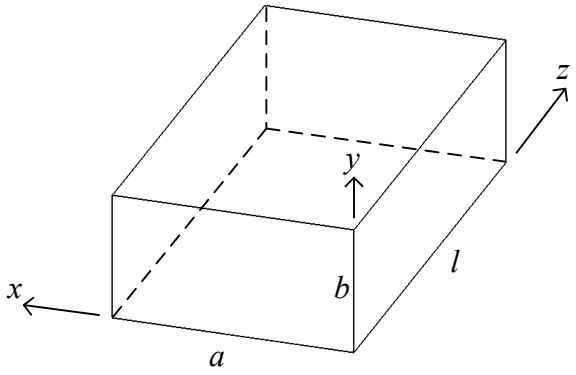

Figure 5.2 Inner sight of a cavity resonator

As shown in Figure 5.2, a cavity resonator is a rectangular waveguide enclosed by a conducting wall at each end. The length of a cavity resonator l is multiple of half-guided wavelength λ_g at the resonant frequency. For dominant mode (TE_{10}), the guided wavelength λ_g is given by (5.2)

$$\lambda_g = \frac{2ac}{\sqrt{4a^2 f^2 - c^2}} \tag{5.2}$$

where f is the mode frequency, a is the width of the rectangular waveguide, c is the speed of light in vacuum.

5.1.3 Coupling Iris

Coupling iris is one type of discontinuity between two rectangular waveguides and is used for coupling.

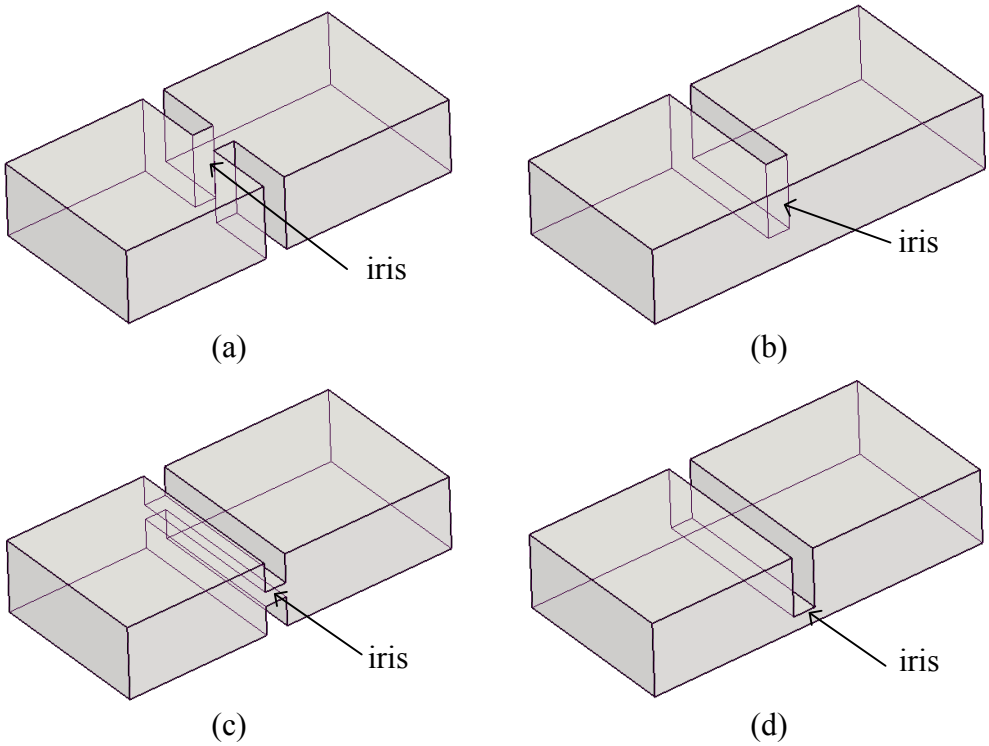

Figure 5.3 Inner views of the rectangular waveguide with different types of coupling irises

Some standard irises are illustrated in Figure 5.3. The iris with vertical slot in Figure 5.3(a) and (b) are the inductive irises. The iris with horizontal slot in (c) and (d) are the capacitive irises.

5.2 Extraction of External Quality Factor Q_e and Coupling Coefficients

To convert the coupling matrix [*m*] into the waveguide form, we need to find the relationship between the values of the matrix entries and the related dimensions of the waveguide components.

5.2.1 Extraction of the External Quality Factor Q_e

Q_{unload} is defined as the ratio of the energy stored and power lost in the reactive element per unit time. The description is given as:

$$Q_{unload} = \omega \frac{\text{Energy stored in the resonator}}{\text{Average power lost}} \tag{5.3}$$

The unloaded quality factor Q_{unload} of a cavity resonator may come from the conductor loss of the cavity wall Q_c, the dielectric Q_d and any radiation Q_r. If the cavity is coupled to a source and a load, the loaded quality factor Q_l is formulated as

$$\frac{1}{Q_l} = \frac{1}{Q_{unload}} + \frac{1}{Q_e} = \left(\frac{1}{Q_c} + \frac{1}{Q_d} + \frac{1}{Q_r}\right) + \frac{1}{Q_e} \tag{5.4}$$

Where Q_e is the external quality factor of the cavity. Q_l can be measured from the $S_{2,1}$ of a single resonator as shown in Figure 5.4. Q_l is formulated as

$$Q_l = \frac{f_c}{BW} \tag{5.5}$$

Where BW is the 3dB bandwidth and f_c is the resonant frequency.

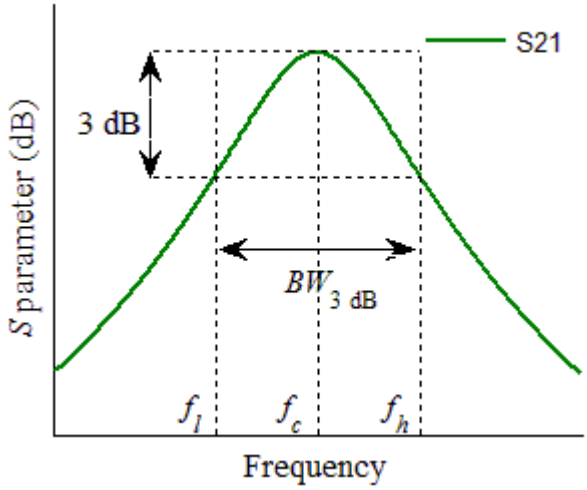

Figure 5.4 $S_{2,1}$ magnitude in dB of a single resonator

To extract Q_e from Q_l, we need to simplify (5.4). There will be no dielectric loss in the waveguide cavity since no dielectric material is used. So $Q_d \to \infty$. As no radiation slots exist, no energy is radiated from the cavity. So $Q_r \to \infty$. For perfect electric conductor simulated

on the EM simulators, the conductor loss can be ignored. So $Q_c \to \infty$. Substituting (5.5) into (5.4), the equation is simplified as

$$\frac{1}{Q_l} = \frac{f_c}{BW} = \frac{1}{Q_e} \tag{5.6}$$

or

$$Q_l = Q_e = \frac{BW}{f_c} \tag{5.7}$$

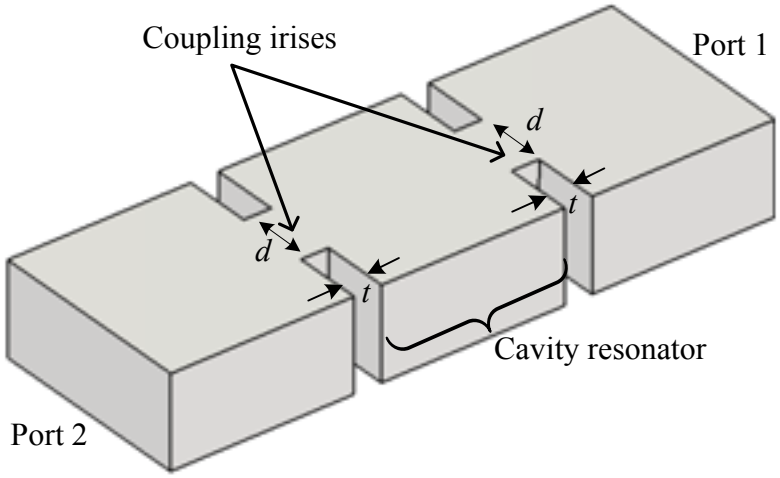

Figure 5.5 A doubly loaded rectangular waveguide resonator. *d* and *t* is the width and thickness of the iris.

In this work, the inductive irises are chosen as the coupling components of the devices. The topology of a doubly loaded waveguide resonator with inductive irises is given in Figure 5.5. Two coupling irises are symmetric to each other. According to [1], the external quality factor of each iris Q_{e_iris} is

$$Q_{e\_iris} = 2 \times Q_e \tag{5.8}$$

Substituting (5.7) into (5.8), we have

$$Q_{e\_iris} = 2 \times Q_l \tag{5.9}$$

Keeping the iris thickness t as 2mm and varying the width d, we can get a set of Q_{e_iris}. Using EM simulator, the relationship between the iris width d and Q_{e_iris} is presented in Figure 5.6

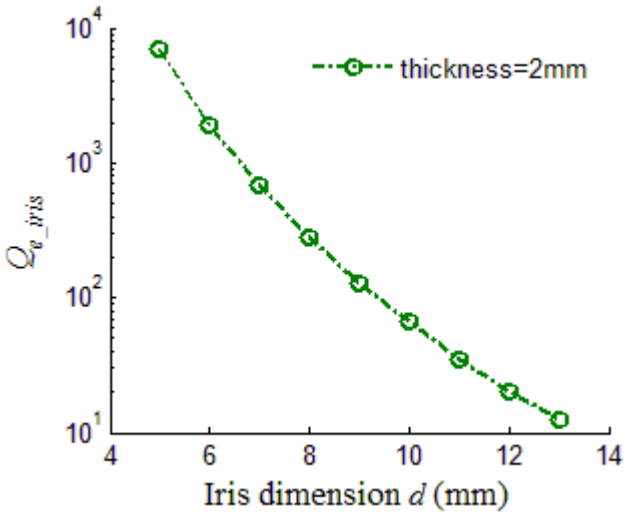

Figure 5.6 The relationship between iris dimensions d and Q_{e_iris}

As shown in Figure 5.6, Q_{e_iris} gets smaller by increasing the width d of the iris. Using (3.67), the external quality factor Q_e can be turned into the external coupling coefficient M_{Pi} for the n+X coupling matrix.

5.2.2 Extraction of the Internal Coupling Coefficient

The internal coupling coefficient between resonators could be an electric, a magnetic or a mixed coupling. The coupled resonators are synchronously tuned if their resonant frequencies are the same, or asynchronously tuned when the coupled resonators have different resonant frequencies.

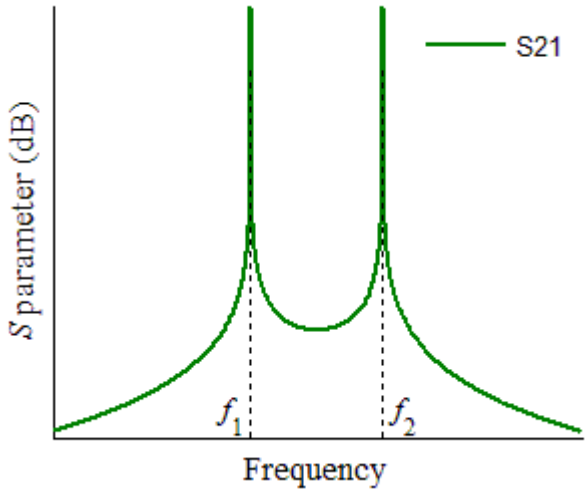

Figure 5.7 $S_{2,1}$ magnitude in dB of the coupled resonators

Figure 5.7 shows the $S_{2,1}$ of the two coupled resonators, f_1 and f_2 are noted as the frequencies of two peaks. The coupling coefficient is denoted as k and can be obtained from the universal formulation as [1]

$$k = \pm\frac{1}{2}\left(\frac{f_{02}}{f_{01}}+\frac{f_{01}}{f_{02}}\right)\sqrt{\left(\frac{f_2^2-f_1^2}{f_2^2+f_1^2}\right)^2-\left(\frac{f_{02}^2-f_{01}^2}{f_{02}^2+f_{01}^2}\right)^2} \tag{5.10}$$

where, f_{01} and f_{02} are the resonant frequencies of each uncoupled resonator.

When the coupled resonators are synchronously tuned (i.e. $f_{01} = f_{02}$), (5.10) is simplified as [1]

$$k = \frac{f_2^2-f_1^2}{f_2^2+f_1^2} \tag{5.11}$$

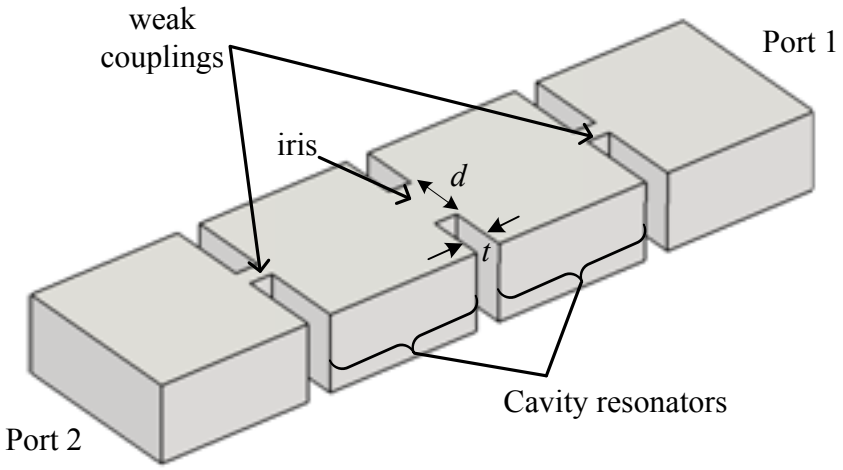

Figure 5.8 Two magnetically coupled resonators with weak external couplings.

A structure of extracting internal coupling coefficient k is given in Figure 5.8. Two resonators are symmetric to each other so that they are synchronously tuned. By altering the width d of the iris between the two cavities, a set of k_{iris} can be obtained in a simulator and by using (5.11). The relationship between d and k_{iris} is given in Figure 5.9.

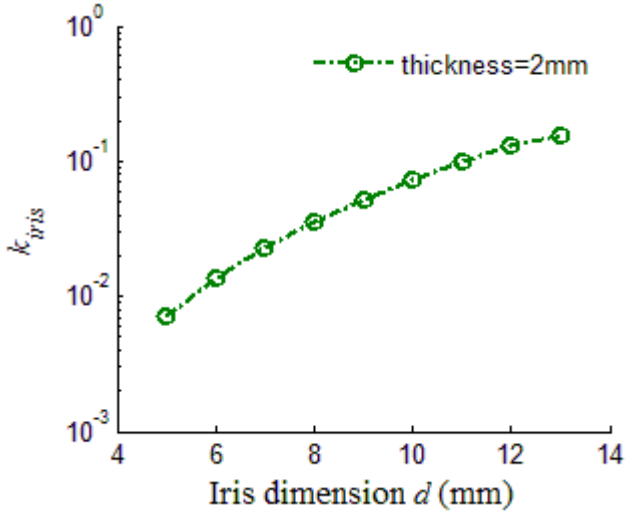

Figure 5.9 The relationship between iris dimensions d and k_{iris}

For asynchronously tuned resonators, when the ratio of two resonant frequencies f_{01} and f_{02} is within a small range ($f_{02}/f_{01} < 1.1, f_{02} \geq f_{01}$), the asynchronously tuning has very little effect on the value of the internal coupling coefficient [3]. So the topology in Figure 5.9 can be

applied to extract the internal coupling of the asynchronously tuned resonators.

5.2.3 Extraction of the Self Coupling $m_{i,i}$

The length l of the cavity resonator is generally half of the guided wavelength λ_g of the resonant frequency. The equation is given as

$$l = \frac{\lambda_g}{2} \tag{5.12}$$

For the synchronously tuned device, the self coupling $m_{i,i}$ equals to 0. Resonator i is oscillating at the centre frequency f_0 of the device. For the dominant mode, according to (5.2) and (5.13), the cavity length l_i of the synchronously tuned resonator i is obtained as:

$$l_i = \frac{\lambda_g}{2} = \frac{ac}{\sqrt{4a^2 f_0^2 - c^2}} \tag{5.13}$$

where c is the light speed in vacuum, a is the width of the rectangular waveguide.

For the asynchronously tuned device, not all the resonators are resonating at the centre frequency f_0 of the device. Resonator i is asynchronously tuned when the coupling matrix of the device [m] has an non-zero diagonal entry $m_{i,i}$,. The relationship between the resonant frequency f_i and the self-coupling $m_{i,i}$ of resonator i are given in (3.63). According to (3.63) and (5.13), the cavity length l_i of the asynchronously tuned resonator i is obtained as:

$$\begin{aligned} l_i &= \frac{\lambda_g}{2} = \frac{ac}{\sqrt{4a^2 f_i^2 - c^2}} \\ &= \frac{ac}{\sqrt{4a^2 f_0^2 \left(\frac{FBW \cdot m_{i,i}}{2} + \sqrt{\left(\frac{FBW \cdot m_{i,i}}{2} \right)^2 + 1} \right)^2 - c^2}} \end{aligned} \tag{5.14}$$

5.3 Example A: 10th Order Diplexer with no Cross-Coupling

5.3.1 The Specifications and Optimised Coupling Matrix of the Diplexer

A 10-resonator rectangular waveguide diplexer working at X-band has been designed, fabricated and tested. The specifications of the diplexer are: the centre frequency f_c=10GHz, the fractional bandwidth FBW=0.1, the bandwidth of each passband is 350MHz. The return loss of S_{11} is 20 dB.

The cut-off frequencies of the lowpass prototype of the diplexer are denoted as $[\Omega_1, \Omega_2]$ for the left passband and $[\Omega_3, \Omega_4]$ for the right passband. According to the specifications, the cut-off frequencies of the diplexer prototype are obtained as

$$\Omega_3 = -\Omega_2 = \frac{\left(\frac{1}{2} f_c \cdot FBW\right) - BW_{\text{each passband}}}{\frac{1}{2} f_c \cdot FBW} = \frac{\frac{1}{2} \cdot 10\text{GHz} \cdot 0.1 - 350\text{MHz}}{\frac{1}{2} \cdot 10\text{GHz} \cdot 0.1} = 0.3 \qquad (5.15)$$

$$\Omega_4 = -\Omega_1 = 1$$

So the set of cut-off frequencies of the diplexer prototype is $[\Omega_1, \Omega_2, \Omega_3, \Omega_4] = [-1, -0.3, 0.3, 1]$. The desired topology of the diplexer is given in Figure 5.10. Port 2 works on the right passband while Port 3 is for the left passband.

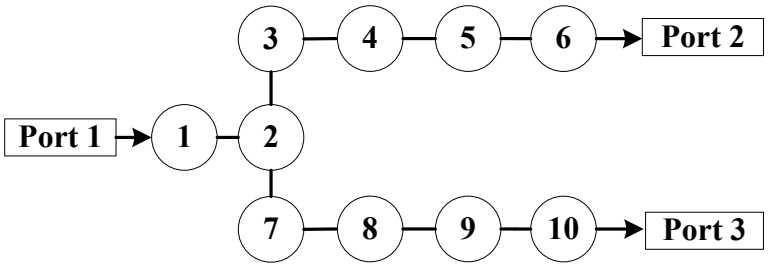

Figure 5.10 Schematic of the 10-resonator diplexer

The diplexer in n+3 coupling matrix is of the form:

	P1	1	2	3	4	5	6	7	8	9	10	P2	P3
P1		x											
1	x	x	x										
2		x	x	x				x					
3			x	x	x								
4				x	x	x							
5					x	x	x						
6						x	x					x	
7			x					x	x				
8								x	x	x			
9									x	x	x		
10										x	x		x
P2							x						
P3											x		

(5.16)

where $m_{P1,1} = 1/\sqrt{q_{e1}}$, $m_{P2,6} = m_{P3,10} = 1/\sqrt{q_{e2}}$. After the optimisation, the values of each entry are given in Table 5.1

Table 5.1 Coupling values of the 10th order diplexer.

	$m_{1,2}$	$m_{2,3}$	$m_{3,4}$	$m_{4,5}$	$m_{5,6}$	$m_{2,7}$	$m_{7,8}$
optimised	0.8	0.3648	0.2290	0.2238	0.3036	0.3648	0.2290
	$m_{8,9}$	$m_{9,10}$	$m_{1,1}$	$m_{2,2}$	$m_{3.3}$	$m_{4,4}$	$m_{5,5}$
optimised	0.2238	0.3036	0	0	0.5727	0.6373	0.6449

	$m_{6,6}$	$m_{7,7}$	$m_{8,8}$	$m_{9,9}$	$m_{10,10}$	q_{e1}	q_{e2}	q_{e3}
optimised	0.6465	-0.5727	-0.6373	-0.6449	-0.6465	1.388	2.775	2.775

The response of the diplexer using the normalised lowpass responses is given in Figure 5.11.

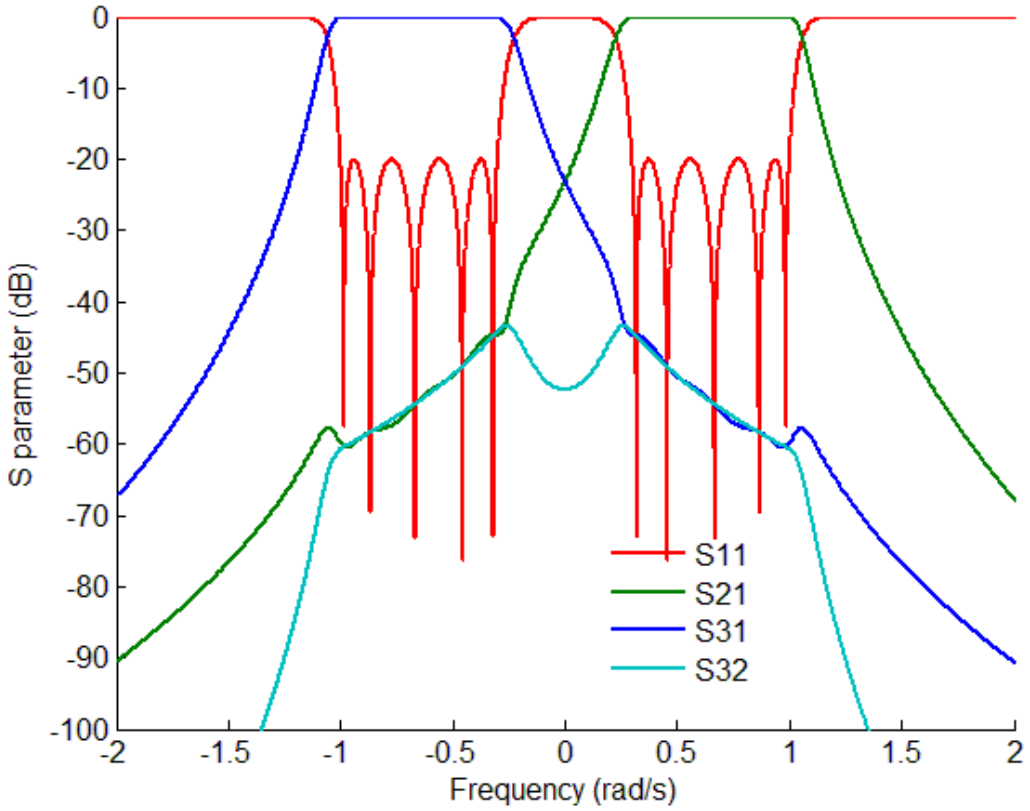

Figure 5.11 The diplexer with normalised response

The lowpass prototype diplexer is transformed to the desired response with f_c=10GHz, FBW= 0.1. According to (3.67) and (3.69), the entry values after the frequency transformation are given in Table 5.2

Table 5.2 Coupling values after the frequency transformation

	$M_{1,2}$	$M_{2,3}$	$M_{3,4}$	$M_{4,5}$	$M_{5,6}$	$M_{2,7}$	$M_{7,8}$
optimised	0.08	0.0365	0.0229	0.0224	0.0304	0.0365	0.0229
	$M_{8,9}$	$M_{9,10}$	$M_{1,1}$	$M_{2,2}$	$M_{3.3}$	$M_{4,4}$	$M_{5,5}$
optimised	0.0224	0.0304	0	0	0.0573	0.0637	0.0645

	$M_{6,6}$	$M_{7,7}$	$M_{8,8}$	$M_{9,9}$	$M_{10,10}$	Q_{e1}	Q_{e2}	Q_{e3}
optimised	0.0647	-0.0573	-0.0637	-0.0645	-0.0647	13.88	27.75	27.75

The S-parameters after frequency transformation is shown in Figure 5.12.

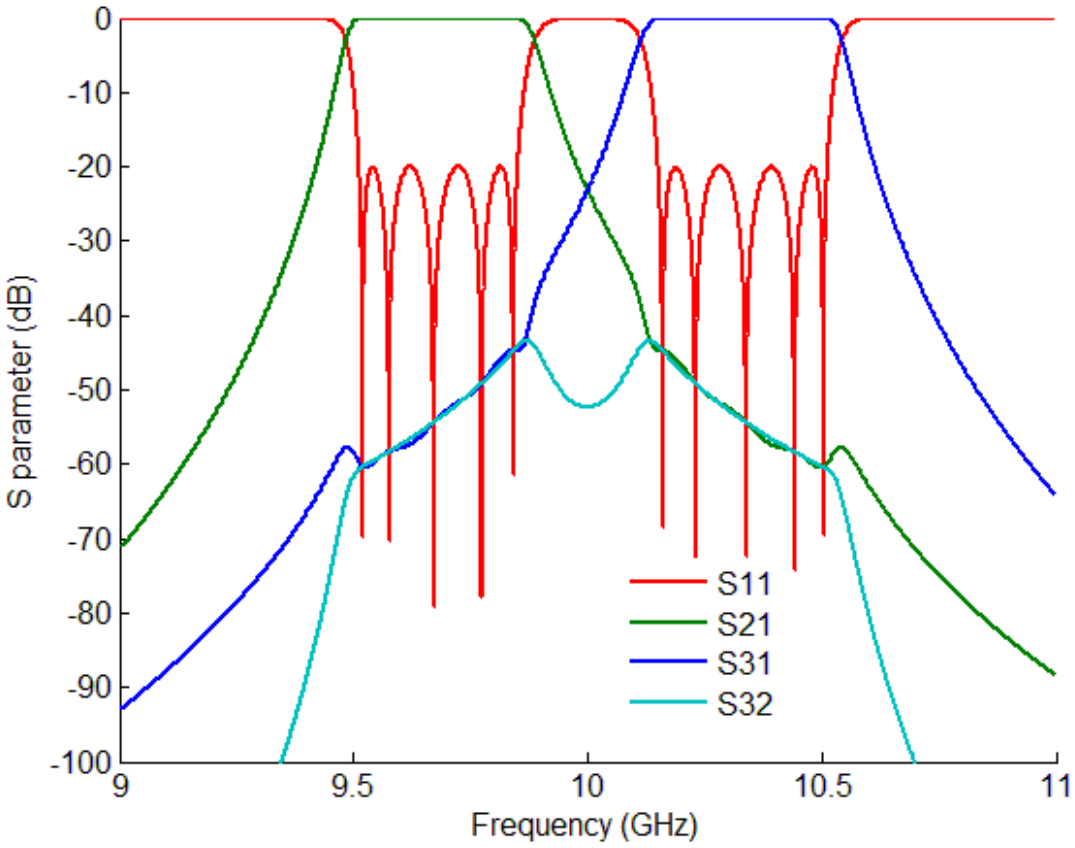

Figure 5.12 S-parameter of the diplexer after frequency transformation

5.3.2 Physical Structure of the Diplexer

To make the device more compact, the resonators of the diplexer are coupled not in a straight line but in a zigzag way as shown in Figure 5.13.

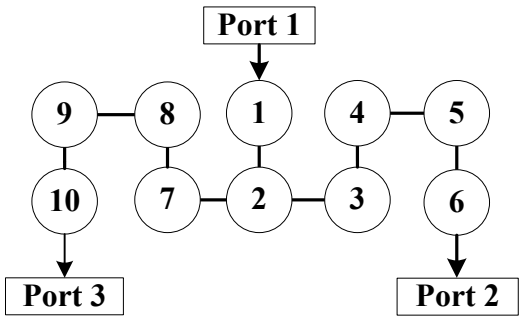

Figure 5.13 Structure of the 10-resonator diplexer in a zigzag topology

In order to facilitate the CNC milling, an H-plane topology with all inductive irises is chosen. The top view of the diplexer in rectangular waveguide is given in Figure 5.14. A 3D structure

is in Figure 5.15.

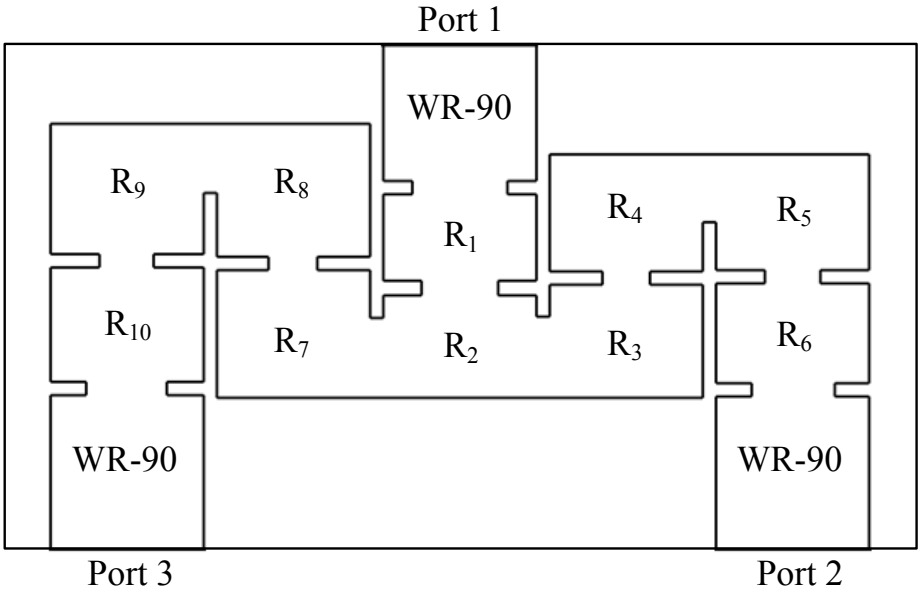

Figure 5.14 Top view of the diplexer. R_1 to R_{10} are the cavity resonators. WR-90 refers to the transmission line between the port and coupled resonator.

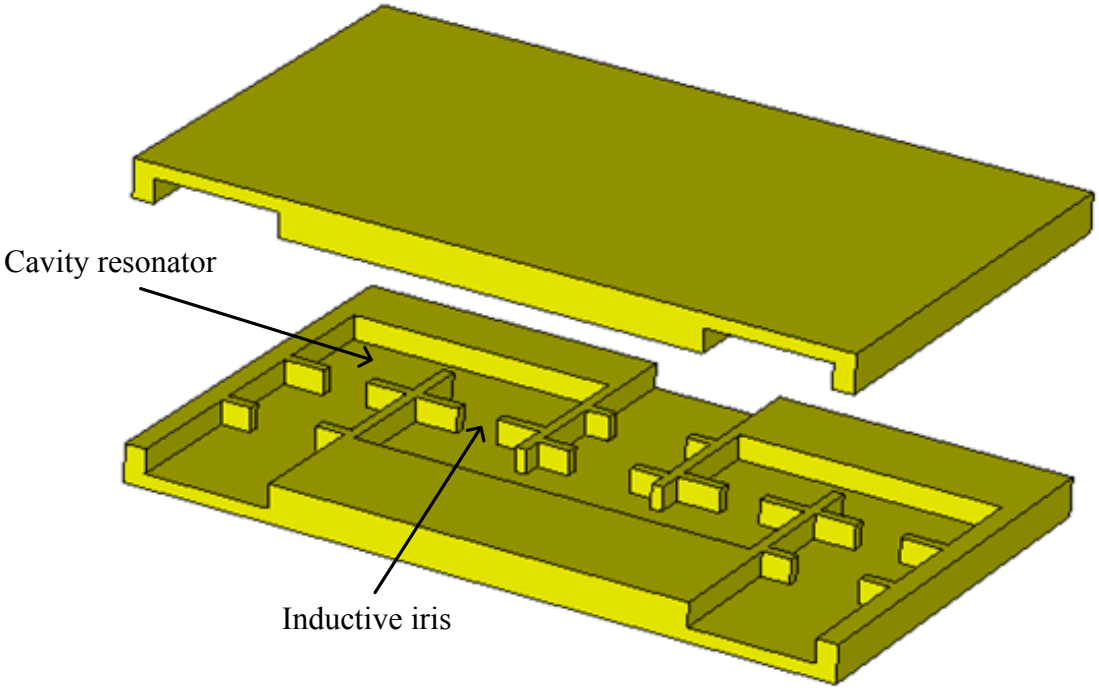

Figure 5.15 3D structure of the diplexer

The next step is to find out the dimensions of each iris and resonator of the diplexer. The methodology of obtaining initial dimensions has been discussed in Section 5.2. CST, one of

the EM simulators, has been utilised to extract the initial dimensions of the waveguide components.

5.3.3 Overall Structure Optimisation

After putting all the components together with the initial dimensions, further optimization, using CST frequency domain solver, on the overall structure is applied to meet the specifications. Both the width *d* of the irises and the length *l* of the cavity resonators are tuned. The optimized simulating responses before manufacturing are plotted in Figure 5.16.

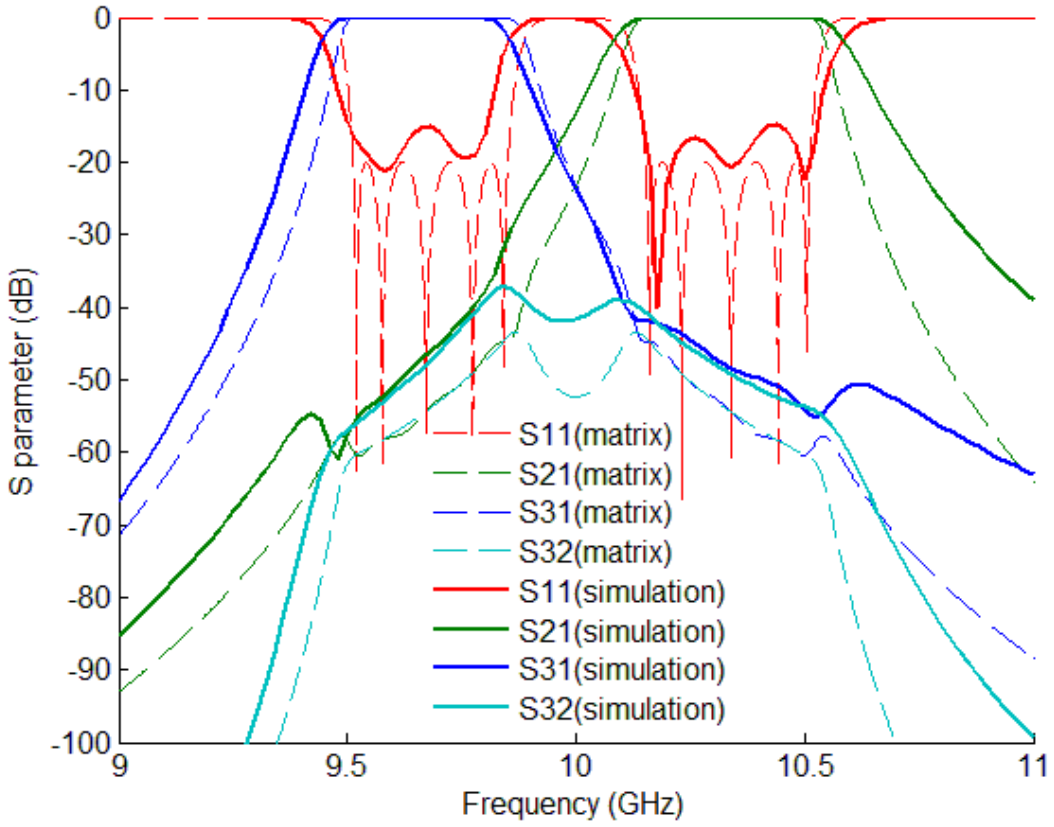

Figure 5.16 Responses comparison between the optimised simulation and the matrix calculation.

The notations and values of the physical dimensions of the fabricated 10th order diplexer are given in Figure 5.17 and Table 5.3.

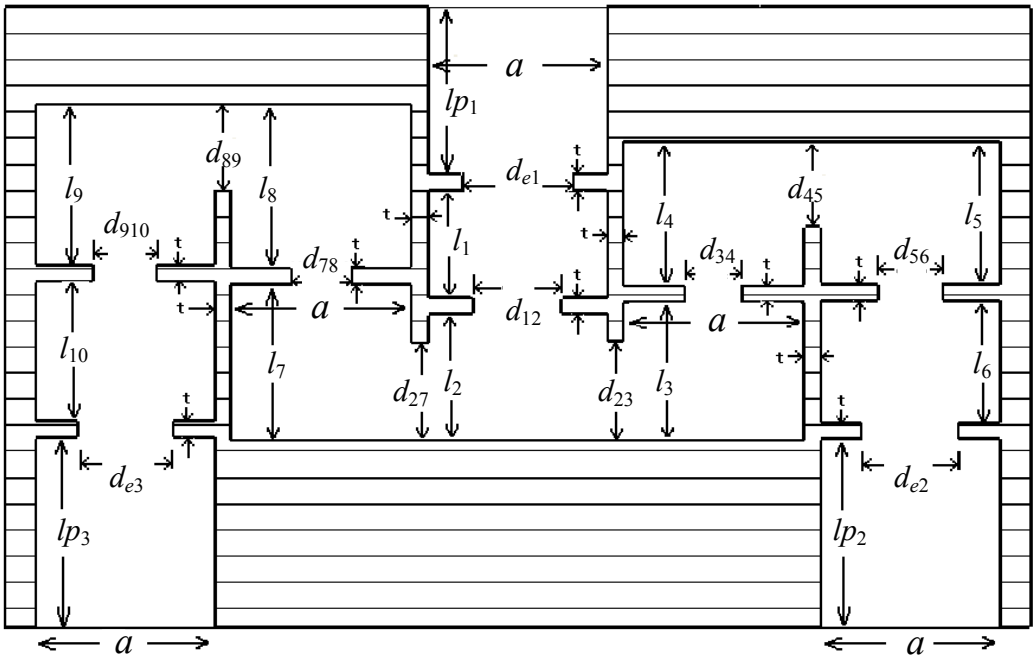

Figure 5.17 Configuration of X-band diplexer structure and its dimensions.

Table 5.3 Dimensions of the fabricated X-band 10th order diplexer (Unit: mm)

	a	b	d_{e1}	d_{e2}	d_{e3}	d_{12}	d_{23}
fabricated	22.86	10.16	14.2	12.312	12.2	11.3	12
	d_{34}	d_{45}	d_{56}	d_{27}	d_{78}	d_{89}	d_{910}
fabricated	7.183	10.048	8.103	11.8	7.39	10.1	8.08
	l_1	l_2	l_3	l_4	l_5	l_6	l_7
fabricated	13.08	15.33	16.778	17.266	17.064	14.739	19
	l_8	l_9	l_{10}	l_{p1}	l_{p2}	l_{p3}	t
fabricated	19.6	19.3	16.87	20	21.811	22	2

5.3.4 Fabrication and Measurement

As shown in Figure 5.15, the construction of the device is split along the H-plane into two pieces. (conductivity $= 3.56\times10^7$ (S/m)). The picture of the fabricated device is shown in Figure 5.18. A response comparison between the simulation and measurement results is given in Figure 5.19. The measured insertion loss is about 0.4 dB in the middle of the passband

while the simulated insertion loss is about 0.2 dB.

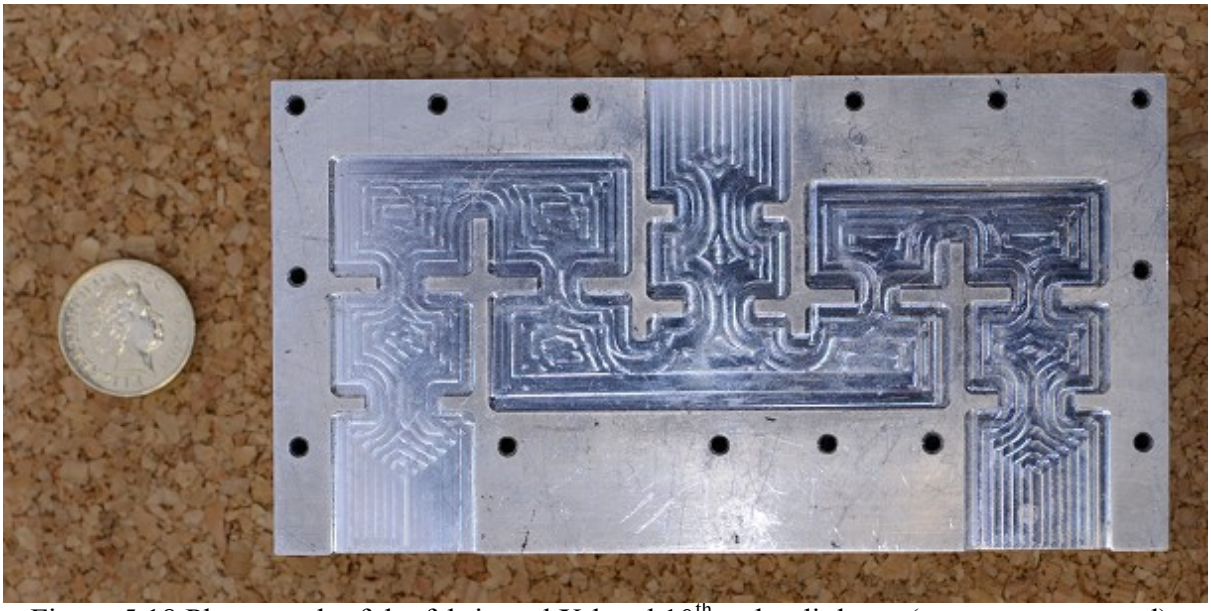

Figure 5.18 Photograph of the fabricated X-band 10th order diplexer (top cover removed).

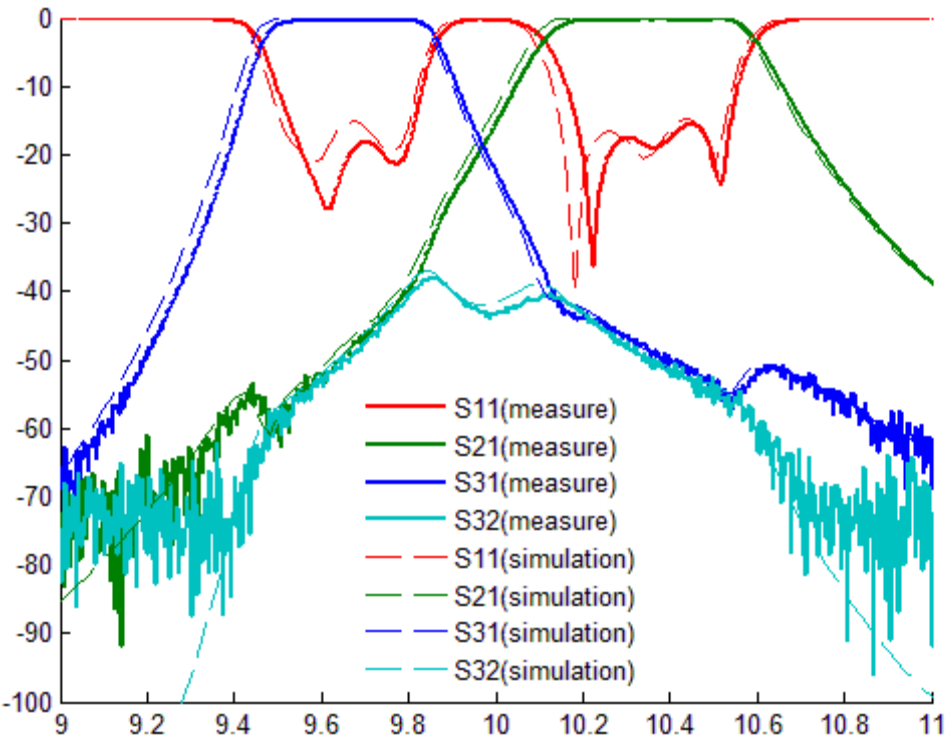

Figure 5.19 Response comparison between the measurement (without tuning screws) and the optimised simulation results of the diplexer.

5.3.5 Screw Tuning

To compensate the manufacture errors and to improve the response for the missing reflection poles, 22 capacitive tuning screws [4] (10 for the cavity resonators and 12 for the coupling irises) are inserted into the device through the top part. By varying the length penetrating into the waveguide, the responses are changed. After the tuning work, two more poles in the lower passband have been found. The return loss of the higher passband has been improved. A comparison of S_{11} between the measured results with tuning and without tuning is given in Figure 5.21.

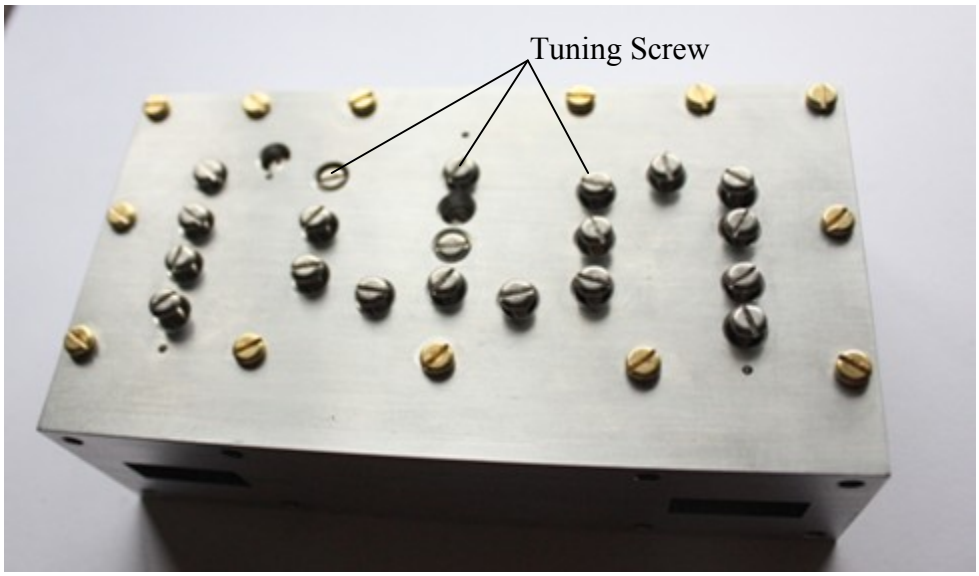

Figure 5.20 Photograph of the cover of the fabricated diplexer. The steel screws are for tuning. The brass screws are for connecting two parts of the device together.

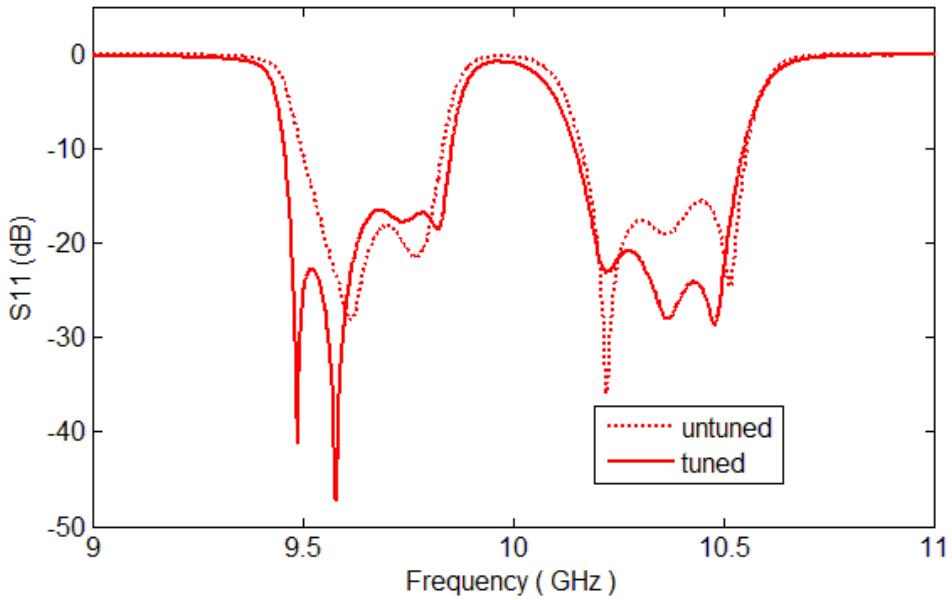

Figure 5.21 Measured return loss comparison between the diplexer being tuned and without tuning.

5.4 Step Tune Method for Rectangular Waveguide Device Design

As presented in Section 5.3, after obtaining the initial dimensions of each cavity and iris, the traditional method is to optimise the overall structure so as to get the desired responses. With a circuit with higher order and/or a complex cross-coupled topology, the overall structure optimisation will be slow and the convergence of the final result is not guaranteed. Here we present a method which overcomes this problem.

The method, which is based on EM simulator [5], will be called the Step Tune method. Instead of traditionally altering all the parameters of the circuit in each optimising iteration, the step-tune method simulates only one resonator of the device in the first step. When finishing tuning the first resonator, one more resonator is added and then the circuit is tuned/optimised again. More resonators are added successively to tuning at each step. In each new step, the dimensions of the old resonators, which have been tuned in the previous steps, are kept the same values. For each step, a new coupling matrix is required for the tuning. As

limited number of physical dimensions needs to optimise in each step, the optimising process works more efficiently and generates more reliable solutions. The key point of this method is to calculate the *S*-parameters in each step and apply the responses as the objective ones for the physical optimising.

To get the responses in each step, we need to convert the internal coupling coefficient $m_{i,j}$ of the coupling iris into its related external quality factor Q_{ei}. The equation is [5]:

$$Q_{ei} = \frac{1}{\frac{n\pi}{2}\left(\frac{\lambda_g}{\lambda}\right)^2 M_{i,j}^2} \tag{5.17}$$

where λ_g is the guided wavelength of the resonant frequency and λ is the free-space wavelength, n is the number of half-wavelengths of the waveguide resonator cavity. Substituting (5.17) into (3. 22), we have

$$M_{Pk,i} = \sqrt{\frac{n\pi}{2}}\left(\frac{\lambda_g}{\lambda}\right) M_{i,j} \tag{5.18}$$

where $M_{Pk,i}$ is the equivalent external coupling coefficient of the internal coupling iris.

The process of optimizing 10-resonator diplexer by Step Tune method is presented in the following parts. Each step, including its topology, the top view of the rectangular circuit and the desired response, is given in Figure 5.22 to Figure 5.28. During the Step Tune, the material of the circuit is set to be the PEC.

Note as the circuits in Figure 5.23 and Figure 5.25 to Figure 5.28 are not well-matched, the insertion loss of each channel is very high leading to a flat reflection response $S_{1,1}$ of each circuit. This is of course no problem and inherent in the Step Tune process.

5.4.1 Step One

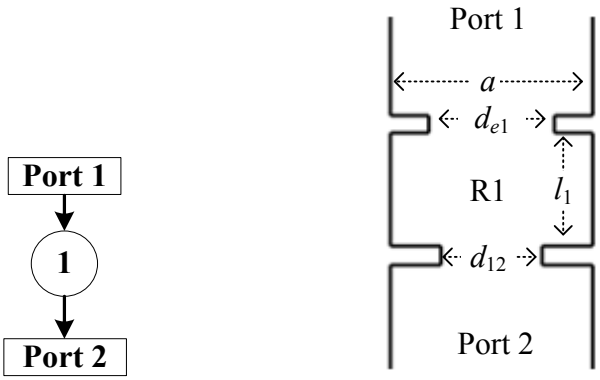

(a) (b)

Figure 5.22 (a) Schematic of Resonator 1 in Step One and (b) its top view of the rectangular waveguide circuit. d_{e1} and d_{12} are the width of the irises. l_1 is the length of the cavity resonator 1. a=22.86mm is the standard width of WR-90.

The Step Tune method starts with optimising Resonator 1 of the diplexer. According to Figure 5.13, Resonator 1 is coupled to Port 1 and Resonator 2. In Step One, Resonator 2 is replaced with a Port 2. Resonator 3 to 10 are removed. The schematic of the circuit in Step One is illustrated in Figure 5.22(a). Resonator 1 is coupled to two ports so the general $n \times n$ coupling matrix cannot be used to derive the responses [6]. An n+2 coupling matrix $[M_{\text{Step\_1}}]_{n+2}$ is applied as

$$[M_{\text{Step\_1}}]_{n+2} = \begin{bmatrix} 0 & M_{P1,1} & 0 \\ M_{1,P1} & M_{1,1} & M_{1,P2} \\ 0 & M_{P2,1} & 0 \end{bmatrix} \tag{5.19}$$

As given in Table 5.2, the related matrix entries of Resonator 1 are

$$M_{P1,1} = 0.2684, \;\; M_{1,1} = 0, \;\; M_{1,2} = 0.08 \tag{5.20}$$

$M_{1,P2}$ in (5.19) is originated from $M_{1,2}$ of the 10$^{\text{th}}$ order diplexer in (5.20). According to (5.18), the internal coupling $M_{1,2}$ is turned into its equivalent external coupling $M_{P2,1}$ as

$$M_{P2,1} = \sqrt{\frac{\pi}{2}}\left(\frac{\lambda_g}{\lambda}\right) M_{1,2} = 0.1324 \tag{5.21}$$

So $[M_{\text{step\_1}}]_{n+2}$ in (5.19) is

$$\left[M_{\text{Step\_1}}\right]_{n+2} = \begin{bmatrix} 0 & 0.2684 & 0 \\ 0.2684 & 0 & 0.1324 \\ 0 & 0.1324 & 0 \end{bmatrix} \tag{5.22}$$

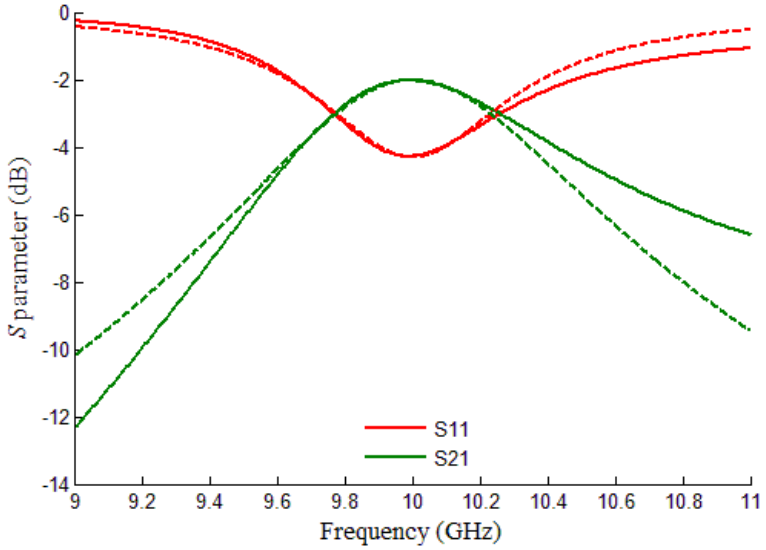

Figure 5.23 Response comparison between the tuned results (in solid lines) and its objective ones (in dashed lines).

According to Figure 5.14, the top view of the equivalent waveguide circuit in Step One is given in Figure 5.22(b). d_{e1}, d_{12} and l_1 are the physical dimensions to tune. The aim of the tuning is to make the simulation results satisfy its objective counterpart obtained from the coupling matrix. The final results of Step One are given in Figure 5.22. The simulation results (in solid lines) meet well with the objective ones (in dashed lines). The objective *S*-parameters in Step One is derived from the coupling matrix in (5.22).

5.4.2 Step Two

After Resonator 1 is optimised in Step One, Resonator 2 is added to the circuit. According to Figure 5.13, Resonator 2 is coupled to Resonator 1, 3 and 7. In Step Two, Resonator 3 and 7

are replaced with two ports. The schematic of the circuit in Step Two is given in Figure 5.24.

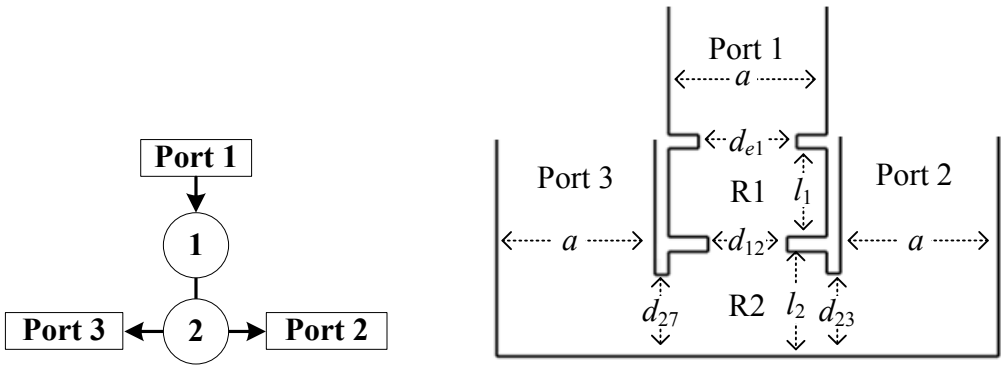

Figure 5.24 (a) Schematic of the circuit in Step Two and (b) its top view of the rectangular waveguide circuit. d_{e1}, d_{12}, d_{23} and d_{27} are the width of the irises. l_1 and l_2 are the length of the cavity resonators.

As the circuit in Figure 5.24(a) has 3 ports, the equivalent coupling matrix of the circuit is extended to an n+3 matrix $[M_{\text{step\_2}}]_{n+3}$ as

$$\left[M_{\text{Step\_2}}\right]_{n+3} = \begin{bmatrix} 0 & M_{P1,1} & 0 & 0 & 0 \\ M_{1,P1} & M_{1,1} & M_{1,2} & 0 & 0 \\ 0 & M_{2,1} & M_{2,2} & M_{2,P2} & M_{2,P3} \\ 0 & 0 & M_{P2,2} & 0 & 0 \\ 0 & 0 & M_{P3,2} & 0 & 0 \end{bmatrix} \tag{5.23}$$

where $M_{2,P2}$ and $M_{2,P3}$ are originated from $M_{2,3}$ and $M_{2,7}$. As given in Table 5.2, the related matrix entries of Resonator 2 are

$$M_{1,2} = 0.08,\ M_{2,2} = 0,\ \ M_{2,3} = M_{2,7} = 0.0365 \tag{5.24}$$

According to (5.18) and (5.24), the internal couplings $M_{2,3}$ and $M_{2,7}$ are turned into the equivalent external couplings $M_{P2,2}$ and $M_{P3,2}$ as

$$M_{P2,2} = M_{P3,2} = \sqrt{\frac{\pi}{2}}\left(\frac{\lambda_g}{\lambda}\right) M_{2,3} = 0.0604 \tag{5.25}$$

So $[M_{\text{step\_2}}]_{n+3}$ is

$$\left[M_{\text{Step\_2}}\right]=\begin{bmatrix} 0 & 0.2684 & 0 & 0 & 0 \\ 0.2684 & 0 & 0.08 & 0 & 0 \\ 0 & 0.08 & 0 & 0.0604 & 0.0604 \\ 0 & 0 & 0.0604 & 0 & 0 \\ 0 & 0 & 0.0604 & 0 & 0 \end{bmatrix} \tag{5.26}$$

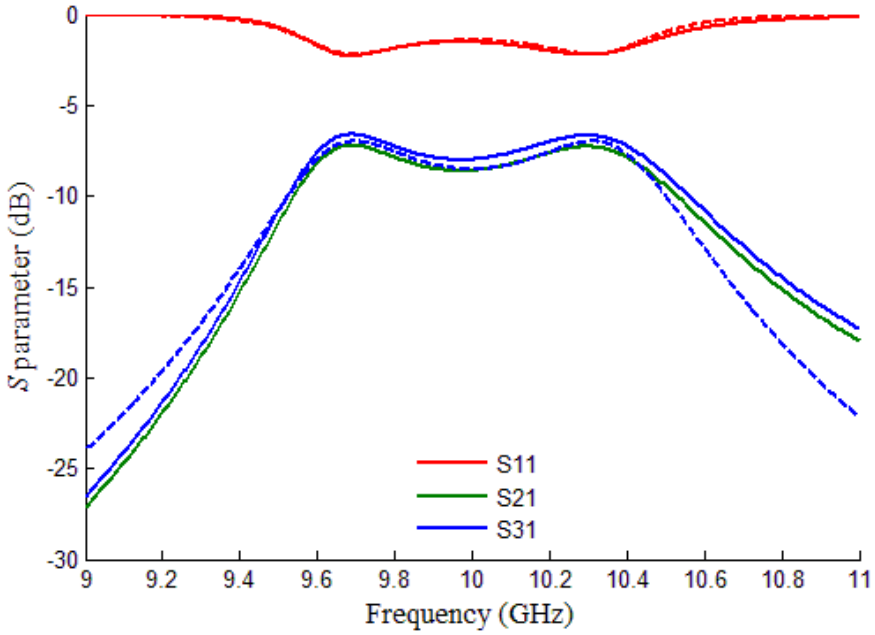

Figure 5.25 Response comparison between the tuned results (in solid lines) and its objective ones (in dashed lines) in Step Two. The objective S_{21} and S_{31} in dashed lines are the same.

According to Figure 5.14, the top view of the equivalent waveguide circuit in Step Two is given in Figure 5.24(b). d_{23}, d_{27} and l_2 are the new dimensions to tune. The values of d_{e1}, d_{12} and l_2, which have been optimised in Step One, are fixed during Step Two. After the tuning, as given in Figure 5.25, the simulation response (in solid lines) gets very close to its objective response (in dashed lines) from the coupling matrix.

5.4.3 Completion of All Steps

Branch resonators are added successively in the remaining steps. The schematics of the circuits in Step Three to Step Six, as well as their rectangular waveguide forms and the objective *S*-parameters, are given in Figure 5.26 to Figure 5.29. In each step, the dimensions of the new added resonators are tuned. The dimensions of the "old" resonators, which have

been optimised in the previous steps, are kept their values in the new step(s).

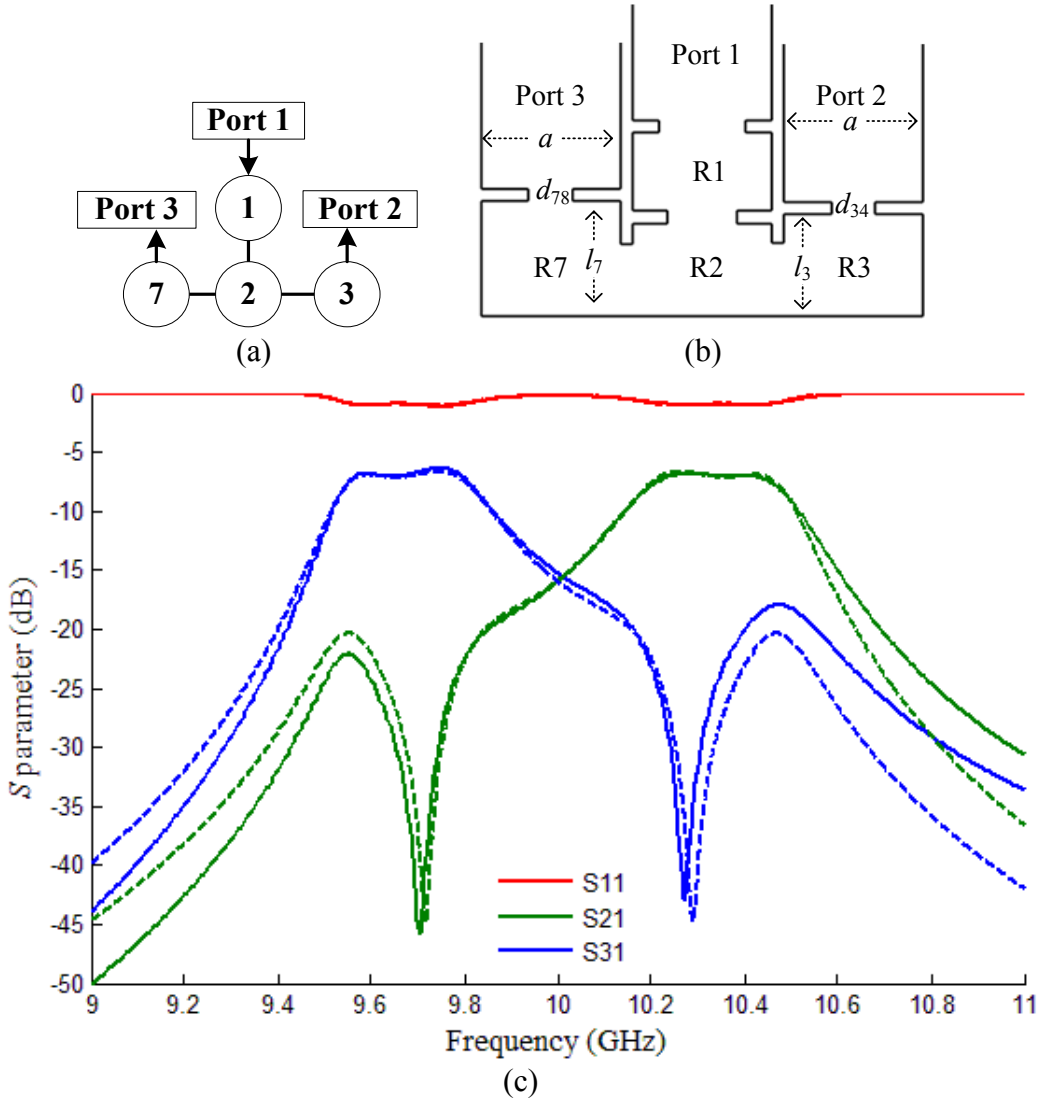

Figure 5.26 (a) Schematic, (b) Top view of the rectangular waveguide circuit in Step Three. d_{34}, d_{78}, l_3 and l_7 are the dimensions to optimise. (c) Response comparison between the tuned results (in solid lines) and its objective ones (in dashed lines).

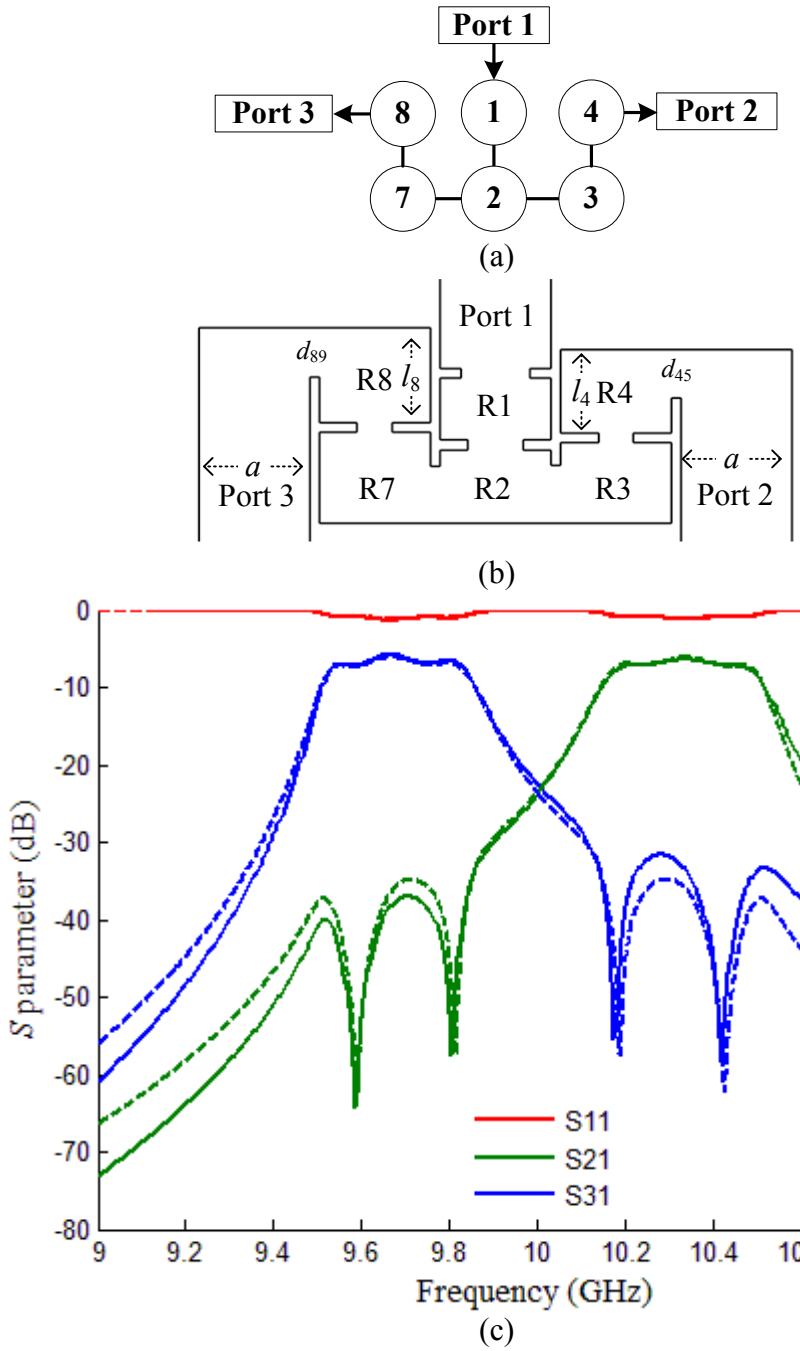

Figure 5.27(a) Schematic, (b) Top view of the rectangular waveguide circuit in Step Four. d_{45}, d_{89}, l_4 and l_8 are the dimensions to optimise. (c) Response comparison between the tuned results (in solid lines) and its objective ones (in dashed lines).

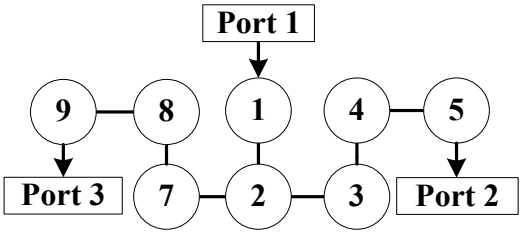

(a)

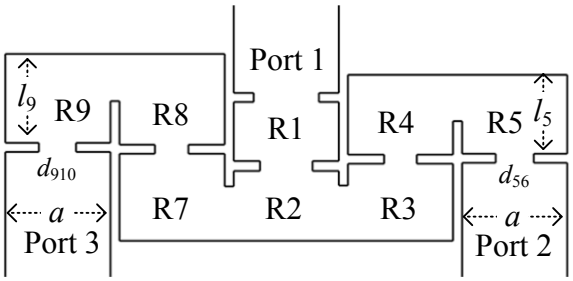

(b)

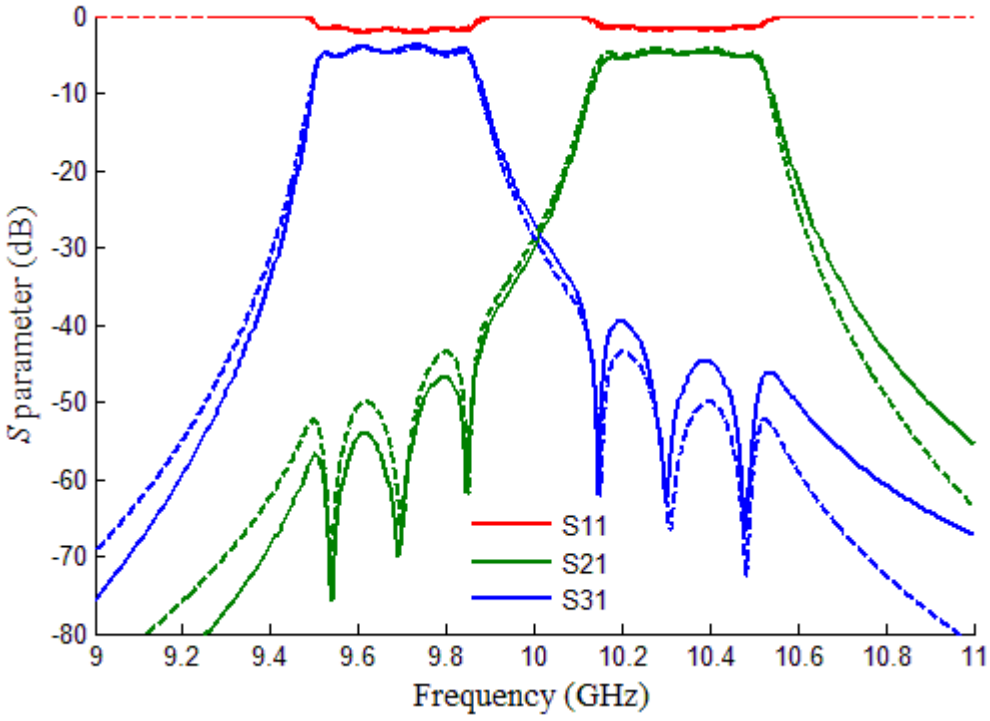

(c)

Figure 5.28(a) Schematic, (b) Top view of the rectangular waveguide circuit in Step Five. d_{56}, d_{910}, l_5 and l_9 are the dimensions to optimise. (c) Response comparison between the tuned results (in solid lines) and its objective ones (in dashed lines).

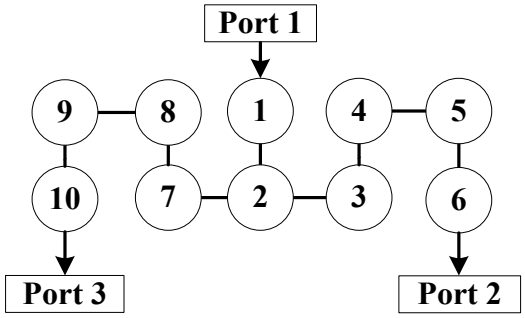

(a)

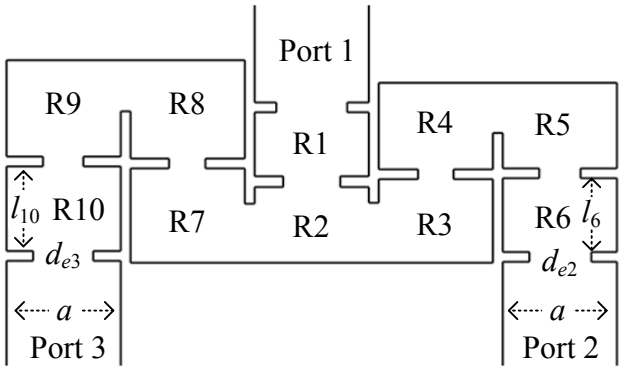

(b)

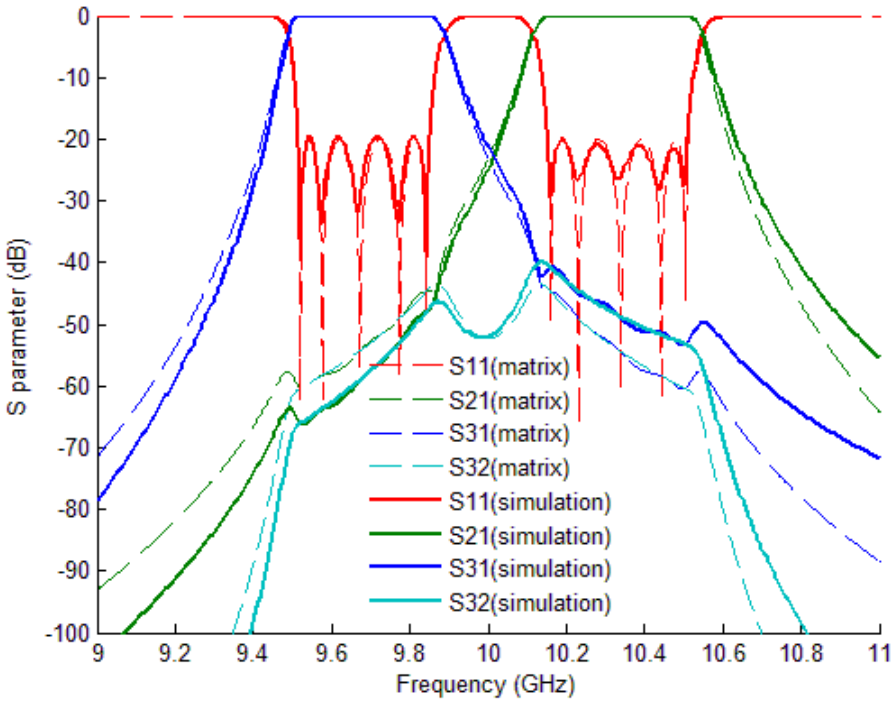

(c)

Figure 5.29 (a) Schematic, (b) Top view of the rectangular waveguide circuit in Step Six. d_{e2}, d_{e3}, $l6$ and l_{10} are the dimensions to optimise. (c) Responses comparison between the simulation results (in solid line) and the matrix calculations (in dashed line).

The simulation results after Step Six are given in Figure 5.29. The notations for the physical

dimensions of the diplexer are given in Figure 5.17. The values of each physical dimension are given in Table 5.4. Although this design has an improvement over the previous one, it was not made so no experimental results are available.

Table 5.4 Dimensions comparison between the fabricated X-band 10th order diplexer and the Step Tune one (Unit: mm)

	a	*b*	*de*1	*de*2	*de*3	*d*12	*d*23
fabricated	22.86	10.16	14.2	12.312	12.2	11.3	12
step-tune	22.86	10.16	12.969	10.906	11.808	10.158	11.134
	*d*34	*d*45	*d*56	*d*27	*d*78	*d*89	*d*910
fabricated	7.183	10.048	8.103	11.8	7.39	10.1	8.08
step-tune	6.755	9.645	7.207	11.304	7.131	10.024	7.829
	*l*1	*l*2	*l*3	*l*4	*l*5	*l*6	*l*7
fabricated	13.08	15.33	16.778	17.266	17.064	14.739	19
step-tune	14.437	16.145	17.196	17.497	17.360	15.527	18.991
	*l*8	*l*9	*l*10	*lp*1	*lp*2	*lp*3	t
fabricated	19.6	19.3	16.87	20	21.811	22	2
step-tune	19.511	19.310	17.145	20	21.759	22	2

[1] J.-S. Hong and M. J. Lancaster, *Microstrip filters for RF/microwave applications*. New York ; Chichester: Wiley, 2001.

[2] R. J. Cameron, C. M. Kudsia, and R. R. Mansour, *Microwave filters for communication systems : fundamentals, design, and applications*. Hoboken, N.J.: Wiley ; Chichester : John Wiley [distributor], 2007.

[3] J. S. Hong, "Couplings of asynchronously tuned coupled microwave resonators," *Microwaves, Antennas and Propagation, IEE Proceedings,* vol. 147, pp. 354-358, 2000.

[4] C. G. Montgomery, R. H. Dicke, and E. M. Purcell, *Principles of Microwave Circuits*: Institution of Engineering & Technology, 1948.

[5] X. Shang, W. Xia, and M. J. Lancaster, "The design of waveguide filters based on cross-coupled resonators," *Microwave and Optical Technology Letters,* vol. 56, pp. 3-8, 2014.

[6] R. J. Cameron, "Advanced coupling matrix synthesis techniques for microwave filters," *Microwave Theory and Techniques, IEEE Transactions on,* vol. 51, pp. 1-10, 2003.

Chapter 6 Diplexer with Cross-Couplings

In the previous chapter, the design procedure of the diplexer with a Tree Topology has been presented. In this chapter, Section 1 discusses comparison of responses between a diplexer with a Tree Topology and a traditional diplexer based on a non-resonant junction. For Tree Topology, it is feasible to add cross coupling to improve isolation and attenuation performance. This is discussed in Section 2. Finally, a coupled-resonator rectangular waveguide based X-band diplexer with cross-coupled structure is designed, fabricated and tested as described in Section 3.

6.1 Response Comparison between the Diplexer with a Tree Topology and the Traditional Diplexer with a Non-Resonant Junction

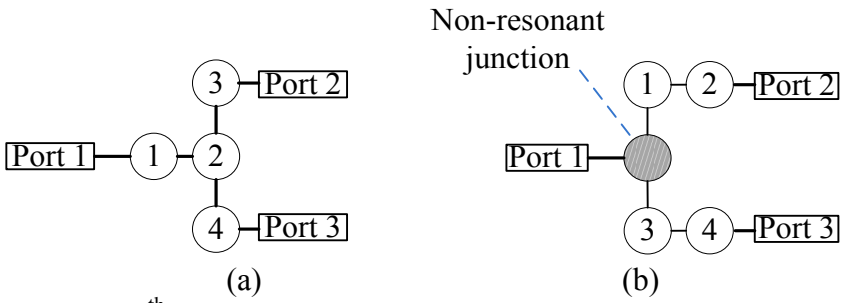

Figure 6.1 Schematic of 4th order diplexers (a) in Tree Topology and (b) with a non-resonant junction.

A diagram of a 4th order diplexer with a Tree-topology is given in Figure 6.1(a). Resonator 1 and 2 are the stem resonators. Resonator 3 and 4 are the branch resonators. The schematic of the 4th order diplexer with a non-resonant junction is given in Figure 6.1(b). To make a response comparison, these two diplexers have the same specifications with cut-off frequencies of the two passbands at [-1, -0.4] and [0.4, 1], and a return loss of the two passbands of 20 dB. Their responses are depicted in Figure 6.2 and Figure 6.3.

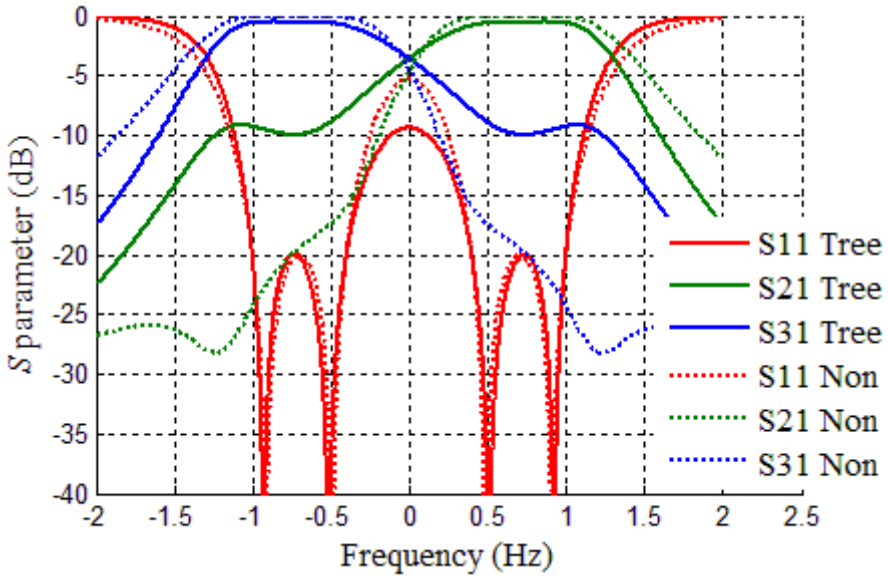

Figure 6.2 S_{11}, S_{21} and S_{31} of the diplexers in Tree Topology and with a non-resonant junction.

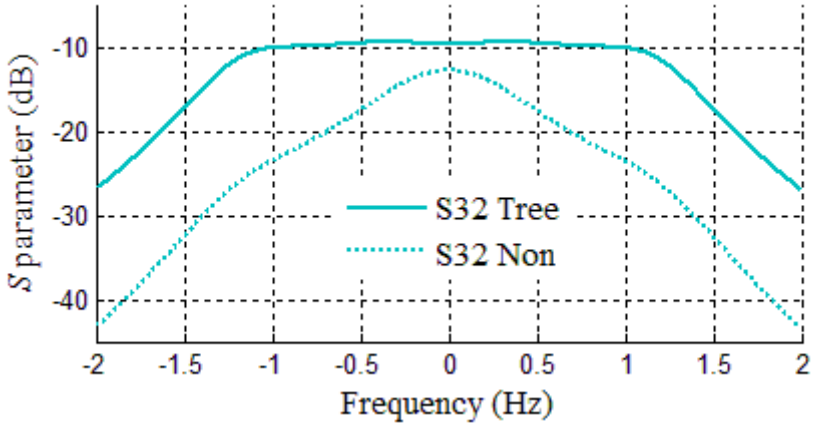

Figure 6.3 The isolation of the diplexers in Tree-topology and with a non-resonant junction.

As shown in Figure 6.2 and Figure 6.3, the response of the diplexer with a Tree Topology is in solid line and the one with a non-resonant junction is in dotted line. The diplexer with a Tree Topology has a relatively poorer close-to-band rejection and isolation, in comparison with the diplexer with a non-resonant junction. The reason for this is the stem resonator plays no role in attenuating signals over the two passbands [1], each channel of the diplexer with a Tree Topology, as given in Figure 6.1(a), has only one branch resonator to attenuate signals with frequencies in the adjacent channel. The diplexer with a non-resonant junction, as given

in Figure 6.1 (b), has two resonators to attenuate signals in each channel. This leads to the lower attenuation and isolation of the diplexer with a Tree Topology. For the Tree Topology, the poor close-to-band rejection also leads to a higher insertion loss of each channel. So the insertion losses of the two diplexers, in Figure 6.2, are different.

The n+3 coupling matrices of these two diplexers, which are obtained by the optimisation technique presented in Chapter 4, are given in Table 6.1 and Table 6.2.

Table 6.1 The coupling matrix of the 4th order diplexer with a Tree Topology.

	P1	1	2	3	4	P2	P3
P1	0	0.943	0	0	0	0	0
1	0.943	0	0.904	0	0	0	0
2	0	0.904	0	0.525	0.525	0	0
3	0	0	0.525	0.586	0	0.667	0
4	0	0	0.525	0	-0.586	0	0.667
P2	0	0	0	0.667	0	0	0
P3	0	0	0	0	0.667	0	0

Table 6.2 The coupling matrix of the 4th order diplexer with a non-resonant junction.

	P1	1	2	3	4	P2	P3
P1	0	0.665	0	0.665	0	0	0
1	0.665	0.841	0.466	0	0	0	0
2	0	0.466	0.716	0	0	0.665	0
3	0.665	0	0	-0.841	0. 466	0	0
4	0	0	0	0.466	-0.716	0	0.665
P2	0	0	0.665	0	0	0	0
P3	0	0	0	0	0.665	0	0

6.2 The Tree Topology with the Cross Couplings

As discussed in Chapter 2, the cross coupled structure can be used to increase the attenuation over some frequency range. To increase the attenuation and isolation of the adjacent passband

of the diplexer in Figure 6.1(a), a cross-coupled structure is investigated in this work. Figure 6.4 shows a cross-coupled structure in order to increase the attenuation of both the left stop band of S_{21} and the right stop band of S_{31}.

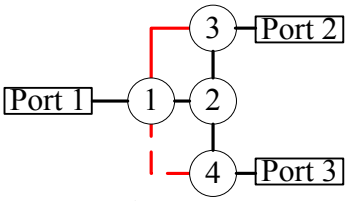

Figure 6.4 Schematic of the 4th order diplexer with cross couplings

As shown in Figure 6.4, the red lines between resonators are denoted as the cross couplings. The cross coupling between Resonator 1 and 3 has the same sign as the main couplings. It is shown as a solid line. The cross coupling between Resonator 1 and 4 has the opposite sign to the main couplings, it is represented using a dashed line. To achieve a symmetric response, the cross coupling values $m_{1,3}$ and $m_{1,4}$ have the relationship as:

$$m_{1,3} = -m_{1,4} \tag{6.1}$$

The coupling matrix of the cross-coupled diplexer is given in Table 6.3. The coupling matrices are obtained by the optimisation method described in Chapter 4. The coupling values of some cross-coupled diplexers with different cross couplings are given in Table 6.4. Their responses are given in Figure 6.5 and Figure 6.6.

Table 6.3 The coupling matrix of the cross-coupled diplexer given in Figure 6.4.

	P1	1	2	3	4	P2	P3
P1		x					
1	x		x	x	x		
2		x		x	x		
3		x	x	x		x	
4		x	x		x		x
P2				x			
P3					x		

Table 6.4 The coupling values of the diplexers with different cross couplings.

	$m_{1,4}$	$m_{1,2}$	$m_{2,3}$	$m_{2,4}$	$m_{3,3}$	$m_{4,4}$	$m_{P1,1}$	$m_{3,P2}$	$m_{4,P3}$
$m_{1,3}$=0.2	-0.2	0.889	0.417	0.417	0.679	-0.679	0.940	0.665	0.665
$m_{1,3}$=0.375	-0.375	0.815	0.295	0.295	0.725	-0.725	0.937	0.662	0.662
$m_{1,3}$=0.5	-0.5	0.716	0.183	0.183	0.735	-0.735	0.933	0.660	0.660

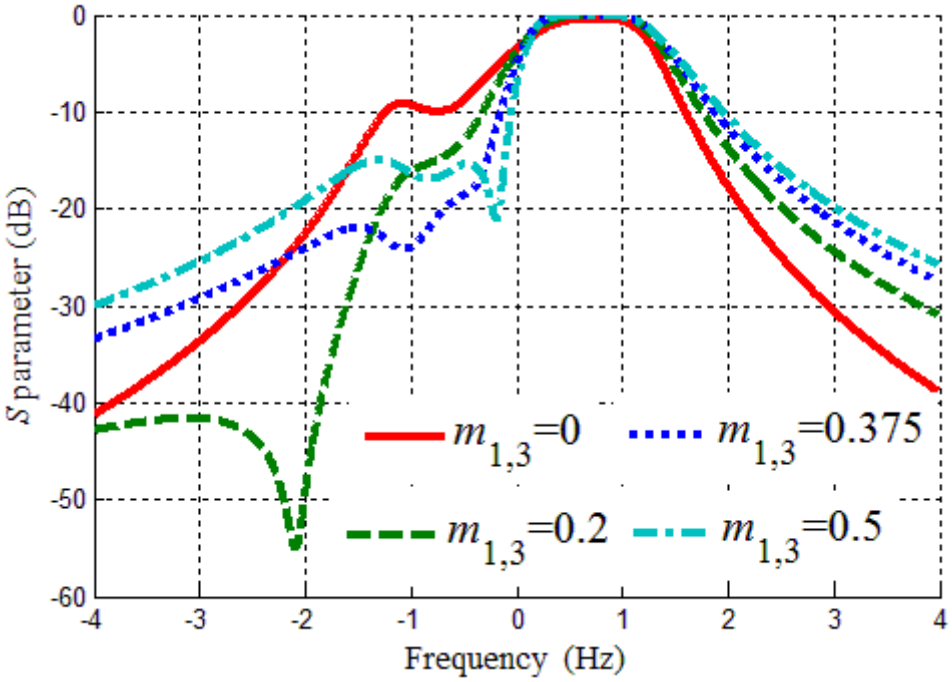

Figure 6.5 Transmission responses with different values of cross-coupling $m_{1,3}$

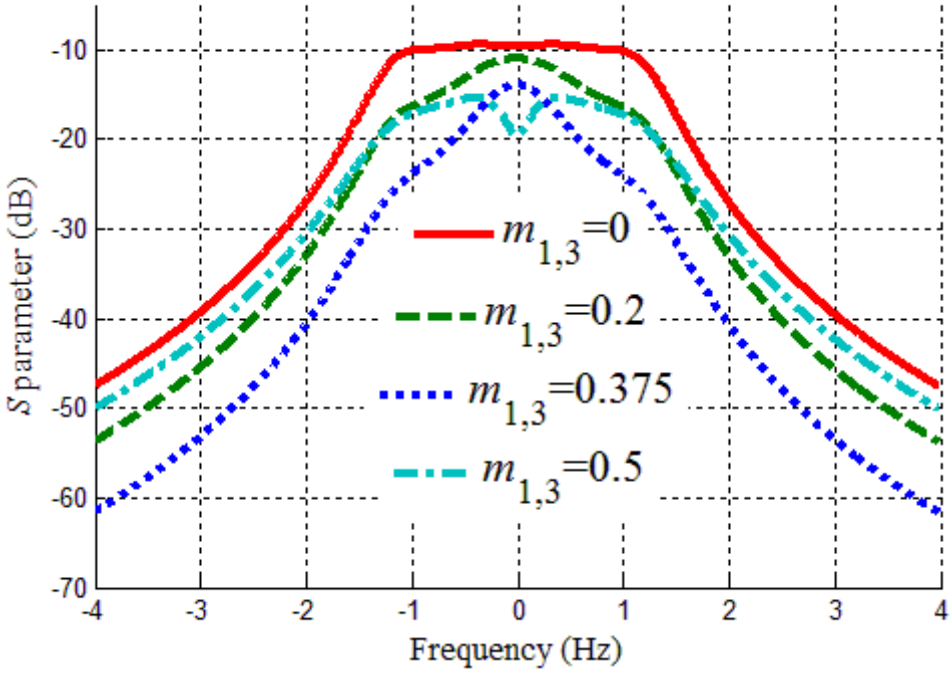

Figure 6.6 Isolations with different values of cross-coupling $m_{1,3}$

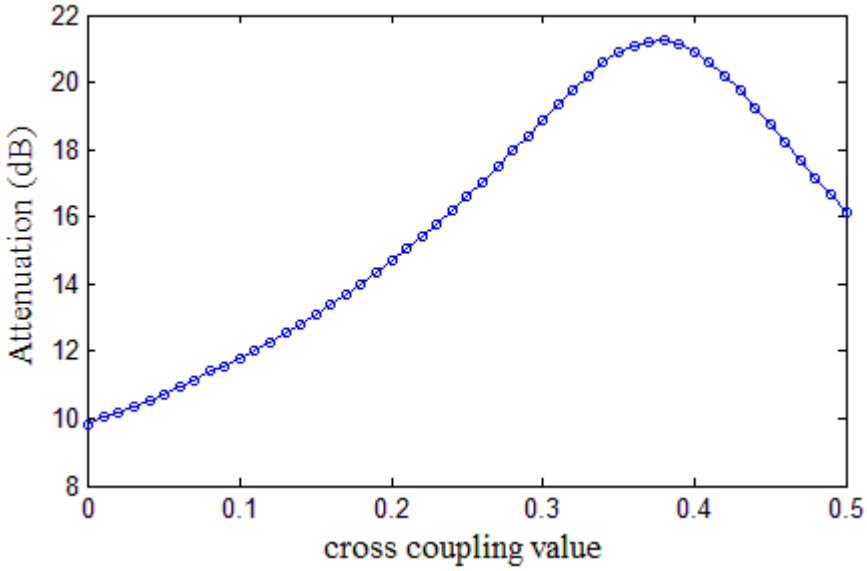

Figure 6.7 The attenuation at the middle of the adjacent passband with different values of $m_{1,3}$

The relationship between the cross coupling value and the attenuation at the middle of the adjacent passband is given in Figure 6.7. The attenuation reaches the highest point when the cross coupling $m_{1,3}$ is 0.375. The response comparisons between the diplexer with the cross coupling $m_{1,3}$=0.375 and the traditional diplexer with non-resonant junction are given in

Figure 6.8 and Figure 6.9.

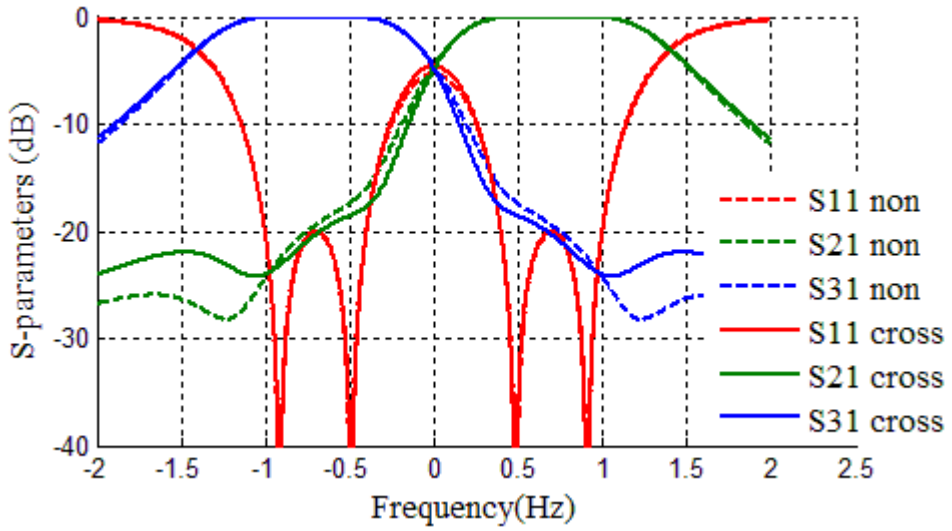

Figure 6.8 S_{11}, S_{21} and S_{31} responses comparison between the diplexer with the cross-coupled Tree Topology and the one with a non-resonant junction.

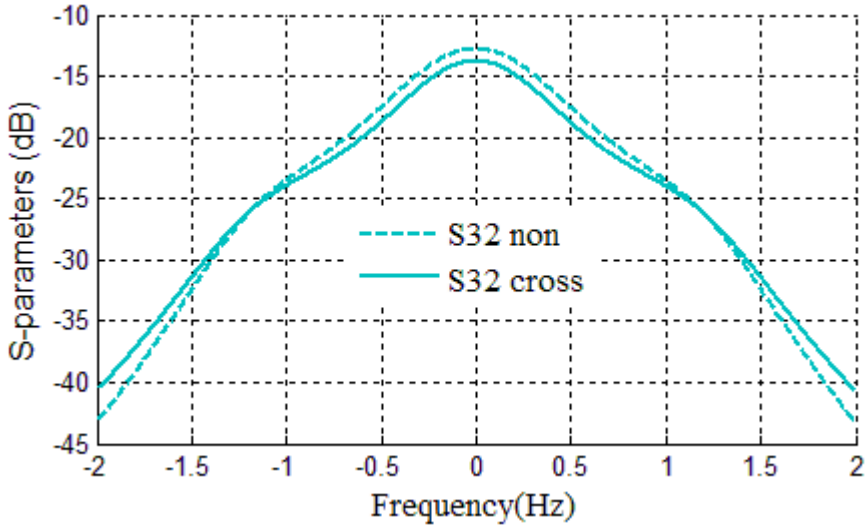

Figure 6.9 S_{32} response comparison between the diplexer with the cross-coupled Tree Topology and the one with a non-resonant junction.

Over the adjacent passband and the middle guard band of each channel, the cross-coupled diplexer with a Tree Topology has the slightly higher attenuation, as shown in Figure 6.8, and isolation, shown in Figure 6.9, than the traditional non-resonant junction one. A compromise exists, with such improvement giving the lower attenuation and isolation over the other stop-

bands of each channel.

6.3 Design Example of the Cross-Coupled Diplexer

6.3.1 Specifications and Coupling Matrix of the Diplexer

A 4th order cross-coupled rectangular waveguide diplexer working at X-band has been designed, fabricated and tested. The specifications of the diplexer are a centre frequency of f_c=10 GHz and an overall fractional bandwidth FBW=0.025. According to Figure 6.7, the cross coupling of the prototype diplexer $m_{1,3}$ is chosen to be 0.375 in order to achieve the highest attenuation at the middle of the adjacent passband of each channel. The coupling values of the prototype diplexer are given in Table 6.4. After the frequency transformation using (3.69), the new coupling matrix is given in Table 6.5.

Table 6.5 The n+3 coupling matrix of the cross-coupled diplexer after the frequency transformation.

	P1	1	2	3	4	P2	P3
P1	0	0.148	0	0	0	0	0
1	0.148	0	0.020	0.009	-0.009	0	0
2	0	0.020	0	0.007	0.007	0	0
3	0	0.009	0.007	0.018	0	0.105	0
4	0	-0.009	0.007	0	-0.018	0	0.105
P2	0	0	0	0.105	0	0	0
P3	0	0	0	0	0.105	0	0

According to Table 6.5, the external quality factors Q_e is calculated by (3.67) and given as

$$Q_{e1} = 17.55, Q_{e2} = Q_{e3} = 35.10$$

The S-parameters after the frequency transformation are given in Figure 6.10.

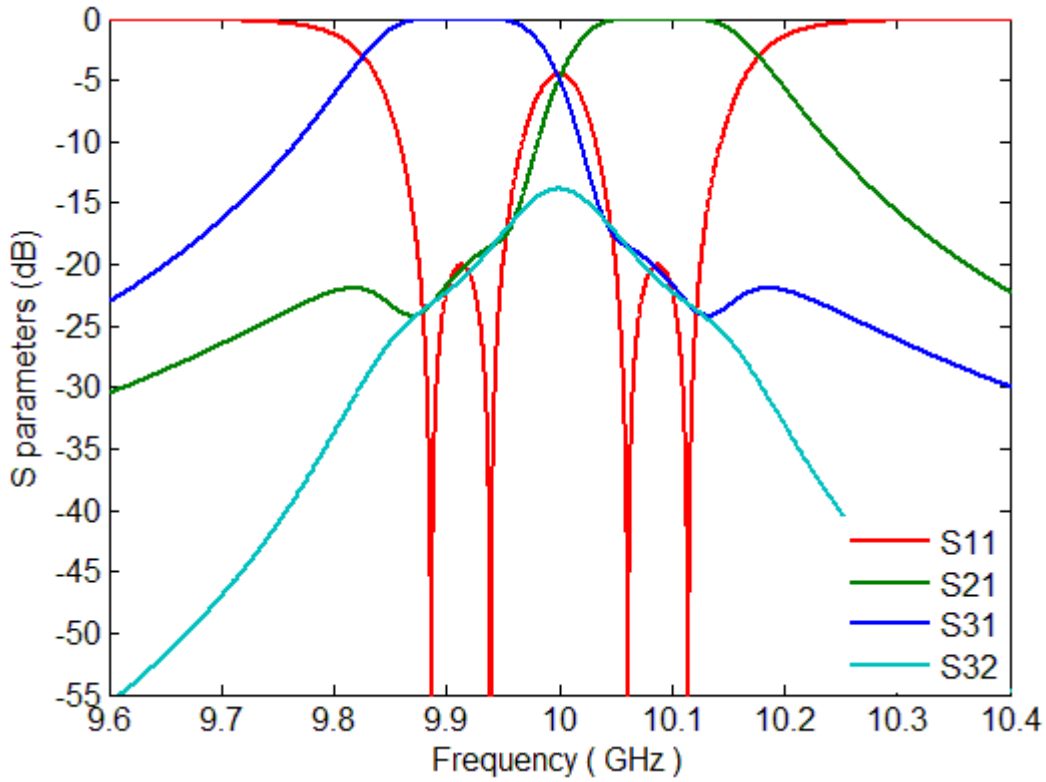

Figure 6.10 *S*-parameters of the 4-th order cross-coupled diplexer after the frequency transformation.

6.3.2 Negative Coupling in the Diplexer

An H-plane planer waveguide topology with all inductive irises is employed to achieve the couplings and the filter is made using CNC milling. A coupling method on the basis of the cavity transformation properties is employed[2] to generate the negative coupling as described below.

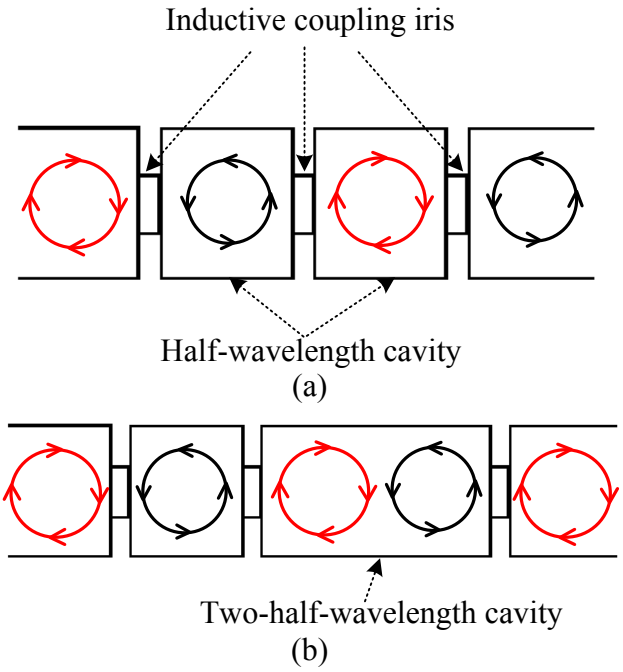

Figure 6.11 Principal magnetic fields of the (a) half-wavelength and (b) two-half wavelength cavity iris coupling. The circle in red represents the field patterns having clockwise direction. The circle in black represents the field patterns having anti-clockwise direction.

Firstly, the direction of the field is determined by the main couplings of the circuit. Secondly, as given in Figure 6.11(a), the direction of the half-wavelength fields coupled by the main coupling iris changes 180°. Finally, as given in Figure 6.11(b), the two-half-wavelength cavity yields a field pair with opposite direction. If the two half-wavelength fields coupled by a cross coupling iris have the same direction, such cross coupling has an opposite sign to the main one, i.e. the cross coupling is a negative coupling if the main coupling is supposed to be positive. A cross coupling has the same sign as the main coupling if the two half-wavelength fields coupled by the cross coupling iris have the opposite direction.

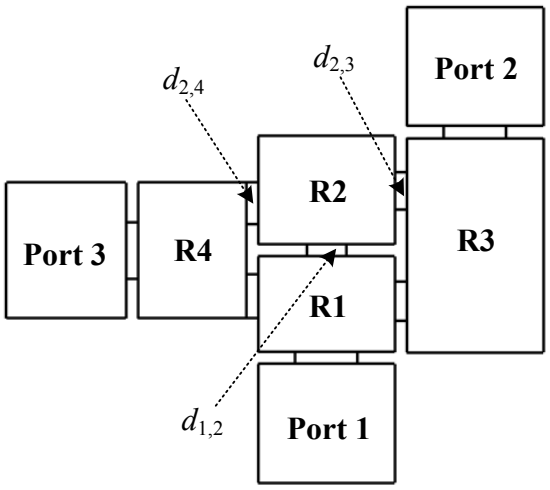

(a)

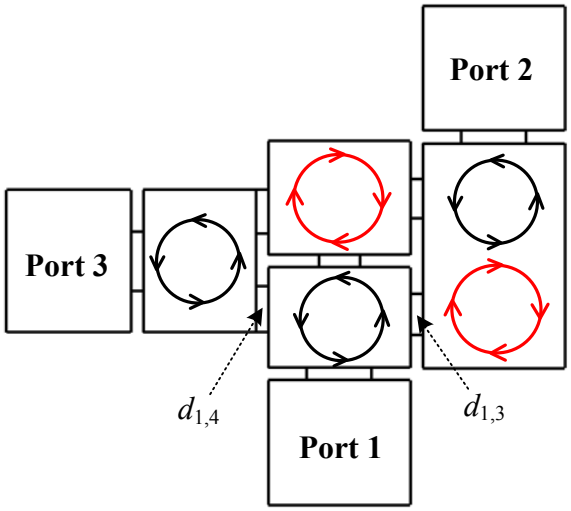

(b)

Figure 6.12 (a) Top view of the diplexer and (b) its principal magnetic field patterns.

The top view of the diplexer topology is given in Figure 6.12(a). A TE_{102} mode cavity is selected as the 3rd resonator (R3) while the rest three resonators (R1, R2 and R4) are operating at the TE_{101} mode. Since the direction of the principal field pattern is determined by the main coupling[2], the directions of the field patterns in Resonator 2, 3 and 4 are determined by the coupling irises $d_{1,2}$, $d_{2,3}$ and $d_{2,4}$. As given in Figure 6.12(b), each circle represents a principal magnetic field patterns. There is a 180° phase difference between the black circle and the red circle. The direction of the black circle is in anticlockwise while the red one is in clockwise.

By inspecting Figure 6.12(b), R1 and R4 exhibit the same field pattern direction. According to [2], the coupling $M_{1,4}$ of the iris $d_{1,4}$ has the opposite sign to the main couplings. Two field patterns with opposite directions are coupled by the coupling iris $d_{1,3}$ so $M_{1,3}$ has the same sign as the main couplings.

The configuration of the X-band diplexer structure is given in Figure 6.13 with the notations of the physical dimensions of each cavity resonator and coupling iris.

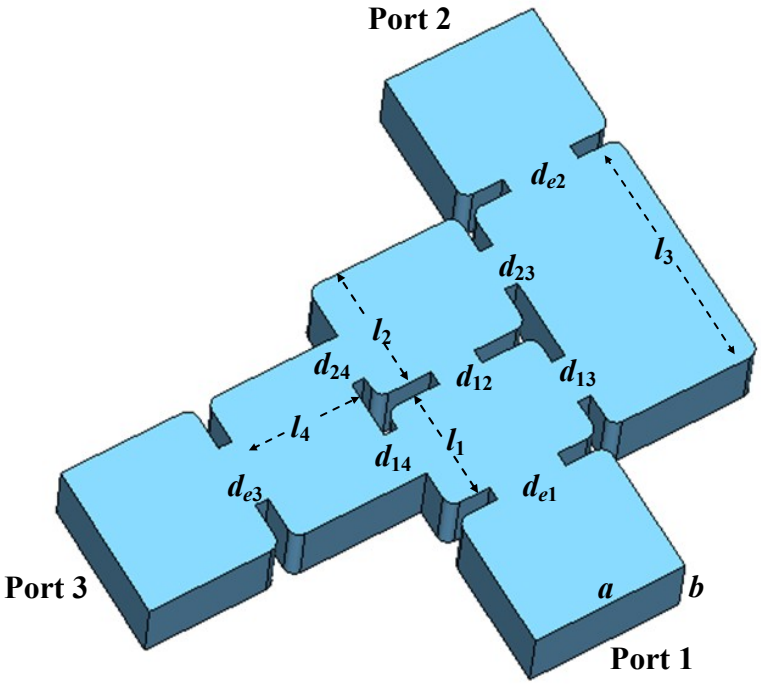

Figure 6.13 Configuration of the X-band diplexer structure. d is the width of the coupling iris and l is the length of the cavity resonator. The width of a=22.86mm and the height of b=10.16mm are the standard dimensions for WR-90.

6.3.3 Step Tune Method

The Step Tune method [3] is applied in optimising the physical dimensions of the cross-coupled diplexer. Similar to the procedures given in Chapter 5, the optimisation is divided into several steps. The schematic, the top view of the rectangular waveguide circuit and the

desired *S*-parameters in each step are given in Figure 6.14 to Figure 6.17. Note as Resonator 2 is the 2 half-wavelength cavity resonator, the internal and external coupling conversion of the coupling iris d_{13} and d_{23} is using (5.18) with n=2.

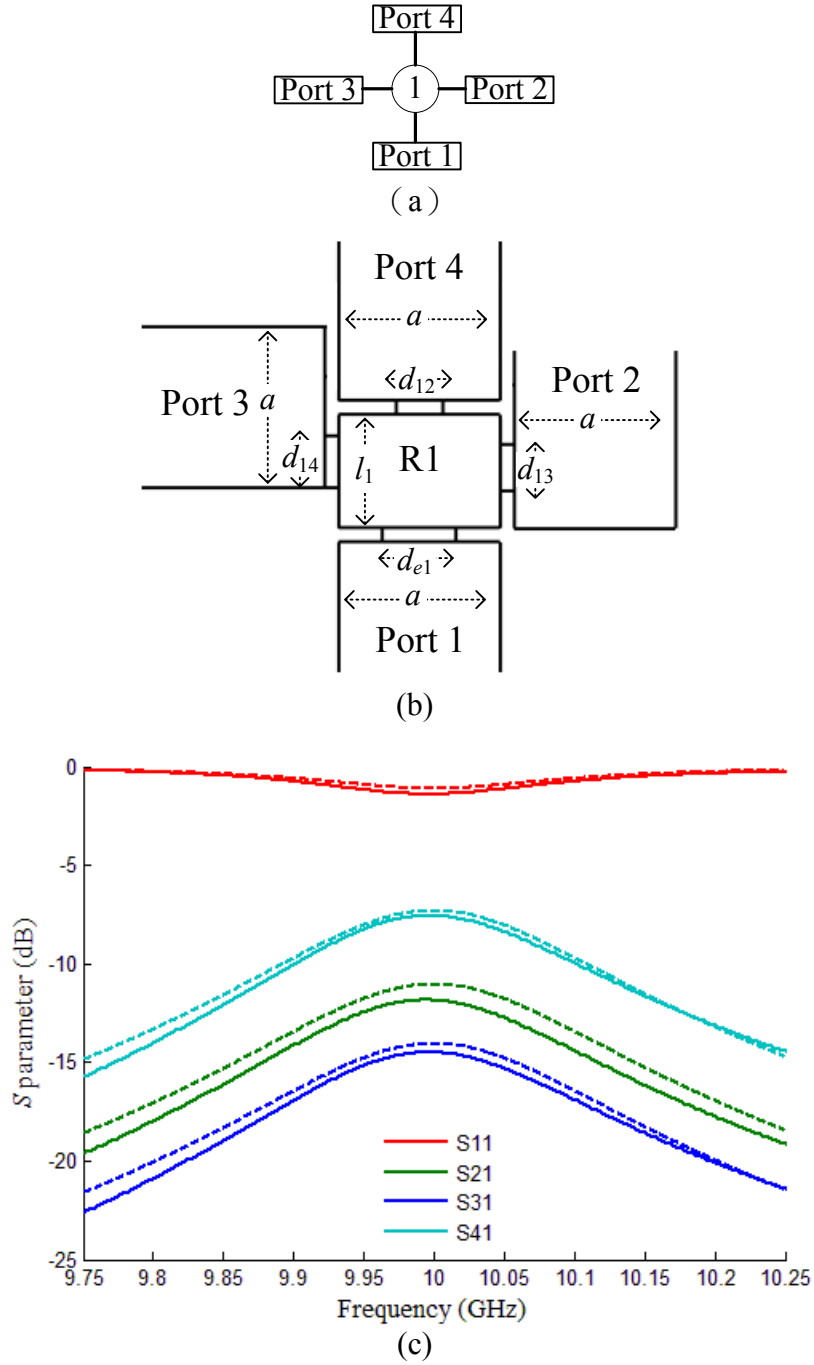

Figure 6.14 (a) Schematic, (b) Top view of the rectangular waveguide circuit in Step One. d_{e1}, d_{12}, d_{13} and d_{14} are the width of the irises to tune. l_1 is the length of the cavity resonator to tune. (c) Response comparison between the tuned results (in solid lines) and its objective ones (in dashed lines).

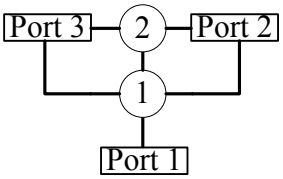

(a)

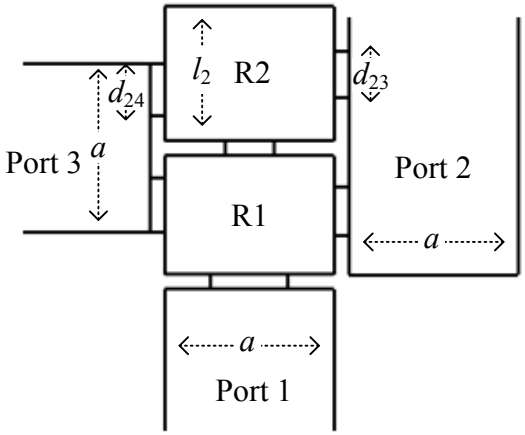

(b)

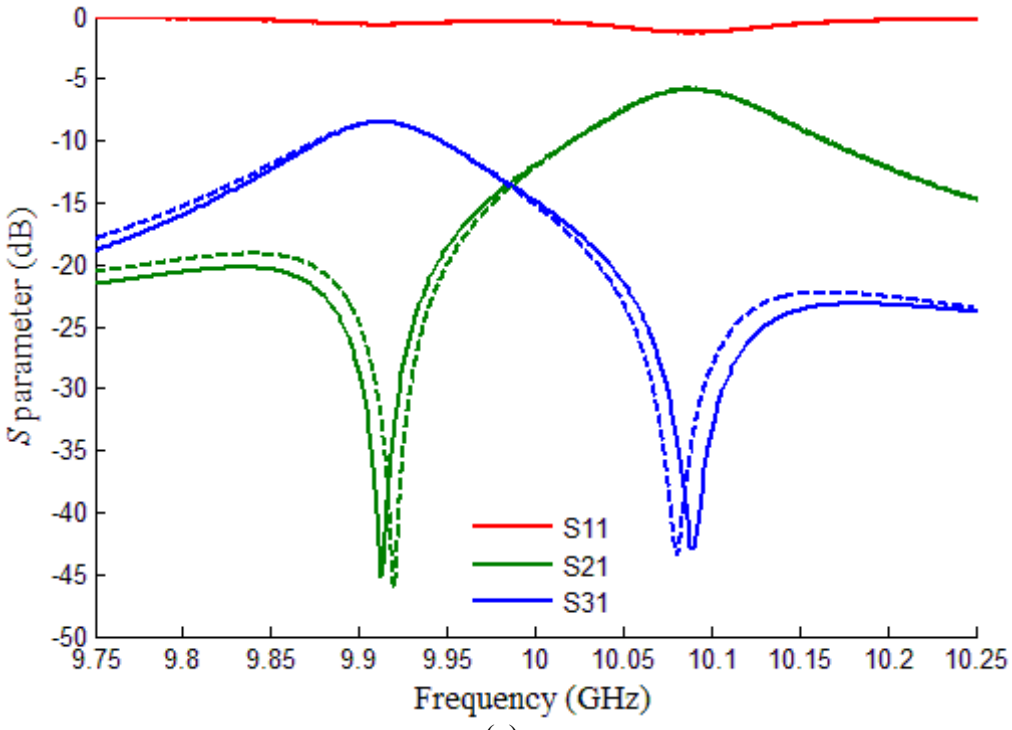

(c)

Figure 6.15 (a) Schematic, (b) Top view of the rectangular waveguide circuit in Step Two. d_{23} and d_{24} are the width of the irises to tune. l_2 is the length of the cavity resonator to tune. (c) Response comparison between the tuned results (in solid lines) and the objective ones (in dashed lines).

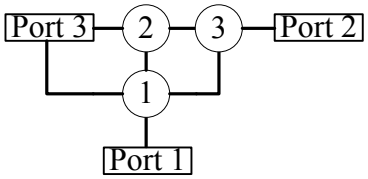

(a)

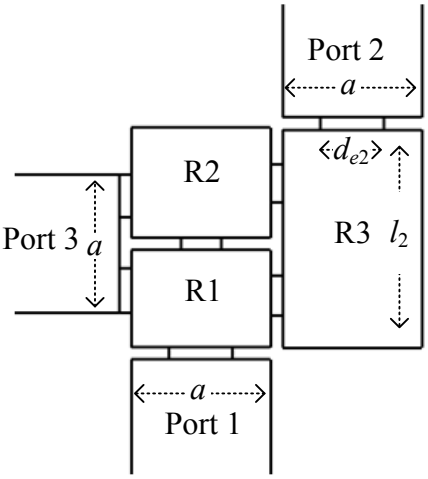

(b)

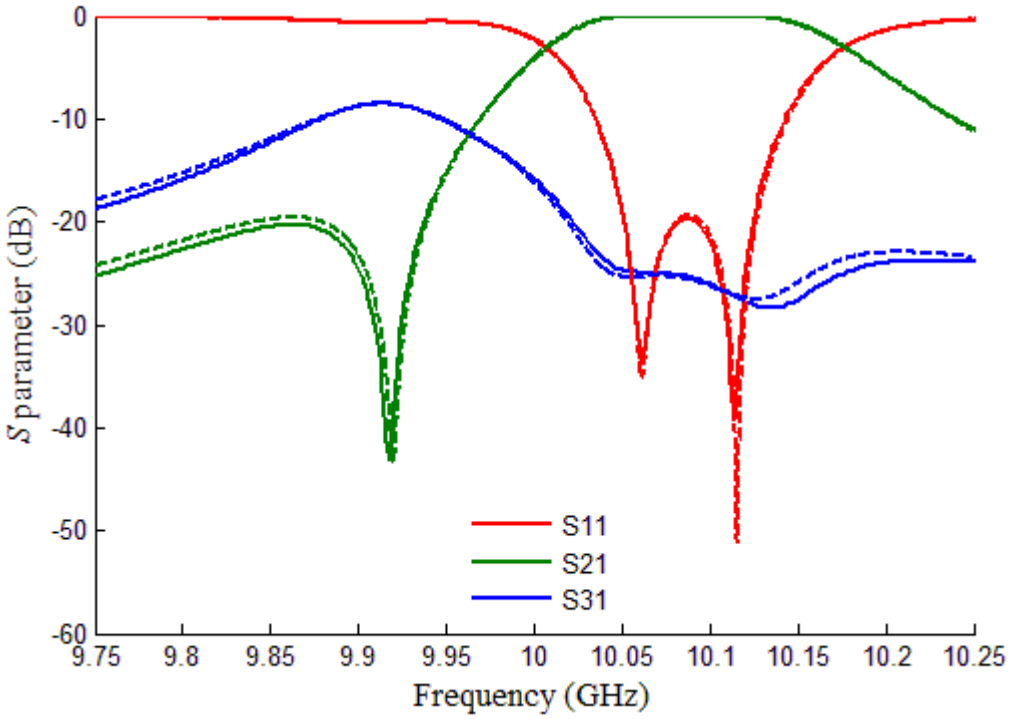

(c)

Figure 6.16 (a) Schematic, (b) Top view of the rectangular waveguide circuit in Step Three. d_{e2} is the width of the iris to tune. l_3 is the length of the cavity resonator to tune. (c) Response comparison between the tuned results (in solid lines) and the objective ones (in dashed lines).

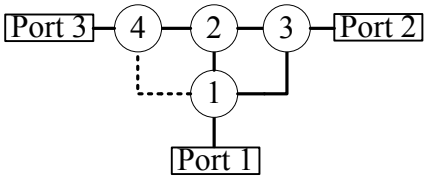

(a)

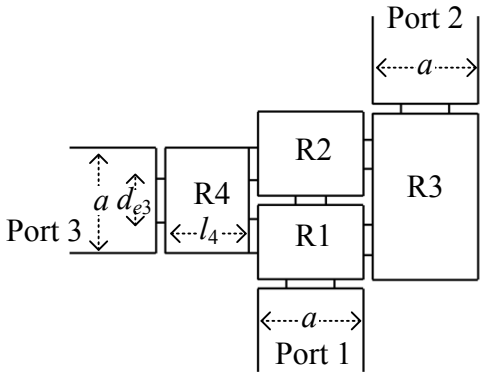

(b)

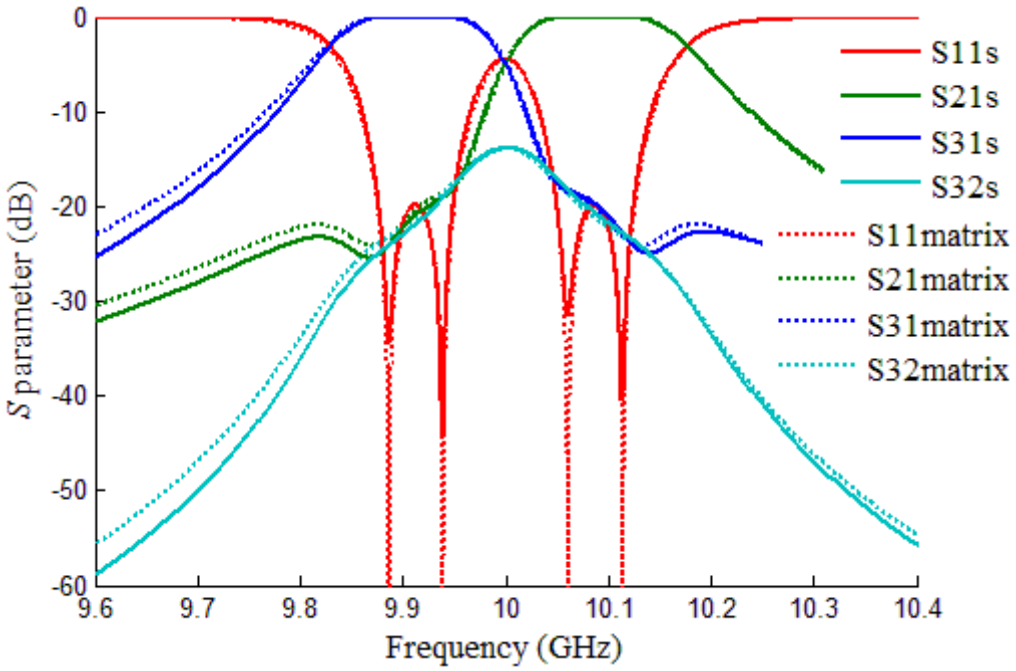

(c)

Figure 6.17 (a) Schematic, (b) Top view of the rectangular waveguide circuit in Step Four. d_{e3} is the width of the iris to tune. l_4 is the length of the cavity resonator to tune. (c) Response comparison between the tuned results (in solid lines) and the objective ones (in dotted lines).

The final response of the diplexer after the Step Tune method is given in Figure 6.17(c). The simulation results are given in solid line. The results in dotted line are calculated from the coupling matrix. The simulation results agree well with the coupling matrix ones.

The optimised dimensions of the 4th order cross-coupled diplexer are given in Table 6.6.

Table 6.6 Dimensions of X-band 4-resonator diplexer with cross couplings (Unit: mm). All the corners have the same radius of 1.6 mm, the thickness of all the coupling irises are 2 mm.

a	b	d_{e1}	d_{e2}	d_{e3}	d_{12}	d_{13}
22.86	10.16	10.406	10.391	9.474	6.560	6.644
d_{14}	d_{23}	d_{24}	l_1	l_2	l_3	l_4
7.413	6.350	7.033	16.146	18.271	36.107	18.088

This device has been fabricated and tested. The result is given in Figure 6.18; the X-band diplexer is made from the aluminium ($\text{conductivity} = 3.56 \times 10^7 \text{(S/m)}$).

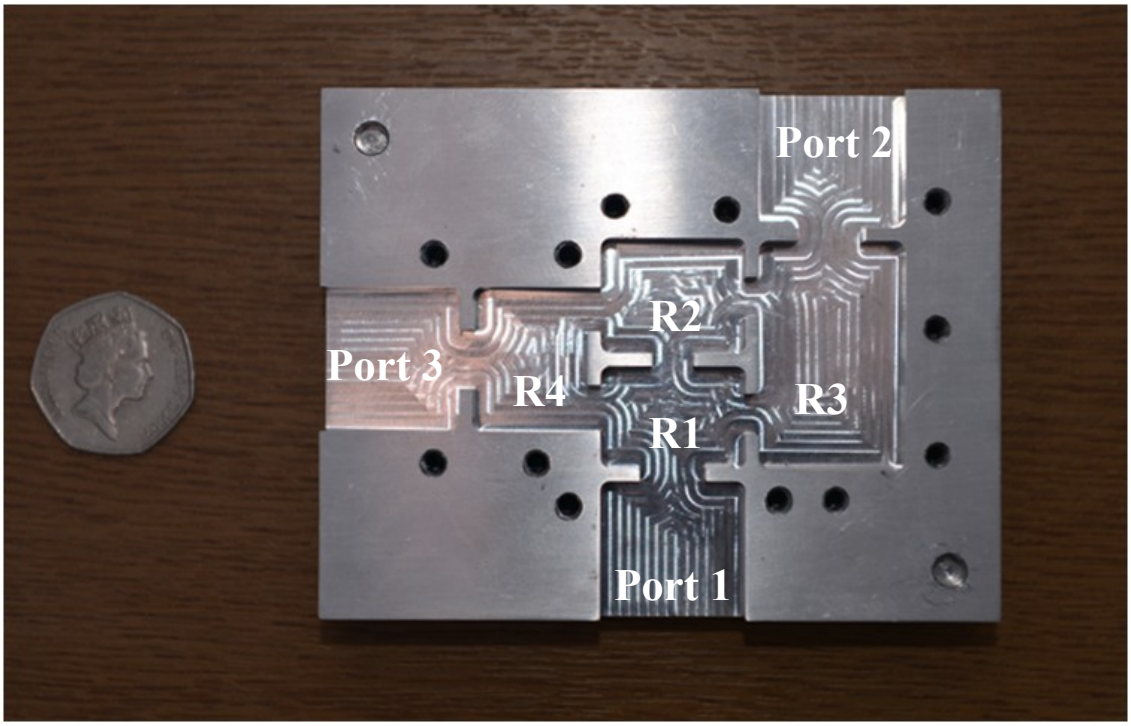

Figure 6.18 Photo of the fabricated X-band diplexer (top cover removed) [4].

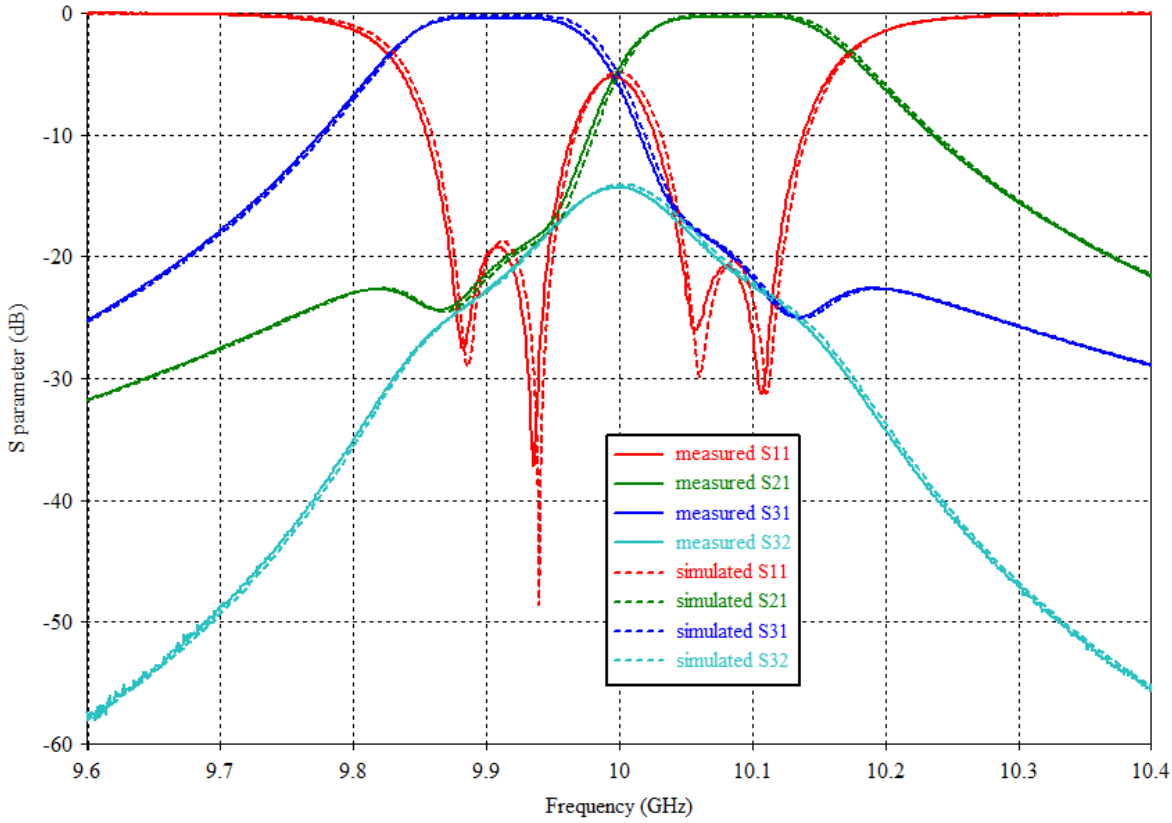

Figure 6.19 Response comparison between the measured results and the simulation.

As given in Figure 6.19, the measurement results are shown as solid lines and the simulation ones are in dashed lines. The measurement results agree well with the simulations.

The insertion loss comparison between the measured result and the simulation is given in Figure 6.20. In comparison with simulations, the measured insertion loss is about 0.2 dB higher at the middle of the left passband and 0.15 dB higher at the middle of the right passband. Both the roughness of the cavity surface and a poor contact between the two parts of the device lead to the additional insertion loss of the measured results [4]. The simulation value is obtained from CST simulation employing aluminium as the lossy material ($\text{conductivity} = 3.56 \times 10^7 \,(\text{S/m})$).

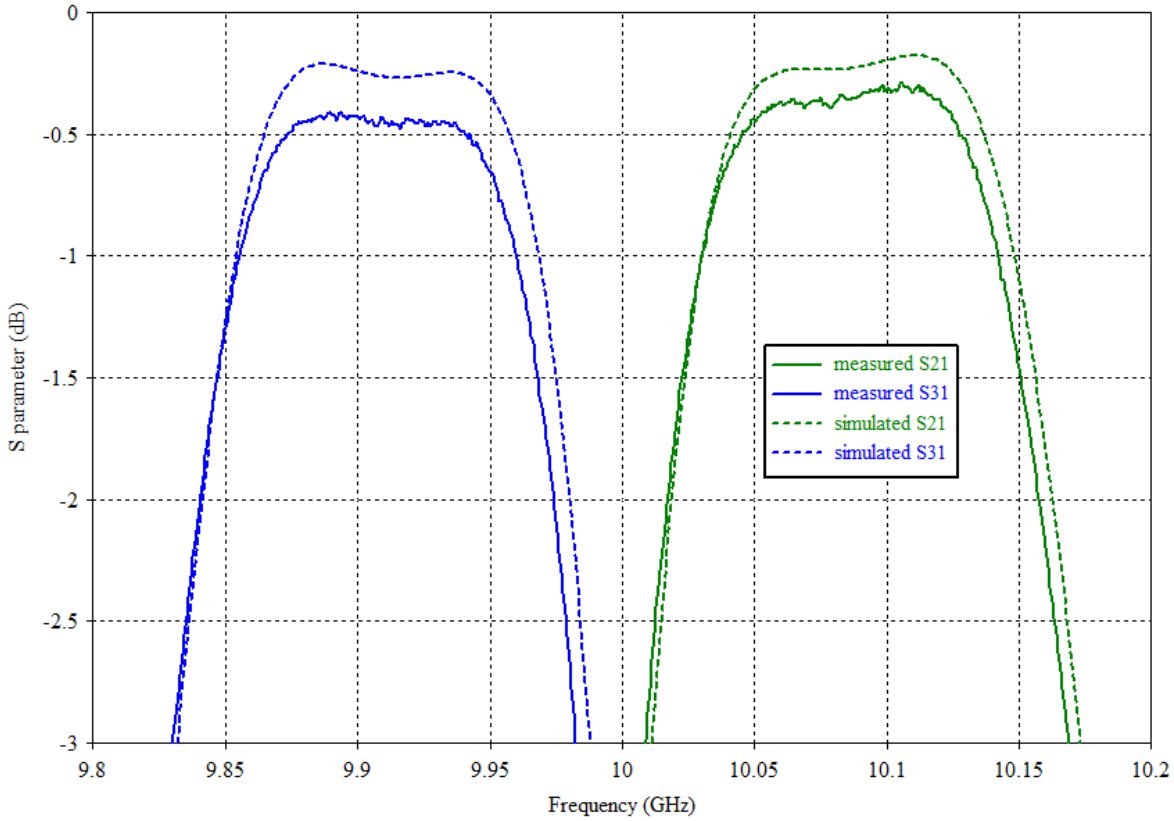

Figure 6.20 Comparison of insertion loss between the measurement and simulation.

[1] W. Xia, X. Shang, and M. J. Lancaster., "Responses comparisons for coupled-resonator based diplexers," in *Passive RF and Microwave Components, 3rd Annual Seminar on*, 2012, pp. 67-75.

[2] U. Rosenberg, "New `Planar' waveguide cavity elliptic function filters," in *Microwave Conference, 1995. 25th European*, 1995, pp. 524-527.

[3] X. Shang, W. Xia, and M. J. Lancaster, "The design of waveguide filters based on cross-coupled resonators," *Microwave and Optical Technology Letters,* vol. 56, pp. 3-8, 2014.

[4] W. Xia, X. Shang, and M. J. Lancaster, "All-resonator-based waveguide diplexer with cross-couplings," *Electronics Letters,* vol. 50, pp. 1948-1950, 2014.

Chapter 7 Multiplexer Implementation

In this chapter, the design procedure of a 4-channel multiplexer with a Tree Topology is presented. In Section 1, one of the practical splitting topologies is chosen to design the multiplexer. The coupling matrix of the multiplexer is given in Section 2. In Section 3, a rectangular waveguide based X-band multiplexer is presented in a zigzag topology, which is similar to the diplexer topology given in Chapter 5. The multiplexer is optimised by using the Step Tune method in Section 4. The multiplexer is fabricated in the workshop and the results are given in Section 5.

7.1 Splitting Topology of the Multiplexer

The design of a 4-channel multiplexer with a Tree Topology has 3 possible splitting topologies with the least number of resonators. These topologies are shown in Figure 7.1.

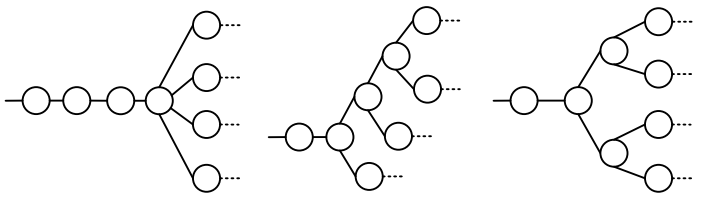

Figure 7.1 Different splitting topologies of the multiplexers. Each circle represents a resonator. Each line between resonators is the coupling element. (a) Topology I: Channels splitting from a single resonator. (b) Topology II and (c) Topology III limit the maximum number of couplings associated with one resonator to 3.

As given in Figure 7.1(a), one of the resonators in Topology I has 5 couplings. It is difficult to design such coupling structure due to the physical implementation of making 5 couplings. Topology II and III have no more than 3 couplings associated with each resonator. Both of these two topologies can be translated into the real physical structures. Topology II is an asymmetric structure while Topology III is a symmetric one. A coupling matrix with a

symmetric structure will have fewer variables in the optimisation based on its symmetry (See Chapter 4). The optimisation program converges to a result more quickly with a lower number of variables. Thus, in the light of a practical symmetric topology, Topology III is chosen as the splitting structure of the multiplexer.

7.2 Coupling Matrix of the Multiplexer

The prototype multiplexer has specifications with normalised cut-off frequencies of the 4 passbands at [-1, -0.75], [-0.417, -0.167], [0.167, 0.417] and [0.75, 1], and a return loss of the 4 passbands of 20 dB. The specifications of the physical multiplexer are a centre frequency of f_c=10 GHz and an overall fractional bandwidth FBW=0.024.

From the specifications, the order of each multiplexer channel is determined to be 4. According to the splitting topology in Figure 7.1(c), the desired schematic of the complete multiplexer is shown in Figure 7.2.

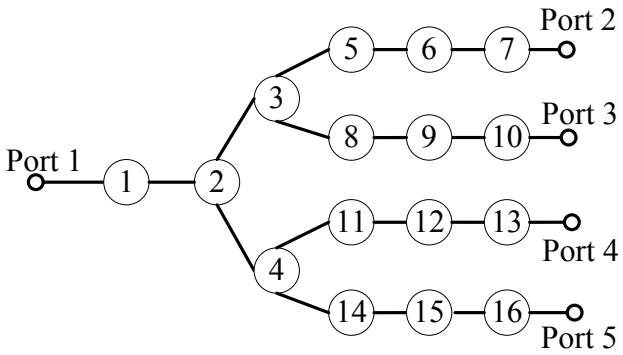

Figure 7.2 Schematic of the 16th order 4-channel multiplexer.

The coupling matrix of the multiplexer is given in (7.1) below. Each non-zero entry is denoted as x.

	*P*1	1	2	3	4	5	6	7	8	9	10	11	12	13	14	15	16	*P*2	*P*3	*P*4	*P*5
*P*1		x																			
1	x		x																		
2		x		x	x																
3			x	x		x			x												
4			x		x							x			x						
5				x		x	x														
6						x	x	x													
7							x	x										x			
8				x					x	x											
9									x	x	x										
10										x	x								x		
11						x						x	x								
12												x	x	x							
13													x	x						x	
14					x										x	x					
15															x	x	x				
16																x	x				x
*P*2								x													
*P*3											x										
*P*4														x							
*P*5																	x				

(7.1)

In (7.1), $P1$ is the source port. $P2$ to $P5$ are the load ports. $m_{P1,1} = 1/\sqrt{q_{e1}}$, $m_{P2,7} = 1/\sqrt{q_{e2}}$, $m_{P3,10} = 1/\sqrt{q_{e3}}$, $m_{P4,13} = 1/\sqrt{q_{e4}}$, $m_{P5,16} = 1/\sqrt{q_{e5}}$.

The coupling matrix with the normalised responses is obtained by the local optimisation method described in Chapter 4. The entry values of the coupling matrix are given in Table 7.1.

Table 7.1 The coupling values of the multiplexer with the normalised responses.

$m_{1,2}$	$m_{2,3}$	$m_{2,4}$	$m_{3,5}$	$m_{5,6}$	$m_{6,7}$	$m_{3,8}$
0.7263	0.4002	0.4002	0.1745	0.0928	0.1151	0.1314
$m_{8,9}$	$m_{9,10}$	$m_{4,11}$	$m_{11,12}$	$m_{12,13}$	$m_{4,14}$	$m_{14,15}$
0.0885	0.1139	0.1314	0.0885	0.1139	0.1745	0.0928
$m_{15,16}$	$m_{3,3}$	$m_{4,4}$	$m_{5,5}$	$m_{6,6}$	$m_{7,7}$	$m_{8,8}$
0.1151	0.4476	-0.4476	0.8195	0.8674	0.8713	0.3028
$m_{9,9}$	$m_{10,10}$	$m_{11,11}$	$m_{12,12}$	$m_{13,13}$	$m_{14,14}$	$m_{15,15}$
0.2928	0.2924	-0.3028	-0.2928	-0.2924	-0.8195	-0.8674

$m_{16,16}$	q_{e1}	q_{e2}	q_{e3}	q_{e4}	q_{e5}
-0.8713	1.8622	7.4078	7.4964	7.4964	7.4078

The normalised responses of the multiplexer are given in Figure 7.3 and Figure 7.4.

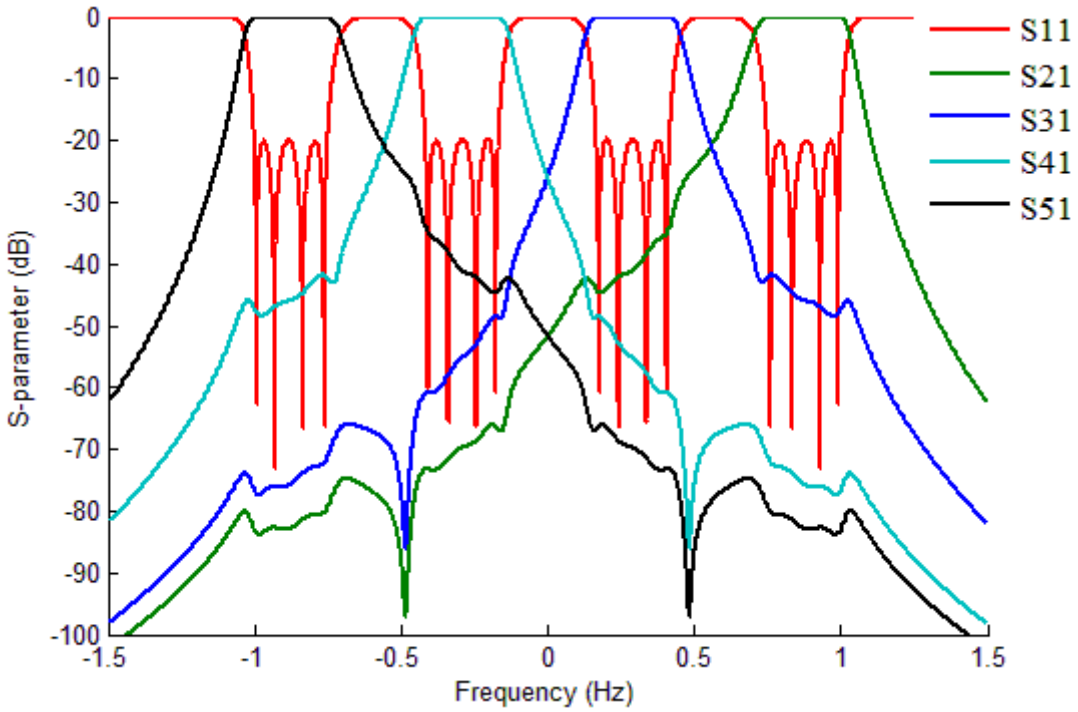

Figure 7.3 S_{11} to S_{51} of the multiplexer with normalised response.

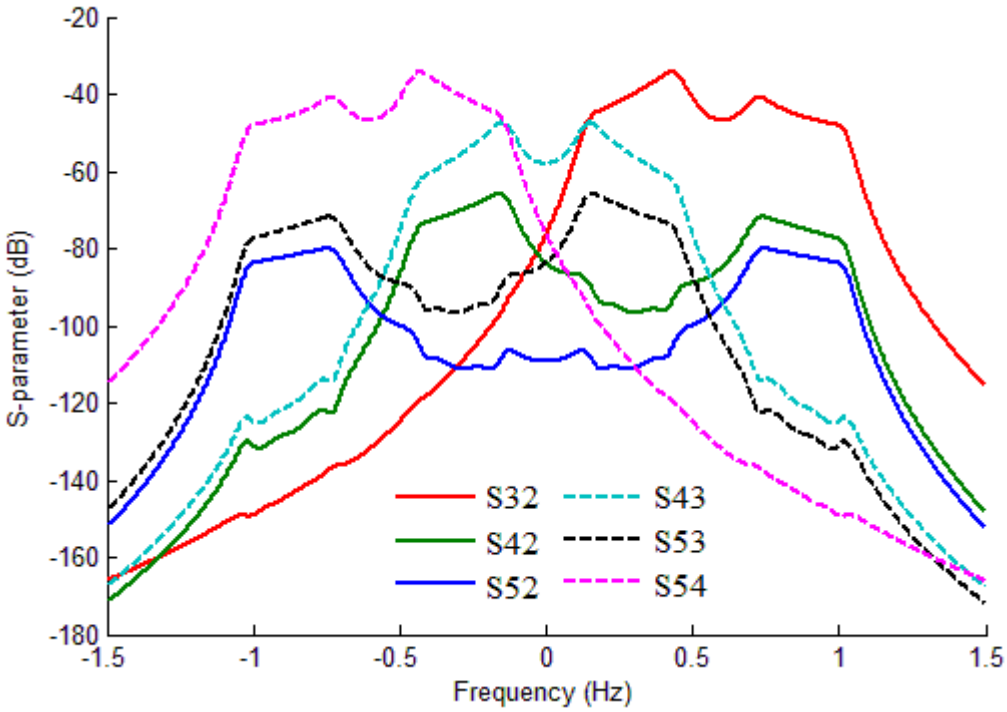

Figure 7.4 Isolations of the multiplexer with normalised response.

As shown in Figure 7.3, the response of the multiplexer, which has no cross coupling, has unexpected transmission zeros on the stop-band. The inter-reaction between the adjacent channels possibly leads to this.

After the frequency transformation using equation (3.69), the response of the multiplexer is given in Figure 7.5. The entry values of the new coupling matrix are given in Table 7.2.

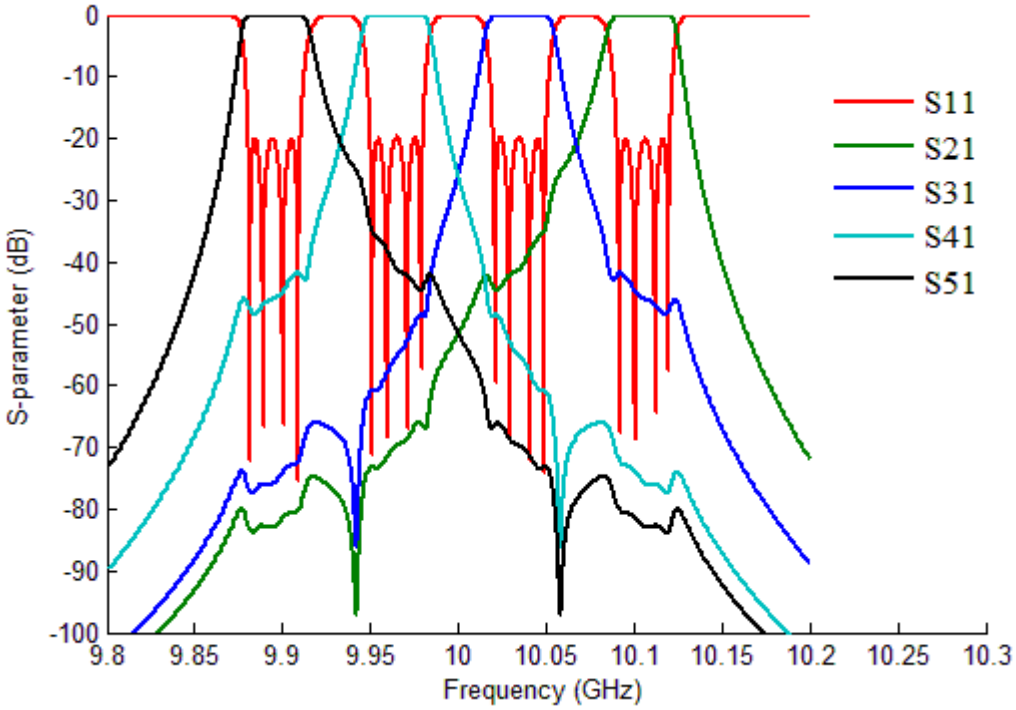

Figure 7.5 S-parameter of the multiplexer after frequency transformation.

Table 7.2 The coupling values of the multiplexer after the frequency transformation.

	$M_{1,2}$	$M_{2,3}$	$M_{2,4}$	$M_{3,5}$	$M_{5,6}$	$M_{6,7}$	$M_{3,8}$
value	0.0174	0.0096	0.0096	0.0042	0.0022	0.0028	0.0032
	$M_{8,9}$	$M_{9,10}$	$M_{4,11}$	$M_{11,12}$	$M_{12,13}$	$M_{4,14}$	$M_{14,15}$
value	0.0021	0.0027	0.0032	0.0021	0.0027	0.0042	0.0022
	$M_{15,16}$	$M_{3,3}$	$M_{4,4}$	$M_{5,5}$	$M_{6,6}$	$M_{7,7}$	$M_{8,8}$
value	0.0028	0.0107	-0.0107	0.0197	0.0208	0.0209	0.0073
	$M_{9,9}$	$M_{10,10}$	$M_{11,11}$	$M_{12,12}$	$M_{13,13}$	$M_{14,14}$	$M_{15,15}$
value	0.0070	0.0070	-0.0073	-0.0070	-0.0070	-0.0197	-0.0208

	$M_{16,16}$	Q_{e1}	Q_{e2}	Q_{e3}	Q_{e4}	Q_{e5}
value	-0.0209	77.59	308.66	312.35	312.35	308.66

According to equation (3.63) and the self couplings $M_{i,i}$ given in Table 7.2, the resonant frequency f_i of each cavity resonator is calculated and listed in Table 7.3.

Table 7.3 Resonant frequencies of the resonators.

Resonator	R1	R2	R3	R4
f_i (GHz)	10.000	10.000	10.054	9.947
Resonator	R5	R6	R7	R8
f_i (GHz)	10.099	10.105	10.105	10.037
Resonator	R9	R10	R11	R12
f_i (GHz)	10.035	10.035	9.964	9.965
Resonator	R13	R14	R15	R16
f_i (GHz)	9.965	9.902	9.897	9.896

7.3 Rectangular Waveguide Multiplexer in a Zigzag Topology

The coupling matrix discussed in the previous section has been used for a 16^{th} order rectangular waveguide multiplexer working at X-band. It has been fabricated and tested. Similar to the 10^{th} order diplexer topology in Chapter 5, the resonators of the multiplexer are coupled in a zigzag topology in order to make the device more compact. The zigzag topology of the multiplexer is given in Figure 7.6(a). In order to facilitate the CNC milling, an H-plane topology with all inductive irises is chosen. The top view of the multiplexer in the rectangular waveguide circuit is given in Figure 7.6(b).

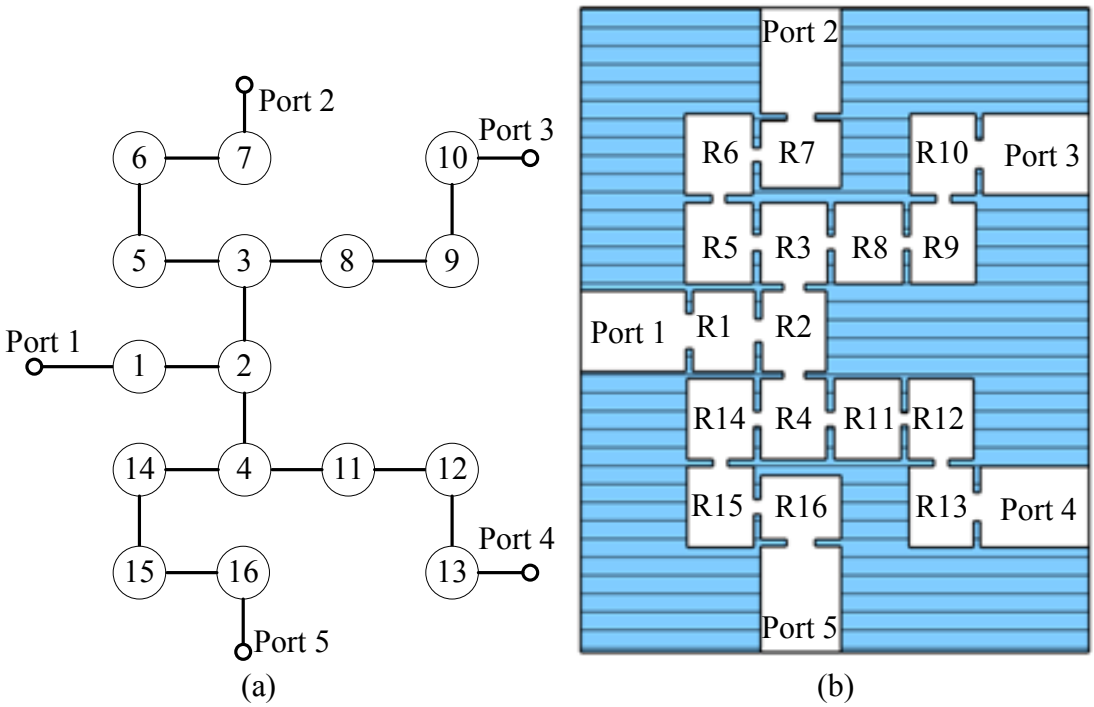

(a) (b)

Figure 7.6 (a) Structure and (b) its top view of the multiplexer.

The methodology of obtaining the initial values of each physical dimension (the length l of each cavity and the width d of each coupling iris) of the multiplexer is presented in Chapter 5.

7.4 Step Tune Method

Similar to the previous chapters, the multiplexer is optimised by using the Step Tune method. Each step, including its topology, the top view of the rectangular circuit and the desired response, is given in Figure 7.7 to Figure 7.12. During the Step Tune, the material is set to be the PEC.

Note as the circuits in Figure 7.7 to Figure 7.11 are not well-matched, the insertion loss of each channel is very high leading to a flat reflection response $S_{1,1}$ of each circuit. This is of course no problem and inherent in the Step Tune process.

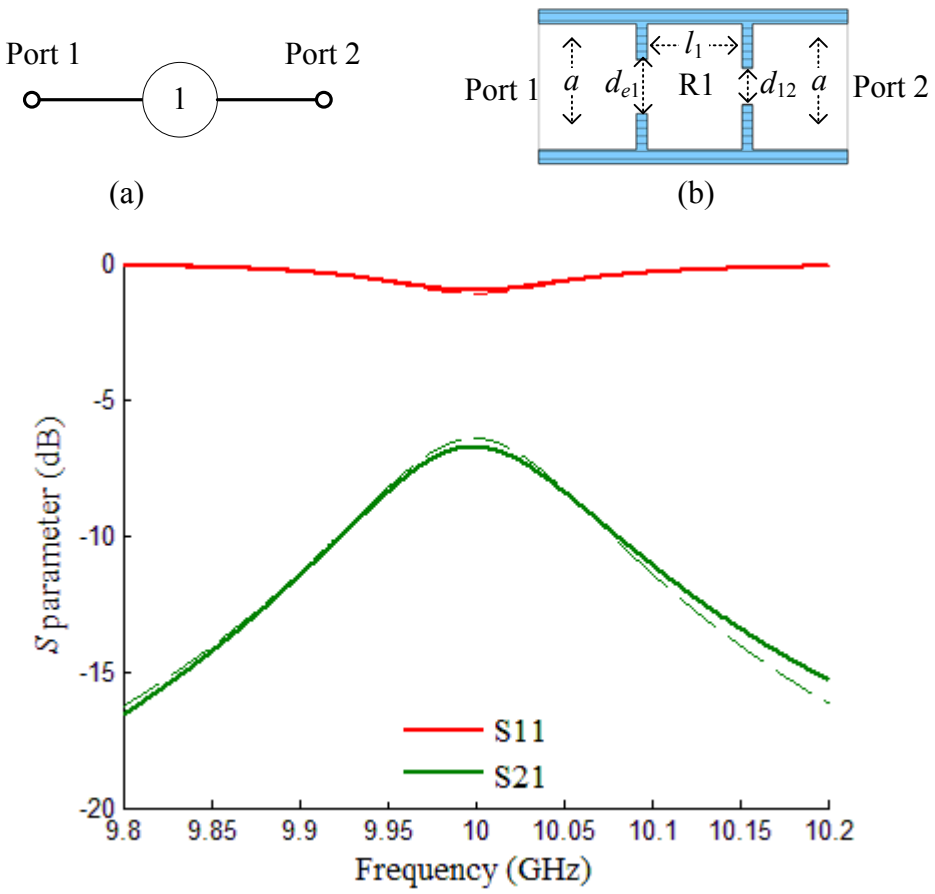

Figure 7.7 (a) Schematic, (b) Top view of the rectangular waveguide circuit in Step One. d_{e1} and d_{12} are the width of the irises to tune. l_1 is the length of the cavity resonator to tune. a=22.86mm is the standard width of WR-90. (c) Response comparison between the tuned results (in solid lines) and its objective ones (in dashed lines).

Resonator 1(R1) is tuned in Step One. Its schematic is given in Figure 7.7(a). As given in Figure 7.7(b), there are three physical dimensions (the width of the coupling irises d_{e1} and d_{12}, and the length of the cavity l_1) to be tuned. The aim of the tuning is to make the simulation results satisfy its objective counterpart obtained from the coupling matrix. The final results of Step One are given in Figure 7.7(c). The simulation results (in solid lines) meet well with the objective ones (in dashed lines).

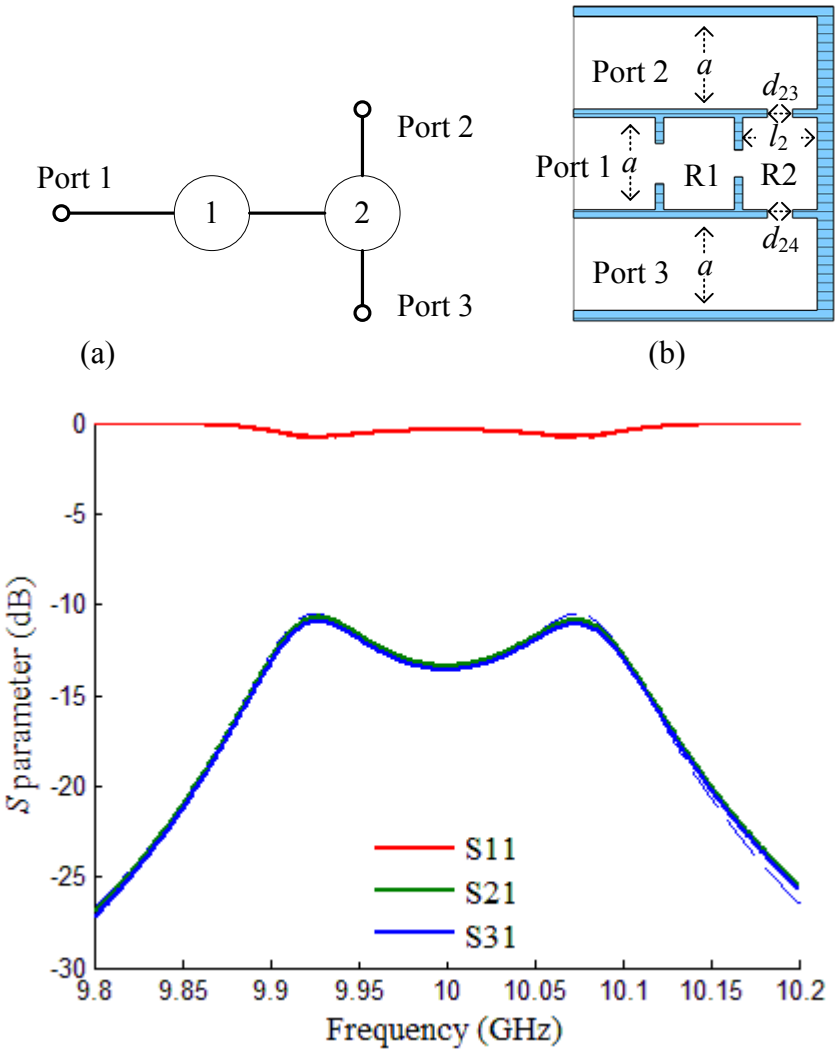

Figure 7.8 (a) Schematic, (b) Top view of the rectangular waveguide circuit in Step Two. d_{23} and d_{24} are the width of the irises to tune. l_2 is the length of the cavity resonator to tune. (c) Response comparison between the tuned results (in solid lines) and its objective ones (in dashed lines).

After finishing Step One, Resonator 2(R2) is added successively and the tuning work moves to Step Two. The schematic of Step Two is given in Figure 7.8(a). As given in Figure 7.8(b), there are three new physical dimensions (width of the iris d_{23} and d_{24}, and the length of the cavity l_2) to be tuned. The values of the old dimensions (d_{e1}, d_{12} and l_1) are kept constant. After the tuning, as given in Figure 7.8(c), the simulation response (in solid lines) gets very close to its objective response (in dashed lines) from the coupling matrix.

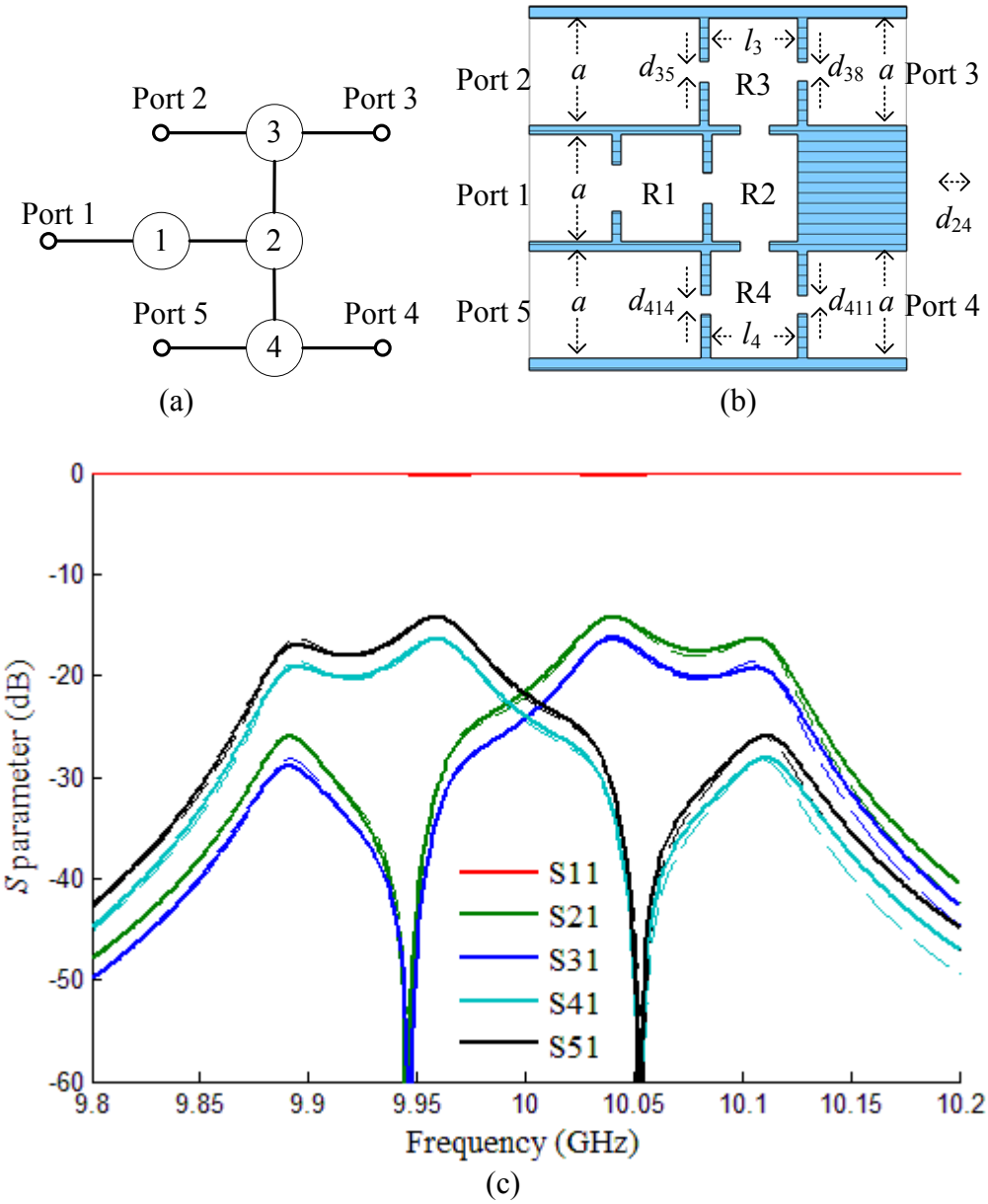

Figure 7.9 (a) Schematic, (b) Top view of the rectangular waveguide circuit in Step Three. d_{35}, d_{38}, d_{411} and d_{414} are the width of the irises to tune. l_3 and l_4 are the length of the cavity resonators to tune. (c) Response comparison between the tuned results (in solid lines) and its objective ones (in dashed lines).

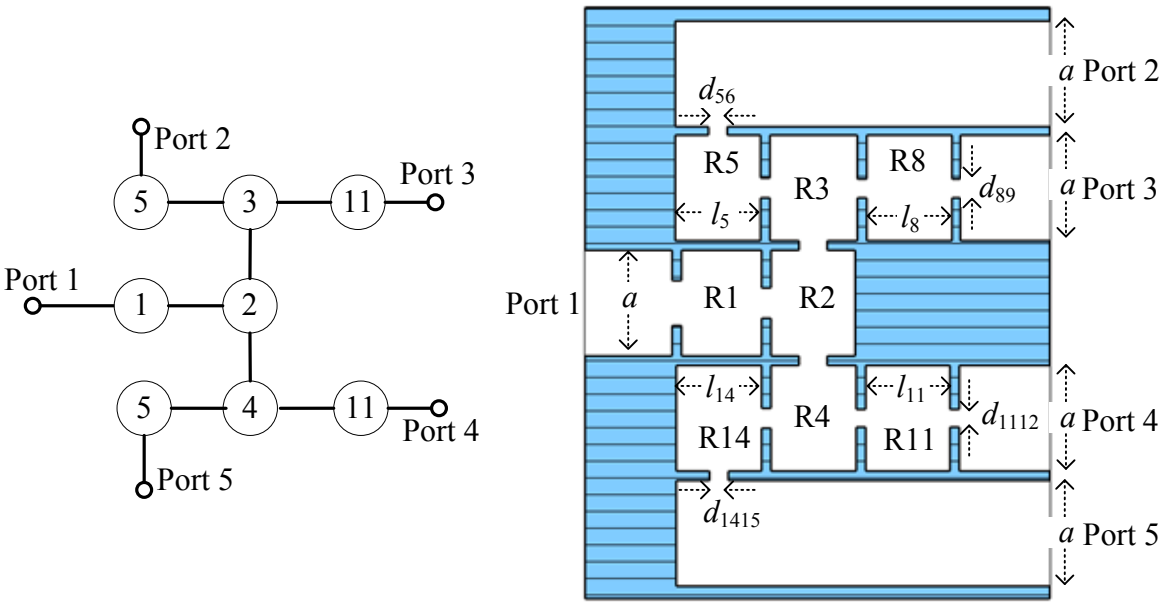

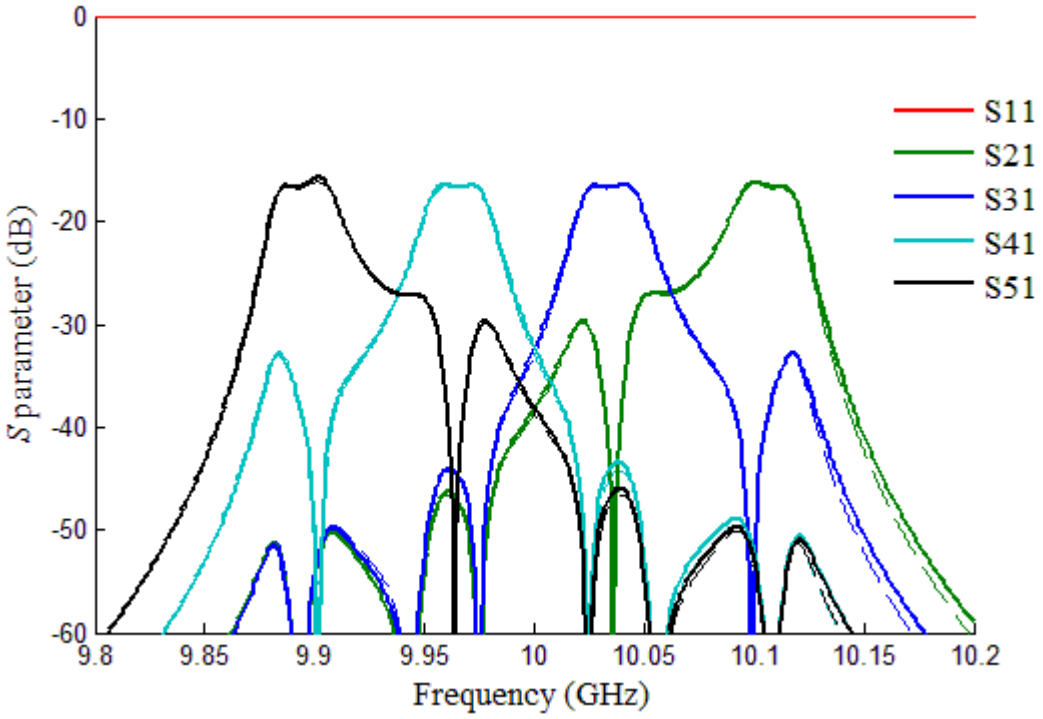

(c)

Figure 7.10 (a) Schematic, (b) Top view of the rectangular waveguide circuit in Step Four. d_{56}, d_{89}, d_{1112} and d_{1415} are the width of the irises to tune. l_5, l_8, l_{11} and l_{14} are the length of the cavity resonators to tune. (c) Response comparison between the tuned results (in solid lines) and its objective ones (in dashed lines).

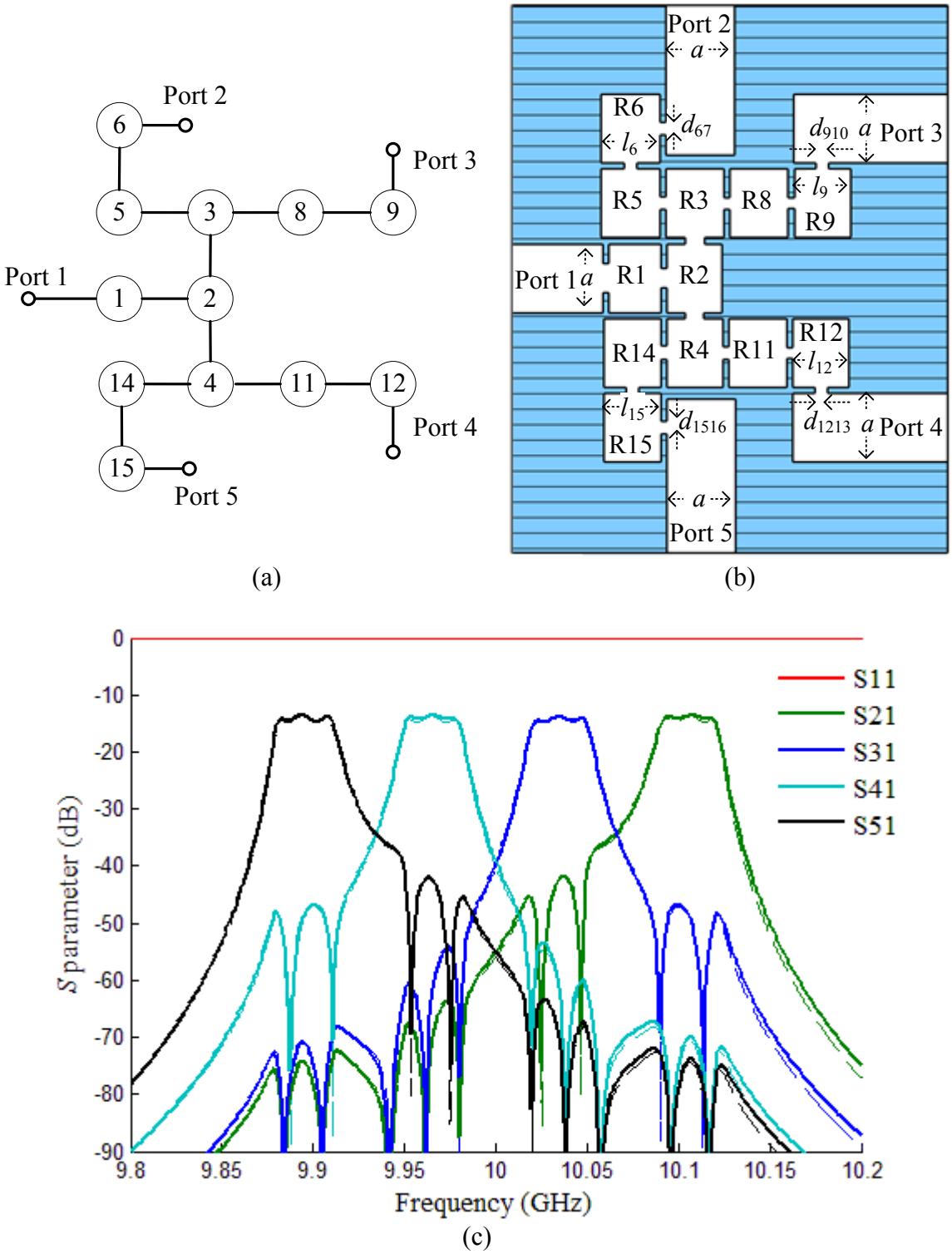

Figure 7.11 (a) Schematic, (b) Top view of the rectangular waveguide circuit in Step Five. d_{67}, d_{910}, d_{1213} and d_{1516} are the width of the irises to tune. l_6, l_9, l_{12} and l_{15} are the length of the cavity resonators to tune. (c) Response comparison between the tuned results (in solid lines) and its objective ones (in dashed lines).

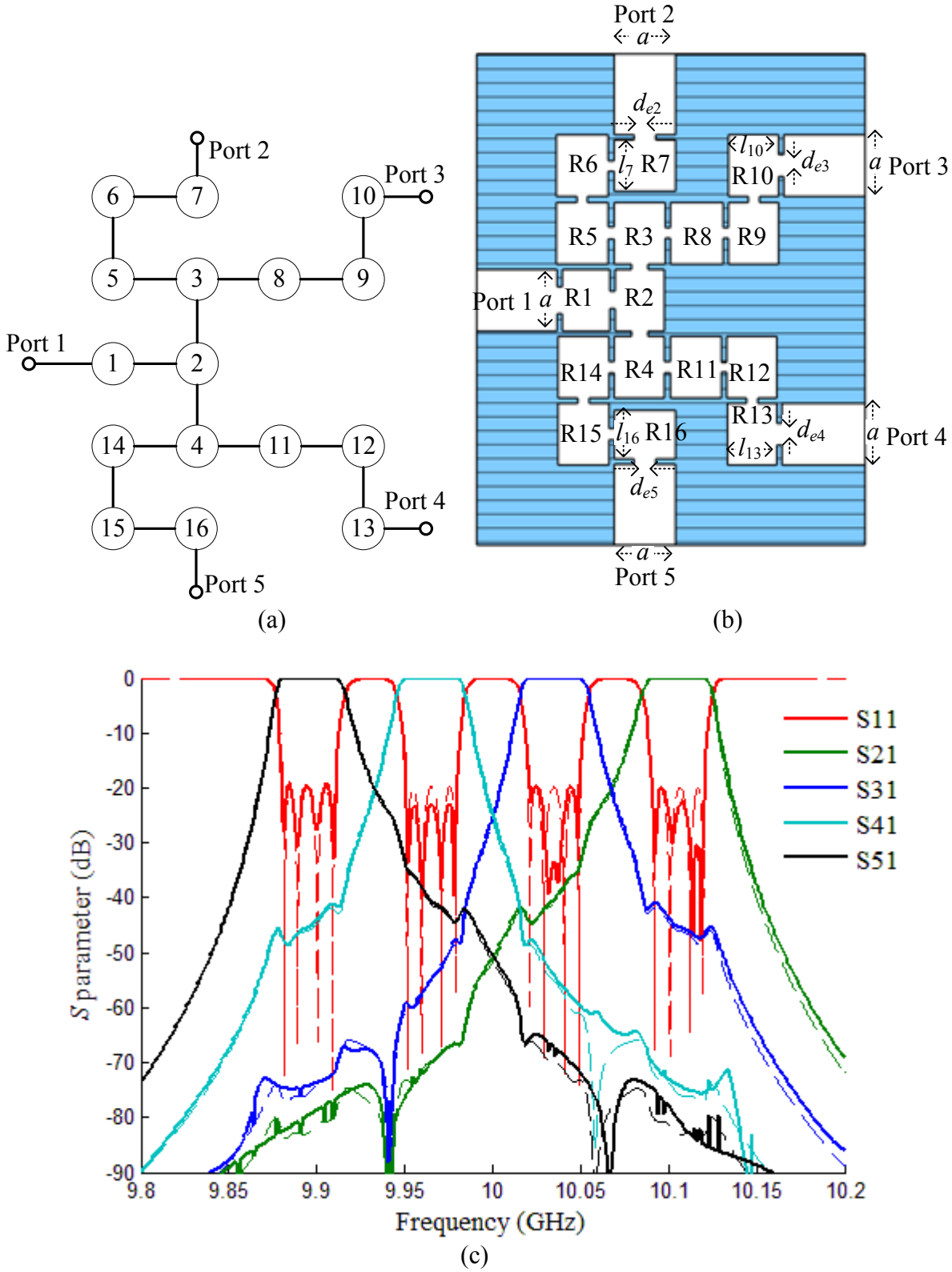

Figure 7.12 (a) Schematic, (b) Top view of the rectangular waveguide circuit in Step. d_{e2}, d_{e3}, d_{e4} and d_{e5} are the width of the irises to tune. l_7, l_{10}, l_{13} and l_{16} are the length of the cavity resonators to tune. (c) Response comparison between the tuned results (in solid lines) and the ones calculated by the coupling matrix (in dashed lines)

The process continues and more resonators are added successively and tuned in the steps shown in Figure 7.9 to Figure 7.12.

After the Step Tune, the final response of the multiplexer is given in Figure 7.13 in solid lines. The material of the device is chosen as the aluminium ($\text{conductivity} = 3.56\times10^{7}(\text{S/m})$). The results in dashed lines are calculated from the coupling matrix. The simulation results agree well with the coupling matrix ones.

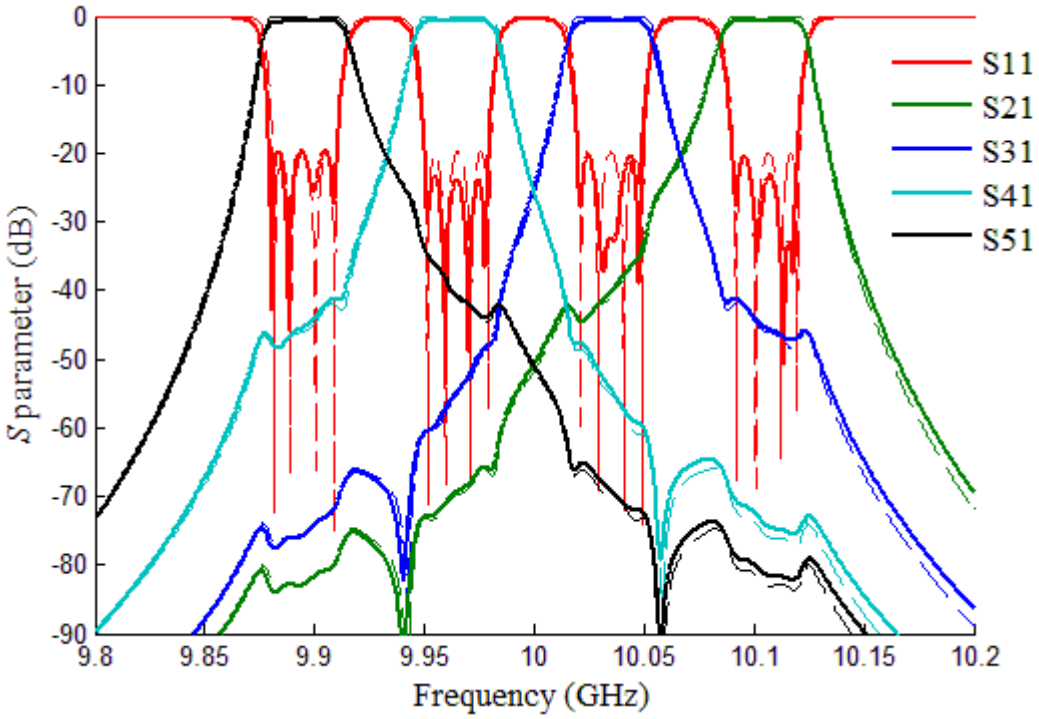

Figure 7.13 Response comparison between the simulation (in solid lines) and coupling matrix (in dashed lines) with the Aluminium used as the material.

The insertion loss and return loss comparison of each channel of the multiplexer are given in Figure 7.14. As shown in Figure 7.14(a), the simulated insertion loss of each channel is about 0.7 dB and as shown Figure 7.14(b), all the reflection zeros are evident and the return loss of each passband is no less than 20 dB.

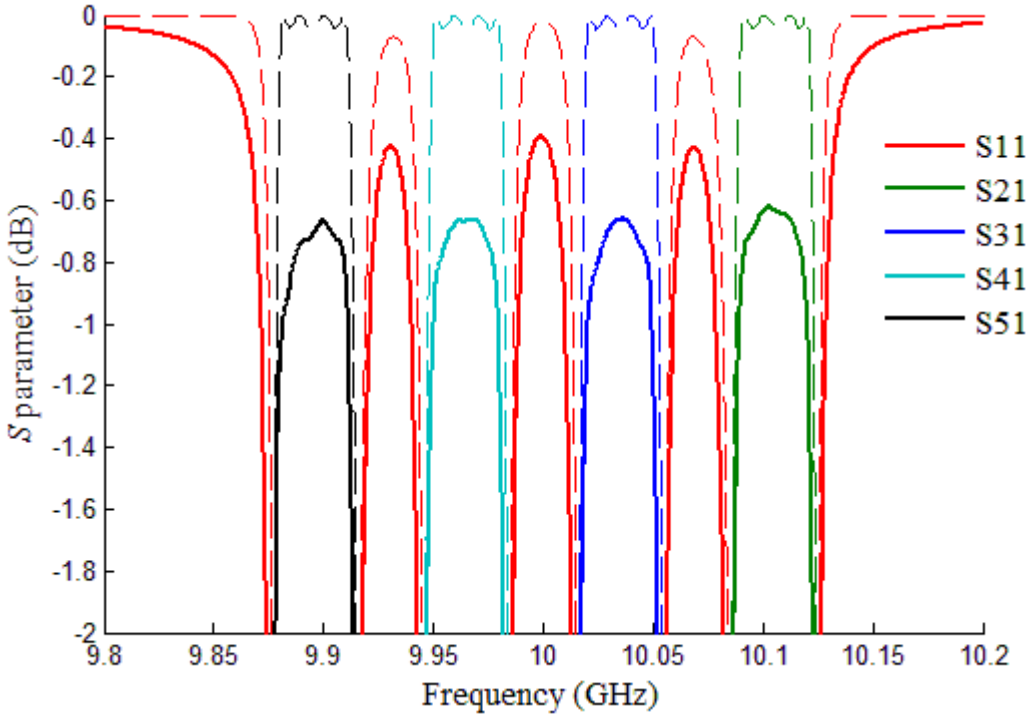

(a)

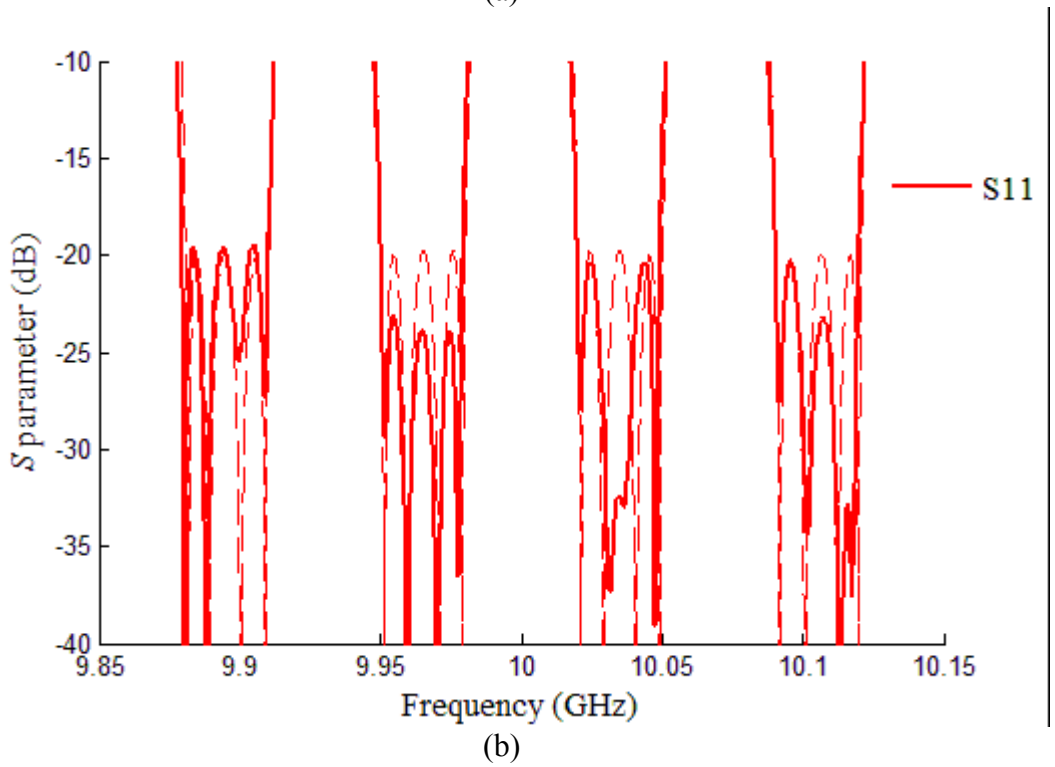

(b)

Figure 7.14 (a) Insertion loss and (b) return loss comparison between the simulation response with conductor loss (in solid lines) and the coupling matrix one with no loss (in dashed lines).

The values of each physical dimension of the final result are given in Table 7.4. *d* is the width

of the iris and l is the cavity length.

Table 7.4 Dimensions of the X-band 16th order multiplexer (unit: mm). All the corners have the same radius of 1.6 mm, the thickness of all the coupling irises are 2 mm.

	a	b	d_{e1}	d_{e2}	d_{e3}	d_{e4}	d_{e5}
step-tune	22.86	10.16	9.79	7.80	7.88	7.88	7.90
	d_{12}	d_{23}	d_{24}	d_{35}	d_{56}	d_{67}	d_{38}
step-tune	6.37	6.00	6.05	4.23	3.95	4.00	3.94
	d_{89}	d_{910}	d_{411}	d_{1112}	d_{1213}	d_{414}	d_{1415}
step-tune	3.55	4.14	3.97	3.57	4.16	4.25	4.03
	d_{1516}	l_1	l_2	l_3	l_4	l_5	l_6
step-tune	4.02	17.37	18.43	18.78	19.13	19.09	19.10
	l_7	l_8	l_9	l_{10}	l_{11}	l_{12}	l_{13}
step-tune	18.27	19.32	19.36	18.47	19.56	19.60	18.71
	l_{14}	l_{15}	l_{16}	t			
step-tune	19.77	19.82	18.96	2			

7.5 Fabrication and Measurement

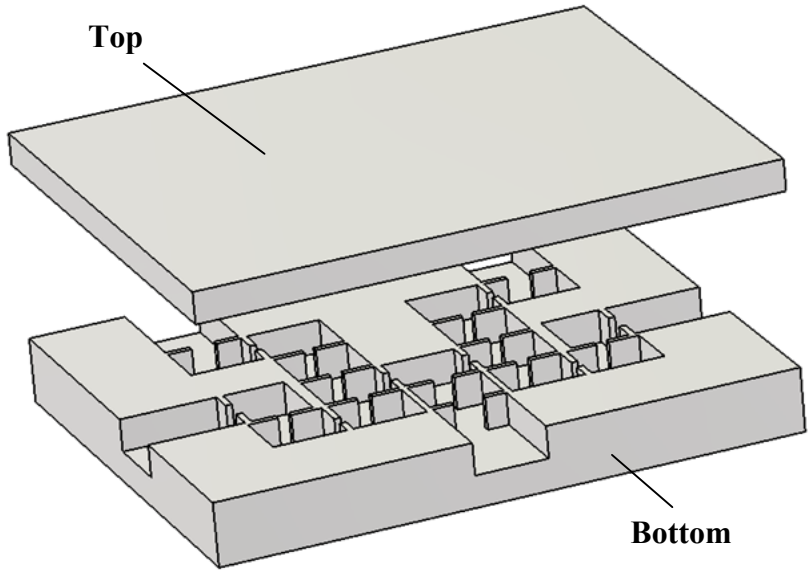

Figure 7.15 3D structure of the multiplexer

As shown in Figure 7.15, the device is split into two pieces, the bottom part and the top cover.

This device has been fabricated. Its bottom part is shown in Figure 7.16. The X-band multiplexer is made from aluminium. Its total size is 182.1×148.0×41.4 (unit:mm).

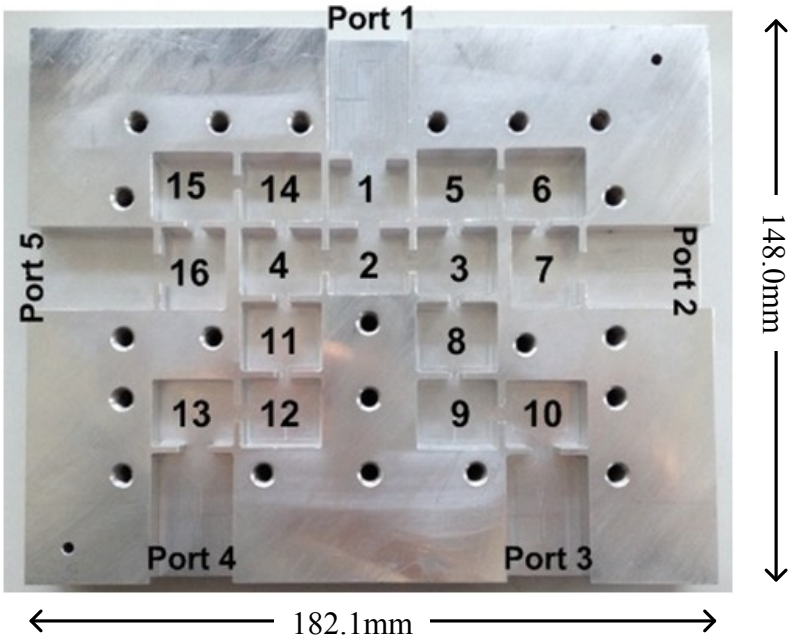

Figure 7.16 Photograph of the fabricated X-band multiplexer (top cover removed). [1]

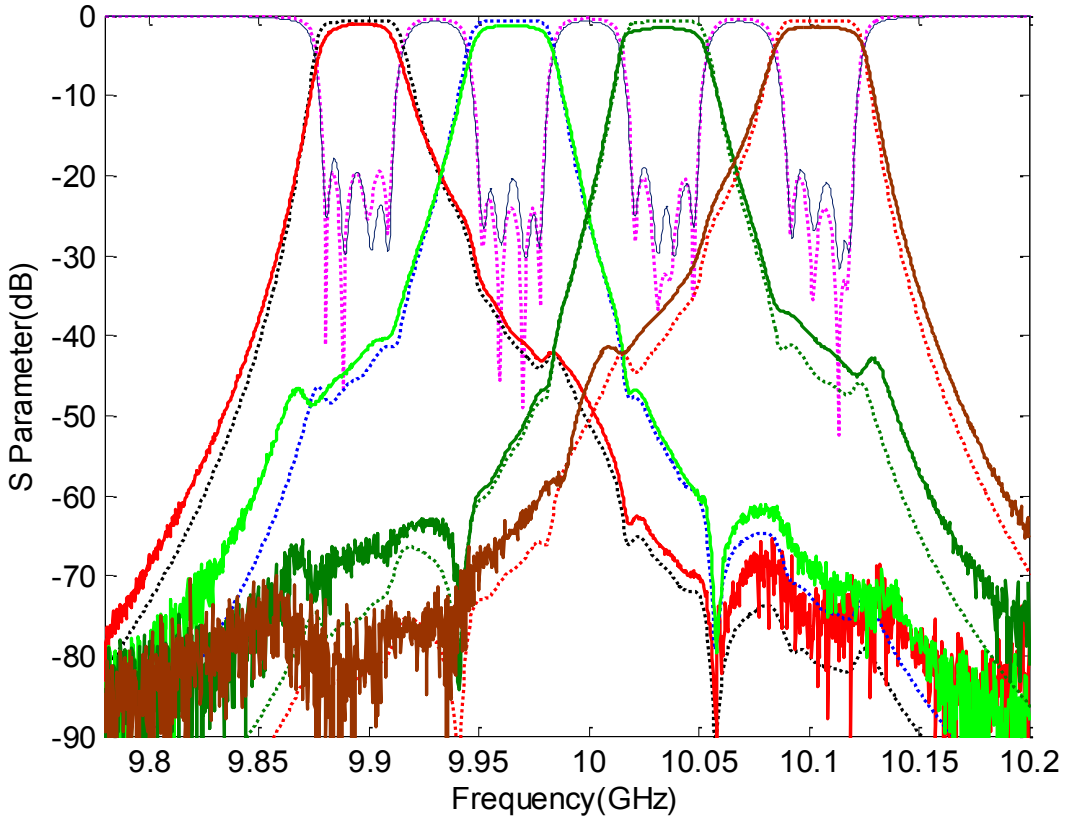

Figure 7.17 Measurement results with tuning screws (in solid line) and simulation results (in dashed line) of the multiplexer. [1]

The tuning screws have been used to compensate the manufacturing errors. The measured results after tuning are given in Figure 7.17. The expected passband insertion loss is 0.7 dB from CST as discussed above and the measured insertion loss of each channel is about 1.5 dB, 1.9 dB, 1.6 dB and 1.8 dB higher[1]. The noticeable difference is mainly contributed by a number of factors. Firstly, the imperfect contact at the joints of the device leads to the additional loss as the multiplexer is split along the H-plane into two pieces (see Figure 7.15). When the current flow crosses the joints, the imperfect contact will lead to the additional loss[2]. Secondly, the power radiation through the tuning screw holes drilled on the top cover has effect on increasing the total loss [1]. Thirdly, the material making up the filter is not perfectly smooth and may not have exactly the same conductivity as the aluminium used in the CST simulation.

[1] X. Shang, Y. Wang, W. Xia, and M. J. Lancaster, "Novel Multiplexer Topologies Based on All-Resonator Structures," *Microwave Theory and Techniques, IEEE Transactions on,* vol. 61, pp. 3838-3845, 2013.
[2] N. J. Cronin, *Microwave and optical waveguides*: Institute of Physics, 1995.

Chapter 8 Conclusions and Future Work

8.1 Conclusions

The work presented in this thesis can be classified into two categories: (i) the *n*+X coupling matrix of a multiplexer with the Tree Topology synthesised by a local optimisation technique and (ii) the multiplexer design using the Step Tune method and its implementation.

The first part is for the coupling matrix theory and its synthesis method. In Chapter 3, the *n*+X coupling matrix of an X-port circuit with *n* coupled resonators has been derived. Magnetic and Electric couplings have been respectively discussed. They are followed by a unified solution which is generalized for both types of couplings or mixed ones. Comparing to the general $n \times n$ coupling matrix, the extended *n*+X coupling matrix has the advantage of its generality. A resonator coupled to multiple ports, as well as a port coupled to multiple resonators, is able to be described by using the *n*+X matrix. A direct coupling between ports is also possible. The relationship between the *S*-parameters of a multi-port circuit and its coupling matrix has been found. The equations have been applied as the basis for the work in the later chapters of the thesis. With the help of the *n*+X coupling matrix, the circuit with (i) a port coupled to multiple resonators, (ii) a resonator coupled to multiple ports and/or (iii) a direct coupling between ports can be described.

The coupled resonator based multiplexers in this thesis are with the Tree Topology. Different from the conventional multiplexers, a multiplexer with the Tree Topology has no additional splitting network and the signal division is done through the coupled resonators, which also produce the filter characteristics. The removal of the additional splitting network reduces the total size of the multiplexer.

The concept of a multiplexer with the Tree Topology having a Chebyshev response is given in Chapter 4. This work has been subjected to a publication [1]. The multiplexer can be divided into 2 parts: (i) the stem part connecting to the shared ports and (ii) the branches connecting to the channel ports. For a diplexer with the Tree Topology, its stem part works as a dual-band bandpass filter [1]. It attenuates signals outside of two passbands and have little effect on splitting signals on these two bands [1]. The two branches of the diplexer work as Chebyshev filters with different centre frequencies. Each branch occupies one of the two passbands of the stem and attenuates signals outside of the passband of the branch [1]. The comparisons in Chapter 4 show the effect on the responses (isolations and bandwidths) of the diplexers with the Tree Topology by altering the number of resonators (length) of the stem and branches. The isolation becomes better with the increasing length of the branches. Also, the longer the length of branch, the closer the response is to the simple Chebyshev one.

A gradient based local optimisation technique is presented to generate the coupling matrix of the multiplexer with desired specifications. When the circuit is in a complex structure with a higher order, a good starting point of the coupling matrix is essential to avoid a local minimum. The principles given in Chapter 4 explain how to get the high quality initial coupling values of the diplexers with the Tree Topology. For diplexers having non-contiguous channels, the external quality factors at the input and two outputs can be calculated directly from the equations. The couplings on the stem can be initialised based on a close approximation. The coupling values on the branches are originated from the Chebyshev ones.

The Tree Topology can be extended to the multiplexers with asymmetric responses and topologies. Some examples are synthesised, including (i) a diplexer with a different return loss of each channel, (ii) a diplexer having a different order of each channel, (iii) a diplexer with contiguous channels and (iv) a triplexer.

The second part of the thesis is the multiplexer implementations using rectangular waveguides. Three devices have been fabricated. Their design procedures are separately given in Chapter 5 to Chapter 7. In order to facilitate the CNC milling, all of the three devices are designed in the H-plane planer waveguide topologies with all inductive irises. The zig-zag topologies are applied to make the three devices compact.

Traditionally, the initial dimensions of each component of the device are generated according to the coupling matrix. After putting all the physical dimensions together, an overall structure tuning is followed to get the desired response. Chapter 5 illustrates how to design a coupled resonator based rectangular waveguide circuit in the traditional way. An X-band 10-resonator rectangular waveguide diplexer is given as an example in Chapter 5. With a higher order and/or complex structure of the circuit, such tuning work consumes a lot of time and the convergence of the final result is not guaranteed.

To overcome the difficulties, a novel EM simulator based design technique, called Step Tune method, has been developed [2]. The procedures can be divided into several steps. By extracting the responses of a part of the circuit, we can simulate and tune the part at the first step. After finishing tuning the part of the circuit, we move on to the second step and one or more resonators are added successively to form a “new” part. The desired responses of the new part are extracted. It is followed by a further tuning work of the new part on the EM simulator. During the tuning work in the second step, the old physical dimensions which have been tuned previously are kept constant. This leads to a reduction of the total number of tuning dimensions in each iteration. The process continues and more resonators are added successively. After the Step Tune, the final simulation result of the whole device can be very close to the desired one calculated from the coupling matrix. The design technique has been subject to a publication [2]. The X-band 10-resonator diplexer in Chapter 5 has been

redesigned by using the Step Tune method. The simulation result of the new design has a great improvement over the previous one. The Step Tune method has provided a unique way to optimize multiport coupled resonator circuits and now makes possible more complex circuit topologies, including cross-coupled structures and multi-channel ones.

For the Tree Topology, there is a drawback that should be pointed out: the isolation between the two output ports of the diplexer decreases with respect to a classical diplexer implementation with a non-resonant junction (for the same overall number of resonators). In Chapter 6, a cross-coupled structure has been applied to improve the response of the diplexer with the Tree Topology. Comparing to the traditional diplexer having a non-resonant junction, a slightly better isolation of the cross-coupled diplexer with the Tree Topology has been achieved. The negative coupling is generated based on the cavity transformation properties [3]. An X-band 4-resonator rectangular waveguide diplexer with cross couplings has been fabricated. The measured results agree well with the simulations. This work has been subject to a publication [4].

Possible splitting structures of the Tree Topology for more channels are discussed in Chapter 7. A practical symmetric splitting topology has been employed to design a 4-channel 16-resonator multiplexer. After using the Step Tune method, an X-band multiplexer based on rectangular waveguides has been fabricated. All the reflection poles are evident after the screw tuning. This work has been subject to a publication [5].

8.2 Future Work

First of all, the multiplexers with the Tree Topology should be extended to more channels with a higher order and a more complex topology. Since the coupling matrix is obtained by a local optimisation technique, the complexity of the optimisation work increases dramatically

with the increase number of resonators and a complex topology. Better strategies of obtaining the coupling matrix are worth exploring. One possible solution is to find the locations of the reflection poles by the polynomials. At the moment, the locations of the reflection poles are obtained by the optimisation. With the help of the polynomials, the poles can be found directly so as to reduce the total number of variables in the optimisation. Another way is to find a more accurate approximation of the starting point of the coupling matrix.

Considering the main application of multiplexers, is it possible to combine the multiplexers and the antennas together? A multiplexer is generally cascaded to an antenna for the signal transmission and reception. The combination removes the need of the additional matching circuit between the multiplexer and the antenna so as to reduce the total size of the device. This work is subject to a publication [6].

Transmission zeros are generally introduced by adding cross couplings into the circuit. As shown in Figure 7.3, however, the response of the multiplexer, which has no cross coupling, has unexpected transmission zeros on the stop-band. The inter-reaction between the adjacent channels possibly leads to this. It is worth exploring how to control their positions in the future work.

For the coupling matrix theory part, it is worth exploring whether the following work could be extended to the active circuits. Currently, the coupling matrix theory is only suited to the passive circuits. As much work [7-9] has been done on the amplifiers working at the microwave frequency range, a coupling matrix including the power gain elements will be useful in the design of the microwave circuits integrated with the amplifiers.

Furthermore, is it possible to describe a whole communication system with a coupling matrix? It is interesting if all the components of a narrow band wireless communication system,

including the antennas, the multiplexers, the power dividers, the couplers, the amplifiers, the converters, the isolators and the mixers, can be absorbed into a single coupling matrix.

[1] W. Xia, X. Shang, and M. J. Lancaster., "Responses comparisons for coupled-resonator based diplexers," in *Passive RF and Microwave Components, 3rd Annual Seminar on*, 2012, pp. 67-75.

[2] X. Shang, W. Xia, and M. J. Lancaster, "The design of waveguide filters based on cross-coupled resonators," *Microwave and Optical Technology Letters,* vol. 56, pp. 3-8, 2014.

[3] U. Rosenberg, "New `Planar' waveguide cavity elliptic function filters," in *Microwave Conference, 1995. 25th European*, 1995, pp. 524-527.

[4] W. Xia, X. Shang, and M. J. Lancaster, "All-resonator-based waveguide diplexer with cross-couplings," *Electronics Letters,* vol. 50, pp. 1948-1950, 2014.

[5] X. Shang, Y. Wang, W. Xia, and M. J. Lancaster, "Novel Multiplexer Topologies Based on All-Resonator Structures," *Microwave Theory and Techniques, IEEE Transactions on,* vol. 61, pp. 3838-3845, 2013.

[6] E. Nugoolcharoenlap, X. Shang, and M. J. Lancaster, "Design of Waveguide Aperture Antenna-Filters using Coupling Matrix Theory," *submitted to MTT*.

[7] T. Dao, S. Huettner, and A. Platzker, "A Low Phase Noise MMIC/Hybrid 3.0W Amplifier at X-Band," in *Microwave Symposium Digest, 1986 IEEE MTT-S International*, 1986, pp. 459-462.

[8] M. Abdolhamidi and M. Shahabadi, "X-Band Substrate Integrated Waveguide Amplifier," *Microwave and Wireless Components Letters, IEEE,* vol. 18, pp. 815-817, 2008.

[9] J. D. Albrecht, M. J. Rosker, H. B. Wallace, and T. Chang, "THz Electronics projects at DARPA: Transistors, TMICs, and amplifiers," in *Microwave Symposium Digest (MTT), 2010 IEEE MTT-S International*, 2010, pp. 1-1.

Appendix Publication List

- W. Xia, X. Shang, and M. J. Lancaster., "Responses comparisons for coupled-resonator based diplexers," in *Passive RF and Microwave Components, 3rd Annual Seminar on*, 2012, pp. 67-75.
- X. Shang, Y. Wang, W. Xia, and M. J. Lancaster, "Novel Multiplexer Topologies Based on All-Resonator Structures," *Microwave Theory and Techniques, IEEE Transactions on,* vol. 61, pp. 3838-3845, 2013.
- X. Shang, W. Xia, and M. J. Lancaster, "The design of waveguide filters based on cross-coupled resonators," *Microwave and Optical Technology Letters,* vol. 56, pp. 3-8, 2014.
- W. Xia, X. Shang, and M. J. Lancaster, "All-resonator-based waveguide diplexer with cross-couplings," *Electronics Letters,* vol. 50, pp. 1948-1950, 2014.

Responses Comparisons for Coupled-Resonator Based Diplexers

Wenlin Xia, Xiaobang Shang, Michael J. Lancaster

School of Electronic, Electrical and Computer Engineering, the University of Birmingham, U.K.

Email: wxx989@bham.ac.uk

Abstract

Previously we have proposed a novel coupled-resonator based multiplexer structure that eliminates the need for an additional common junction [2] such as a manifold, T-junction or power splitter. This new approach to multiplexer design is able to achieve reductions in the size and volume of the circuit. In this paper, the relationships between the responses and topologies of this novel type of diplexer structures are investigated.

Introduction

Diplexers and multiplexers are known as frequency selective components. They are used to combine or split signals from the shared port in a multi-port circuit. A diplexer is the simplest multiplexer being only two ports. Conventional diplexers are based on the combination of two channel filters with a common junction. A diplexer with T-junction is illustrated in Figure 1.

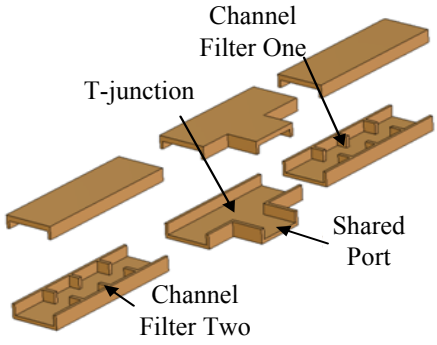

Figure 1 Waveguide diplexer with T-junction

The channel filters in multiplexers and two-port filters can be designed based on coupled resonator circuits [2-4]. Coupled resonator circuits are very important in RF/microwave filters design, especially for the narrow-band passband filters. The topology and transmission characteristics of a filter based on a coupled resonator network can be described by its coupling matrix and external quality factors, whatever the physical structure of the device. This filter design method is extended to multiplexer design where the device is only based on the coupled resonators, without an additional common junction. This allows a significant reduction in size of the multiplexer, due to the suppression of the removal of the common junction used in conventional multiplexers [5].

The coupled-resonator based diplexers, without additional common junction, introduced in this paper, is derived from one described in reference [2]. One example is illustrated in Figure 2, it is a schematic of a diplexer with 8 resonators. Each circle represents a resonator, and the short lines between resonators are internal couplings. The ar-

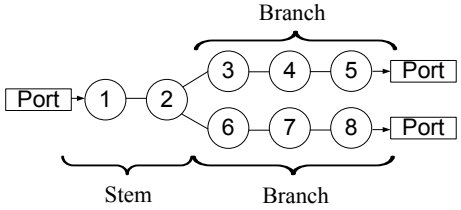

Figure 2 An 8-resonator based diplexer

rowed lines between resonators and ports represent external couplings. The very leading part, containing resonators 1 and 2 we call the stem; two branches are coupled to the second resonator of the stem. The stem of the diplexer has the characteristics of a dual band all-pole bandpass filter [6], while the branches work as Chebyshev bandpass filters.

Similar work, known as Star-Junction diplexer, has been done by G. Macchiarella and S. Tamiazzo [3], in which channels are split from only the first resonator.

Coupling Matrix of Diplexers

The coupling matrix of n coupled resonators in a diplexer has been derived from the equivalent circuit by formulation of impedance matrix for magnetically coupled resonators or admittance matrix for electrically coupled resonators in a similar way to the two-port formulation and is given in [1]. A general normalized coupling matrix $[A]$ in terms of coupling coefficients and external quality factors has been derived [2] as shown in equation (1)

$$[A] = [q] + p[U] - j[m] \tag{1}$$

$$= \begin{bmatrix} \frac{1}{q_{e1}} & \cdots & & \cdots & \\ \vdots & \ddots & \vdots & \vdots & \vdots \\ 0 & \cdots & & \cdots & \\ & & q_{e2} & & \\ \vdots & \vdots & \vdots & \ddots & \vdots \\ 0 & \cdots & & \cdots & \\ & & & & q_{e3} \end{bmatrix} + p \begin{bmatrix} 1 & \cdots & & 0 \\ \vdots & \ddots & \vdots & \vdots \\ & & 1 & \\ 0 & \cdots & & 1 \end{bmatrix} - j \begin{bmatrix} m_{11} & \cdots & & m_{1n} \\ \vdots & \ddots & \vdots & \vdots \\ m_{(n-1)1} & \cdots & & m_{(n-1)n} \\ m_{n1} & \cdots & & m_{nn} \end{bmatrix}$$

where $[U]$ is the $n \times n$ identity matrix, n is the number of the resonators, p is the low-pass prototype frequency, $[m]$ is the coupling matrix and entry m_{ij} is the normalized coupling coefficient between resonators i and j, $[q]$ is an $n \times n$ matrix with all entries zero except for $q_{mm} = \frac{1}{q_{eM}}$ (m refers to resonators connecting to ports) where q_{eM} is the scaled external quality factor of resonator m to port M.

The scattering parameters derived from the general coupling matrix [2] are as follow:

$$S_{11} = \pm\left(1 - \frac{2}{q_{e1}}[A]^{-1}_{11}\right) \quad S_{M1} = 2\frac{1}{\sqrt{q_{e1} \cdot q_{eM}}}[A]^{-1}_{M1} \quad (M = 2 \ \ to \ \ 3) \tag{2}$$

The design procedure of the diplexer coupling matrix is done by applying a gradient-based local optimisation technique, which is similar to the approach in [2],[7-8]. It is based on minimisation of a cost function that is evaluated the values of scattering parameters at frequency locations including reflection zeros, maximum return points and passband edges. The initial starting values for the optimisation are based on a dual band filter for the stem and simple Chebyshev filters for the branches.

Principles and Responses of the Coupled-Resonator Based Diplexer

The stem of the coupled-resonator based diplexer works as a dual-band bandpass filter. It attenuates signals outside of two passbands but plays no role in splitting signals on these two bands. The two branches of the diplexer work as Chebyshev filters with different centre frequencies. Each branch occupies one of two pass-bands of the stem and attenuates signals outside of the passband of the branch. Signals passing through the stem will be guided to one of these two branches and reflected by the other. As a result, signals are split to different ports.

The topology of the coupled-resonator based diplexers is flexible by altering the length (number of resonators) on the stem and branches. The structures of 10-resoantor diplexers, with different number of resonators on the stem and their responses are shown in Figure 3.

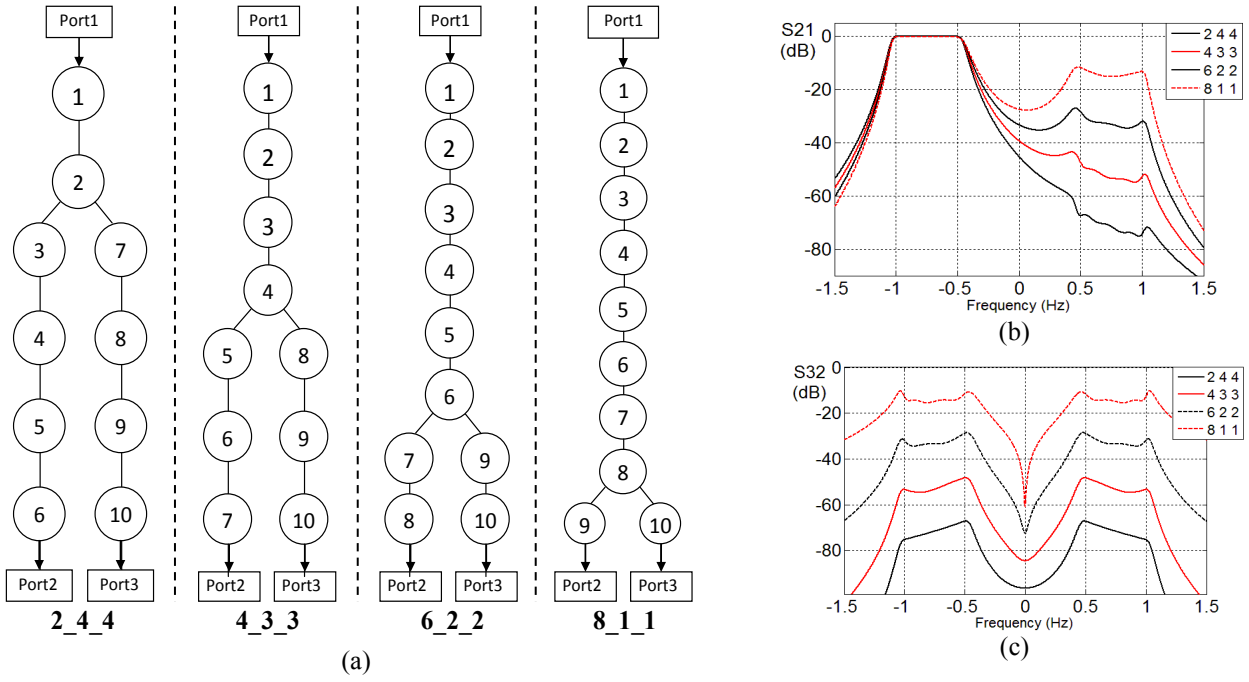

Figure 3 (a) The structures of 10-resonator diplexers, (b) Transmission responses and (c) Isolations of the prototype ones. The notation of the diplexer *M_N_N* indicates the number of resonators on stem part and branches respectively. (e.g. 2_4_4 refers to a diplexer with 2 resonators on the stem part and 4 resonators on each branch).

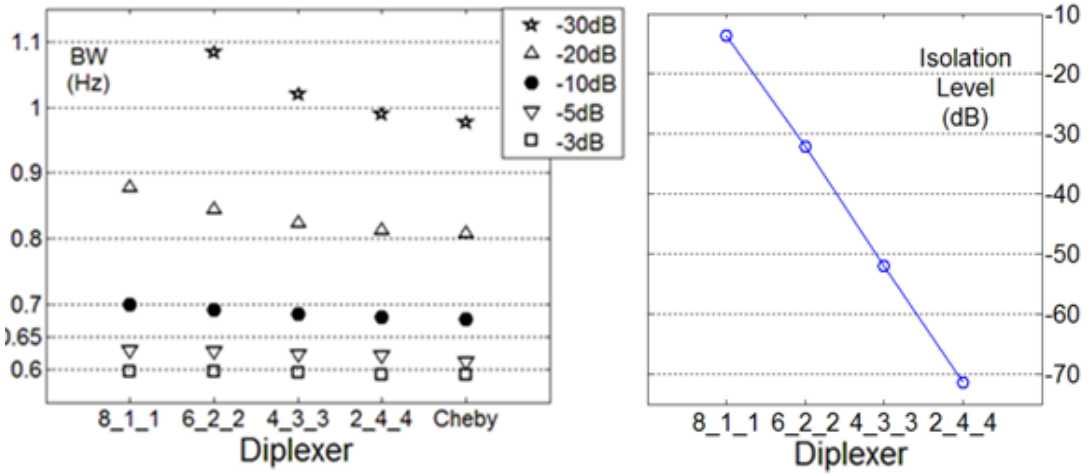

Figure 4 (a) Comparison of bandwidth from diplexers and equivalent 5-order Chebyshev bandpass filter (b) Isolations of diplexers

Figure 4(a) shows the effect on the bandwidths of the diplexers by altering the length of stem and branches. It shows various bandwidth definitions from the -3dB bandwidth to the -30dB bandwidth. The longer the length of branch, the closer the response is to the simple Chebyshev. The comparison of isolations, in Figure 4(b), shows that such responses become better with increasing length of the branches.

The coupling matrices of the diplexers shown in Figure 3(a) are listed here.

2_4_4 : $m_{i,i+1}=m_{i+1,i}$ =[0.8205, 0.2850, 0.1620, 0.1594, 0.2166, 0, 0.2850, 0.1620, 0.1594, 0.2166]

$m_{2,7}=m_{7,2}$= 0.2850; $m_{i,i}$=[0, 0, 0.7008, 0.7443, 0.7477, 0.7484, -0.7008, -0.7443, -0.7477, -0.7484]

4_3_3 : $m_{i,i+1}=m_{i+1,i}$ =[0.8205, 0.4033, 0.7168, 0.2317, 0.1613, 0.2170, 0, 0.1613, 0.2170]

$m_{4,8}=m_{8,4}$=0.2317 ; $m_{i,i}$ =[0, 0, 0, 0, 0.7186, 0.7448, 0.7466, -0.7186, -0.7448, -0.7466]

6_2_2 : $m_{i,i+1}=m_{i+1,i}$ =[0.8175, 0.4040, 0.7140, 0.3287, 0.7310, 0.2286. 0.2190, 0, 0.2190]

$m_{6,9}=m_{9,6}$=0.2286 ; $m_{i,i}$ =[0, 0, 0, 0, 0, 0, 0.7236, 0.7444, -0.7236, -0.7444,]

8_1_1 : $m_{i,i+1}=m_{i+1,i}$ =[0.8145, 0.4054, 0.7107, 0.3315, 0.7226, 0.3290, 0.7280, 0.3023, 0]

$m_{8,10}=m_{10,8}$= 0.3023; $m_{i,i}$ =[0, 0, 0, 0, 0, 0, 0, 0, 0.7112, -0.7112]

The external quality factors of four diplexers are exactly the same and are given by:

$q_{e1}=1.943;\ \ q_{e2}=q_{e3}=2\times q_{e1}=3.886$

Conclusions

In this work, the responses and topologies of new diplexer structures are investigated. These diplexers have flexible topology by altering the number of resonators on the stem and branches. Higher isolation and lower bandwidths occur with increasing numbers of resonators in the branches.

Reference

[1]. J.S. Hong and M.J. Lancaster, "Microstrip filters for RF/microwave applications". 2001, New York: Wiley.

[2] T. Skaik, M. Lancaster, and F. Huang, "Synthesis of Multiple Output Coupled Resonator Microwave Circuits Using Coupling Matrix Optimization," IET Journal of Microwaves, Antenna & Propagation, vol.5, no.9, pp. 1081-1088, June 2011.

[3] G. Macchiarella, S. Tamiazzo, "Synthesis of Star-Junction Multiplexers"; Microwave Theory and Techniques, IEEE Transactions on, Volume: 58, Issue: 12, Dec. 2010, Pages: 3732 – 3741.

[4]]. F. Loras-Gonzalez, S. SobriNo-Arias, I. Hidalgo-Carpintero, A. Garcia-Lamperez and M. Salazar-Palma, "A Novel Ku-band Dielectric Resonator Triplexer Based on Generalized Multiplexer Theory," 2010 IEEE MTT-S International Microwave Symposium Digest, May 2010, Pages: 884 – 887.

[5] T. Skaik, "A Synthesis of Coupled Resonator Circuits with Multiple Outputs using Coupling Matrix Optimisation", Part 4.5, Chapter 5, Page 123. PhD Thesis, March 2011, School of Electronic, Electrical and Computer Engineering, the University of Birmingham.

[6] D. Deslandes and F. Boone, "Iterative Design Techniques for All-Pole Dual-Bandpass Filters," IEEE microwave and wireless components letters, vol. 17, no. 11, November 2007

[7]. A.B. Jayyousi, and M.J. Lancaster, "A gradient-based optimisation technique employing determinants for the synthesis of microwave coupled filters," IEEE MTT-S International Microwave Symposium, USA, vol. 3, pp. 1369-1372, June 2004.

[8] X. Shang, Y. Wang, G.L.Nicholson, and M. J. Lancaster, "The Design of Multiple-Passband Filters using Coupling Matrix Optimisation", In press by IET Microw. Antennas Propagat.

Novel Multiplexer Topologies Based on All-Resonator Structures

Xiaobang Shang, Yi Wang, *Senior Member, IEEE*, Wenlin Xia, Michael J. Lancaster, *Senior Member, IEEE*

***Abstract*— This paper presents two novel multiplexer topologies based on all-resonator structures. Such all-resonator structures remove the need for conventional transmission-line based splitting networks. The first topology is a diplexer with transmission zeros in the guard band, shared by both channels. These transmission zeros are generated by introducing a cross coupling in a quadruplet in resonators common to both channels. A twelfth order diplexer, with a pair of transmission zeros is presented here as an example. The second topology is a multiplexer with a bifurcate structure which limits the connections to any resonator to three or less, regardless of the number of output channels. A sixteenth order four-channel multiplexer is presented as an example. Both topologies have been demonstrated at X-band using waveguide technology. Good agreements between measurements and simulations have been achieved.**

***Index Terms*—Multiplexer, diplexer, resonator filters, coupling matrix optimization.**

1. INTRODUCTION

A multiplexer is a multiple port frequency distribution circuit, usually employed in a communication system to split input signals from a common port into several channels operating at different frequencies. It can also be used to combine several channels into a single composite signal for transmission through a common antenna. The common approach to the synthesis of a multiplexer involves designing each channel filter individually, and combining with a frequency distribution network formed of circulators [1]-[2], hybrid couplers [3]-[4], or manifolds [5]-[9]. A multiplexer configuration consisting of a resonant junction (i.e. an extra resonator apart from those in the channel filters) is proposed in [10]-[11]. In this case channel filters are connected via this resonant junction, and the interaction between channel filters can be taken into consideration during the multiplexer synthesis. In [12]-[14], multiplexer structures based on only resonators (without external resonant junctions) are proposed, and here we expand these studies to four channels and the use of transmission zeros in the design. We also experimentally demonstrate the ideas in waveguide. For this all resonator structure, resonators at the junctions are not only employed as the frequency distribution network, but also as resonator poles for the filter responses. This multiplexer structure eliminates the need for separate transmission-line based frequency distribution networks leading to a reduction in the overall component size and volume. The synthesis of this all-resonator multiplexer is based on optimization of coupling matrices. Various topologies can be explored by simply adding coupling coefficients into the matrix during the synthesis. This extra freedom offers new possibilities in selecting achievable topologies, such as the two novel multiplexer structures presented in this paper (as shown in Fig. 1).

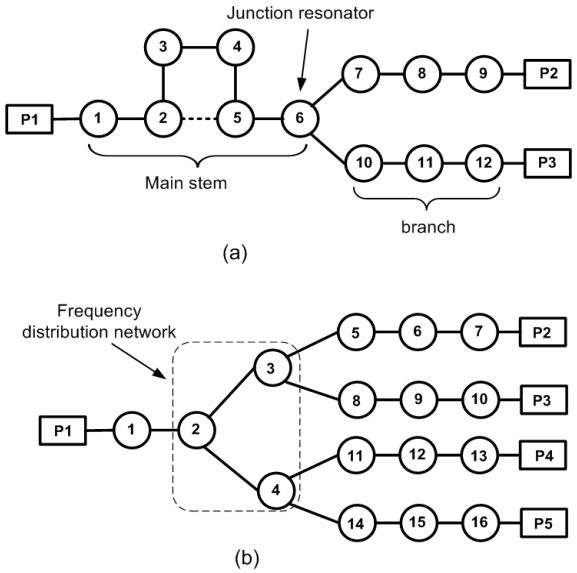

Fig. 1. Two novel multiplexer topologies proposed in this paper. (a) A diplexer with transmission zeros in guard band shared by both channels. (b) A four-channel multiplexer structure.

Conventionally, to obtain the desired quasi-elliptic filtering responses for a specified channel, cross couplings need to be introduced to the corresponding channels in order to generate transmission zeros. In this work, we demonstrate a novel diplexer design with two transmission zeros located at the middle guard band. These two transmission zeros are shared by both channels, and are generated by introducing a cross coupling in a quadruplet in the main stem, as shown in Fig. 1

Manuscript received March 22, 2013. This work was supported by the U.K. Engineering and Physical Science Research Council (EPSRC) under contract EP/H029656/1.

Xiaobang Shang, Wenlin Xia and Michael J. Lancaster are with the School of Electronics, Electrical and Computer Engineering, the University of Birmingham, B15 2TT, U.K. (e-mail: x.shang@bham.ac.uk).

Yi Wang is with the School of Engineering, University of Greenwich (Medway Campus), Central Avenue, Chatham Maritime, Kent ME4 4TB, U.K. (email: yi.wang@greenwich.ac.uk)

(a). This significantly improves the rejection in the guard band

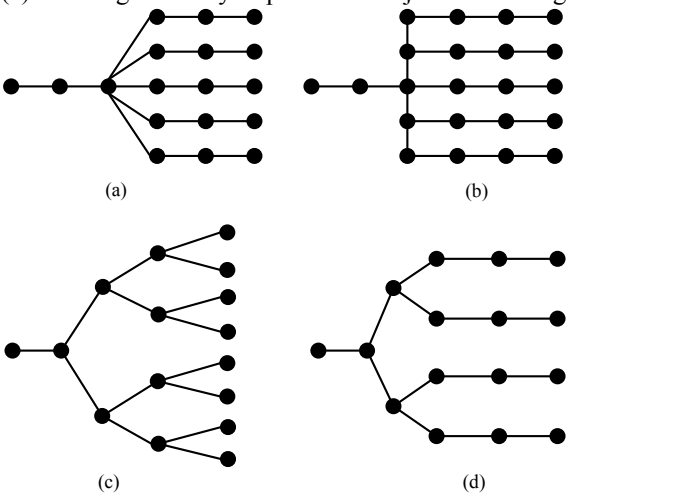

Fig. 2. Different topologies of multiplexers. (a) A star-junction topology [11]. (b) A multiplexer topology which limits the maximum connections to any resonator to four [15]-[16]; (c) A novel topology presented in [15]. The bifurcated structure reduces the maximum number of couplings associated with one resonator to three; (d) A simplified structure to the one shown in (c). This topology is essentially the same as the one shown in Fig. 1 (b).

without the penalty of increasing the number of resonators or cross-couplings. This diplexer topology can be implemented using any type of resonators. In this work, X-band waveguide resonators operating at TE_{101} mode are used.

For a multiplexer with multiple outputs, the topologies shown in Fig. 2 (a) and (b) can be employed to divide the input signal into many sub-bands. Both topologies contain a resonator which has four or more connections. This increases the difficulty of physical implementation. In some scenarios, where there are more than four channels, it may be difficult or even impossible to connect all the channel filters to the same resonator. This problem can be addressed by using a bifurcate topology shown in Fig. 2 (c). In this case, none of the resonators has more than three connections, regardless of the number of outputs. For a four-channel multiplexer, the topology, consisting of three junctions as shown in Fig. 2 (d), can be used. This work demonstrates such a sixteenth order four-channel multiplexer (see Fig. 1 (b)) at X-band using waveguide technology.

The paper is organized as follows: The all-resonator multiplexer structure is discussed in Section II, followed by detailed descriptions of the above-mentioned topologies in Section III and IV. The experimental results of both devices are presented in Section V and a conclusion is given in Section VI.

2. ALL-RESONATOR MULTIPLEXER STRUCTURE

In this work, the design technique for two-port coupled resonator filters [17] is extended to the design of all-resonator based multiplexers. The coupling matrix of a multiplexer based on n-coupled resonators can be derived in a similar way as the filter network discussed in detail in [13]. A general matrix $[A]$ can be expressed as

$$[A]=[q]+p[U]-j[m] \tag{1}$$

where $[U]$ is the $n\times n$ unit matrix, p is the complex low-pass frequency variable, $[q]$ is a $n \times n$ matrix with all entries zero except for $q_{ll}=1/q_{el}$ (l stands for the index of the resonator connected to external ports), $[m]$ is the general normalized coupling matrix including elements m_{ij} and m_{ii} Where m_{ij} is the normalized coupling coefficient between resonators i and j. The non-zero diagonal entries m_{ii} accounts for asynchronous tuning that determine the resonant frequency of the i^{th} resonator. The scattering parameters (reflection S_{11}, transmission S_{l1} and isolation $S_{l1,l2}$) derived from the general coupling matrix may be written in terms of a generalized coupling matrix $[A]$ as follows

$$\begin{aligned} S_{11} &= \pm\left(1-\frac{2}{q_{e1}}[A]_{11}^{-1}\right) \\ S_{l1} &= 2\frac{1}{\sqrt{q_{e1}\cdot q_{el}}}[A]_{l1}^{-1} \\ S_{l_1l_2} &= 2\frac{1}{\sqrt{q_{el_1}\cdot q_{el_2}}}[A]_{l_1l_2}^{-1} \end{aligned} \tag{2}$$

In this work, a gradient-based local optimization technique has been applied to synthesize the coupling matrices. The optimization is based on minimization of a cost function that evaluates the values of scattering parameters at critical frequency locations, including reflection zeros, transmission zeros (if specified), peak return loss points and each channel's passband edges, as reported in detail in [13]. The efficiency of numerical methods, employing local optimization algorithms, depends highly on the quality of the initial values. The initial coupling coefficients of resonators on the branches have been obtained from corresponding Chebyshev responses. Given the high quality initial values, the gradient-based local optimisation algorithm has successfully optimized coupling matrices of multiplexers with various topologies.

Fig. 3 illustrates an example of a twelfth order triplexer, with symmetrical and equal-bandwidth filtering response, as shown in Fig. 4. The initial values of this triplexer are calculated from three Chebyshev filters with the same bandwidth of 2 rad/s centred at -3.5, 0 and 3.5 rad/s. The optimised normalized coupling coefficients and external quality factors are q_{e1}=0.3116, q_{e4}=0.9765, q_{e8} = q_{e12}= 0.9423, $m_{1,2}$ = 1.5678, $m_{2,3}$ = 0.6906, $m_{3,4}$ = 0.882, $m_{5,6}$ = $m_{9,10}$ =0.9167, $m_{6,7}$ = $m_{10,11}$ =0.7178, $m_{1,5}$ = $m_{1,9}$ = 2.1702, $m_{7,8}$ = $m_{11,12}$ = 0.9107, $m_{5,5}$ = -$m_{9,9}$ = -2.7214, $m_{6,6}$ = -$m_{10,10}$ = -3.3159, $m_{7,7}$ = -

$m_{11,11}$ = -3.4502, $m_{8,8}$ = -$m_{12,12}$ = -3.4775. Resonators of the left channel filter (i.e. S_{31}) and right channel filter (i.e. S_{41}) have negative and positive self-coupling coefficients, respectively. These self-couplings are used to offset the resonant frequencies into their corresponding passbands.

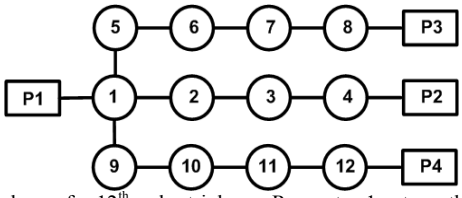

Fig. 3. Topology of a 12th order triplexer. Resonator 1 acts as the frequency distribution component as well as one pole to the final triplexer responses.

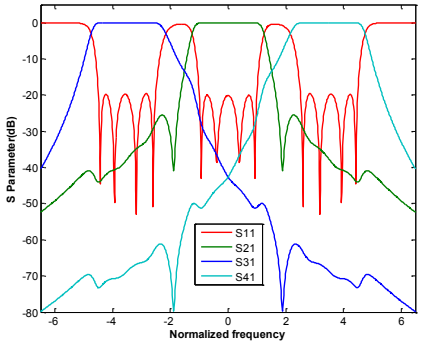

Fig. 4. *S* parameters over the normalized frequency of the triplexer with a topology shown in Fig. 3.

As shown in Fig. 4, this twelve-order triplexer has twelve reflection zeros. The junction resonator 1 acts as both a frequency distribution element and a resonator pole of the triplexer. It may be noted that two transmission zeros occur by the middle channel's transmission response (S_{21}), as shown in Fig. 4. This is attributed to the combined effect of the left and right channels, which operate like a shunt inductor and a shunt capacitor loaded to the middle channel.

3. TOPOLOGY-I

A twelfth order diplexer, with a coupling topology shown in Fig. 1 (a) and *S* parameter response depicted in Fig. 5, is now discussed. A cross coupling between resonators 2 and 5 is introduced in a quadruplet to provide a pair of transmission zeros for both channels. For comparison, the response of a diplexer without the cross coupling is also plotted in Fig. 5. It is evident that the two transmission zeros provide significant (20 dB) improvement on the attenuation at the middle guard band with only a small penalty of slightly worsening rejection level at the outer stopbands. It should be noted that additional cross couplings could be added to the branches to achieve transmission zeros at the outer stopband.

This cross-coupled diplexer can be roughly treated as a combination of three separate parts: a sixth order dual-band filter in the stem (resonators 1-6) and two third-order all-pole Chebyshev filters in the branches. The dual-band main stem splits the input signal into two passbands and feeds into two all-pole bandpass filters with different centre frequencies. This property has been utilised to generate initial values for the coupling matrix optimisation.

The final optimised coupling coefficients for the normalized prototype are: q_{e1} = 1.4329, q_{e9} = q_{e12}=2.9957, $m_{1,2}$ = 0.8326, $m_{2,3}$ = 0.3944, $m_{2,5}$ = 0.2894, $m_{3,4}$ = 0.4201, $m_{4,5}$ = 0.2745, $m_{5,6}$ = 0.6913, $m_{6,7}$ =$m_{6,10}$ = 0.2644, $m_{7,8}$ = $m_{10,11}$= 0.2015, $m_{8,9}$ = $m_{11,12}$ = 0.2757, $m_{7,7}$ = -$m_{10,10}$ = -0.663, $m_{8,8}$ = -$m_{11,11}$ = -0.6855, $m_{9,9}$ = -$m_{12,12}$ = -0.6822. It should be noted that all the coupling coefficients for the main stem are positive. The presence of finite transmission zeros is attributed to the destructive interference between signals from different paths [18]. The diplexer has been implemented using waveguide cavity resonators operating at TE_{101} mode coupled together through

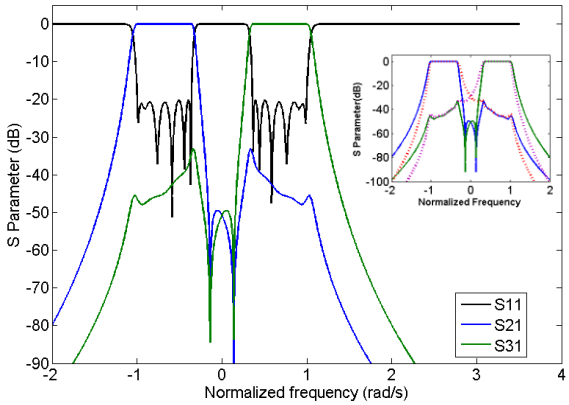

Fig. 5. *S* parameter responses of the diplexer over the normalized frequency. The inset shows the comparison in transmission responses between the diplexer with cross-coupling (solid lines) and the one without cross-coupling (dashed lines).

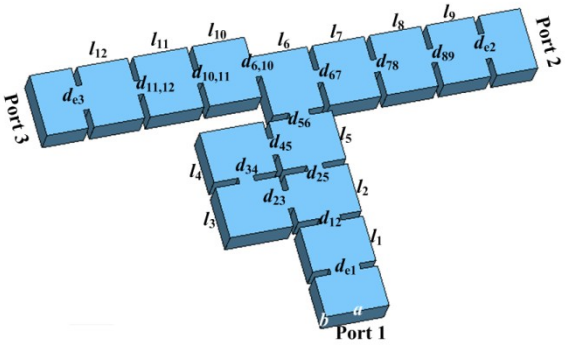

Fig. 6. Configuration of the twelfth order X-band diplexer structure. *a*=22.86, *b*=10.16, l_1=16.85, l_2=17.94, l_3=18.97, l_4=18.76, l_5=18.33, l_6=18.56, l_7=18.76, l_8=18.68, l_9=17.28, l_{10}=18.85, l_{11}=19.47, l_{12}=18.22, d_{e1}=10.77, d_{e2}=9.58, d_{e3}=9.27, d_{12}=7.31, d_{23}=6.84, d_{25}=5.53, d_{34}=5.41, d_{45}=6.36, d_{56}=6.99, d_{67}=4.88, d_{78}=4.78, d_{89}=5.34, $d_{6,10}$=7.69, $d_{10,11}$=4.94, $d_{11,12}$=5.27. Unit: mm. All the irises have the same thickness of 2 mm.

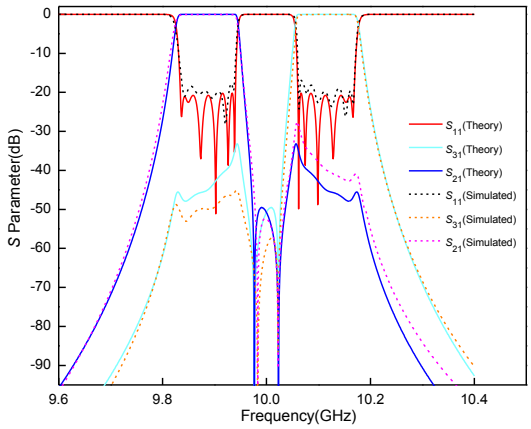

Fig. 7. *S* parameter responses of the X-band diplexer from simulation (dashed lines) and coupling matrix (solid lines).

inductive irises, as shown in Fig. 6.

The diplexer is designed to be centered on 10 GHz, and the passband centre frequency is 9.885 GHz for channel 1 and 10.115 GHz for channel 2; the channel bandwidth is 0.11 GHz; the passband return loss of each channel is 20 dB, and the attenuation at the middle guard band is 49.5 dB. Fig. 7 shows the diplexer responses obtain from CST [19] simulations using the dimensions given in Fig. 6.

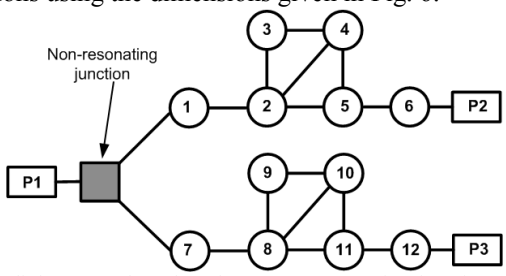

Fig. 8. A diplexer topology based on a non-resonating junction to achieve transmission zeros at guard-band for both channels [20]. In order to achieve two transmission zeros for each channel, four cross-couplings are added to the resonators at branches.

A comparison has been made [20] with a same order diplexer with a non-resonating junction and separate cross-couplings at the two branches, as shown in Fig. 8. Given the same specifications, it has been found that the topology in Fig. 8 exhibits a larger attenuation level at the middle guard-band and a higher isolation between two channels. However, the topology in Fig. 1 (a) has advantages in terms of (i) better out-of-band rejection; (ii) lower number (one versus four) of cross-couplings; and (iii) therefore easier physical implementation.

4. TOPOLOGY-II

A sixteenth order 4-channel multiplexer with a topology shown in Fig. 1 (b) has been designed. This topology uses three resonators (i.e. resonators 2, 3 and 4) to split the input signal into four channels. All the resonators have three or less links with other resonators. This topology can be further extended for multiplexers with more than 4 channels. For the 4-channel multiplexer presented here, its coupling matrix is optimised using the same technique described in Section II. A more detailed discussion on the coupling matrix optimisation for this type of structure is given in [21].

The final optimised normalised coupling coefficients, together with external quality factors are: q_{e1} = 1.8622, q_{e7} = 7.4078, q_{e10} =7.4964, q_{e13} =7.4947, q_{e16} =7.4078, $m_{1,2}$ =0.7263, $m_{2,3}$ = $m_{2,4}$ = 0.4002, $m_{3,3}$ = -$m_{4,4}$ = -0.4476, $m_{3,5}$ = $m_{4,14}$ =0.1745, $m_{3,8}$ = $m_{4,11}$ = 0.1314, $m_{5,5}$ = -$m_{14,14}$ = -0.8195, $m_{5,6}$ = $m_{14,15}$ = 0.0928, $m_{6,6}$ = -$m_{15,15}$ = -0.8674, $m_{6,7}$ = $m_{15,16}$ = 0.1151, $m_{7,7}$ = -$m_{16,16}$ = -0.8713, $m_{8,8}$ = -$m_{11,11}$ = -0.3028, $m_{8,9}$ = $m_{11,12}$ = 0.0885, $m_{9,9}$= -$m_{12,12}$ = -0.2928, $m_{9,10}$ = $m_{12,13}$ = 0.1139, $m_{10,10}$ = -$m_{13,13}$ =-0.2924. This topology is demonstrated at X-band using inductive irises coupled TE_{101} cavities. Fig. 9 shows the structure of this multiplexer together with the final dimensions. Resonators of the channel filters are folded to form a compact structure. Again the multiplexer is designed to be centred at 10 GHz with equally spaced four channels. The central frequencies of the four channels are 9.895 GHz, 9.965 GHz, 10.035 GHz and 10.105 GHz. Each channel has a bandwidth of 0.03 GHz and a desired passband return loss of 20 dB. Fig. 10 shows the simulated *S*-parameter responses of the multiplexer with the dimensions given in Fig. 9. The simulation results agree extremely well with the theoretical ones calculated from coupling matrix. Both CST [19] and μwave wizard [22] have been used to simulate the multiplexer. The two simulators produce very close results. Although the multiplexer presented here exhibits non-contiguous passbands, it is possible to achieve continuous-band multiplexer using the same topology (see Fig. 1 (b)) and coupling matrix optimisation approach, as reported in [21]. In additional, non-contiguous multiplexer with different guard-band to pass-band ratios are also feasible [21].

Both the 12th order diplexer and 16th order multiplexer have a large number of resonators and complex inter-resonator couplings. Therefore it is difficult to obtain the desired physical dimensions for these two devices by following the conventional design approach for direct coupled filters [17]. Here, an alternative design approach [23], based on electromagnetic (EM) simulations, has been used to extract the dimensions. The multiplexer structure is constructed by successively adding one resonator at a time in the simulation. At each step, only the dimensions of one cavity and its connecting irises are significantly tuned towards the desired responses calculated from the corresponding coupling coefficients of the sub-matrix. This reduces the number of dimensions to be simultaneously optimized during the design. This procedure also eliminates the need of a global optimisation on all the dimensions within an electromagnetic simulator, as discussed in detail in [23].

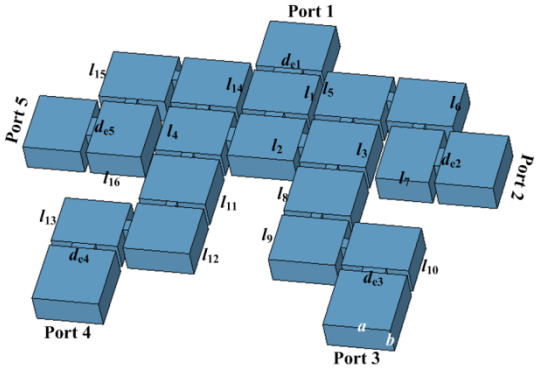

Fig. 9. Configuration of the X-band multiplexer structure. a=22.86, b=10.16, resonator lengths: l_1=17.37, l_2=18.43, l_3=19.13, l_4=18.78, l_5=19.77, l_6=19.82, l_7=18.96, l_8=19.56, l_9=19.60, l_{10}=18.71, l_{11}=19.32, l_{12}=19.36, l_{13}=18.47, l_{14}=19.09, l_{15}=19.10, l_{16}=18.27, coupling gaps between adjacent resonators: d_{e1}=9.79, d_{e2}=7.90, d_{e3}=7.88, d_{e4}=7.88, d_{e5}=7.80, d_{12}=6.37, d_{23}=6.05, d_{24}=6.00, d_{35}=4.25, d_{38}=3.97, d_{56}=4.03, d_{67}=4.02, d_{89}=3.57, $d_{9,10}$=4.16, $d_{4,11}$=3.94, $d_{11,12}$=3.55, $d_{12,13}$=4.14, $d_{4,14}$=4.23, $d_{14,15}$=3.95, $d_{15,16}$=4.00. Unit: mm. All the irises have the same thickness of 2 mm.

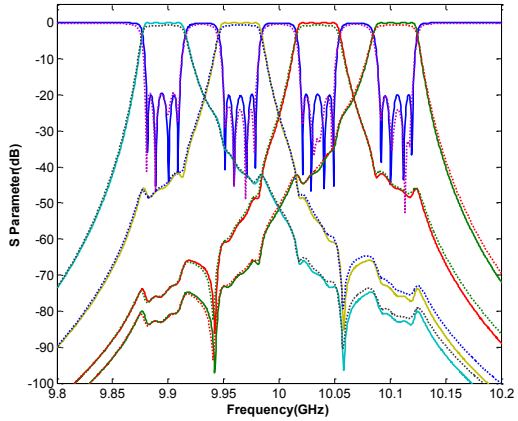

Fig. 10. *S* parameter responses of the multiplexer from simulation (dashed lines) and coupling matrix (solid lines).

5. EXPERIMENTAL VERIFICATION

The diplexer is machined from copper and is shown in Fig. 11. The measurement results (after tuning) agree very well with the simulated responses as shown in Fig. 12. The passband insertion loss is measured to be around 0.6 dB, which is close to the expected value of 0.4 dB obtained from CST simulations based on the conductivity of copper (i.e. 5.96×10^7 S/m). The passband of channel 1 has a measured maximum return loss of 18 dB, whereas the passband of channel 2 has a maximum return loss of 14 dB. The isolation between two bands is measured to be over 25 dB.

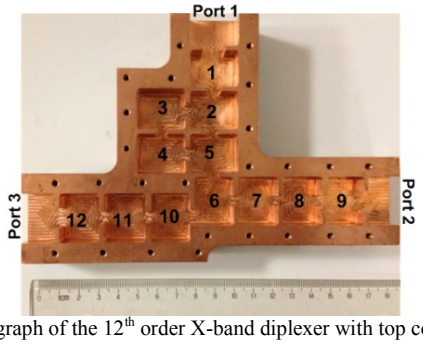

Fig. 11. Photograph of the 12th order X-band diplexer with top cover removed.

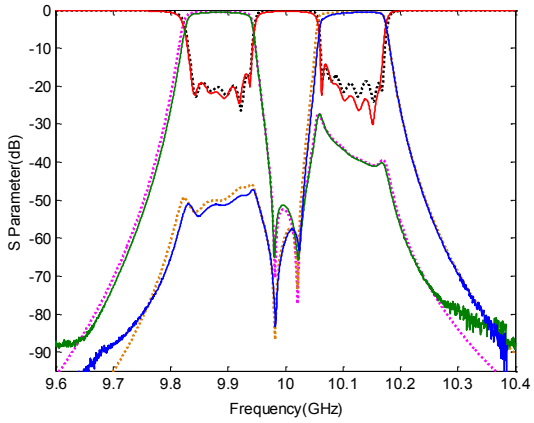

Fig. 12. Measurement results (solid lines) and simulation results (dashed lines) of the diplexer. The simulations were performed in CST [19] using a conductivity of copper (5.96×10^7 S/m).

The multiplexer is made from aluminum and is shown in Fig. 13. The measurement results (after tuning) are depicted in Fig. 14. Again, good agreement has been achieved between simulation and measurement. All 16 poles are identifiable. The insertion loss for the four channels is measured to be 1.8 dB, 1.6 dB, 1.9 dB and 1.5 dB, respectively, whereas the expected passband insertion loss obtained from CST simulations is 0.7 dB. The noticeable higher-than-simulated loss is mainly attributed to (i) the way the multiplexer is constructed (The multiplexer is split along H-plane into two pieces. Imperfect contact at the joints in the two pieces results in additional loss, as current flows across these joints [24]); (ii) the effect of the tuning screw holes drilled on the top cover.

Both measurements are subject to a full two-port TRL (Thru, Reflect, Line) calibration. It should be noted that tuning screws have been utilized for both devices to compensate for any fabrication inaccuracies and the inner rounded corners of the resonators caused by the milling tool.

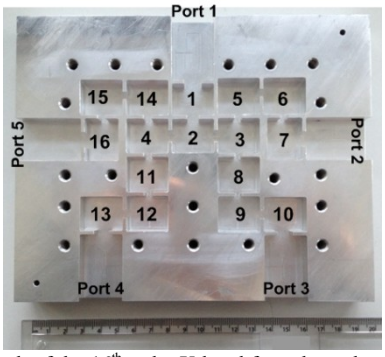

Fig. 13. Photograph of the 16th order X-band four channel multiplier with top cover removed.

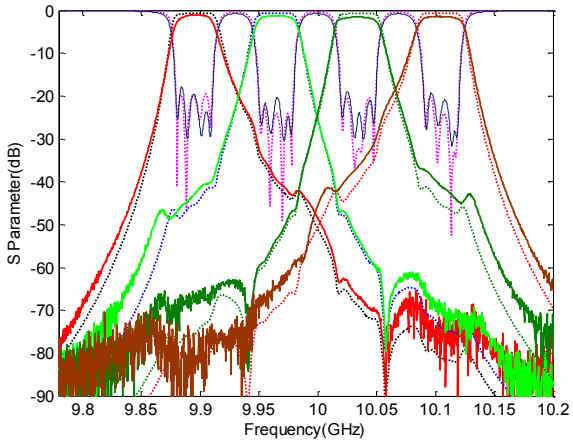

Fig. 14. Measurement results (solid lines) and simulation results (dashed lines) of the four-channel multiplexer. The simulations were performed in CST [19] using a conductivity of aluminium (3.56×10^7 S/m).

6. Conclusion

In this paper we have reported two novel multiplexer topologies based on all-resonator based filtering networks. The first topology employs a cross-coupling in the main stem to produce a pair of transmission zeros at the middle guard-band, for both channels. This topology facilitates the design of diplexers with a sharp roll-off in the guard band or reduced guard-bandwidth. The second topology utilised a bifurcate structure, which will find useful application in multiplexers with a large number of sub channels. The maximum number of connections of any resonator is limited to three. These all-resonator based multiplexers are fully characterized using the coupling matrix. Gradient-based local optimisation is performed on the coupling coefficients to achieve desired responses. The relationships between the multiplexer coupling coefficients and the standard Chebyshev filters and dual-band filters have been investigated. These relationships have been employed to produce good quality initial values which are critical to the convergence of the local optimisation algorithm. Both topologies have been demonstrated at X-band using waveguide cavities operating at TE_{101} mode. The measurement results for both devices agree very well with simulations.

Acknowledgment

The authors would like to thank Prof. Giuseppe Macchiarella with Politecnico Di Milano, Italy, for carrying out the comparison between diplexers with different topologies. Appreciation also goes to Mr. Warren Hay with the University of Birmingham, UK, who has fabricated the diplexer.

References

[1] R. R. Mansour, S. Ye, V. Dokas, B. Jolley, G. Thomson, W.Tang, C. M. Kudsia, "Design considerations of superconductive input multiplexers for satellite applications," *IEEE Trans. Microw. Theory Tech.,* vol.44, No.7, pp.1213-1228, July 1996

[2] R. R. Mansour, "Design of superconductive multiplexers using single-mode and dual-mode filters," *IEEE Trans. Microw. Theory Tech.,* vol.42, No.7, pp.1411-1418, July 1994

[3] S. H. Talisa, M. A. Janocko, D. L. Meier, J. Talvacchio, C. Moskowitz, D. C. Buck, R. S. Nye, S. J. Pieseski, and G. R. Wagner, "High temperature superconducting space-qualified multiplexers and delay lines," *IEEE Trans. Microw. Theory Tech.*, vol. 44, no. 7, pp. 1229-1239, Jul. 1996.

[4] T.K. Kataria, S Shih-Peng., A. Corona-Chavez, T. Itoh, "New approach to hybrid multiplexer using composite right-left handed lines," *IEEE Microw. Wireless Comp. Lett.*, vol. 21, no.11, pp. 580 – 582, Nov. 2011

[5] J.D. Rhodes, R. Levy, "Design of general manifold multiplexers," *IEEE Trans. Microw. Theory Tech.*, vol. 27, no. 2, pp. 111-123, Feb. 1979

[6] D.J. Rosowsky, D. Wolk, "A 450-W output multiplexer for direct broadcasting satellites," *IEEE Trans. Microw. Theory and Tech.*, vol. 30, no. 9, pp. 1317-1323, Sep. 1982

[7] R. J. Cameron, M. Yu, "Design of manifold-coupled multiplexers," *IEEE Microw. Magazine*, vol. 8, no. 5, pp. 46-59, Oct. 2007

[8] D. Bariant, S. Bila, S., D. Baillargeat, S. Verdeyme, P. Guillon, D. Pacaud, J.-J. Herren, "Method of spurious mode compensation applied to manifold multiplexer design," in *IEEE MTT-S International*, 2002, pp. 1461 - 1464

[9] L. Accatino, M. Mongiardo, "Hybrid circuit-full-wave computer-aided design of a manifold multiplexers without tuning elements," *IEEE Trans. Microw. Theory and Tech.*, vol. 50, no.9, pp. 2044-2047, Sep 2002

[10] G. Macchiarella, S. Tamiazzo, "Novel approach to the synthesis of microwave diplexers," *IEEE Trans. Microw. Theory Tech.*, vol. 54, no. 12, pp. 4281-4290, Dec. 2006

[11] G. Macchiarella, S. Tamiazzo, "Synthesis of star-junction multiplexer," *IEEE Trans. Microw. Theory Tech.*, vol.58, No.12, pp.3732-3741, Dec. 2010.

[12] A. Garcia-Lamperez, M. Salazar-Palma, T. K. Sarkar, "Compact multiplexer formed by coupled resonators with distributed coupling," in *IEEE Antennas Propagation Society International Symposium*, July 3-8 2005, pp. 89-92

[13] T. Skaik, M. Lancaster, and F. Huang, "Synthesis of multiple output coupled resonator microwave circuits using coupling matrix optimization," *IET Journal of Microwaves, Antenna & Propagation*, vol.5, no.9, pp. 1081-1088, June 2011

[14] W. Xia, X. Shang, and M. Lancaster, "Responses comparisons for coupled-resonator based diplexers," in *IET 3rd Annual Seminar on Passive RF and Microwave Components*, London, March 2012.

[15] M. J. Lancaster, "Radio frequency filter," W.I.P.O patent WO/01/69712, 2001.

[16] Isidro Hidalgo Carpintero et al, "Generalized multiplexing network," US patent 2006/0114082 A1, 2006

[17] J.S. Hong and M.J. Lancaster, "Microstrip filters for RF/microwave applications". 2001, New York: Wiley.

[18] J. Brian Thomas, "Cross-Coupling in Coaxial Cavity Filters-A Tutorial Overview," *IEEE Trans. Microw. Theory and Tech.*, 51, (4), pp.1368-1376, 2003

[19] CST Microwave Studio Germany, CST GmbH, 2006.

[20] G. Macchiarella, private communication

[21] Y. Wang, M. J. Lancaster, " An investigation on the coupling characteristics of a novel multiplexer configuration," *submitted to the 2013 European Microwave Conference*

[22] μwave wizard, Mician GmbH, 2012

[23] X. Shang, W. Xia, M. J. Lancaster, " The design of waveguide filters based on cross-coupled resonators," *submitted to the 2013 European Microwave Conference*

[24] N. J. Cronin, "Microwave and optical waveguides". 2010, John Wiley and Sons

The design of waveguide filters based on cross-coupled resonators

Xiaobang Shang[1*], Wenlin Xia[2*], Michael J. Lancaster[3*]
[*]School of Electronics, Electrical and Computer Engineering, the University of Birmingham, Birmingham, B15 2TT, U.K.
[1]x.shang@bham.ac.uk; [2]wxx989@bham.ac.uk; [3]m.j.lancaster@bham.ac.uk

***Abstract*— This paper addresses the physical realization of cross-coupled waveguide filters based on electromagnetic (EM) simulations. For this design procedure, the filter structure is simulated by successively adding one resonator at a time. The desired filter response is achieved without the need of a global optimisation on all the mechanical dimensions within an electromagnetic simulator. This reduces the design time required for a cross-coupled waveguide filter and allows the possibility of building high-order waveguide filters with complex cross-couplings. A sixth order X-band dual-band filter with a centre frequency of 10 GHz and a fractional bandwidth of 1% is designed using this procedure and presented here as an example. Excellent agreement between simulation results and theoretical results from coupling matrix verifies the proposed approach.**

Keywords—filter; waveguide; cross-coupling; coupling matrix; dual-band filter

1 INTRODUCTION

A microwave filter is a two-port network employed to transmit and attenuate signals in specified frequency bands. Microwave filters have found wide applications in modern communication systems, radar systems and laboratory measurement equipments [1]. Filters based on cross-coupled resonators, with real or complex transmission zeros (TZs), have been extensively used to (i) improve the close-to-band selectivity; (ii) achieve in-band group delay linearity; (iii) divide the single-band into multiple passbands. However, compared with the conventional in-line resonator coupled filter, the cross-coupled filter is more difficult to be physically implemented, due to the interactions introduced by the cross-couplings.

Traditionally, the design methods for direct coupled filters have been applied to extract the dimensions for cross-coupled filters. This design process usually involves the following four main steps: (i) identify the filter order and filter functions according to specification requirements; (ii) synthesis or optimise the coupling coefficients ($M_{i,j}$) and external quality factors (Q_e) that can realize the desired filter function; (iii) choose the filter type (waveguide, microstrip, etc), and obtain dimensions which can achieve desired specified Q_e and $M_{i,j}$ from EM simulations on one resonator and two weakly coupled resonators; (iv) construct the filter in the simulator to get its initial responses [1]-[2]. For cross-coupled filters, this approach ignores the influences from cross-couplings, and therefore normally requires a global optimisation on all the physical dimensions. This global optimisation is time-consuming, and in some special scenario, where the filter consists of a large number of resonators and/or complex cross-couplings, the final optimisation may fail to converge to an acceptable solution, due to the large amount of control parameters. In [3], a design procedure, which eliminates the need of global optimisation, has been presented for a cross-coupled folded waveguide filter. A fourth order and a sixth order cross-coupled single-band waveguide filters have been successfully demonstrated using this design approach. However, this design approach is limited to waveguide filters with folded topologies.

In this paper, we present an EM-based design approach for determining the physical dimensions of a cross-coupled waveguide filter with any type of topology. This design procedure enables us to account for the attributions of cross-couplings, and provides precise desired dimensions without the need of a final global optimisation. This approach may find useful application in the design of resonator based cross-coupled waveguide filters or multiplexers [4].

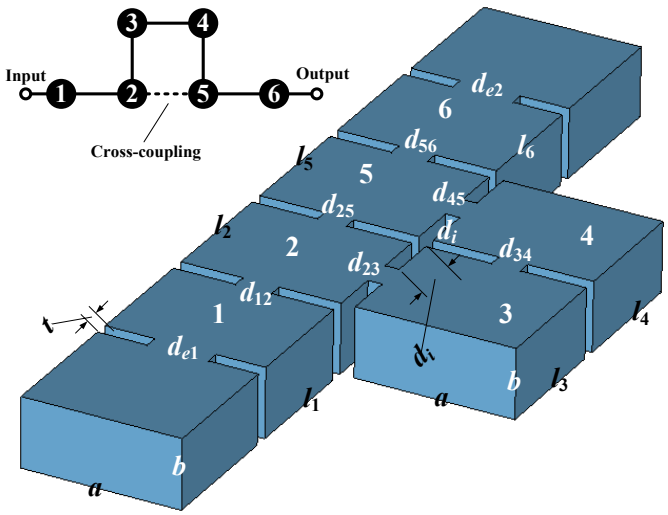

Fig. 1. Illustration of a 6th order X-band dual-band waveguide filter and its topology. There is a cross coupling between resonators 2 and 5. These six resonators are operating at TE_{101} mode and they are coupled together through inductive irises. All the irises have the same thickness t of 2 mm, a=22.86 mm, b=10.16 mm, d_i=5.19 mm.

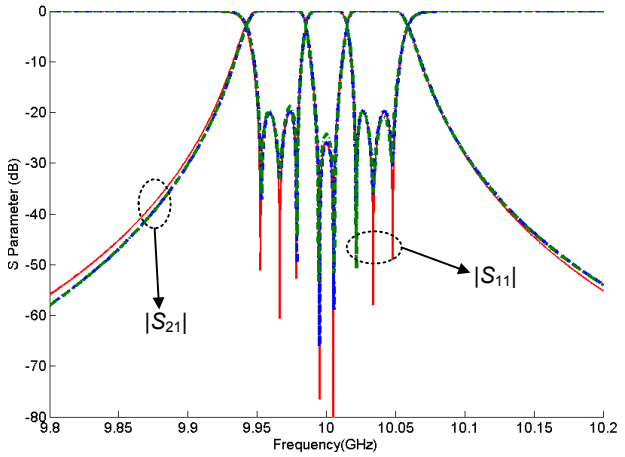

Fig. 2 The X-band dual-band filter results from coupling matrix (red solid lines), μwave wizard simulations (dashed blue lines) and CST simulations (dotted green lines). Dimensions obtained at Step 6 shown in Tables I and II have been used in these simulations.

2 DESIGN STEPS

The design approach is demonstrated by a sixth order X-band dual-band waveguide filter. Fig. 1 illustrates the topology and the structure of this filter. This filter is designed to have the following specifications: the centre frequency is 9.965 GHz for the first passband and 10.035 GHz for the second passband, both passbands have a desired return loss of 20 dB and the same bandwidth of 30 MHz, the attenuation level for the middle stopband is better than 26 dB. The $N\times N$ coupling matrix of this dual-band filter, as depicted below, is generated by a synthesis technique described in [5]. Their corresponding *S*-parameter responses can be found in Fig. 2. A pair of symmetrical transmission zeros positioned at 9.995 GHz and 10.005 GHz occur at the in-band to split it into two symmetrical passbands. These two transmission zeros are attributed to the cross-coupling between resonators 2 and 5. As all the coupling coefficients are positive, thereby all inductive irises have be utilised by this filter.

$$M = \begin{pmatrix} 0 & 0.00852 & 0 & 0 & 0 & 0 \\ 0.00852 & 0 & 0.00372 & 0 & 0.00388 & 0 \\ 0 & 0.00372 & 0 & 0.00384 & 0 & 0 \\ 0 & 0 & 0.00384 & 0 & 0.00372 & 0 \\ 0 & 0.00388 & 0 & 0.00372 & 0 & 0.00852 \\ 0 & 0 & 0 & 0 & 0.00852 & 0 \end{pmatrix}$$

$Q_{e1}=Q_{e6}=145.77$.

The design can be divided into six sub-steps, as shown in Fig. 3. At work step, rather than optimising dimensions for the entire structure, only the dimensions of one cavity and its connecting irises are significantly tuned towards the desired responses. This reduces the number of dimensions to be adjusted during the design, which in return yields faster and more reliable convergence. Especially for large scale filter structure, in which case it is virtually impossible to optimise all the mechanical dimensions at the same time. The calculation of the physical dimensions for the sixth order dual-band filter shown in Fig. 1 comprises the following steps.

(1) Calculate the approximate initial dimensions for all the resonators and irises using the equivalent circuit models based on the coupling matrix as described in [1], [6]-[7].

(2) Using the coupling matrix values calculated for the entire filter, obtain just the responses for the first resonator (see Fig 3 (a)). Use the full-wave simulator (in our case, μwave wizard [8]) to evaluate resonator 1 together with its two adjacent irises, and optimize this simulated response towards the desired one from coupling matrix, by changing the resonator length (l_1) and iris dimensions (d_{e1} and d_{12}).

(3) Use the EM simulator for both resonators 1 and 2 and their connecting irises (see Fig. 3(b)). Adjust the length of resonator 2 (l_2) and iris dimensions (d_{23} and d_{25}) to match the responses with the target ones derived from the coupling matrix. The dimensions associated with resonator 1 obtained in Step 2 should be slightly adjusted to account for the influence of resonator 2. This can be done with optimisations and has a fast convergence due to the final result being close to the optimum.

(4) Progress through the filter structure by adding only one resonator into the simulated structure at each time, as illustrated in Fig. 3. Optimise the dimensions of the subsequent resonator towards the desired *S*-parameter responses calculated from coupling matrix. A slight readjustment of the dimensions of the preceding resonators may be required to factor in the influence from the new added resonator. Normally this small adjustment in dimensions is only required for adjacent resonators. For instance, at the last step (see Fig. 3 (f)), the dimensions of resonator 1 will remain the same as the ones obtained in Step 5, since resonator 6 has a negligible impact on resonator 1.

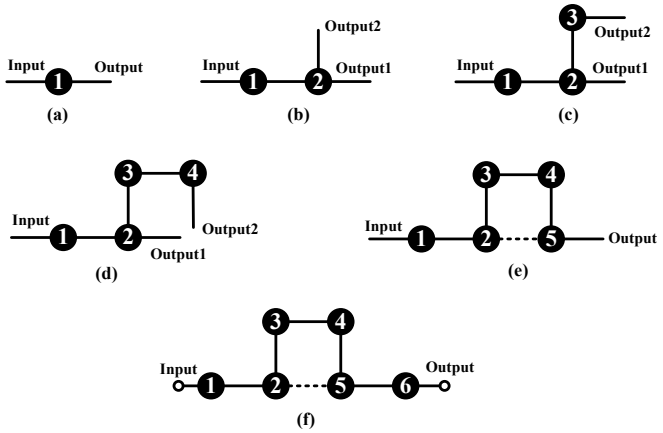

Fig. 3. The dual-band filter structure shown in Fig. 1 is constructed successively by adding one resonator at a time. The six steps of this design procedure are shown in (a)-(f) in sequence.

For this design approach, the middle stage S-parameter responses are calculated from their corresponding coupling coefficients, and act as the objective responses for the tuning. To plot the desired responses at each stage, the inner coupling coefficient needs to be converted into external quality factor. For instance, at Step 1, Q_{e2} should be calculated from M_{12}. After expressing both the external quality factor (Q_e) and internal coupling coefficients (M_{ij}) using inverter value K [1], the relationship between M_{ij} and Q_e can be found as:

$$M_{ij}^2 \cdot Q_e = \frac{1}{\frac{\pi}{2} \cdot \left(\frac{\lambda_g}{\lambda} \right)^2} \tag{1}$$

where λ_g is guided wavelength and λ is the free-space wavelength. For an X-band waveguide filter operating at a centre frequency of 10 GHz, $M_{ij}^2 \times Q_e$ is calculated to be 0.3625. Consequently, M_{ij} can be converted to its corresponding Q_e. It is interesting to note that, the value of $M_{ij}^2 \times Q_e$ does not depend on the fractional bandwidth (FBW) of the filter.

In additional, it may be observed from Fig. 3 that, for work steps 2 to 5, there are three external ports. However, both equations of $N \times N$ [2] and $(N+2) \times (N+2)$ [1] matrix are derived for a two-port network circuit. In the following, the equations for $(N+3) \times (N+3)$ matrix, which can be applied to calculate S-parameter responses of a three-port filter network, will be derived and given.

Reference [4] reports equations for computing three-port filter network *S*-parameter responses. However, these equations are derived following the similar approach to a $N \times N$ coupling matrix [2], and therefore has a restriction that the resonators number should be larger than the number of external ports. In the work presented here, there exists a case that the resonator number is less than the number of ports (see Fig. 3 (b)), thereby a similar approach to the $(N+2) \times (N+2)$ matrix synthesis is applied in this work to derive the equations. Here, the relationship between the *S*-parameters and the coupling matrix is extracted by analysing the node voltage and current of the three-port network's equivalent circuits, as described in detail in [1], [2] and [4]. The matrix m for a general three-port network consists of N coupled resonators, one input port (S) and two output ports ($L1$, $L2$) can be written in the following form:

$$m = \begin{array}{c|cccccccc} & S & 1 & 2 & 3 & \dots & N & L1 & L2 \\ \hline S & & m_{s,1} & m_{s,2} & m_{s,3} & \dots & m_{s,N} & m_{s,L1} & m_{s,L2} \\ 1 & m_{1,s} & m_{1,1} & m_{1,2} & m_{1,3} & \dots & m_{1,N} & m_{1,L1} & m_{1,L2} \\ 2 & m_{2,s} & m_{2,1} & m_{2,2} & m_{2,3} & \dots & m_{2,N} & m_{2,L1} & m_{2,L2} \\ 3 & m_{3,s} & m_{3,1} & m_{3,2} & m_{3,3} & \dots & m_{3,N} & m_{3,L1} & m_{3,L2} \\ \vdots & \vdots & \vdots & \vdots & \vdots & & \vdots & \vdots & \vdots \\ N & m_{N,s} & m_{N,1} & m_{N,2} & m_{N,3} & \dots & m_{N,N} & m_{N,L1} & m_{N,L2} \\ L1 & m_{L1,s} & m_{L1,1} & m_{L1,2} & m_{L1,3} & \dots & m_{L1,N} & & m_{L1,L2} \\ L2 & m_{L2,s} & m_{L2,1} & m_{L2,2} & m_{L2,3} & \dots & m_{L2,N} & m_{L2,L1} & \end{array} \tag{2}$$

The above matrix is symmetrical about the principal diagonal and it includes the couplings between external ports and the internal resonators. Additionally, it is also possible to accommodate the direct couplings between external ports, such as $m_{S,L1}$, $m_{S,L2}$ and $m_{L1,L2}$. The dual-band filter presented here does not include any direct coupling between ports, as shown in Fig. 3, therefore $m_{S,L1}$, $m_{S,L2}$ and $m_{L1,L2}$ are assigned to zero here. The highlighted part (using grey colour) represents the core $N \times N$ matrix, whose entries are normalised coupling coefficients ($m_{ij}=M_{ij}$/FBW). The coupling coefficients between external ports and inner resonators can be calculated by

$$m_{S,1} = \frac{1}{\sqrt{q_{e1}}},\ m_{N1,L1} = \frac{1}{\sqrt{q_{e2}}},\ m_{N2,L2} = \frac{1}{\sqrt{q_{e3}}} \tag{3}$$

where q_{ei} is the normalized external quality factors of the external port i ($q_{ei}=Q_{ei} \times$FBW), N_1 and N_2 refer to the resonator number connecting to the output ports ($L1$ and $L2$). For instance, at Step 3 as shown in Fig. 3 (c), $N_1=2$, $N_2=3$. The general matrix A can be expressed as below

$$[A] = [R] + p[U] - j[m] \tag{4}$$

where U is similar to a $(N+3) \times (N+3)$ unit matrix, except that $U(1,1) = U(N+2,N+2) = U(N+3,N+3) = 0$, R is a $(N+3) \times (N+3)$ matrix whose only nonzero entries are $R(1,1) = R(N+2,N+2) = R(N+3,N+3) = 1$, p is the low-pass frequency variable, which can be written in terms of FBW and the filter centre frequency (ω_0) as

$$p = j \frac{1}{FBW} \left(\frac{\omega}{\omega_0} - \frac{\omega_0}{\omega} \right) \tag{5}$$

Then the *S*-parameter responses of a three-port filter network can be expressed as:

$$\begin{aligned} S_{11} &= 1 - 2[A]_{1,1}^{-1} \\ S_{21} &= 2[A]_{N+2,1}^{-1} \\ S_{31} &= 2[A]_{N+3,1}^{-1} \end{aligned} \tag{6}$$

For the case where there are more than three external ports, similar equations can be derived accordingly by adding extra rows at the bottom and extra columns at the right, to the coupling matrix shown in equation (2).

3 RESULTS

The six sub-step responses for the structures shown in Fig. 3 are depicted in Fig. 4. In Fig. 4, the dashed lines refer to the theoretical responses plotted using the equations described in Section II, and these responses are served as goals of the dimensional tuning. The μwave wizard [8] based on mode-matching technique is employed in the simulations. The

simulated responses using the optimised dimensions are denoted as solid lines in Fig. 4.

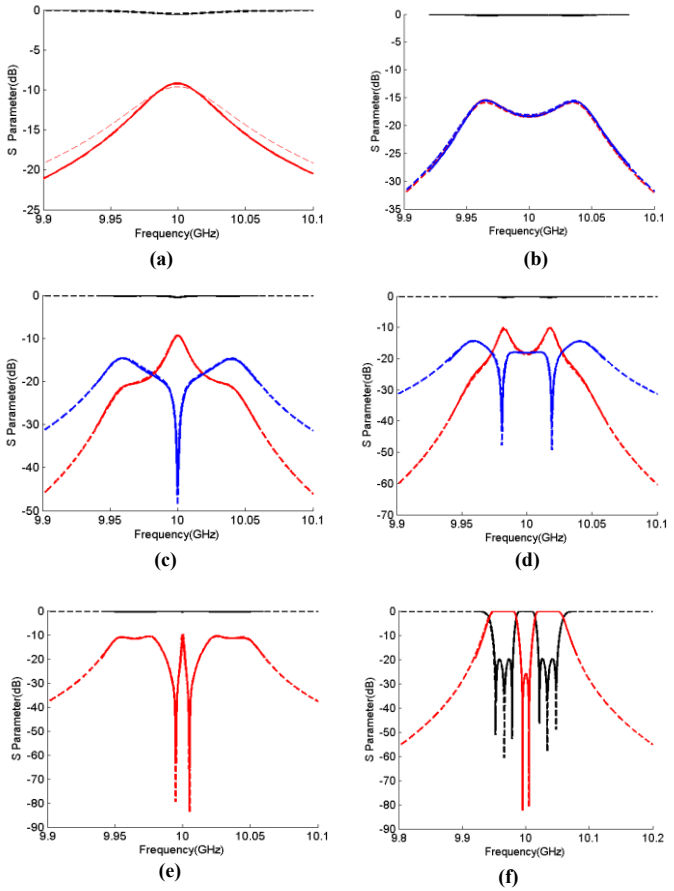

Fig. 4. *S*-parameters of the dual-band filter as successive resonators are added and tuned. Their corresponding topologies can be found in Fig. 3. Note that, S_{11} responses are included and represented using black lines in all six graphs. The dashed lines represent the desired responses which are plotted from coupling matrix, whereas the solid lines correspond to the responses from simulations using the optimised dimensions given in Table I and II.

At each sub-step, initially only one resonator's dimensions (three or less parameters) are tuned in the simulations. Therefore, a desired set of dimensions, whose corresponding responses match the objective ones, can be obtained within a short time. The dimensions from the previous stages may also be slightly altered to tune the responses towards the desired ones, as shown in Tables I and II. It can be observed that, only very small adjustments are required on the dimensions achieved in the foregoing stages, to account for the influence from the subsequent resonators.

The final dimensions of the dual-band filter are shown in Tables I and II (Step 6), and their corresponding simulation results can be found in Fig. 2. It can be observed that, without any global optimization, the final acquired dimensions have extremely close responses with the theory ones from coupling matrix. It should be pointed out that, both µwave wizard and CST microwave studio [9] have been employed to simulate the dual-band filter. These two EM simulators produce very close results, as shown in Fig. 2.

TABLE I: Dual-band filter iris dimensions at each step.

Step	Dimensions of iris (mm)							
	d_{e1}	d_{12}	d_{23}	d_{25}	d_{34}	d_{45}	d_{56}	d_{e2}
1	8.42	5.06	-	-	-	-	-	-
2	8.71	5.17	4.41	4.14	-	-	-	-
3	8.70	5.18	4.65	4.13	4.13	-	-	-
4	8.73	5.15	4.67	4.13	4.14	4.38	-	-
5	8.70	5.17	4.63	4.12	4.13	4.62	5.17	-
6	8.70	5.17	4.63	4.12	4.13	4.62	5.17	8.76

TABLE II: Dual-band filter resonators length at each step.

Step	Length of resonators (mm)					
	l_1	l_2	l_3	l_4	l_5	l_6
1	18.2	-	-	-	-	-
2	18.06	19.01	-	-	-	-
3	18.07	18.99	19.39	-	-	-
4	18.06	18.99	19.39	19.41	-	-
5	18.06	18.99	19.39	19.40	18.99	-
6	18.06	18.99	19.39	19.40	18.98	18.05

4 CONCLUSIONS

A mechanical dimensions calculation method for cross-coupled waveguide filters has been described. During this design procedure, the filter structure is constructed step by step by adding one resonator to the simulated structure at a time. Dimensions of this resonator are tuned towards the desired target middle stage responses. Equations have been derived and provided in this paper to plot the middle stage responses from coupling matrix. A sixth order dual-band X-band filter with a pair of symmetrical transmission zeros has been successfully demonstrated using this approach. This approach eliminates the need of a global EM-based dimensional optimisation, and therefore leads to a reduction in the time required. Moreover, it also opens the possibility of building high-order waveguide filters with complex cross-couplings.

REFERENCES

5 R. J. Cameron, C. M. Kudsia, R. R. Mansour, Microwave Filters for Commmunication Systems. John Wiley & Sons, Inc., 2007.

6 J. S. Hong, M. J. Lancaster, Micrsotrip Filters for RF/microwave Applications, New York: Wiley, 2001.

7 J. Kocbach, K. Folgero, " Design procedure for waveguide filters with cross-couplings," in the 2002 IEEE MTT-S Digest, pp. 1449-1452.

8 T. F. Skaik, M. J. Lancaster, F. Huang, " Synthesis of multiple output coupled rsoantor circuits using coupling matrix optimisation," IET Microw. Anten. Propag., 2011, vol. 5, no. 9, pp.1081-1088.

9 X. Shang, Y. Wang, G. L. Nicholson, M. J. Lancaster, "Design of multiple-passband filters using coupling matrix optimisation," IET Microw. Anten. Propag., 2012, vol. 6, no. 1, pp.24-30.

10 F. M. Vanin, D. Schmitt, R. Levy, " Dimensional synthesis for wideband waveguide filters," in the 2004 IEEE MTT-S Digest, pp. 463-466.

11 F. M. Vanin, D. Schmitt, R. Levy, " Dimensional synthesis for wide-band filters and diplexers," IEEE Trans. Microw. Theory Tech., 2004, vol. 52, no. 11, pp. 2488-2495.

12 µwave wizard, Mician GmbH, 2012

13 CST Microwave Studio Germany, CST GmbH, 2006.

All-Resonator Based Waveguide Diplexer With Cross-Couplings

Wenlin Xia, Xiaobang Shang, M.J. Lancaster

This paper reports on an investigation into new diplexer topologies, based on all-resonator structures with cross-couplings between common resonators (shared by both channels) and branch resonators. This all-resonator structure eliminates the need for separate frequency distribution networks and uses resonators to achieve this functionality. For diplexers based on such all-resonator structures, cross-couplings can be added between the common resonators and branch resonators to achieve some desired specification (e.g. improved isolation). Two diplexer topologies with such cross-couplings are presented. The first topology is implemented at X-band using waveguide technology. Excellent measurement results verified the proposed topology as well as the design procedure.

Introduction: Diplexers are critical components to a communication system, where there is need to separate or combine two RF channels. Many design and implementation techniques for diplexer circuits have been developed. Among these techniques, the most common approaches are to design each channel filter separately and then combine them with a frequency distribution network such as a manifold [1], a resonant junction [2], a circulator [3] or a hybrid coupler [4]. Recently, diplexers based on all-coupled resonators have been proposed [5-7]. In this approach, a resonator can not only be used to provide a reflection zero, but also as a signal distribution element. This effectively reduces the size of the diplexers by removal of the conventional distribution network. In addition, as the diplexer is formed of only resonators, a single coupling matrix can be used to fully characterise its response, and therefore the coupling between different channel filters can be accurately determined during the synthesis. In [7], such a diplexer, based on all-resonators, with a cross-coupling between common resonators (i.e. resonators in the main stem) has been reported. Its topology is shown in Fig.1*a*.

Here, we extend the study into utilising cross-couplings between common resonators and branch resonators. This increases the possible frequency responses significantly, and facilitates the designs with some challenging and difficult specifications, such as a high isolation and a sharp rejection. Two diplexer topologies, with such cross-couplings, as shown in Fig. 1, are investigated and presented here. The first diplexer (Fig. 1*b*) is demonstrated at X-band using waveguide technology. Excellent agreement between simulation results and experiment results are achieved. To the best of authors' knowledge, this is the first-ever reported diplexer with cross-coupling between common resonators and branch resonators.

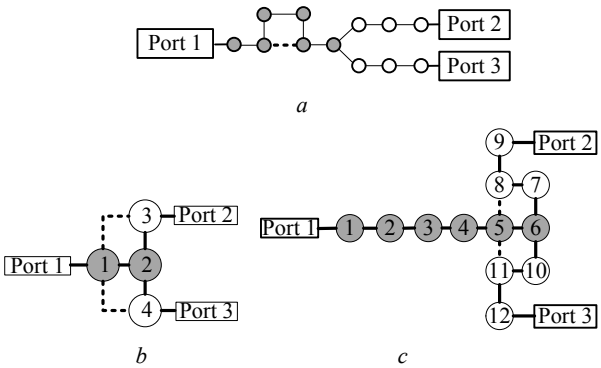

Fig. 1. *Novel diplexer topologies with cross-couplings (denoted using dotted lines) between common resonators (grey colour filled) and branch resonators (white background).*
a 12th order diplexer with a cross-coupling [7]
b Topology 1: 4th order diplexer. Two cross-couplings (i.e. $m_{1,3}$ and $m_{1,4}$) are introduced to improve the port isolation performance.
c Topology 2: 12th order diplexer. $m_{5,8}$ and $m_{5,11}$ are employed to generate transmission zeros which are capable of increasing the out-of-band attenuation.

Coupling matrix design: The coupling matrices for both topologies are obtained using a gradient-based optimization technique [7]. Fig. 2 shows *S*-parameter responses of Topology 1 with the cross-coupling ($m_{1,3}$= 0.375) and for comparison purposes without the cross-coupling ($m_{1,3}$= 0). For both cases, the return loss is designed to be 20 dB and the two bands are located at a normalised frequency of [-1, -0.4] and [0.4, 1]. Their corresponding coupling coefficients and external quality factors are:

With cross-coupling: $m_{1,3}$=-$m_{1,4}$=0.375, 2q_{e1}=q_{e3}=q_{e4}=2.280, $m_{1,2}$= 0.815, $m_{2,3}$=$m_{2,4}$=0.295, $m_{3,3}$=-$m_{4,4}$=0.725. No cross-coupling: $m_{1,3}$=-$m_{1,4}$ =0, 2q_{e1}=q_{e3}=q_{e4}= 2.250, $m_{1,2}$=0.525, $m_{2,3}$=$m_{2,4}$=0.525, $m_{3,3}$=-$m_{4,4}$=0.586.

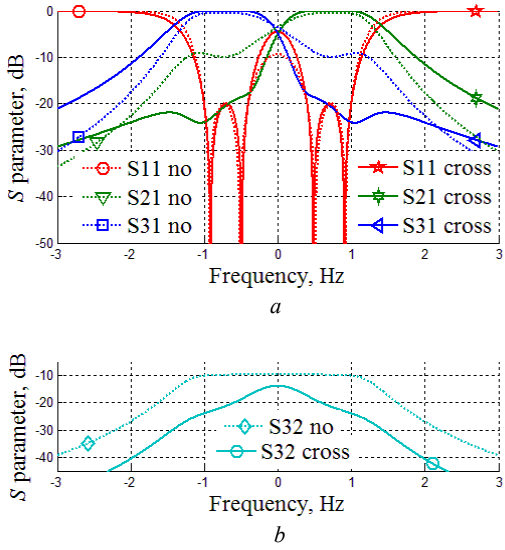

Fig. 2. *S parameter responses with and without cross-coupling $m_{1,3}$, $m_{1,4}$= -$m_{1,3}$.*
a S11, S21 and S31 responses.
b Isolation responses.

As can be observed in Fig.2*b*, by introducing cross-coupling, the isolation is improved (around 10 dB better in the middle of the passband) and the rejection is much better at the near-band frequencies. Whereas, such cross-coupling leads to a penalty of decreased far-out stopband attenuation.

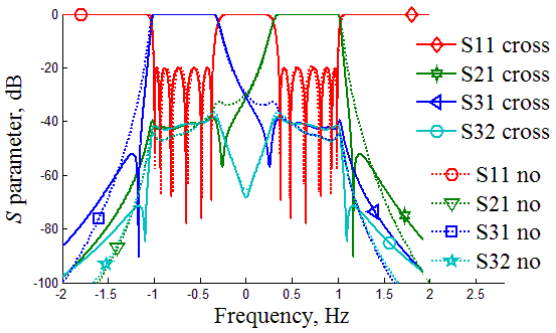

Fig. 3. *Theoretical S parameter responses of 12th order diplexer (Topology 2) with cross-coupling (in solid lines) and without cross-couplings (in doted lines).*

Using the same synthesis technique, the coupling matrix of Topology 2 has been obtained and its corresponding normalized responses are shown in Fig.3. The return loss for both bands is designed to be 20 dB and two bands are located at frequencies of [-1, -0.358] and [0.358, 1]. The coupling coefficients are: 2×q_{e1}=q_{e9}=q_{e12}=3.096, $m_{1,2}$=0.792, $m_{2,3}$= 0.477, $m_{3,4}$=0.635, $m_{4,5}$=0.404, $m_{5,6}$=0.635, $m_{6,7}$= $m_{6,10}$=0.282, $m_{5,8}$= $m_{5,11}$=-0.08, $m_{7,8}$= $m_{10,11}$=0.184, $m_{8,9}$= $m_{11,12}$=0.271, $m_{7,7}$= -$m_{10,10}$=0.733, $m_{8,8}$= -$m_{11,11}$= 0.668, $m_{9,9}$= -$m_{12,12}$= 0.671.

As shown in Fig. 3, each channel has two transmission zeros, the presence of which are due to cross-couplings $m_{5,8}$ and $m_{5,11}$. These

transmission zeros result in a sharp roll-off at the near-out-band region while at the same time maintaining sound isolation between two ports.

4th order diplexer (Topology 1) implementation: Topology 1 has been implemented using X-band waveguide technology. It is designed by following an approach in [8]. For this approach, the diplexer is constructed by successively adding one resonator at a time in an electromagnetic (EM) simulator. This eliminates the need of a global optimization on all the mechanical dimensions and thereby reduces the design time. Fig. 4 shows the diplexer structure as well as the final dimensions.

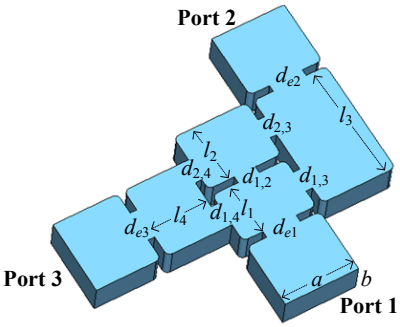

Fig. 4. *Configuration of X-band diplexer structure and its dimensions. a=22.86, b=10.16, l_1=16.15, l_2=18.27, l_3=36.11, l_4=18.09, de1=10.41, de2=10.39, de3=9.47, d_{12}=6.56, d_{13}=6.64, d_{14}=7.41, d_{23}=6.35, d_{24}=7.03, all corners have the same radius of 1.6. Unit: mm*

For this diplexer, the coupling between the 1st and 4th resonators is negative and all the other inter-resonator couplings are positive. A TE_{102} cavity is specially chosen as the 3rd resonator to provide for this coupling [9]. This is different to the other three resonators which are operating at TE_{101} mode. In order to facilitate the CNC milling, all inductive irises are employed for the couplings. To eliminate the need

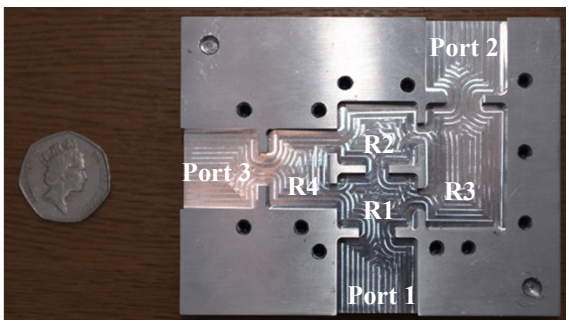

Fig. 5. *Photograph of fabricated X-band diplexer (top cover removed). Four resonators are denoted as R1-R4. Resonator 3 is operating at TE_{102} mode and the other three resonators are TE_{101} cavities. All resonators are coupled through inductive irises.*

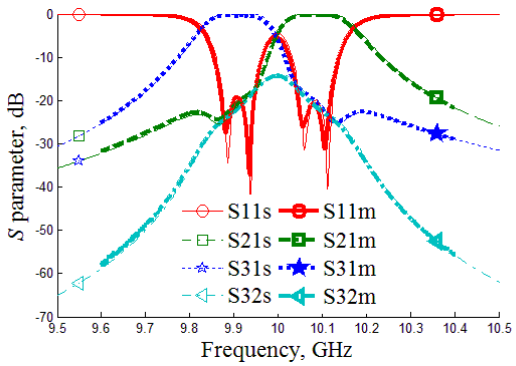

Fig. 6. *Measurement (no tuning) and simulation results of diplexer.*

for any tuning, the round inner corners with a radius of 1.6 mm, which are introduced by the milling tools, are considered during the design.

Experimental verification: The diplexer is machined from aluminium and is shown in Fig.5. The measurement results agree very well with the simulated responses, as shown in Fig. 6. The insertion loss in the middle of the passband is measured to be around 0.4 dB. The expected value is 0.25 dB obtained from CST simulations using the conductivity of aluminium. The additional insertion loss is mainly originated from the construction of the diplexer which is split along the H-plane into two pieces. The loss occurs when current flows across the imperfect contact between the two pieces [10]. The measured return loss is below 20 dB in both passbands. Tuning screws have not been utilised for this diplexer.

Conclusion: In this paper, we have presented novel diplexer topologies with cross-couplings between common resonators and branch resonators. Such cross-couplings facilitate the selection of topologies and improve the isolation performance. Two cross-coupled diplexers have been synthesised and are given here as examples. The first diplexer has been demonstrated at X-band using waveguide cavities operating at TE_{101} and TE_{102} modes. The measurement results agree well with simulations.

Acknowledgment: The authors would like to thank Mr W. Hay, University of Birmingham, Edgbaston, Birmingham, U.K., for fabricating the X-band diplexer.

Wenlin Xia, Xiaobang Shang and Michael Lancaster (School of Electronic, Electrical and Systems Engineering, University of Birmingham, U.K.)

E-mail: wxx989@bham.ac.uk

References

1. Cameron, R.J., Ming, Y.: 'Design of manifold-coupled multiplexers', *Microwave Magazine, IEEE*, 2007, **8**, (5), pp. 46-59
2. Macchiarella G., Tamiazzo S. : 'Novel Approach to the Synthesis of Microwave Diplexers', *Microwave Theory and Techniques, IEEE Transactions on*, 2006, **54**, (12), pp. 4281-4290
3. Mansour, R.R., Shen, Y., Dokas, V., Jolley, B., Thomson, G., Tang, W., Kudsia, C,M.: 'Design considerations of superconductive input multiplexers for satellite applications', *Microwave Theory and Techniques, IEEE Transactions on*, 1996, **44**, (7), pp. 1213-1228
4. Talisa, S.H., Janocko, M.A., Meier, D.L., Talvacchio, J., Moskowitz, C., Buck, D.C., Nye, R.S., Pieseski, S.J., Wagner, G.R.: 'High temperature superconducting space-qualified multiplexers and delay lines', *Microwave Theory and Techniques, IEEE Transactions on*, 1996, **44**, (7), pp. 1229-1239
5. Garcia-Lamperez, A., Salazar-Palma, M., and Sarkar, T. K.: 'Compact multiplexer formed by coupled resonators with distributed coupling', in *Antennas and Propagation Society International Symposium,* Washington, DC, USA, July, 2005, **1A**, pp. 89-92
6. Bastioli, S., Marcaccioli, L., Sorrentino, R.: 'An original resonant Y-junction for compact waveguide diplexers', in *Microwave Symposium Digest, 2009. MTT '09. IEEE MTT-S International*, Boston, MA, USA, June, 2009, pp. 1233-1236
7. Shang, X., Wang, Y., Xia, W., Lancaster, M.J.: 'Novel Multiplexer Topologies Based on All-Resonator Structures', *Microwave Theory and Techniques, IEEE Transactions on*, 2013, **61**, (11), pp. 3838-3845
8. Shang, X., Xia, W., Lancaster M.J.: 'The design of waveguide filters based on cross-coupled resonators', *Microwave and Optical Technology Letters*, 2014, **56**, (1), pp. 3-8
9. Rosenberg, U.: 'New `Planar' waveguide cavity elliptic function filters', in *Microwave Conference, 25th European*, Bologna, Italy, September, 1995, **1**, pp. 524-527
10. Cronin, N.J.: 'Microwave and optical waveguides' (John Wiley and Sons, Hoboken, NJ , USA, 2010)